On the Origins of the Ice Ages: Insolation Forcing, Age Models, and Nonlinear Climate Change

by

Peter Huybers

Submitted to the Department of Earth, Atmospheric and Planetary Sciences
in partial fulfillment of the requirements for the degree of

Doctor of Science in Climate Physics and Chemistry

at the

MASSACHUSETTS INSTITUTE OF TECHNOLOGY

May 2004

Author .....
Department of Earth, Atmospheric and Planetary Sciences
May, 2004

Certified by .....
Carl Wunsch
Cecil and Ida Green Professor of Physical Oceanography
Thesis Supervisor

Accepted by .....
Maria Zuber
Head, Department of Earth, Atmospheric and Planetary Sciences

On the Origins of the Ice Ages: Insolation Forcing, Age Models, and Nonlinear Climate Change

by

Peter Huybers

Submitted to the Department of Earth, Atmospheric and Planetary Sciences
on May, 2004, in partial fulfillment of the
requirements for the degree of
Doctor of Science in Climate Physics and Chemistry

Abstract

This thesis revolves about the relationship between orbital forcing and climate variability. To place paleo and modern climate variability in context, the spectrum of temperature variability is estimated from time-scales of months to hundreds of thousands of years using a patchwork of proxy and instrumental records. There is an energetic background continuum and rich spatial structure associated with temperature variability which both scale according to simple spectral power-laws. To complement the spatial and temporal analysis of temperature variability, a description of the full insolation forcing is also developed using Legendre polynomials to represent the spatial modes of variability and singular vectors to represent seasonal and long-term changes. The leading four spatial and temporal modes describe over 99% of the insolation variability making this a relatively simple and compact description of the full insolation forcing. Particular attention is paid to the insolation variations resulting from the precession of the equinoxes. There is no mean annual insolation variability associated with precession — precession only modulates the seasonal cycle. Nonlinear rectification of the seasonal cycle generates precession-period variability, and such rectification naturally occurs in the climate system but also results from the seasonality inherent to many climate proxies. One must distinguish this latter *instrumental* effect from true climate responses. Another potential source of spurious low-frequency variability results from the stretching and squeezing of an age-model so that noise in a record is made to align with an orbital signal. Furthermore, and contrary to assertions made elsewhere, such *orbital-tuning* can also generate an eccentricity-like amplitude modulation in records that have been narrow-band-pass filtered over the precession bands.

An accurate age-model is the linchpin required to connect insolation forcing with any resulting climatic responses, and to avoid circular reasoning, this age-model should make no orbital assumptions. A new chronology of glaciation, spanning the last 780 kilo-years, is estimated from 21 marine sediment cores using a compaction corrected depth scale as a proxy for time. Age-model uncertainty estimates are made using a stochastic model of marine sediment accumulation. The *depth-derived* ages

are estimated to be accurate to within $\pm 9,000$ years, and within this uncertainty are consistent with the orbitally-tuned age estimates. Nonetheless, the remaining differences between the depth and orbitally derived chronologies produce important differences in the spectral domain. From the δ^{18}O record, using the depth-derived ages, evidence is found for a nonlinear coupling involving the 100KY and obliquity frequency bands which generates interaction bands at sum and difference frequencies. If an orbitally-tuned age-model is instead applied, these interactions are suppressed, with the system appearing more nearly linear.

A generalized phase synchronization analysis is used to further assess the nonlinear coupling between obliquity and the glacial cycles. Using a formal hypothesis testing procedure, it is shown that glacial terminations are associated with high obliquity states at the 95% significance level. The association of terminations with eccentricity or precession is indistinguishable from chance. A simple excitable system is introduced to explore potential mechanisms by which obliquity paces the glacial cycles. After tuning a small number of adjustable parameters, the excitable model reproduces the correct timing for each termination as well as the linear and nonlinear features earlier identified in the $\delta^{18}O$ record. Under a wide range of conditions the model exhibits a chaotic amplitude response to insolation forcing. One chaotic mode gives a train of small and nearly equal amplitude 40KY cycles. Another mode permits ice to accumulate over two (80KY) or three obliquity cycles (120KY) prior to rapidly ablating and thus, on average, generates 100KY variability. The model spontaneously switches between these 40 and 100KY chaotic modes, suggesting that the Mid-Pleistocene Transition may be independent of any major shifts in the background state of the climate system.

Thesis Supervisor: Carl Wunsch
Title: Cecil and Ida Green Professor of Physical Oceanography

Acknowledgments

Above all, thanks goes to Downing. I would also like to thank my friends who made my work here a pleasure, recognize the many scientists who have shared their insights with me, and acknowledge the mentorship provided by Carl Wunsch. Funding was provided by the National Defense Science and Engineering Graduate Fellowship Program as well as NASA award NAG5-7857, NAG5-11933, and NSF award OCE-9730071.

Contents

1 Temperature variability from modern to glacial timescales **15**

1.1 A spectral patchwork 16

1.1.1 Spectral peaks 17

1.1.2 The spectral continuum 24

1.2 Heterogeneous climate variability 28

1.2.1 Spatial variability 29

1.2.2 Temporal variability 33

1.2.3 Further remarks 35

1.3 Appendix 37

1.3.1 Data 37

1.3.2 Power-density spectra 39

1.3.3 Aliasing 42

2 On Insolation Forcing **47**

2.1 Earth's orbital parameters 48

2.1.1 Eccentricity 49

2.1.2 Obliquity 50

2.1.3 Precession 51

2.2 Precession amplitude modulation: confirmation of orbital climate control or signal processing artifact? 53

2.2.1 Precession frequency and amplitude modulation 54

2.2.2 Narrow-band-pass filtering and amplitude modulation 55

2.2.3 Eccentricity modulation of precession 58

2.3 Rectification and precession signals in the climate system 62

2.3.1 Introduction 62

2.3.2 Obtaining precessional rectification 63

2.3.3 A more complete discussion . . . 66
2.3.4 Further considerations . . . 67
2.3.5 Conclusion . . . 70
2.4 Simplifications of insolation variability . . . 70
2.5 A Compact representation of insolation . . . 74
2.5.1 Spatial variability . . . 75
2.5.2 Temporal variability . . . 79
2.5.3 A simple example . . . 79
2.5.4 Interpretation . . . 80
2.5.5 Take home messages . . . 88

3 A Depth-Derived Age-Model and Nonlinear Climate Change 89
3.1 Introduction . . . 90
3.2 Data . . . 91
3.3 Time and sediment accumulation . . . 96
3.3.1 A random walk model . . . 96
3.3.2 Determining the stochastic element . . . 97
3.3.3 Sediment accumulation with autocovariance . . . 98
3.4 The depth-derived age-model . . . 101
3.4.1 Uncertainty analysis . . . 102
3.4.2 Comparison with other age-models . . . 108
3.5 The δ^{18}O signal and nonlinear climate change . . . 111
3.5.1 The spectral description of the δ^{18}O record . . . 112
3.5.2 Higher-order spectral analysis . . . 115
3.5.3 The importance of age-models . . . 116
3.6 Conclusions . . . 118
3.7 Appendix . . . 119
3.7.1 Compaction correction . . . 119
3.7.2 The XCM tuning algorithm . . . 123
3.7.3 The impact of orbital-tuning . . . 124
3.7.4 Auto-bicoherence . . . 128
3.7.5 Averaging Geophysical Records with Uncertain Age-Models . 130

4 Are the Glacial Cycles Paced by Orbital Variations? 143
4.1 Introduction . . . 144

4.2 Features of an orbital hypothesis . . . 146
4.2.1 Identifying glacial terminations . . . 148
4.2.2 Orbital phase . . . 150
4.2.3 Nonlinear coherence (Rayleigh's R) . . . 152
4.3 Lessons from the Titius-Bode "Law" . . . 154
4.4 Testing the orbital hypotheses . . . 156
4.4.1 The null-hypotheses . . . 157
4.4.2 Discussion . . . 160
4.5 Obliquity pacing of the glacial cycles . . . 163
4.6 Appendix . . . 165
4.6.1 Linear and nonlinear coherence . . . 165
4.6.2 The power of the obliquity test . . . 169

5 A Simple Deterministic Model of the Glacial Cycles 173
5.1 Introduction . . . 174
5.2 The Imbrie model . . . 176
5.2.1 Fitting to EOF1 . . . 178
5.2.2 A new source of low-frequency variability . . . 182
5.3 The Paillard model . . . 184
5.4 A new model . . . 189
5.4.1 Qualitative features . . . 189
5.4.2 A quantitative expression . . . 191
5.5 Robustness . . . 193
5.5.1 Initial conditions . . . 194
5.5.2 Parameterizations . . . 194
5.5.3 Other measures of robustness . . . 198
5.6 Comparing model and observational results . . . 201
5.6.1 Correlation and degrees of freedom . . . 201
5.6.2 Periodograms . . . 202
5.6.3 Power-laws . . . 204
5.6.4 Auto-bicoherence . . . 204
5.6.5 Summary of model comparisons . . . 206
5.7 Dynamical interpretations . . . 207
5.7.1 Excitable systems . . . 208
5.7.2 Trajectories . . . 210

5.7.3 Chaos 213
5.7.4 Multiple climate states 215
5.8 Are we still in the 40KY world? 218
5.9 Predictions and closing remarks 220

6 Summary and Conclusions **223**

Introduction

While one can make mathematical approximations to the climate system, or produce phenomena of a limited spatial scale and duration in a laboratory, the climate experiment most relevant to us has been run once. The fate of the other known planets, at best, provides a remote analogue to the Earth's climate. As climate science is primarily driven by observations and because the instrumental record is short relative to many of the climate phenomena of interest, one must piece together an understanding of past climates from the available evidence contained in historical, biological, and geological records. With the aid of such climate proxies, many inroads have been made into understanding the structure of long-term climate variability, often utilizing an approach whereby a systems model is constructed which is consistent with the available data [e.g. *Imbrie et al*, 1992, 1993]. Owing to more accurate and abundant proxies of past climate, it is now increasingly possible to objectively test many of the plausible climatic inferences which have been drawn from the proxy record of climate change.

Much attention has been paid to a few relatively narrow bands of the low-frequency variability in the paleoclimate record, and these receive due attention throughout the thesis. It is, however, also important to recognize the energetic background continuum of climate variability [e.g. *Imbrie and Shackleton*, 1990; *Wunsch*, 2003a]. After all, a linear response to insolation forcing is a narrow and untenable description of the climate record. One expects fluctuations in the circulation of heat in the atmosphere and ocean to contribute a rich low-frequency spectral behavior to temperature spectra. Furthermore, significant temperature influences are expected from feedbacks associated with long-term changes in ice-sheets, ground cover, atmospheric composition, etc. Much work remains to be done in understanding what controls the background spectrum of temperature variability at these longer timescales.

When it comes to interpreting the narrow-band behavior of the climate at lower frequencies, many theories invoke a response to insolation forcing. At the obliquity and precession bands, one expects and finds a climatic response to insolation variability [*Hays et al*, 1976]. What is less certain is the origin of the energetic 1/100KY

band which contains the majority of the energy at frequencies below 1/10KY [e.g. *Wunsch*, 2004]. This 1/100KY band is identified with the late Pleistocene glacial cycles, and understanding the mechanisms which control this variability remains an outstanding question in the climate sciences.

One of the most fundamental and long-standing questions regarding the glacial cycles is whether they are deterministic or stochastic [e.g. *Kominz and Pisias*, 1979; *Wunsch*, 2004]. The contending explanations for the glacial variability can be divided into two categories: those which are wholly internal to the climate system [e.g. *Ghil*, 1994; *Saltzman*, 2002; *Wunsch*, 2003a], and those which call upon orbital forcing [e.g. *Hays et al.*, 1976; *Paillard*, 1998; *Gildor and Tziperman*, 2000]. The latter can be further categorized according to orbital parameter. The most widely accepted version of the orbital forcing of the glacial cycles is that a nonlinear response to the precession forcing demodulates the eccentricity envelope and generates a roughly 100KY timescale [e.g. *Imbrie and Imbrie*, 1980; *Imbrie et al*, 1993].

Other theories call directly upon the eccentricity forcing to pace the glacial cycles [e.g. *Benzi et al.*, 1982], but the insolation changes this causes are only on the order of a few W/m^2 and are probably too small to be of much climatic relevance. While eccentricity has the attractive quality of varying at a frequency near 1/100KY, the 1/400KY frequency is in fact more energetic so that its absence from Pleistocene climate variability must be explained. *Rial* [1999] goes so far as to suggest that the frequency modulation associated with the 1/400KY eccentricity band is responsible for causing the 1/100KY variability, but a known physical mechanism which would behave in this way is conspicuously absent.

Obliquity has played a more obscure role in theories of the glacial cycles, largely because it is not obvious how a forcing dominated by 41KY variability can be related to a roughly 100KY climatic signal. Unlike the climatic precession, the amplitude and frequency modulation of obliquity are small, but it has nonetheless been suggested that these modulations are related to the 100KY glacial cycles [*Liu et al*, 1998]. *Ridgwell et al* [1999] briefly consider that the glacial cycles may be paced by two or three obliquity cycles, but dismiss the idea as yielding results inconsistent with the spectra associated with the SPECMAP climate record [*Imbrie et al*, 1984]. Later this hypothesis of obliquity pacing of the glacial cycles is revisited in greater detail.

Given the abundance of plausible explanations for the glacial cycles, at this point it is necessary to find some means of distinguishing between theories. *Roe and Allen*

[1999] made a pioneering statistical comparison of six simple models which assume either a deterministic orbital response to insolation forcing or the existence of a free oscillation internal to the climate system, but were unfortunately unable to distinguish between the various hypotheses. *Wunsch* [2004] discusses a number of difficulties in statistically differentiating between the various glacial hypotheses: these are (1) the uncertainty associated with Pleistocene age-models, (2) the small number of Pleistocene glacial cycles (there are seven), and (3) the fact that narrow band spectral processes are embedded within an energetic background continuum. These three hurdles to making a definitive test for the origins of the glacial variability can each be overcome.

1. Serious effort has gone into dating the Pleistocene glacial cycles. The chronology of the last deglaciation is well known [e.g. *Hughen et al*, 2000], but there are conflicting estimates for the age of the penultimate deglaciation which argue for [e.g. *Broecker*, 1968; *Bard*, 1990] and against [e.g. *Henderson and Slowey* 2000; *Gallup*, 2002] orbital control. Similarly, orbital control of the earlier deglaciations can be argued for [e.g. *Herbert*, 2001] or against [e.g. *Winograd et al*, 1997]. In Chapter 3 a new age-model is introduced which, following the suggestion of *Shaw* [1964], uses depth as a proxy for time. This *depth-derived* chronology builds on earlier efforts [*Shackleton and Opdyke* 1972, from 900 to 0 KY BP; *Hays et al.* 1976, 500-0 KY BP; *Williams* 1988, 1900-0 KY BP; *Martinson et al.* 1987, 300-0 KY BP; and *Raymo* 1997, 800-0 KY BP] by incorporating nearly double the number of sediment core records, making an important correction for down-core compaction, and rigorously deriving uncertainty estimates. The resulting chronology is sufficiently accurate to permit testing of the orbital hypothesis of climate change.

2. When it comes to increasing the skill associated with statistical tests for the origins of the glacial cycles, it is impractical to wait for the number of glacial cycle realizations to increase, but one can decrease the degrees of freedom associated with the hypotheses. That is, each of the models considered by *Roe and Allen* [1999] have at least six free parameters associated with them; given that the models are compared against seven realization of the glacial cycles, there is little surprise that the results are inconclusive. In Chapter 4, a generalized model is developed which has no free parameters and, accordingly, fairs better in distinguishing between the various glacial hypotheses.

3. As noted, the low-frequency spectral peaks reside amid a significant background variability, suggesting that much of climate variability is stochastic and/or nonlinear. Fourier based techniques can only go so far in distinguishing between stochastic internal variability and nonlinear orbital control of the glacial cycles [e.g. *Huybers and Wunsch*, 2004]. In Chapter 4 a new technique is applied for determining the coupling between orbital variability and the glacial terminations based on concepts associated with phase synchronization [e.g. *Rosenblum and Pikovsky*, 2003]. Also, a new statistic is introduced — termed the *nonlinear coherence* — which quantifies the phase coupling in a nonlinear system. The nonlinear coherence proves a useful statistic for testing the hypothesis of orbital control of the glacial cycles.

Much has been done to determine the causes of the glacial cycles [e.g. *Imbrie et al* 1992; 1993]. This thesis seeks to gather together the relevant data and tools, and hone these toward making a definitive test for the origins of the glacial cycles. Apart from those discussed above, other implements include a compact representation of the full spatial and temporal variations in insolation forcing, an exploration of how the proxy record will record climate responses to insolation forcing, and the use of simple models to aid in the physical interpretation of identified statistical relationships.

This thesis attempts to cover a lot of ground, and a road map may prove useful to the reader. Chapters 1 and 2 respectively provide an overview of climate and insolation variability, both on timescales ranging from months to hundreds of thousands of years. Chapter 3 is devoted to developing a chronology for marine sediment cores which is independent of orbital assumptions; the chapter is repeated verbatim from *Huybers and Wunsch* [2004]. Chapter 4 uses the new chronology to test whether the glacial cycles are paced by orbital variations. A significant association is identified between obliquity and glacial terminations whose meaning is further explored in Chapter 5 using very simple climate models. An effort has been made to place technical discussion which is less central to the thesis into appendices at the end of each chapter.

Chapter 1

Temperature variability from modern to glacial timescales

Processes affecting Earth's climate occur at all scales, ranging in size from the molecular to planetary scales and in time from nearly instantaneous to billions of years. These space and time scales of variability are intimately coupled so that, for example, sea-ice thermodynamics influences the oceanic circulation of heat; cloud micro-physics influences Earth's albedo. Thus, to understand climate variability at any one scale requires some understanding of the whole. This Chapter attempts to place some aspects of paleoclimate variability in relation to the modern variability. The discussion provides a bird's eye perspective of Earth's climate variability; along the way attention is drawn to topics which will be discussed in more detail in the subsequent chapters.

A number of related studies have also discussed climate variability over a wide range of timescales. *Mitchell* [1976] gave a qualitative description of climate variability over timescales of hours to billions of years. *Pelletier* [1998] made a quantitative estimate of atmospheric temperature variability from ice-core proxy and instrumental records. *Shackleton and Imbrie* [1990] pieced together temperature estimates from marine sediment-cores spanning timescales of thousands to millions of years. *W. Curry* [personal communication] has extended the approach of *Shackleton and Imbrie* [1990] to monthly timescales using higher-resolution marine sediment proxies as well as coral records for tropical sea surface temperatures. Here, the more recent results of *Pelletier* [1998] and of *W. Curry* are built on to further investigate tropical sea-surface temperature and high-latitude surface air temperature variability.

An analogy can be made between the interpretation of temperature variability and other state variables in the climate system. One example is the study of modern sea-level records, which provides insight into the response of the ocean to periodic tidal forcing as well as stochastic forcing owing to weather and baroclinic ocean fluctuations. Impressively, oceanographic theory explicitly accounts for roughly 90% of the total sea-level variance between periods of hours and decades [e.g. *Wunsch*, 1972]. At lower frequencies, however, the attribution of causes becomes much more uncertain. Accordingly, this overview aims at a quantitative description of temperature variability, in some places pointing out potential mechanisms, but cannot be said to explicitly account for the structure of the temperature variability. A true explanation of the spectral structure of long-term temperature variability awaits the development of a detailed theory of climate.

1.1 A spectral patchwork

To compare modern climate variability at monthly resolution with glacial-interglacial timescales requires spanning six orders of temporal magnitude; such a span cannot be estimated in one shot. No single timeseries has a short enough sampling interval to resolve seasonal variability over a duration long enough to resolve glacial-interglacial variability. Instead, temperature variability is estimated through a patchwork of instrumental records and proxy temperature records. The data and references are discussed in Appendix A.

Temperature variability is quantified in terms of power-density spectra, computed using the multi-taper method [*Thomson*, 1990] with three windows. To compare spectral estimates from records of differing lengths and sampling intervals, it is important to consider the normalization employed. In this study the normalization gives a power-density independent of record length for stochastic processes, but periodic processes have increasing power-density with record length. A post-hoc correction is made so that periodic variability is commensurate between records of varying length. Appendix B discusses the multi-taper method and the normalization of power-density in more detail.

An effort is made to avoid orbitally-tuned age-models as these can bias records towards showing an assumed behavior [see Chapter 3 for more details]. Of the records analyzed here, only the Mg/Ca [*Lea et al.*, 2000 and 2003] and Vostok δD [*Petit et*

al, 1999] age-models contain orbital assumption. In the following, attention is called to where these orbital age assumptions may influence the results, particularly with respect to enhanced orbital band concentrations of variability.

Figure 1-1 shows the power density spectrum of tropical sea surface temperatures (SSTs), and Figure 1-2 shows the power density spectrum of high-latitude surface atmospheric temperatures (SATs). The structure of these composite spectra are describable in terms of the concentrations of variability at selected frequencies and the power-law processes of the background spectral variability. The concentrations of spectral energy, or peaks, are discussed first.

1.1.1 Spectral peaks

Concentration of variability in climate spectra help identify regions in frequency space where the climate system behaves uniquely, thus providing handles by which to grasp some of the mechanisms responsible for climate variability. For reference in identifying significant concentrations of variability, Figures 1-1 and 1-2 have vertical marks indicating the approximate 95% confidence level at which spectral estimates are considered inconsistent with being simply part of the background variability: the dot indicates the level of background variability and the line segments indicate positive and negative excursions from this background level. Significant positive excursions from the background variability indicate a relative excess of energy at a particular band of frequencies, and these will be referred to as spectral peaks. Spectral peaks are thus associated with both quasi-periodic (e.g. El Niño) and periodic processes (e.g. the tropical, as opposed to anomalistic, year). Given sufficient resolution, the spectrum of a periodic process will appear as a line; but due to noisy records, imprecise age-models, and finite record duration it is often difficult to distinguish between periodic and quasi-periodic processes.

One or more of the spectral estimates shown in Figures 1-1 and 1-2 have peaks above the 95% confidence level at the annual and semi-annual cycles, and a number of lower frequencies: 1/1.5, 1/22, 1/41, and 1/100KY. Each peak is briefly considered in order of highest to lowest frequency. The most obvious explanation for some of these spectral peaks are as a responses to changes in the distribution and intensity of the insolation forcing. To facilitate comparison, the spectrum of diurnally averaged insolation at 65°N is also shown in Figure 1-1.

It is tempting to ignore the annual variability in insolation because of its very

high frequency relative to paleoclimate timescales, and perhaps also because of its familiarity. But the sheer strength of the annual cycle relative to any other temperature variability, excepting perhaps the diurnal cycle, strongly suggest its affects should be considered. Phenomena such as aliasing [e.g. *Pisias and Mix*, 1988; *Wunsch and Gunn*, 2003], nonlinear responses to the annual cycle[1] [e.g. *Imbrie and Imbrie*, 1980], and nonlinear recording of the annual cycle [e.g. *Huybers and Wunsch*, 2003] makes consideration of the annual cycle and its effects of prime importance for understanding paleoclimate variability — Chapter 2 discusses these issues in greater detail. Figures 1-1 and 1-2 show the dramatic concentration of temperature variability at annual and semi-annual periods. The semi-annual periods are due to a variety of effects, including the suns twice annual zenith in the tropics, clipping due to polar night at high-latitudes, and nonlinear climatic responses.

To facilitate comparison between the high and low-frequency quasi-periodic[2] processes, the power density of the annual and semi-annual peaks were adjusted to the expected value for a record with an 800KY duration for SSTs (the length of the planktonic $\delta^{18}O$ records) and 420KY duration for SATs (the length of the Vostok ice-core record). For the tropical SSTs, this results in annual and semi-annual periods having over three times as much energy as that contained at all frequencies below 1/15KY, and indicates the first order importance of the annual variability. The logarithmic plotting convention used in Figures 1-1 and 1-2 compresses the high-frequency variability. To further compare the orbital and annual bands, Figure 1-3 shows these same spectra after multiplying each band by its associated frequency and plotted on log-linear axes, thus giving an area preserving scaling and making the dominance of the annual variability strikingly clear.

Moving to paleoclimate timescales, there is a significant concentration of energy near 1/1.5KY in proxies of Greenland temperature [see *Mayewski et al.*, 1997; Figure 1-2]. Because there is no obvious orbital forcing at this period [*Munk et al*, 2002], its presence is difficult to rationalize, though there are some theories [e.g. due to solar-variability, *Bond et al*, 1997]. Wunsch [2000] has suggested that the variability near periods of 1.5 KY in the Greenland $\delta^{18}O_{\text{ice}}$ record could result from an alias of

[1] As discussed later, any climatic precession signal requires a nonlinear response to the annual cycle.

[2] The term quasi-periodic is used here to refer to a signal with variable amplitude and frequency but which returns to the same phase after roughly equal time intervals. The changes in Earth's orbit are quasi-periodic as is the anomalistic (as opposed to tropical) annual cycle; a point discussed in more detail in Chapter 2.

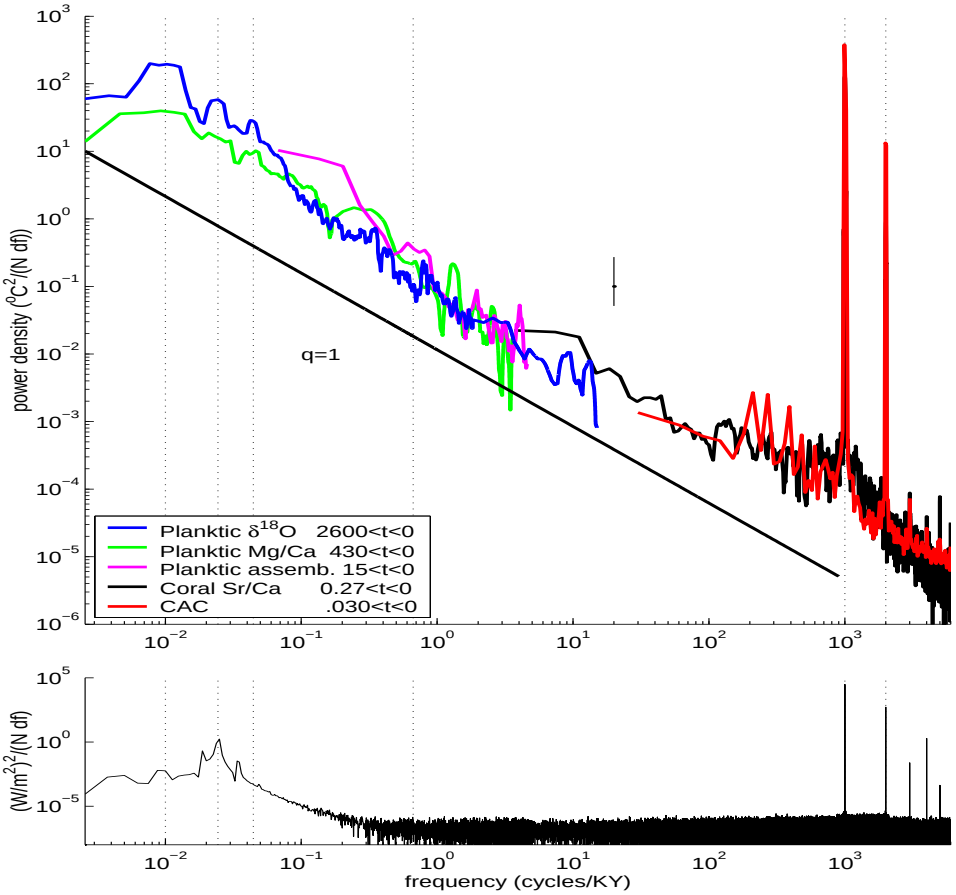

Figure 1-1: **top:** Power-density spectra of tropical sea surface temperature variability. Temperature variability is estimated using, from lowest to highest frequency, marine planktic $\delta^{18}O$ (blue), planktic Mg/Ca measurements (green), planktic assemblages (magenta), coral Sr/Ca (black), and instrumental tropical pacific sea surface temperatures from the Climate Analysis Center (red). The length of each record is indicated in the legend in KY BP; references are provided in Appendix A. A least squares estimate of the spectral slope between 1/100 and 1000 cycles/KY gives a power law relationship with $q \approx 1$. At frequencies above the annual cycle, the power-law steepens to about 2 (not shown). The annual and semi-annual estimates are adjusted to have the power-density expected for a record 800 KY long — the duration of the planktic $\delta^{18}O$ records. **bottom** Periodogram of diurnally averaged insolation at 65°N over the last 1000 KY BP and sampled monthly. Vertical dashed lines indicate bands centered on 1/100, 1/41, 1/23, 1/1.5, 1000, and 2000 cycles per KY. The power-density units are in degrees Celsius squared divided by the number of samples, N, and the spectral band-width, df. The vertical bar indicates the approximate 95% confidence level. Estimates are made using the multi-taper method with three windows. This insolation spectra is discussed more fully in Chapter 2, specifically with regard to the weak 1/100KY and absence of energy at the 1/23KY precession band.

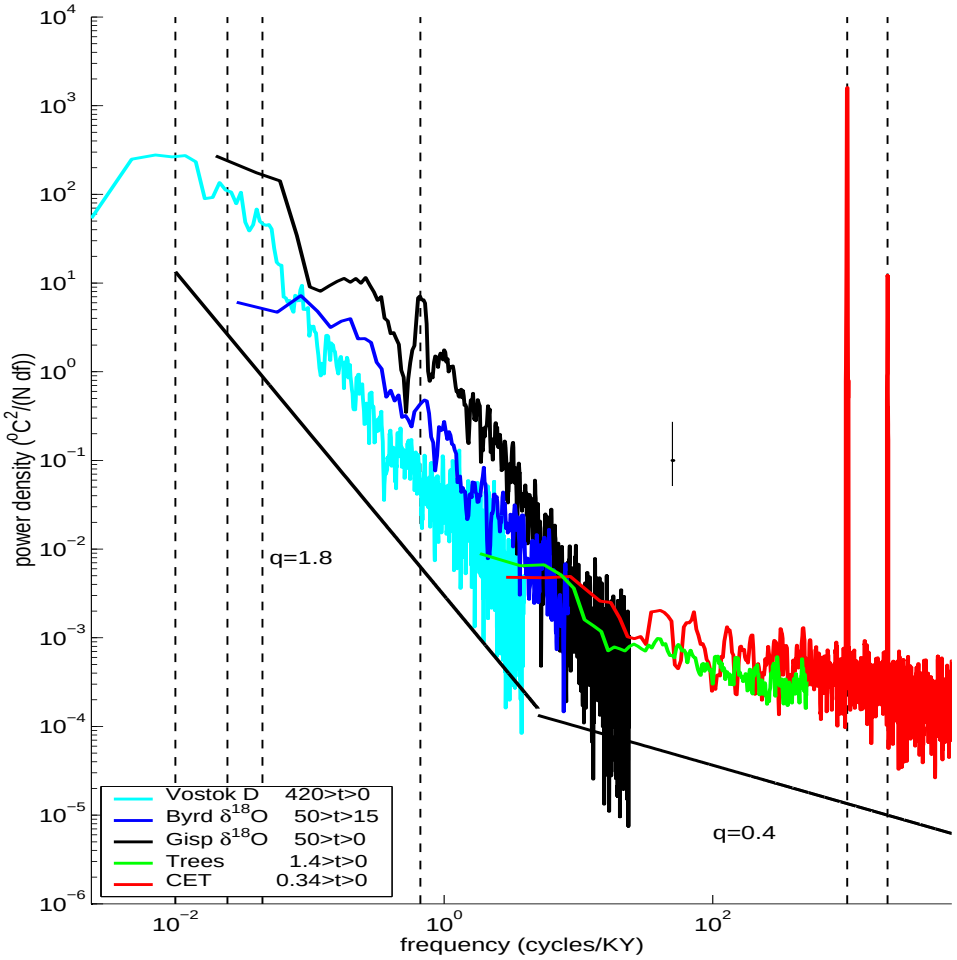

Figure 1-2: Similar to Figure 1-1 but now for the power-density spectra of surface air temperature. Estimates are derived from measurements of Deuterium (D) from the Vostok ice-core (cyan), $\delta^{18}O$ form Byrd (blue), $\delta^{18}O$ from GISP2 (black), tree-ring densities (green), and the Central England instrumental temperature observations (red). The length of each record is indicated in the legend in units of KY BP. The annual and semi-annual estimates were adjusted to have the power-density expected for a record that is 400 KY long — the Vostok record length. Least squares estimates of the power law scaling give a q of roughly 2 between 1/100 and 5 cycles per KY, and a q of 0.4 between 1/200 and 6 cycles per year. Compared with the tropical SST estimates, the low-frequency power-law is steeper. The high-frequency power-law is more nearly white and extends over a greater band-width.

the annual cycle. The massive energy concentrated in the annual band suggests that even a small leakage of energy from the annual cycle to this lower frequency could be responsible for the peak. Appendix C discusses the phenomenon of aliasing in more detail.

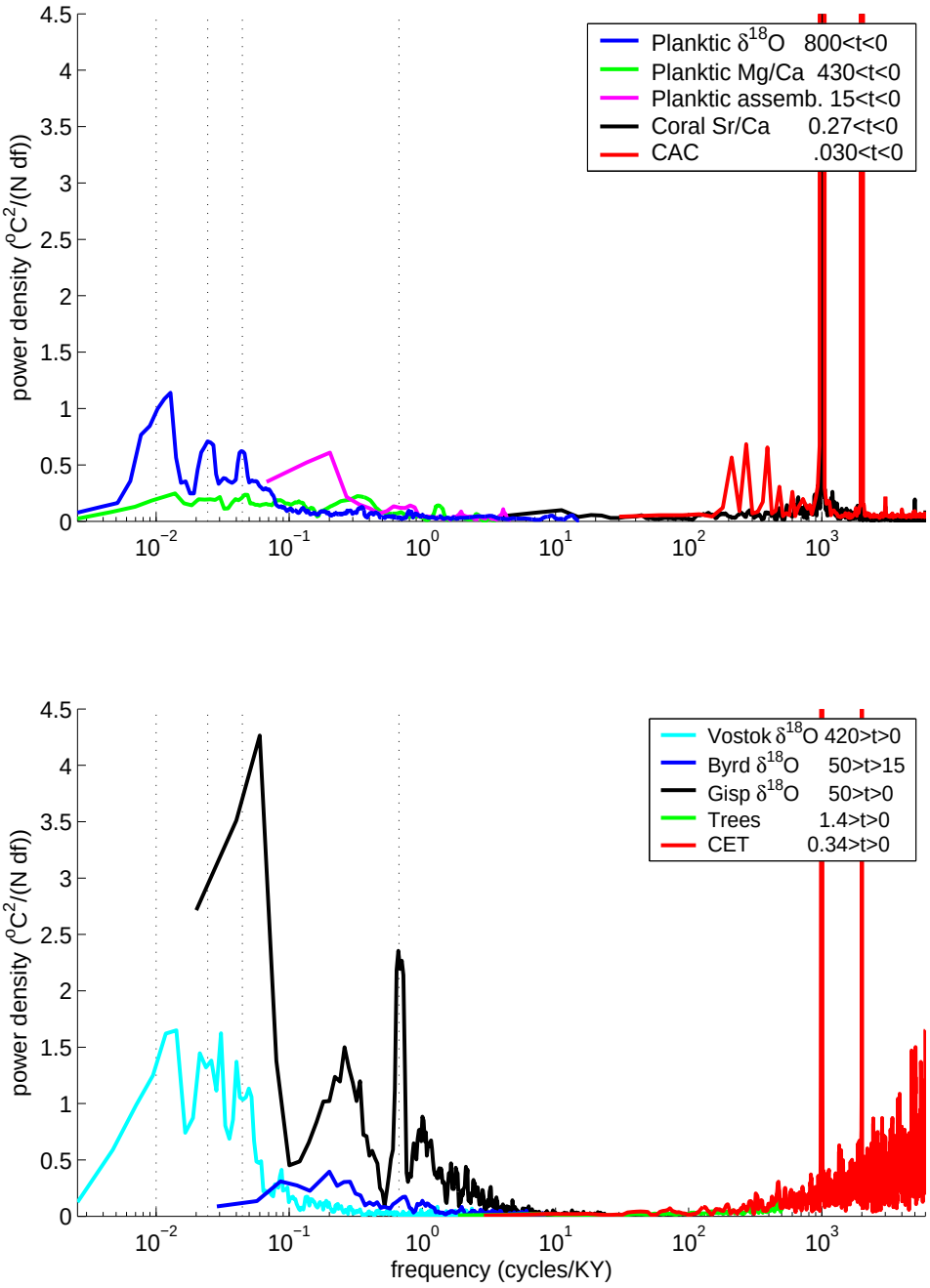

Figure 1-3: Similar to Figure 1-1 (tropical SST, top) and Figure 1-2 (high-latitude SAT, bottom) but now with the spectral estimates scaled by frequency, plotted with a linear y-axis, and having an area beneath the curve proportional to energy. Both plots indicate a relative minimum in energy between the orbital and annual bands roughly centered on 1/100 years. Figures are truncated for visual clarity: the energy at the annual cycles is roughly 40,000 and 80,000 $°C^2 f/(Ndf)$ respectively for SSTs (top) and SATs (bottom).

At the next lowest frequency there exists a small spectral peak in marine $\delta^{18}O$ near 1/22KY [see Figure 1-1]. This 1/22KY peak is also weakly present in the Mg/Ca SST estimates and Vostok deuterium measurements [Figure 1-2]. Concentrations of variability near 1/22KY in climate records are typically attributed to precession period insolation forcing [e.g. *Hays et al.*, 1976; *Ruddiman and McIntyre*, 1981; *Imbrie et al.*, 1992], but because precession only modulates the seasonal cycle, there is no true precession-period variability in the solar forcing [see Figure 1-1; Chapter 2; *Rubincam*, 1994]. If the peaks in temperature variability are due to insolation forcing, a nonlinear mechanism must be involved. Once a nonlinearity is involved, the field of possibilities is much wider: concentrations of variability may indeed owe their existence to precessional modulation, but also to the manner in which the records are sampled, insolation forcing at some other period (e.g. the first overtone of obliquity at 2/41KY), or internal climate variability. Chapters 2 and 3 further discuss the interpretation of precession period signals in proxy records.

The 41KY temperature variability indicated in Figure 1-1 is attributable to a linear response to the insolation shifts caused by changes in Earth's obliquity [*Hays et al.*, 1976]. Similar to the 1/22KY band, a spectral peak at 1/41KY is observed in the marine $\delta^{18}O$ record [Figure 1-1] and to a lesser extent in the Mg/Ca SST [also Figure 1-1] and Vostok deuterium records [Figure 1-2]. *L. Hinnov* [personal communication] has suggested that a more accurate age-model for the GISP2 ice-core gives a more pronounced obliquity peak. Also, *Bender* [2002] has shown that O_2/N_2 ratios from the Vostok ice-core have a pronounced obliquity band variability and appear to respond to local changes in insolation. The attribution of the 41KY climate variability to changes in Earth's obliquity is straightforward, but the physical mechanisms which translate a shift in insolation into a change in temperature remains a topic of debate. One dynamical possibility is that because high-latitude insolation increases with obliquity, causing snow and ice to melt, Earth's albedo decreases, and global mean temperatures increase [e.g. *Milankovitch*, 1941]. Another possibility is that increased obliquity reduces the meridional gradient of insolation in the summer hemisphere, thus reducing atmospheric vapor transport and decreasing albedo [e.g. *Raymo and Nisancioglu*, 2003]. As a final possibility, increased obliquity may cause reduced oceanic heat loss at high-latitudes, and assuming a fixed heat budget, a deepening of the tropical thermocline resulting in permanent El Niño like conditions and an associated mean SST warming [*Philander and Fedorov*, 2003]. Thus, power

density spectra help connect the forcing and response, but determining the dynamical pathway requires more detailed observations and examination of the dynamics.

For perspective, it is useful to estimate the fraction of variability contained in these Milankovitch bands. Estimates are made by interpolating the spectra of each climate record to a standard resolution, averaging all SST or SAT spectral estimates available at each band, summing the average energy in the bands $1/22 \pm 1/200$KY and $1/41 \pm 1/200$KY, and then dividing by the total energy at frequencies below a year. The Milankovitch bands are estimated to account for 11% of the SST variability and 21% of the SAT variability at frequencies below the annual cycle. Note that these fractions are positively biased by the inclusion of the background variability in the Milankovitch band energy estimates as well as the use of orbital-tuning to estimate the ages of the Vostok δD SAT record and the Mg/Ca SST record. As only a few orbitally-derived age-control points were used in constraining the Vostok age-model [*Petit et al.*, 1999] and since the $\delta^{18}O$ record is much more energetic than the Mg/Ca record at the SST Milankovitch bands, it is expected that, in this case, orbital-tuning has only a minor effect on the estimated fraction of variance in the Milankovitch bands. Furthermore, the Milankovitch band energy estimates are also likely to be negatively biased by age-model errors which diminish the energy concentrated in spectral peaks [see Chapter 3]. At this point, the net bias on the Milankovitch band energy owing to age-model errors, orbital-tuning, and background variability is unclear. Future work will address the net affect of these sources of uncertainty on the Milankovitch band energy estimates. That the Milankovitch bands account for nearly twice as much SAT variability, as compared with the SST variability, probably owes to both orbital-tuning and the more rapid decrease in SAT energy at frequencies above the Milankovitch bands.

Some comment is required as to why the relatively small fractions of Milankovitch variability command so much of the attention in this thesis. There are two reasons. First, the presence of concentrations of climate variability in bands related to orbital variations provides an opportunity to assess the climate response to a known forcing. This permits application of well understood techniques for evaluating the response of a system to a nearly periodic forcing, particularly in the case of the linear obliquity response. Second, following *Hays et al.* [1976], many paleoclimate studies operate under the assumption that the Milankovitch bands control low-frequency climate variability. However, outside of the narrow bands centered on the obliquity and

(maybe) the precession frequencies, the applicability of the Milankovitch hypothesis remains uncertain. It is thus important to continue evaluating the scope and accuracy of the Milankovitch hypothesis.

Perhaps the most intriguing band of variability is centered at 1/100KY [see Figures 1-1 and 1-2] and is associated with the glacial-interglacial transitions. This 1/100KY band of variability accounts for roughly half of the spectral energy at frequencies below the annual cycle in both SAT and SST. It is tempting to link this glacial variability with the small insolation peak near 1/100KY due to eccentricity variability, but eccentricity proves an unlikely candidate due to its weak influence on insolation [e.g *Hays et al.*, 1976] and lack of evidence for the earth resonating at such a frequency [e.g. *Imbrie et al.*, 1993; *Wunsch*, 2003a]. In Chapter 4 evidence is presented that the relative phasing between eccentricity variations and the glacial cycles also argues against a relationship. Some theories call on the eccentricity modulation of precession variability to *pace* the glacial variability [e.g. *Hays et al.*, 1976; *Imbrie and Imbrie*, 1980]. In Chapters 4 and 5 it is argued that obliquity is a better candidate for the orbital pacing of the glacial cycles.

1.1.2 The spectral continuum

When it comes to the spectra of paleoclimate variability, the peaks receive much more attention than the back-ground continuum. In a sense, this focus on the peaks is at odds with modern climate studies. For the atmospheric sciences, weather holds greater interest than the annual temperature cycle; in oceanography, mixing garners more interest than tidal cycles. This focus could be because the annual cycle and tides are largely solved problems. A better comparison might be made between the quasi-periodic ice-ages and the North Atlantic Oscillation or El Niño variability. Regardless, just as the modern spectral continuum embodies a rich set of physics, one should expect the spectral continuum at low-frequencies to provide insight into the processes which govern long-term climate variability.

A useful description of the background spectrum observed in Figures 1-1 and 1-2 is the *spectral power-law*, q, which relates power-density, Φ, to frequency, s,

$$\Phi = As^{-q}.$$

A is a multiplicative factor which sets the level of the background spectrum. Spectra

with a positive q are referred to as *red*, in analogy with visible light being red at its lowest-frequencies. For the same reason a negative q is *blue*, and an approximately zero q indicates a *white* spectrum. Because of uncertainties in the proxy measurements, spatial variability, and temporal nonstationarity (discussed in Appendix A and the subsequent sections) these power-laws estimates should be thought of as indicators of the scaling relationships in temperature variability, not physical constants. A particular concern, detailed in Appendix C, is that aliased higher-frequency energy will bias the power-law estimates towards being too red. While establishing how applicable the observed scaling laws are to the global temperature variability will require much further work, the relatively simple power-law behavior and the agreement between multiple different proxies found here suggests the power-law estimates provide a useful description of tropical SST and high-latitude SAT variability. The influence of age-model errors and orbital-tuning on spectral power-laws is largely unknown; pending further study, it is assumed that the effect is small.

In keeping with most geophysical records, tropical SSTs have red spectra. In this case, the power-law is remarkably stable, with a value of one between frequencies of 1/100KY and 1/1yr — five orders of magnitude. This behavior is well replicated in multiple proxies, giving some confidence in its accuracy (but see Appendix C for other ways of producing such a power-law). At frequencies above the annual cycle, the spectrum falls off more quickly with frequency, with $q \approx 2$. There is a bulge of energy centered on 1/100KY so that for slightly lower frequencies, the power-law is briefly blue. *Imbrie and Shackleton* [1990] find that at even lower frequencies, a power-law near one resumes.

The power-density spectrum of high-latitude SATs [see Figure 1-2], has a more complicated power-law behavior than tropical SSTs. From the highest resolved frequencies to 1/200yr, the spectrum has a power-law relationship of 0.4, while frequencies between 1/200yr and 1/100KY are more red with a power-law near two. At the millennial timescales there are marked differences between the power-laws derived from the three ice-cores records included here. The most energetic millennial scale variability is observed in temperatures estimated from the Greenland Ice-sheet Project 2 (GISP2) ice-core, followed by the Antarctic Byrd and then Vostok records. As one approaches the 100KY timescale, the power-density of the three ice-cores converges. This touches on the topic of spatial changes in temperature variability: in the following section the spatial and temporal shifts in temperature variability are

discussed in more detail.

Comparison of the power-law structures shown in Figures 1-1 and 1-2 indicates roughly equal decadal variability in tropical SSTs and high-latitude SATs, greater centennial SST variability, and for periods longer than centuries greater high-latitude SAT variability. The greater SAT variability at lower frequencies agrees with estimates indicating tropical SSTs underwent relatively small glacial to interglacial changes relative to high-latitude temperatures [e.g. *CLIMAP Project Members*, 1981]. Apart from tropical/high-latitude differences, the spectral structure probably also reflect differences between atmospheric and sea-surface temperature variability and/or inaccuracies in the proxy measurements.

Figure 1-3 shows the composite spectra from Figures 1-1 and 1-2 after multiplying the power-density by frequency. This representation has the virtue of making the area under a log-linear plot proportional to the variance contained within each band. Another effect of multiplying by frequency is to remove a power-law of one from each composite spectra. That is, the area preserving plots scale as,

$$\Phi = As^{-q} \times s = As^{-q+1}.$$

Because $q \approx 1$ for the SAT and SST variability, the area preserving representation removes the trend in the background continuum and makes the detailed structure more evident. High-latitude SAT shows a relative minimum in scaled energy near frequencies of 1/100year (this minimum was identified as a change in the spectral slope in Figure 1-2.) The scaled tropical SST spectra also shows a weak minimum at the same 1/100year band. Qualitatively, this spectral structure suggests that the mechanisms responsible for climate variability change near the 1/100year timescale. As insolation forcing is weak between the annual and secular periods of variability, it is tempting to identify the structure of the climatic background continuum with high and low-frequency responses to the insolation forcing. Other possibilities are that slow temperature fluctuations associated with the deep oceans and cryosphere only become important at the 1/100year timescale. Determining the cause of this apparent change in slope, however, awaits further investigation into the mechanisms controlling the background variability of the climate spectrum.

The estimates presented here generally agree with previous studies of the background spectrum. At periods shorter than 200yr, *Pelletier* [1998] finds nearly the same SAT spectral structure, including a greater decline in subannual SAT variabil-

ity for stations near marine environments, in qualitative agreement with the SST spectrum. One difference is that, on the basis of a Lomb-Scargle periodogram analysis [e.g. *Press et al*, 1999] of the Vostok deuterium record, *Pelletier* [1998] suggests the spectral continuum of SAT is white at frequencies below 1/40 KY. Given the bulge of energy expected near the 100KY periods, and that the Vostok record cannot resolve frequencies below 1/420KY, it is difficult to draw inferences regarding such low-frequency behavior from analysis of the ice-core record. It appears safer to assume that at long periods SATs behave like SSTs, and continue to have a red power-law behavior.

The power-laws of climate records are also discussed by *Wunsch* [2003b]. For ice-core $\delta^{18}O_{\text{ice}}$ and deuterium records his results agree with those shown in Figure 1-2. *Wunsch* [2003b] does find a steeper power-law for marine sediment-core $\delta^{18}O$, but this is not an unexpected result. In focusing on the 100KY variability, *Wunsch* [2003b] estimated the power-law behavior of $\delta^{18}O$ over frequencies of 1/100 to roughly 1/10KY. This band of variability is steeper than other parts of the $\delta 18O$ spectrum [see *Imbrie and Shackleton*, 1990; Figure 1-1] and, as argued in Appendix A, is probably strongly influenced by ice-volume variability. In support, note that the Mg/Ca estimates shown in Figure 1-1 are not sensitive to ice-volume and maintain a power-law relationship much closer to one. Note *Wunsch* [2003b] interpreted the $\delta^{18}O$ record as indicative of climate, not temperature, variability.

The origins of the background climate continuum remain an important question. One possibility is for the climate system to have a long memory, causing high-frequency variations to accumulate into progressively larger and longer period variability. *Wunsch* [2003b] has presented a simple random walk model of ice accumulation which is driven at all frequencies (a white forcing spectrum) but generates an energetic quasi-100KY variability and, at higher-frequencies, a background continuum with a power-law of two. Generalizing this idea to temperature, the power-law relationship observed in Figures 1-1 and 1-2 could represent the organization of high frequency temperature variability into progressively larger and longer timescale variations — similar to the SST variability modeled by *Hasselmann* [1976], but extending over longer timescales. In a recent paper, *Pelletier* [2003] has suggested an explanation for the overall spectral shape of the temperature record in terms of a coherence resonance model incorporating radiative, ice-sheet, and lithospheric deflection processes. Apart from creating an excess of energy near the 100KY timescale, the most

notable feature of the modeled temperature variability is a transition in the spectral power-law relationship from $q = 2$ to $q = 0.5$ near 1/2 KY, similar to observations.

The possibility also exists that the background variability observed in Figures 1-1 and 1-2 is related to the annual cycle, at least in part. Chapter 2 discusses how rectification of the annual cycle causes precession period variability to appear. Such rectification also causes a transfer of energy to the background continuum between 1/100 and 1 cycle per KY. The background continuum of rectified insolation has a steep power-law at low-frequencies and a transition to a more white spectrum at higher-frequencies, in qualitative agreement with Figure 1-2. Alternatively, low frequency insolation forcing could drive a low-frequency temperature response which cascades towards higher frequency temperature variations. In certain regimes, such as Kolmogorov's turbulent spectra, this flow of energy from low to high frequencies is well known. A larger scale example is the conversion of potential energy, supplied by the meridional insolation gradient, into synoptic scale variations by baroclinic instability [e.g. Eady, 1949; Charney and Stern, 1962]. A variety of plausible mechanisms exist to explain the background spectrum of climate variability; further observations and dynamical research are needed to quantify and understand the mechanisms responsible for the continuum energy at these broad range of frequencies.

1.2 Heterogeneous climate variability

In many ways referring to *the* climate spectrum is a misnomer. Different state variables of the climate system will, in general, have different spectral descriptions, as suggested in the discussion of ice-volume versus temperature variability in Appendix A. Furthermore, as shown by comparing tropical SST variability and high-latitude SAT variability, observations of the same state variable in different mediums and/or regions can have significantly different spectral representations. Developing an understanding of how measurements at a point in space over a finite period of time are related to the greater system is crucial for interpreting climate records.

Temperature estimates over the last 50 years from the NCEP/NCAR reanalysis [e.g. *Trenberth*, 1991] are used to develop a quantitative estimate of how climate variability itself varies in space and time. Two-meter temperatures are used because these are less influenced by the prescribed annual cycle in surface conditions, but for convenience these are nonetheless referred to as surface air temperatures (SATs). The

reanalysis temperatures come gridded in latitude and longitude for each month, but rather than temperature at a point, we seek a representation in terms of spatial and temporal scales. Quantitative estimates of the variability at different spatial scales are made by projecting the reanalysis output onto a spherical harmonic basis[3] [e.g. *Jackson*, 1999]. A computer code was written to compute the spherical harmonic loadings using the Gaussian meridional grid employed by NCEP. The temporal scales of variability are estimated by computing the spectra of the spherical harmonic loadings with respect to time and summing together estimates with equal spatial scales. For further discussion of this transformation, but applied to sea surface height, see *Wunsch* [1991]. The transformation is normalized so that the spectra ($P(s,n)$) are in units of $^{\circ}\mathrm{C}^2$ and are a function of frequency (s in cycles/year) and spherical harmonic degree number (n). As an example, the spectrum with $\{s = 0, n = 0\}$ describes the mean global temperature, and $\{s = 1, n = 1\}$ primarily describes the annual inter-hemispheric gradient in temperature. If a quantity only varies in latitude, the spherical harmonic description reduces to the Legendre polynomials; these are discussed in greater detail in Chapter 2.

1.2.1 Spatial variability

A plot of $P(s,n)$ is shown in Figure 1-4, along with the frequency spectrum ($P(s) = \sum_n P(s,n)$) and the spatial spectrum ($P(n) = \sum_s P(s,n)$) of variability. As expected, the dominant feature of $P(s,n)$ is a ridge at annual periods with a maximum at degree number $n = 1$. Ridges are also apparent at the higher frequency harmonics of the annual cycle, i.e. 2,3,4... cycles/year, and each of these ridges appear as peaks in the frequency spectrum, $P(s)$. As observed in the earlier atmospheric temperature records [Figure 1-1], away from the peaks, the frequency spectrum is characterized by a power law process with $q = -0.4$. The degree number spectrum also shows greater energy towards longer spatial scales, but with a broad peak surrounding an n of roughly five.

Because the SAT response to the annual cycle is so large, it obscures the behavior of the background continuum. Removing mean monthly temperatures, as calculated at each grid point, suppresses the energy associated with the annual cycle and its higher harmonics. Results are shown in Figure 1-5. The background continuum asso-

[3]Because the NCEP/NCAR reanalysis uses a spectral model, it should be possible to find the spherical harmonic loadings without ever transforming into the gridded domain.

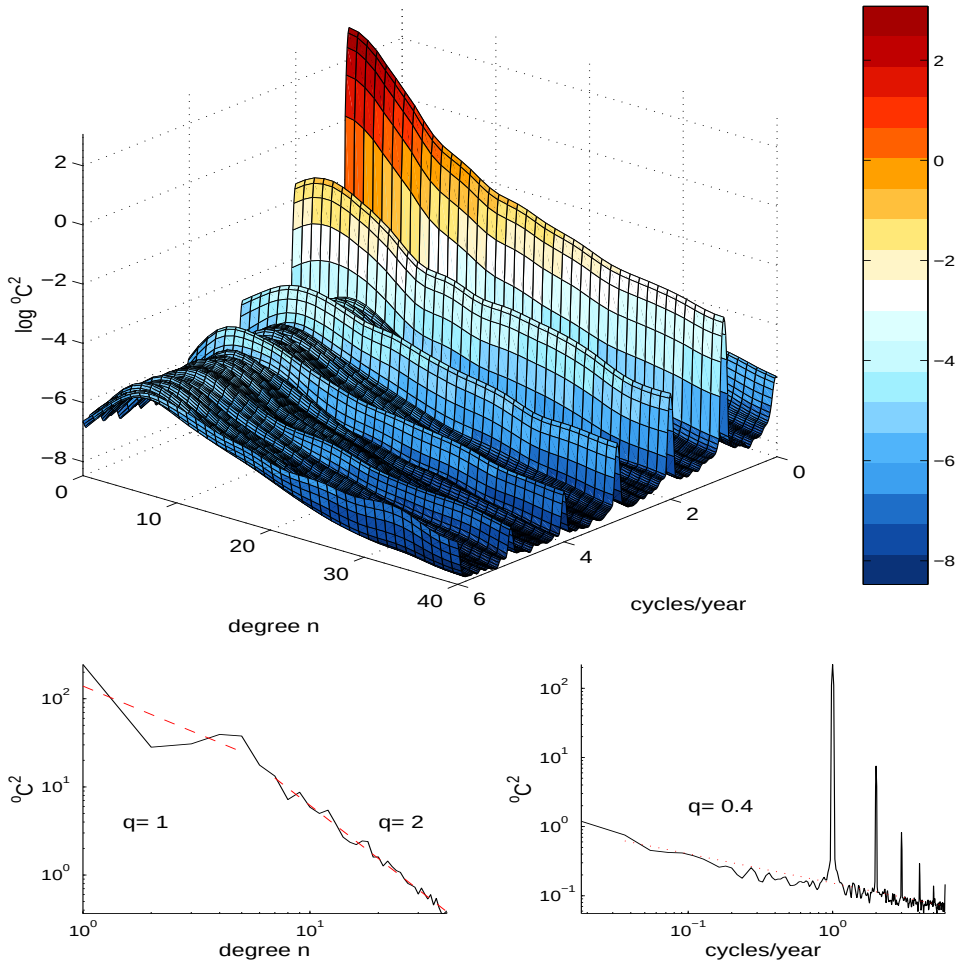

Figure 1-4: **top** The spectrum of spherical harmonic coefficients for NCEP temperature variability plotted as a function of spatial degree number (n) and frequency (s) measured in cycles/year. Spectral estimates are made using the multi-taper method with three windows, and the resulting n by s field is smoothed using a tapered 5x5 window. **bottom** A summation over frequency yields the degree n spatial spectrum (left), while summation over spatial scales yields the frequency spectrum (right). The degree n spectrum increases towards larger spatial scales with $q = 2$ up to $n = 7$, and then increases more weakly with $q = 1$, as indicated by the dashed red-lines. In the frequency spectrum, the concentration of energy at the annual cycle and its higher harmonics is evident, and the background variability has $q = 0.4$.

ciated with the frequency spectra of the filtered and unfiltered monthly temperature estimates is nearly the same, but after filtering the degree number spectrum now shows enhanced variability at $n = 5$ to 7, with power rolling off remarkably steadily with $q = .9$ for $n < 5$ and $q = -2$ for $n > 7$. Thus it appears that temperature variability, at monthly to decadal timescales, predominantly occurs at spherical har-

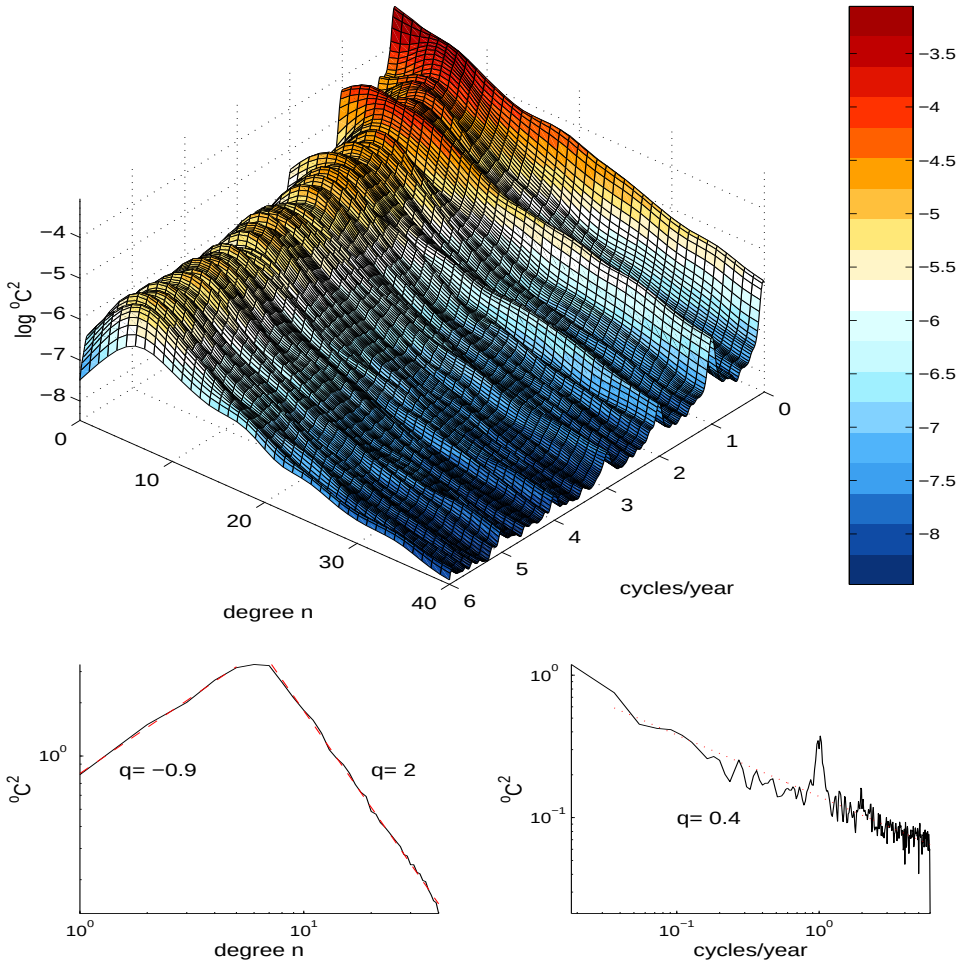

Figure 1-5: Similar to Figure 1-4 but for NCEP temperature variations with the monthly averages removed. Most notable is the peak of energy at degree $n = 6$ and 7, with energy diminishing at an exponential rate towards the larger and smaller scales.

monic degree number 6. Note that taking the monthly average of SAT effectively filters out the synoptic scales of variability; these shorter scales were the focus of the study by *Trenberth and Solomon* [1993]. At periods longer than a month, the most active spatial-scales of temperature variability are on the order of continents and oceans, and are probably associated with the land-sea temperature contrast, as well as hemispheric meridional temperature gradients. Connecting these results with the synoptic scale variability could prove useful, but is not further pursued here.

Figure 1-6 shows the first moment of the spatial scale as a function of frequency

and weighted by the fraction of temperature variance,

$$M_1(s) = \frac{\sum_n nP(s,n)}{\sum_n P(s,n)}. \tag{1.1}$$

Small values of M_1 indicate relatively more energy at large spatial scales, and will be interpreted as greater *organization* of the temperature variability. Away from the annual cycles and its higher-harmonics, M_1 hovers around eleven. At the annual cycles M_1 drops to four because the annual cycle is spatially organized. At two cycles per year, a weak organizing effect is evident, while at higher harmonics slightly greater disorganization is observed — an unexpected result. For temperatures with their monthly means removed, M_1 remains close to 11 showing only minor variability at the annual cycle and its harmonics. The consistency of spatial organization at timescales ranging from months to decades suggests that the spatial description of climate variability is no simpler at long timescales than it is at the monthly timescales. This result is apparently at odds with *Mitchell*'s [1976] suggestion of larger spatial scales of variability at longer timescales, and is in some sense surprising. One might expect that dissipative systems such as the atmosphere and ocean would not maintain strong gradients over long timescales. But perhaps the persistence of features such as the atmospheric jets, western boundary currents, land/ocean configuration, mountains, ice-sheets, vegetation, etc. is more telling. Suffice it to say that the long-term behavior of fluids on a rough, heterogeneous, and rotating planet is not easily intuited, particular when dynamical interactions with the cryosphere, geosphere, and biosphere come into play.

The spectra discussed in conjunction with Figures 1-4 and 1-5 contain a lot of information but are rather abstract. To provide a more tangible example, the cross-correlations between temperature at a single location with temperature at every other point (the one-point correlation) is shown in Figure 1-7. To focus on the inter-annual timescales of interest, all timeseries were first filtered to remove the energy at the annual and higher frequencies. First, the GISP2 site in Greenland is considered. There is a strong local correlation extending over parts of the Arctic, Northeastern Canada, and Siberia. Interestingly, there also exists weak positive correlation with the Atlantic and Antarctic. But the overall result is patchy. Given only observations from Greenland, it would be difficult to infer inter-annual temperature variability outside of the Northern N. Atlantic.

Another record which has aroused attention comes from Devils Hole in Nevada

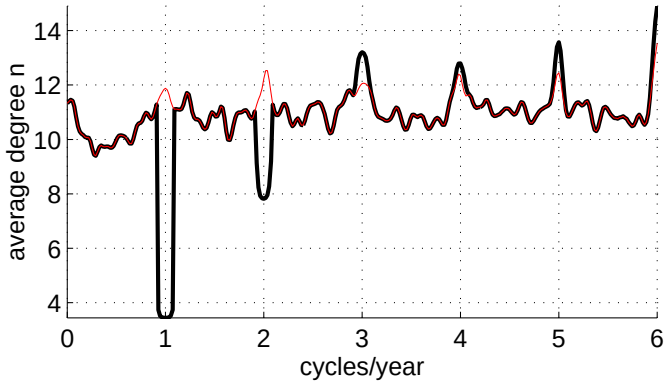

Figure 1-6: The first moment of the degree number, weighted according to the spectral energy associated with each n (see Figure 1-4), and plotted as a function of frequency. Results for the monthly filtered (red) and unfiltered (black) temperatures are shown. The background variability has an average degree number which hovers around eleven, while the annual and semi-annual bands for unfiltered temperatures have much larger scales (smaller n). Conversely, at harmonics of three cycles per year and higher, the spatial scale is slightly smaller than the background variability.

[e.g. *Winograd et al.*, 1992; also discussed in Chapter 3]. The one-point correlation for this site is also shown in Figure 1-7 to make the somewhat obvious point that inter-annual temperatures in California do not have a simple relationship with the rest of the globe. In general, global temperatures are weakly positively correlated, but there are broad features which are weakly anti-correlated such as the Southern ocean. The point is that one cannot a priori connect low-frequency phenomena with large-scale phenomena and that reconstructing climate variability on long timescales will probably require numerous detailed records from around the globe. Obtaining proxy information which both constrains the climate state and can be accurately synchronized with other proxy measurements represents a major scientific challenge which has only begun to be addressed.

1.2.2 Temporal variability

In addition to spatial variability in climate signals, the variability associated with climate at a point can vary as a function of the background state. Perhaps the most notable example is the dramatic variations observed in Greenland temperatures during the last glacial, often referred to as Dansgaard-Oeschger events, which are absent during the Holocene. Figure 1-8 shows power-density spectra from successive

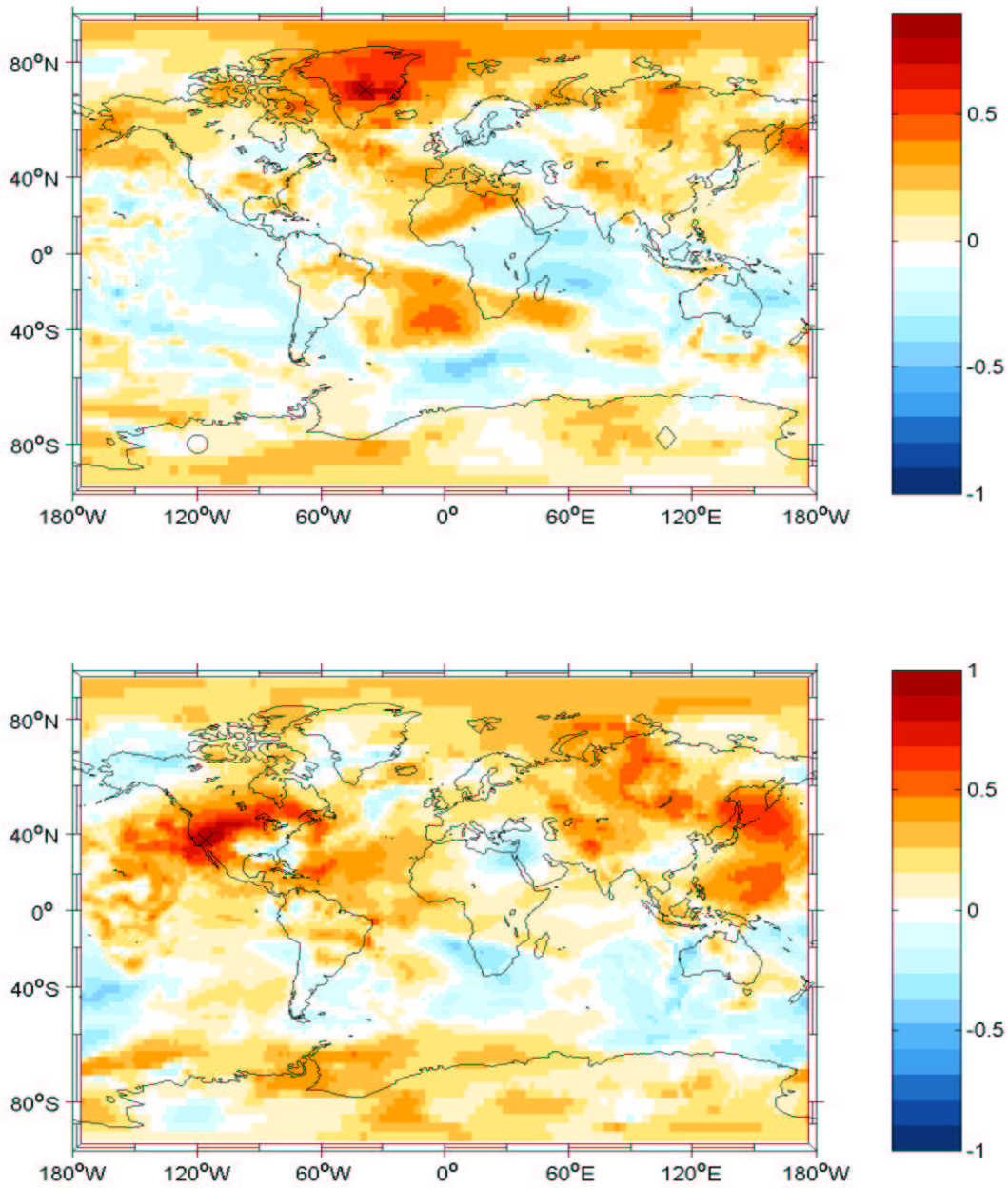

Figure 1-7: Examples of spatial correlation. **top** Cross-correlations of NCEP two-meter surface air temperatures with temperature at the GISP2 site in Greenland (indicated by an x). Also the location of the Byrd site is indicated by a circle in Antarctica, and for Vostok by a diamond. **bottom** Cross-correlations with the location of Devils Hole in Nevada. Prior to computing cross-correlations, the timeseries of temperature at each grid point were low-pass filtered to remove the annual and higher-frequency variability. The trends in temperature were also removed, due to concerns regarding their accuracy [M. Serreze, personal communication].

10KY increments of the GISP2 $\delta^{18}O$ record. At millennial timescales, the power-density is one to two orders of magnitude greater for intervals occurring in the last glacial than for the Holocene. Also shown are histograms of Holocene and Last Glacial temperature variability, with a roughly Gaussian and bimodal distribution respectively. Apparently, the transitions from glacial to inter-glacial states causes the crossing of some threshold in the dynamics associated with temperature variability. It thus appears that the Greenland record is nonstationary, but rigorously proving such an assertion is difficult [see *Wunsch*, 2000]

This raises the question of how representative the low-frequency spectra shown in Figures 1-1 and 1-2 are of temperature variability in general, or whether they are only indicative of conditions during a certain interval. For the case of Greenland, it appears the steep millennial portion of the spectrum is only indicative of glacial variability. Likewise, the higher-frequency portion is probably also sensitive to the glacial state. For example, if one assumes greater sea-ice in the North Atlantic during glacial times, the reduced buffering of temperature by the oceanic mixed layer would probably result in a larger annual cycle in air temperature. Without subannual resolution records of temperature during glacial climates, or an accurate model of glacial climate, the answer remains poorly constrained. It does appear likely, however, that major shifts in temperature variability occur at millennial and shorter timescales as the glacial state of the climate varies.

1.2.3 Further remarks

The foregoing discussion sought to give a broad overview of climate variability. One theme was the importance of the highly energetic annual cycle — for tropical SSTs it has over three times more energy than the glacial-interglacial variability. The next chapter further explores how changes in Earth's orbital parameters influence the annual cycle and discusses how climate and climate proxies can respond to changes in the annual forcing.

Another theme was the disparity between the spectrum of the orbital forcing and the spectrum of the climate system. Excepting at the obliquity and annual bands, there is no linear explanation for why the climate system should exhibit narrow-band behavior. This opens the possibility of internal quasi-periodic climate variability as well as nonlinear responses to insolation forcing. In practice, nonlinear means most everything, and the possible explanations proliferate quickly. Chapter 4 seeks to clar-

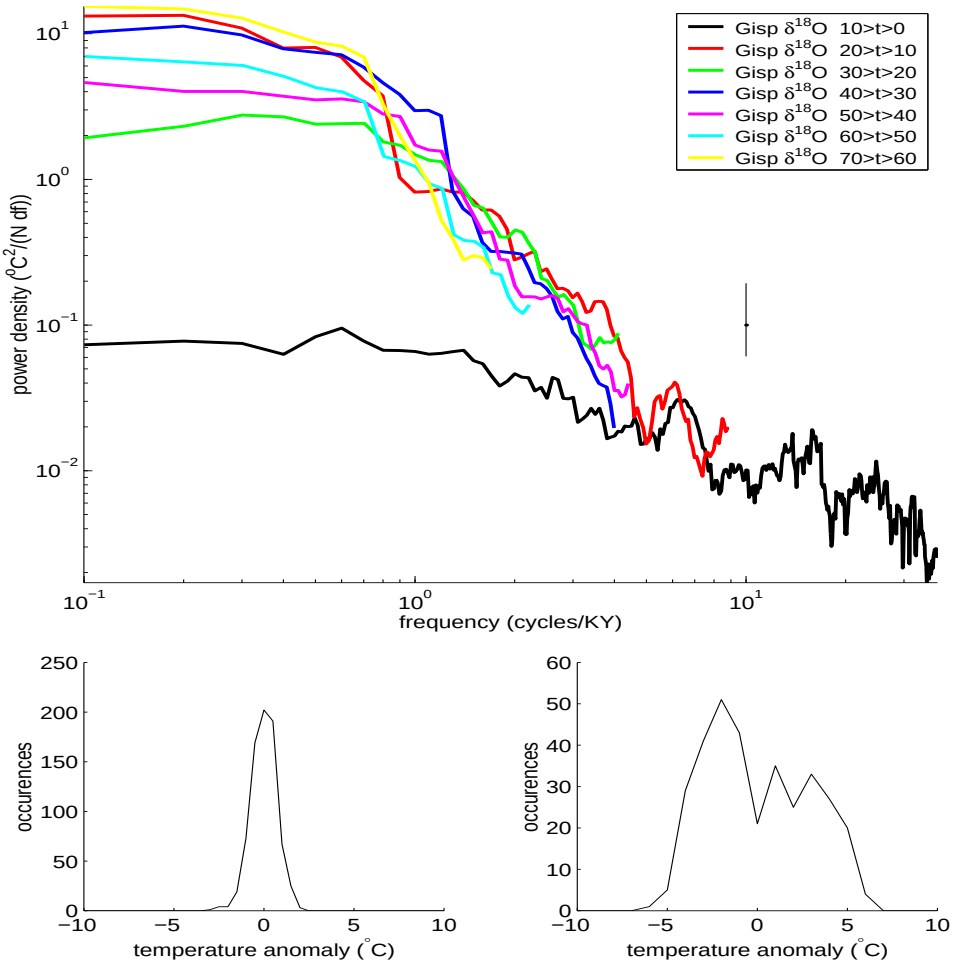

Figure 1-8: Power-density spectra of temperature estimates from GISP2 for 10KY intervals starting near the beginning of the last glacial, 70 to 60 KY BP, and ending during the Holocene, 10 to 0 KY BP. At periods longer than a KY, the last glacial temperatures monitored by Greenland ice-cores are more than one order of magnitude more variable than Holocene temperatures. This difference greatly exceeds the confidence interval (vertical black bar). It thus appears that climate is nonstationary and that the climate spectrum will depend on the measurement interval.

ify the mechanisms responsible for quasi-periodic climate variability by formulating objective tests of the relationship between insolation and climate.

Finally, some examples of the spatial and temporal changes in temperature variability were discussed. This reinforces the notion that any one climate record gives but a small window into the workings of the climate system. In this view, synthesizing the information content of multiple paleoclimate records is crucial for unraveling the causes of climate variability. One essential feature of such a synthesis is the place-

ment of multiple records on a single chronology: age-models are the primary topic of Chapter 3.

1.3 Appendix

1.3.1 Data

Tropical Sea Surface Temperatures

Two different compilations of data are made: one recording equatorial sea-surface temperature [see Figure 1-1], and another recording high-latitude tropospheric temperatures [see Figure 1-2]. The equatorial records are described first, in order from the highest sampling resolution to the lowest. Because it is important to distinguish between climate variability and variability due to proxy behavior, some discussion of the uncertainties associated with each proxy is also included. For a more general discussion of these proxies see the textbooks by *Cronin* [1999] and *Bradley* [1999].

The most accurate tropical SST observations come from the instrumental network. I use mean monthly tropical Pacific observations from the Climate Analysis Center [available at http://ingrid.ldeo.columbia.edu/SOURCES/.CAC/] which extend over the last 30 years. A complementary set of coral proxy observations is available from the subtropical South Pacific at approximately monthly resolution over the period 1726 to 1997 [*Linsley et al.*, 2000]. The spectrum of these coral proxy temperatures are impressively similar to the instrumental spectrum where the bands overlap and the corals have the added advantage of resolving centennial timescales.

High-resolution planktic $\delta^{18}O$ records also resolve centennial timescales. By combining the spectra of these high-resolution records with lower resolution planktic $\delta^{18}O$, power-density estimates are extended to periods of 800KY. Where multiple $\delta^{18}O$ records overlap, the average spectrum is used. Spectra are computed from the $\delta^{18}O$ records between 10∘N and 10∘S listed in Table 2.1, using the depth-derived age-model [see Chapter 3], as well as three higher-resolution records: OCE205-103GGC from the Little Bahama Bank [W. Curry and D. Oppo unpublished data], EW9209-1JPC from the Ceara Rise [*Curry and Oppo*, 1997], and C166-8GGC from the Florida Margin south of Dry Tortugas [*Lund and Curry*, submitted to Paleoceanography]. Temperature was estimated from planktic calcite $\delta^{18}O$ using a conversions of 4°C per $\delta^{18}O$ per mill, in agreement with empirical estimates [e.g. *Bemis* et al, 1998]. Because calcite

$\delta^{18}O$ is also sensitive to the ambient sea water $\delta^{18}O$, there is a significant contribution from changes in ice-volume. While the LGM to Holocene change in sea-water $\delta^{18}O$ is close to 1 per mil [*Ed Boyle* personal communication; also see *Adkins and Schrag*, 2001; *Adkins et al*, 2002; *Adkins and Schrag*, 2003], the centennial variability is virtually unknown. Here I make the assumption that ice-volume changes slowly relative to centennial scale temperature variability, and thus at centennial and shorter periods the calcite $\delta^{18}O$ signal reflects temperature, not ice-volume variations. By this assumption, converting all the calcite $\delta^{18}O$ variability to its equivalent in temperature is expected to give power-density estimate of the correct magnitude at high-frequencies, but to over estimate power-density at the lowest frequencies. In total, the amplitude of $\delta^{18}O$ variations owing to temperature and ice-volume is about twice that expected from ice-volume alone [*Bill Curry*, personal communication].

Independent estimates of lower-frequency temperature variability are also included from foram assemblage reconstructions of sea surface temperature from the subtropical Atlantic [*deMenocal et al.*, 2000]. Finally, planktic Mg/Ca measurements from the tropical Pacific [*Lea et al.*, 2000] and Cariaco basin [*Lea et al.*, 2003] are also included. At frequencies between 1/300yr and 1/10KY the power-density of the Mg/Ca and foram assemblage temperature estimates are in good agreement with calcite $\delta^{18}O$ temperatures, while at frequencies below 1/10KY the $\delta^{18}O$ estimates have greater power-density than the Mg/Ca estimates. This difference agrees with the assumptions regarding slowly varying ice-volume, and suggests ice-volume variability significantly influences calcite $\delta^{18}O$ variations at timescales longer than 10KY.

High-Latitude Atmospheric Temperatures

The longest continuous instrumental timeseries of surface air temperature comes from Central England, and begins in 1659 [*Manley*, 1974]. Tree ring density measurements are used to resolve the next longer timescales. There exists a serious limitation with most temperature estimates derived from trees, called the segment length curse [*Cook et al.*, 1995], whereby low-frequency variability is obscured by systematic changes in ring-density and ring-width as a tree develops. *Briffa et al.* [2001] have attempted to address this problem through a technique known as the age-band decomposition standardization procedure, and have provided multiple standardized tree-density records from N. America and Europe. The spectral estimate is made by averaging the power-density of the seven longest tree-density records, spanning the period between 1443

and 1983 at annual resolution.

Temperature estimates derived from ice-cores are employed to extend the analysis to periods of tens to hundreds of thousands of years. The $\delta^{18}O_{\text{ice}}$ signature recorded in Greenland ice-cores are correlated with past local temperature changes in a ratio of roughly 1.85°C per unit $\delta^{18}O_{\text{ice}}$ [*Caillon et al.*, 2001]. The spectrum is estimated from the second Greenland Ice-Sheet Project (GISP2) $\delta^{18}O$ measurements averaged at two meter intervals [*Grootes and Stuiver*, 1997]. Because the flow of an ice-sheet acts to thin the annual layers with depth, the time resolution of the $\delta^{18}O_{\text{ice}}$ record decreases significantly with depth. Temperature estimates from Antarctica are also included. Temperature is estimated from the Byrd ice-core [*Blunier and Brook*, 2001] using a conversion factor of 1.5°C per unit $\delta^{18}O_{\text{ice}}$ per mil [*Salamatin et al.*, 1998], and from the Vostok ice-core [*Petit et al.*, 1999] with a conversion factor of 1°C per 9 units δD_{ice} per mill. The GISP2 record is the most highly resolved, having an average sampling interval of less than a hundred years over the last 50KY, while the Vostok record is the longest, extending to 420KY BP.

1.3.2 Power-density spectra

To compare a broad range of climate spectra, ideally, one wants a normalization which is independent of both sampling interval and record length — but in most cases this is an impossibility. The choices which arise when normalizing spectral estimates can be illustrated via taking the Fourier transform of a real, discretely sampled signal, x_n $n = 0, 1, 2, 3...N$. For convenience, assume the total number of data points, N, is odd. Then

$$x_n = \sqrt{2} \sum_{n=1}^{(N-1)/2} a_k \cos\left(\frac{2\pi kp}{N}\right) + b_k \sin\left(\frac{2\pi kp}{N}\right), \qquad n = 1, ...N,$$

where the Fourier coefficients are given by,

$$a_k = \frac{\sqrt{2}}{N} \sum_{n=1}^{N} x_n \cos\left(\frac{2\pi kp}{N}\right), \qquad k = 1, ...\frac{N-1}{2},$$

$$b_k = \frac{\sqrt{2}}{N} \sum_{n=1}^{N} x_n \sin\left(\frac{2\pi kp}{N}\right), \qquad k = 1, ...\frac{N-1}{2}.$$

The factor of a square root of two multiplying the expressions for x_n and the a_k, b_k gives a particularly simple expression for the Parseval relationship [e.g. *Bracewell*,

2000],

$$\frac{1}{N}\sum_{n=1}^{N} x_n^2 = \sum_{k=1}^{(N-1)/2} (a_k^2 + b_k^2). \tag{1.2}$$

The Parseval relationship states that the variance in timeseries x_n must equal the sum of the squared Fourier coefficients and indicates that the energy dissipated by a system is intimately related to the square of the Fourier coefficients. This relationship will be useful when considering how the frequency representation of climate records should be normalized. Also note that there are as many Fourier coefficient as values in x; if the mean of x were non-zero, we would have to include an a_o term making the total number of Fourier coefficient equal to N. The squared sum of the a and b Fourier coefficients is referred to as the periodogram,

$$\Psi(k) = a_k^2 + b_k^2, \qquad s = \frac{k}{N\triangle t},$$

where the physical frequency, s, is related to k by the sampling interval, $\triangle t$, and number of samples N.

Normalization

Due to the normalization employed for the periodogram, an increase in the record length, N, of a stochastic process will lead to a decrease in the expected value of each estimate, $< \Psi(s) >$. To see this, observe that the expected variance, $< \frac{1}{N}\sum_{n=1}^{N} x_n^2 >$, will remain constant, and that by Eq. 1.2 the sum of the squared Fourier coefficients will equal this variance. Because increasing the record length increases the number of Fourier coefficients, the average value of the Periodogram estimates must diminish.

To compensate for this inverse dependence of the Fourier coefficient magnitudes on N, it is useful to multiply $\Psi(s)$ by N. How shall the quantity then be interpreted? One possibility is to note that the duration of the record, $N\triangle t$, is the inverse of the frequency interval associated with each Fourier coefficient, $\triangle s$. Thus, if the periodogram is also multiplied by $\triangle t$ it is equivalent to dividing each periodogram estimate by its associated bandwidth. When the periodogram is normalized by the bandwidth, the resulting estimate is termed the power-density, denoted by Φ.

An unavoidable side-effect of multiplying by $N\triangle t$, or dividing by $\triangle s$, is that spectra of periodic processes are no longer independent of record length. Instead, the energy in the spectral peak associated with a harmonic process will grow linearly

with record length. Again, appealing to Eq. 1.2, but now having multiplied both sides by $N\triangle t$, the left term will grow with record length, and because the process is periodic, this energy will be concentrated within a single band. No single normalization can render the spectral representation of both periodic and stochastic processes independent of record length. Because climate varies both stochastically and periodically, some compromise must be made. Here power-density spectra are used so that estimates of stochastic processes are independent of record length, and a post-hoc correction is applied to the magnitude of power-densities associated with periodic processes. The correction is,

$$\Phi'(s) = \frac{N_o}{N}\Phi(s),$$

were N is the number of observations associated with $\Phi(s)$ and N_o is the number of observations required to span the longest duration considered. For instance, if one has thirty years of tropical Pacific temperatures sampled monthly, but the longest record considered is a million years long, the scaling factor is $N_o/N = (12 \times 10^6 \text{ months})/(12 \times 50 \text{ months}) = 2 \times 10^4$.

Multi-taper spectral estimates

The periodogram of geophysical processes tends to be noisy and difficult interpret. Generally, a much better approach is to use the *multi-taper* method [*Thomson*, 1990]. This method employs a set of orthogonal weights known as discrete prolate spheroidal sequences, $h_{(n,m)}$, to partition x_n into a number of nearly orthogonal components. By calculating the periodogram associated with each nearly orthogonal component and averaging the results, a more stable estimate of the power-density spectrum is achieved,

$$\Phi(s) = \frac{N\triangle t}{M}\sum_{m=1}^{M}\Psi_m(s).$$

$\Phi(s)$ is referred to as the multi-taper power-density spectral estimate. The rational for multiplying Φ by $N\triangle t$ was discussed in the previous section. M is the selected number of tapers, yielding approximately $2M$ degrees of freedom in the spectral estimate (each estimate comes from a complex value with two degrees of freedom). The trade-off for increasing the degrees of freedom is a decrease in resolution. Further refinements are possible, for example employing adaptive weights to maximize both resolution and degrees of freedom. See *Percival and Walden* [1993] for a comprehensive description of the multi-taper method.

1.3.3 Aliasing

The normalization issues discussed in Appendix B are benign in that they are easily corrected. A more insidious problem arises in that unresolved variability in a climate record will masquerade as lower frequency variability — a phenomenon Tukey called aliasing. First, a simple example of aliasing is given, and afterward the requirements for correcting for its affects are discussed.

Origins

The origins of aliasing can be understood by considering a discretely sampled signal, x_n, where the spectrum exists for frequencies $1/(N\triangle t), 2/(N\triangle t), ...1/(2\triangle t)$. Now consider what happens to the spectrum when x_n is sampled at half the rate, $v_n = x_{2n}$. To compute the spectrum of the subsampled series, define another vector that has every other index of x set to zero,

$$\begin{aligned} u_n &= \begin{pmatrix} x_n, & n \text{ even} \\ 0 & n \text{ odd} \end{pmatrix} \\ &= \frac{1}{2}(x_n + x_n \times (-1)^n). \end{aligned} \tag{1.3}$$

The utility of this second vector is that u_{2n} equals x_{2n}. The final relationship suggests the effects of subsampling is to combine $x(n)$ with a higher frequency process, which becomes more clear after taking the Fourier transform,

$$\hat{u}_k = \frac{1}{2N}\left[\sum_{n=0}^{N} x_n e^{-\frac{i2\pi kn}{N}} + \sum_{n=0}^{N} x_n e^{-\frac{i2\pi n(k+N/2)}{N}}\right], \quad k = 1, 2, ...\frac{N-1}{2}.$$

The $(-1)^n$ in Eq 1.3 contributes an $e^{-in\pi}$ to the second term on the right hand side of the above equality. It is straight-forward to relate v_n and u_{2n} because u_n is zero at odd indices. Substituting into the above equation yields,

$$\hat{v}_k = \frac{1}{2(N/2)}\left[\sum_{m=0}^{N/2} x_{2m} e^{-\frac{i2\pi k2m}{N}} + \sum_{m=0}^{N/2} x_{2m} e^{-\frac{i2\pi 2m(k+N/2)}{N}}\right], \quad k = 1, 2, ...\frac{N/2-1}{2}$$

where the total number of observation, N, is now cut in half. The expected periodogram becomes,

$$\Psi_v(s) = \left[\Psi_x(s) + \Psi_x(s + \frac{1}{2\triangle t})\right],$$

assuming the frequencies s and $s + 1/2\triangle t$ are uncorrelated. Decreasing the sampling resolution by a factor of two results in the power which is no longer resolved, frequencies $\frac{1}{2\triangle t}$ to $\frac{1}{\triangle t}$, being folded into the resolved band, $\frac{1}{N\triangle t}$ to $\frac{1}{2\triangle t}$. That is, all the energy in $\Psi_x(s)$ is present in $\Psi_v(s)$ but in half the number of estimates. This result can be generalized to any degree of undersampling, [see e.g. *Priestley*, 1984] where the estimated spectrum is related to the *true* spectrum, $\Psi_t(s)$,

$$\Psi_v(s) = \sum_{r=0}^{\infty} \Psi_t(s + \frac{r}{2\triangle t}). \tag{1.4}$$

All spectral energy above the Nyquist frequency will alias into the resolved lower frequencies, biasing those estimates towards too large of values. See *Wunsch and Gunn* [2003a] for a general discussion of the effects of aliasing on the interpretation of paleoclimate records.

Effect on power-law processes

Aliasing can have serious effects on power-law estimates made from records of varying lengths and sampling intervals. Assume Ψ_t represents a band-limited white noise process with a uniform spectral distribution between zero frequency and a cutoff frequency, s_c, and is zero at all higher frequencies. If the sampling interval gives a Nyquist frequency greater than or equal to the cut-off frequency, $1/2\triangle t \geq s_c$, no aliasing will occur. Building from the previous example, assume a sampling interval, $\triangle t = \frac{2^{(h-1)}}{s_c}$. When $h = 0$ the spectrum of Ψ_t is fully resolved, but for $h > 0$ aliasing will occur; from Eq 1.4,

$$\Psi_v = \sum_{r=0}^{2^{(h-1)}} \Psi_t(s + \frac{r}{2\triangle t}).$$

In the case of white noise this reduces to,

$$\Psi_v = 2^{(h-1)}\Psi_t(s).$$

The Nyquist frequency of each spectral estimate is $s_c 2^{-h}$, and the mean frequency is $s_c 2^{-(h+1)}$. Writing the ratio of power density to the mean frequency gives,

$$\frac{2^{(h-1)}\Psi_t}{2^{-(h+1)}s_c} = \frac{2^h \Psi_t}{2^{-h}s_c},$$

showing that the power density of the composite spectra with $h = 0, 1, 2...$ will scale as, $2^h/2^{-h}$. In logarithm-power and logarithm-frequency space this will be, $h\log(2)/-h\log(2)$, giving rise to a spurious red spectrum with a power law of $q = 1$ (the power-law is defined as s^{-q} so that positive q's indicate that energy decreases with higher frequency). Note that the aliased version of each individual spectra will itself be white, but because greater amounts of aliasing occurs for the lower-frequency spectral estimate, the overall power-law estimated from the composite spectra will be red.

If one seeks to correct for the effects of aliasing, assumptions about the unresolved higher-frequency variability are required. *Wunsch* [1972] gives an example of accounting for the bulge in the high-frequency spectral estimates of a tidal-gauge record by assuming a constant power-law with $q = 2$ and applying Eq 1.4. The solution involves an infinite sum, which only converges when q is greater than one. This implies that if one measures a finite spectrum with a power-law of one or less, in order to keep the total energy bounded, at higher frequencies the power-law must become more red. Therefor a plausible assumption regarding unresolved high-frequency temperature variability would be a steady power-law up to a cut-off frequency, above which there exists negligible energy.

So far the discussion has focused on stochastic processes. A further consideration is that when the annual cycle is not resolved we can expect its energy to be aliased to lower-frequencies. Were paleo-proxies sampled at a uniform sampling interval, it would be straight-forward to calculate where the annual variability would appear. In practice, this is hardly ever the case, and the *jitter* in the sampling interval is expected to distribute the unresolved annual variability over a broad range of frequencies [see *Moore and Thomson*, 1991]. As a final consideration, the manner in which each proxy averages the climate variability will also influence the degree of aliasing. For example, if a tree-ring record represented a uniform average over the year, an annually resolved record would have no aliasing. But if the tree has a differing sensitivity to temperature at different times of the year, and different points in its growth cycle, some aliasing is inevitable. Then, in addition to a model of high-frequency temperature behavior, one needs to model the proxy sampling characteristics when assessing the effects of aliasing. Such a detailed analysis is not further pursued here.

The power-law found for aliased white noise, when successive records are sub-sampled by a factor of two, is the same as for tropical sea surface temperatures [see Figure 1-1]. The scope of the bias in the proxy records is unclear, but it appears that

for white, or nearly white, signals there will be a general trend towards increasingly over-estimated spectra as the sampling interval grows. This will tend to bias power-laws towards being too red. Some further observations can be made that argue against the power-law estimates being wholly an artifact of aliasing. First, multiple different proxies of tropical sea surface temperature variability are each consistent with a power-law of one. Second, the high-frequency estimates which resolve the annual variability are consistent with the low-frequency estimates where they overlap. Further study of the impact of aliasing on power-law processes is required.

Chapter 2

On Insolation Forcing

The previous chapter presented a spectral description of the spatial and temporal variations in long-term climate variability. Much of climate variability is characterized by simple spectral power-laws. While there remain important questions regarding the origins of the climate continuum, the following Chapters focus on the Milankovitch bands of variability. Such a focus can be justified by the wide-spread interpretation of long-term climate variability as being strongly influenced by orbital forcing which can be traced back to the identification of Milankovitch bands of variability in deep-sea cores by *Hays et al.* [1976]. In seeking to better assess the role of orbital forcing in causing climate variability, this chapter investigates the orbital variations, the attendant changes in insolation forcing, and the manner in which these signals are likely to appear in the climate recorded.

The spatial and temporal variations in insolation are examined from a signal processing point of view, with attention paid to the frequency and amplitude modulation occurring at both the annual and longer period timescales. Two aspects of precession variability are considered in detail. First discussed is how precession period signals in the climate record should be interpreted; there are a number of potential sources, and there are certain requirements the climate system must meet in order to produce this variability. Second, the frequency modulation of the precession variability is discussed in relation to orbitally derived age estimates. It is shown that the amplitude modulation of precession period signals cannot be used to test the accuracy of these orbital age-estimates.

The concentrations of insolation variability at both the annual and secular[1] timescales

[1]In astronomy, secular changes refer to the long-term variations in a planet's orbit. There are many short-term variations due to, for example, the gravitational influence of other planets, but

makes insolation difficult to represent and interpret. Often, the representation of insolation variability is simplified to a single one-dimensional low-frequency signal, inevitably altering or ignoring important features of the variability. These simplifications are briefly reviewed and compared with one another, after which a more complete representation of the insolation forcing is presented. The new representation is developed in terms of spatial modes of variability, and retains a full description of the seasonal and secular variability. The description is accurate and compact, and provides insight into how the spatial modes of insolation forcing vary seasonally and at long time periods.

2.1 Earth's orbital parameters

The insolation for any time and point on the globe can be represented as [e.g. *Vernekar*, 1972],

$$I = I_o \left(\frac{1 + e\cos(\lambda_s - \varpi)}{(1 - e^2)} \right)^2 (\sin\phi \sin\theta \sin\lambda_s + \cos\phi \cos\theta \cos\lambda_s \cos(\lambda - \eta)), \qquad I \geq 0, \tag{2.1}$$

where I_o is the solar constant (about $1368 W/m^2$), ϕ latitude, λ longitude, e orbital eccentricity, θ obliquity, ϖ the argument of perigee, λ_s solar longitude, and η the hour angle. The frequency of variation for the last five variables is $e \sim (400\text{Kyr})^{-1}$ and $(100\text{Kyr})^{-1}$, $\theta \sim (41\text{Kyr})^{-1}$, $\varpi \sim (21\text{Kyr})^{-1}$, $\lambda_s = 1\text{yr}$, and $\eta = 1$ day; thus the frequency range extends over more than seven orders of magnitude. The '$\sim$' symbol indicates a band of variability centered on the specified frequency. All of the orbital parameters are frequency modulated [*Hinnov*, 2002] and thus, in fact, can only be partially described using a single frequency. A diagram of earth's present orbital configuration is shown in Figure 2-1. The form of Eq. 2.1 indicates the secular variations in insolation are controlled by eccentricity, obliquity, and the argument of perigee — each orbital parameters is discussed in turn.

which over relatively short periods average to zero.

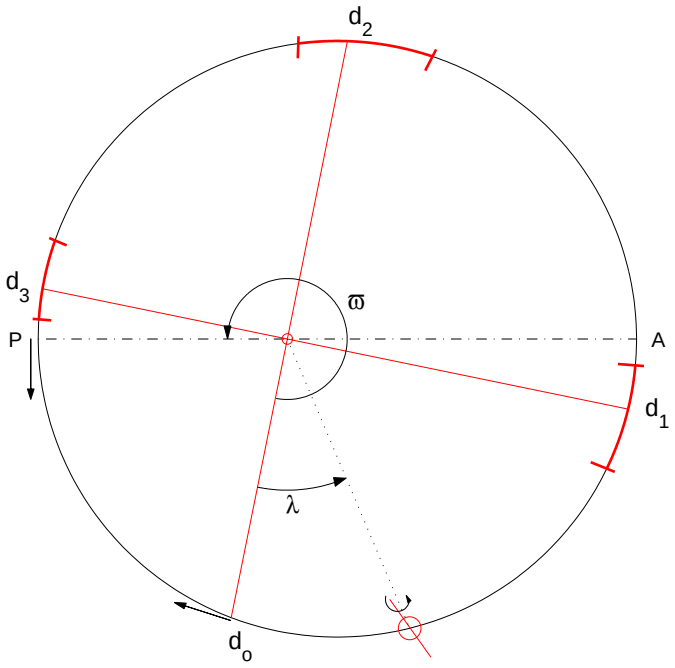

Figure 2-1: Earth's orbit around the sun. The argument of perigee (ϖ), measured from the vernal equinox (d_o) to perihelion (P), is shown with its current configurations, but for visual purposes, the eccentricity of the orbit is shown with ten times the current value. Relative to the fixed stars, d_o has a fixed period of 25.8 KY while P moves with periods varying from 100 to 400 KY. Relative to one another the motions of d_o and P give a climatic precession period ranging from 23 to 18 ka. The vernal equinox currently occurs on March 20th, and up to the small variations caused by the non-integer number of days in the year (hence the use of leap-years), has a fixed solar-longitude. Also shown are Northern Hemisphere summer solstice ($\lambda = 90°$), autumnal equinox ($\lambda = 180°$), and winter solstice ($\lambda = 270°$), which currently occur on June 21st (d_1), September 22nd (d_2), and December 21st (d_3) respectively. These latter set of dates are associated with varying solar-longitudes, depending on the degree of eccentricity and on the argument of perigee. The maximum variations in solar-longitude associated with the dates of each solstice and spring equinox over the last 1000KY are indicated on the above figure by the red arc segments.

2.1.1 Eccentricity

Eccentricity is measured as

$$e = \sqrt{1 - \left(\frac{L_{\text{major}}}{L_{\text{minor}}}\right)^2}, \tag{2.2}$$

where L represents the length of the major and minor orbital axis. Currently, the eccentricity of the earth is 0.01672. This produces a 7% annual-period change in the insolation incident at the top of the atmosphere from 354 W/m^2 during perihelion to 331 W/m^2 during aphelion. The difference in insolation is primarily due to the sun's displacement from the geometric center of the earth's orbit to one of the two foci of the orbital ellipse. For illustrative purposes, the ellipse shown in Figure 2-1 has an eccentricity of 0.1672, ten times the present value.

Eccentricity is unique among the orbital parameters in that it affects net annual insolation, in proportion to $I_o(1-e^2)^{-2}$. The timeseries and periodogram of eccentricity are shown in Figure 2-2 where the orbital solution of *Berger and Loutre* [1992] is used as throughout this thesis. While eccentricity is dominated by a few low-frequency terms, it also has a significant broadband component. Note however, that at timescales of less than 10 million years, the orbital parameters are deterministic [e.g. *Laskar*, 1993], and the frequency domain behavior of eccentricity is not that of a stochastic process. This broadband behavior has to be included in any discussion of the effects of eccentricity on climate.

2.1.2 Obliquity

The obliquity term appears in the final right-hand portion of Eq. 2.1, and varies the meridional distribution of incoming insolation, but does not affect the global total insolation on any timescale. Obliquity is a measure of the angle between earth's equatorial and orbital planes and is currently 23.5^o. The earth's equatorial plane precesses with a period of 25.8KY and the earth's orbital plane precesses with a period of 70KY. Obliquity measures the difference between these two planes and results in the climatically relevant $1/25.8 - 1/70 = 1/41$KY frequency [see *Muller and MacDonald*, 2000]. Apart from the $\approx 7\%$ change in insolation due to eccentricity and timed by precession, the obliquity of the Earth's orbital axis with respect to the orbital plane accounts for the magnitude of the seasonal insolation variations.

The amplitude of the obliquity variations ranges from 2.4° to 0.7°, primarily due to changes in the inclination of the orbital plane as measured relative to the invariant plane. The orbital and invariant planes rotate with respect to one another with a roughly 100KY period where the invariant plane is the plane perpendicular to the total angular momentum vector of the planets [e.g. *Muller and MacDonald*, 2000]. The periodogram of the obliquity variations has a central peak flanked by minor side-

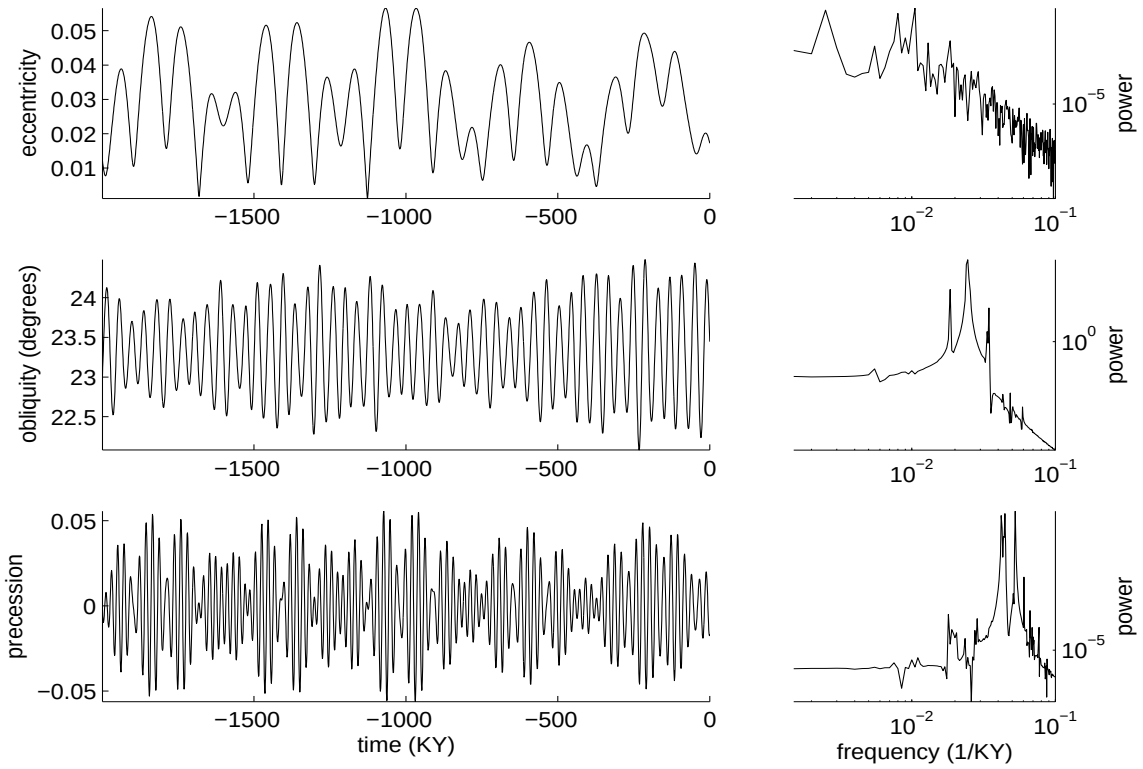

Figure 2-2: Each orbital parameter is shown over the last two million years (left) along with the associated periodogram (right). For eccentricity (top) variability is primarily concentrated in bands near 1/400, 1/125, and 1/95KY; obliquity (middle) variability is concentrated at 1/41KY; and climatic precession (bottom) variability is at 1/19, 1/22, and 1/24KY.

lobes, the latter owing to the amplitude and frequency modulations [see *Berger et al*, 1998].

2.1.3 Precession

The precession of the equinoxes occurs because of the torque exerted on its equatorial bulge by the moon and sun, and to a lesser extent by the other planets. Of the secular motions associated with the Earth's orbit, the interpretation of precession is the most complex. The Oxford English Dictionary defines precession of the equinoxes as,

> "the earlier occurrence of the equinoxes in each successive sidereal year, due to the retrograde motion of the equinoctial points along the ecliptic, produced by the slow change of direction in space of the earth's axis, which moves so that the pole of the equator describes a circle (approximately:

see nutation) around the pole of the ecliptic once in about 25,800 years. Hence commonly used to denote this motion of the equinoctial points, of the earth's axis, or of the celestial pole or equator; also the motion of the earth itself which manifests itself as the precession of the equinoxes."

The climatic relevance of the precession of the equinoxes, however, is only in its relation to Earth's eccentric orbit — at zero eccentricity there is no precession effect. In particular, one would like a quantity indicating how the argument of perigee is related to insolation variations. If one takes the spatial and diurnal average of insolation, and neglects terms involving e^2 and higher, then the insolation becomes,

$$I \approx \frac{I_o}{4} \left[1 + 2e \cos\left(\lambda_s - \varpi\right)\right].$$

Milankovitch [1941] hypothesized that the amount of insolation during summer is of prime importance for causing deglaciations. Setting the solar longitude to the summer solstice, $\lambda_s = 90°$, then yields,

$$I \approx \frac{I_o}{4} \left[1 + 2e \sin\left(\varpi\right)\right],$$

where the relationship,

$$e \cos\left(90° - \varpi\right) = -e \sin\left(-\varpi\right) = e \sin\left(\varpi\right),$$

was used. The last term above is called the *climatic precession parameter* [e.g. *Berger*, 1993], or just the *precession parameter*. The precession parameter measures the sine of the angle between vernal equinox and perihelion and scales with the eccentricity of the earth's orbit. It is approximately proportional to the spatial and diurnal average of insolation during the summer solstice.

Rubincam [1994] has expanded the diurnally averaged version of Eq. 2.1 in terms of Legendre polynomials, and has shown that each of the leading order terms involving ϖ all vary at periods equal to or less than a year. That is, for example, terms are of the form $\sin(\varpi + M)$ where M is the mean anomaly and has a period of one tropical year. The frequency associated with the precession plus mean anomaly term is $d(\varpi + M)/dt \sim dM/dt \sim 1/year$, or one cycle per anomalistic year. The difference between the tropical and anomalistic years are discussed in more detail later.

The precession parameter has a rich behavior that requires careful interpretation. The remainder of this chapter is devoted quantifying and interpreting the behavior of precessional variability in four different contexts:

- Section 2.2 shows that the amplitude and frequency modulation of the precession parameter are linked. This linkage causes the accuracy of many paleoclimate age-models based on orbital assumptions to be questionable.
- Section 2.3 points out that precession-band energy appearing in the climate record requires the existence of a seasonal-cycle rectifier. Such rectifiers appear both in the climate system itself, and also in the recording devices, making the origins of precession energy in climate proxies indeterminate.
- Section 2.4 calls attention to how simplifications of insolation tend to emphasize one or another mode of insolation variability, and neglect others.
- Finally, in Section 2.5, a compact yet full expression of insolation variability is developed. This expression provides an accurate and relatively simple description of how the spatial patterns of insolation forcing evolve over timescales ranging from seasons to millions of years.

2.2 Precession amplitude modulation: confirmation of orbital climate control or signal processing artifact?

The appearance of precession-like amplitude modulation in paleoclimate records has been cited as lending strong support for the existence of orbital forcing within the climate system, as well as *validating* the accuracy of paleoclimate age-models. While there are other lines of evidence which support the existence of orbitally forced climate change, as well as the accuracy of orbitally derived age-models [see Chapter 3], here the question is raised as to whether the orbital results have been received with greater confidence than is warranted. For example, *Imbrie et al.* [1984] state that the "statistical evidence of a close relationship between the time-varying amplitudes of orbital forcing and the time-varying amplitudes of the isotopic response implies that orbital variations are the main external cause of the succession of late Pleistocene ice ages."

More recently *Shackleton et al.* [1995] conclude, "Probably the most important feature through which the orbital imprint may be unambiguously recognized in ancient geological records is the amplitude modulation of the precession component by the varying eccentricity of the Earth orbit." As a final example, in comparing a narrow-band-passed SPECMAP record with precession, *Paillard* [2001] states "It is remarkable that both time series have a quite similar modulation of their amplitude. This is probably one of the strongest arguments in favor of a simple causal relationship between the precessional forcing and the climatic response in this frequency band. Indeed, in contrast to other techniques, amplitude modulation is not affected by tuning."

In this context, tuning refers to the practice of stretching and squeezing the age-model of a paleoclimate record so as to sharpened and enhance features of its orbital variability. Obviously tuning can affect the frequency of signals within a record; less obviously, and contrary to the above author's conclusions, when narrow-band-pass filtering is required (as it usually is), this also affects estimates of the amplitude of precession band variability in paleoclimate records. An example of how orbital-tuning can influence the amplitude of the precession variability was first pointed out by *Neeman* [1993], but which has not been paid much attention. Here, a more thorough investigation of how eccentricity-like amplitude modulation can be generated is undertaken.

2.2.1 Precession frequency and amplitude modulation

Over the last million years, the mean frequency of the precession parameters has been 1/20.4KY. This frequency is higher than the 1/25.8KY frequency associated with the precession of the equinoxes because the longitude of perihelion rotates towards the vernal equinox at an average rate of 1/97KY where 1/97KY+1/25.8KY=1/20.4KY [see Figure 2-1]. The mean frequency of the precession parameter, however, provides only a partial description as the perihelion tends to move episodically. The episodic motions are generated by Earth's gravitational interaction with other planets and cause the instantaneous frequency of the precession parameter to be highly variable.

To further examine the perturbations to the precession parameter's frequency it is useful to model the influence of other planets on Earth's orbit as impulsive forces,

$$F = R\hat{r} + N\hat{h} + T\hat{h} \times \hat{r}, \tag{2.3}$$

Here F has vector components, $\hat{r}$, pointing from the sun to the earth and, $\hat{h}$, perpendicular to the orbital plane. The change in the longitude of perihelion resulting from F is [e.g. *Danby* Eq. 11.5.11, 1992],

$$d\varpi' = \frac{\sqrt{1-e^2}}{nae}\left\{-R\cos v + T\sin v\frac{2+e\cos v}{1+e\cos v}\right\}dt \tag{2.4}$$

where n is earth's average orbital angular velocity, v is the angle between perihelion and the earth, and a is earth's mean distance from the sun. The equation is meaningful over at least the last 5Ma as eccentricity, e, is always greater than zero. Note that only those components of the impulse in the orbital plane (R and T) act to change ϖ. The instantaneous frequency associated with the precession parameter, $d\varpi/dt$, is the sum of the instantaneous frequency associated with the longitude of perihelion, $d\varpi'/dt$, plus the (nearly) constant 1/25.8KY precession of the equinoxes term. As stated earlier, the longitude of perihelion has a mean frequency of $\overline{d\varpi'}/dt = 1/97$KY giving an averaged climatic precession parameter frequency of 1/25.8+1/97=1/20.4KY.

Importantly, Eq 2.4 shows that the longitude of perihelion is more susceptible to perturbations when the eccentricity is small. That is, one expects the magnitude of $d\varpi'/dt$ to be largest when the eccentricity is smallest. Figure 2-3 shows the instantaneous amplitude and frequency associated with precession parameter over the last 5 million years (Ma) calculated using a Hilbert transform [see e.g *Bracewell*, 2001] of the orbital solution of *Berger and Loutre* [1991]. As expected from Eq. 2.4, there is a clear relationship between large excursions in instantaneous frequency and low values of the eccentricity. To quantify this relationship, Figure 2-3 also shows the absolute deviations in instantaneous frequency, $|d\varpi'/dt - \overline{d\varpi'}/dt|$, plotted against inverse eccentricity, $1/e$. The squared-cross-correlations between the absolute frequency deviations and inverse eccentricity over the last 5 Ma is 0.56, indicating that variations in eccentricity account for the majority of the frequency variability in the climatic precession parameter.

2.2.2 Narrow-band-pass filtering and amplitude modulation

In the last section it was shown that variations in eccentricity cause changes in both the amplitude and frequency of the precession parameter. In this section it is shown that frequency modulation can be transformed into an amplitude modulation as a result of standard narrow-band-pass filtering of a signal. In a geophysical context,

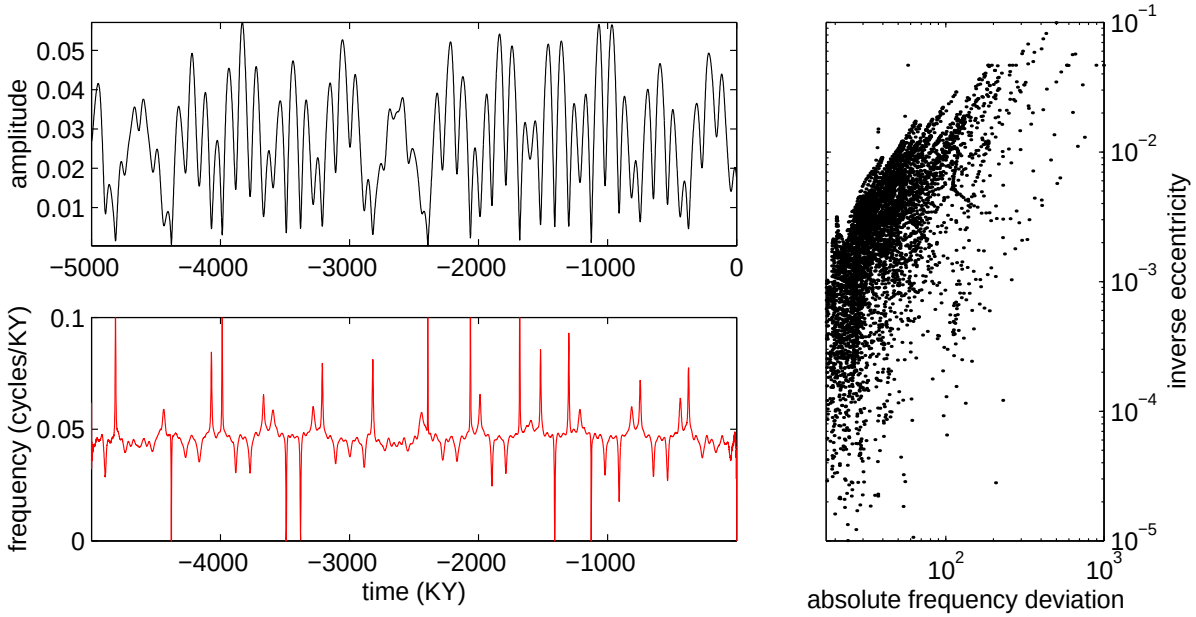

Figure 2-3: **Top left**, The instantaneous amplitude of the precession parameter which, by definition, is the eccentricity. **Bottom left**, the instantaneous frequency of the precession parameter measured in cycles per KY and estimated using a Hilbert transform. The average frequency of the precession parameter over the last 5Ma is 1/20.4KY. Significant excursions from the mean are observed to occur during times of low eccentricity, as expected from Eq. 2.4. **Right**, To highlight the coupling between eccentricity and the precession frequency, the absolute deviations in instantaneous frequency, $|d\varpi/dt - 1/20.4KY|$, are plotted against inverse eccentricity, $1/e$. Note the plot is logarithmically scaled. A strong positive cross-correlation of 0.75 exists between the variability in $|d\varpi/dt - 1/20.4\text{KY}|$ and $1/e$.

narrow-band-pass filtering is often utilized to isolate a narrow-band signal of interest from the broad-band continuum or other narrow-band signals. Therefor it is natural that narrow-band filtering is often used to isolate precession variability in paleoclimate records [e.g. *Imbrie et al.*, 1984; *Imbrie et al.*, 1993]. It is shown below that when the signal of interest has a frequency modulation associated with it, the resulting filtered signal will have an amplitude modulation related to its frequency modulation.

To see how narrow-band-pass filtering can generate amplitude modulation it is first useful to review some aspects of amplitude and frequency modulated signals. Consider a pure cosine, $\cos(2\pi t f_1)$, of *carrier frequency* f_1 multiplied by another cosine of frequency f_2. Then,

$$\mu(t) = \cos(2\pi t f_1)\cos(2\pi t f_2) = \cos(2\pi t(f_1 + f_2)) + \cos(2\pi t(f_1 - f_2)) \qquad (2.5)$$

here the carrier frequency, f_1, is split into two new frequencies, $f_1 \pm f_2$, in the process known as amplitude modulation. A power spectrum of $\mu(t)$ would display peaks not at f_1, but at $(f_1 \pm f_2)$, that is, with two-sidebands.

If instead a cosine is frequency modulated by another cosine we have,

$$\begin{aligned} \mu(t) &= \cos(2\pi t f_1 + 2\pi\delta\cos(2\pi t f_2)) \\ &= \cos(2\pi t f_1)\cos(2\pi\delta\cos(2\pi t f_2)) + \sin(2\pi t f_1)\sin(2\pi\delta\cos(2\pi t f_2)). \quad (2.6) \end{aligned}$$

Using a simple identity [*Olver* 1962, Eqs 9.1.44-45] Eq. (2.6) is,

$$\begin{aligned} \mu(t) &= cos(2\pi t f_1)[J_o(2\pi\delta f_2) + 2\sum_{k=1}^{\infty} J_{2k}(2\pi\delta f_2)\cos(4\pi k t f_2)] \\ &\quad - \sin(2\pi t f_1)\sum_{k=0}^{\infty} -1^k J_{2k+1}(2\pi\delta f_1)\cos(2\pi(2k+1)t f_2), \quad (2.7) \end{aligned}$$

where the J_p are Bessel functions. Now $\mu(t)$ has spectral peaks at $f_1 \pm k f_2$ for $k = [0, 1, 2...]$ with the relative amplitudes determined by the strength of the modulation term and the displacement from the carrier frequency.

The relevant point to be drawn from Eq 2.7 is that generating a frequency modulated signal, which is not amplitude modulated, requires contributions from frequencies extending out to infinity. Thus, any narrow-band-pass filtering of a frequency modulated signal will produce some amplitude modulation. The exact form of the amplitude modulation will depend on the frequency modulation and on the specifications of the narrow-band-pass filter which is employed.

To be specific, a version of Eq 2.6 is used with

$$\begin{aligned} \mu(t) &= \cos\left(\frac{2\pi t}{21} + w'\right) \quad (2.8) \\ w' &= \frac{2\pi}{5}\left[\cos\left(\frac{2\pi t}{100}\right) + 1\right] \end{aligned}$$

where the frequency modulation term, w', is non-negative and has a 100KY period in rough analogy with the eccentricity variability. The frequency modulated signal, $\mu(t)$, is shown in Figure 2-4. Also shown is the periodogram of $\mu(t)$ which displays side-bands at $1/21 \pm k/100$ for $k = \{0, 1, 2...\}$ as predicted by Eq. 2.7. Up to this point $\mu(t)$ has no amplitude modulation, but now consider the effects of narrow-band-pass filtering. For clarity, a simple filtering technique is adopted whereby the Fourier transform of $\mu(t)$ is taken, all the Fourier coefficients outside of a frequency band $1/25$

to 1/17KY are set to zero, and then the inverse Fourier transform of the modified Fourier coefficients gives the filtered signal, $\tilde{\mu}(t)$. $\tilde{\mu}(t)$ is shown in Figure 2-4 along with its periodogram.

The narrow-band-pass filtering suppresses spectral energy outside of the band between 1/25 to 1/17KY, leaving only two dominant frequency components in $\tilde{\mu}(t)$ at 1/23KY and 1/23+1/100=1/19KY of nearly equal magnitude. Thus, the filtered signal can be approximated as

$$\tilde{\mu}(t) \approx \cos\left(\frac{2\pi t}{23}\right) + \cos\left(\frac{2\pi t}{19}\right).$$

Eq. 2.5 shows that the sum of two cosines can be re-written as an amplitude modulated signal; in this case giving

$$\tilde{\mu}(t) \approx \cos\left(\frac{2\pi t}{200}\right) \times \cos\left(\frac{2\pi t}{20.6}\right).$$

One further modification is now necessary to relate the amplitude modulation of $\tilde{\mu}(t)$ to the frequency modulation, w'. The amplitude modulation term, $\cos(\frac{2\pi t}{200})$, becomes negative whereas the instantaneous amplitude is typically defined as a positive quantity. The absolute value of the amplitude modulation term can be written,

$$\begin{aligned} \text{AM} \quad &= \quad \left[\cos\left(\frac{2\pi t}{200}\right)^2\right]^{\frac{1}{2}}, \\ \tfrac{1}{\sqrt{2}}\times \quad &\left[\cos\left(\frac{2\pi t}{100}\right) + 1\right]^{\frac{1}{2}}, \end{aligned} \tag{2.9}$$

where the relationship $\cos(f)^2 = cos(2f) + 1$ was used. Thus, both the amplitude modulation, AM, and frequency modulation, w', terms are positive and periodic at 100KY. Figure 2-4 shows the excellent correspondence when both these terms are plotted against one another.

2.2.3 Eccentricity modulation of precession

For the simple periodic modulation of a cosine by another cosine it was shown that narrow-band-pass filtering can generate an amplitude modulation with a period similar with the original frequency modulation. Now we turn to the more complicated precession signal. It was shown earlier that both the amplitude and precession of the climatic precession parameter are modulated by the eccentricity variability. In this

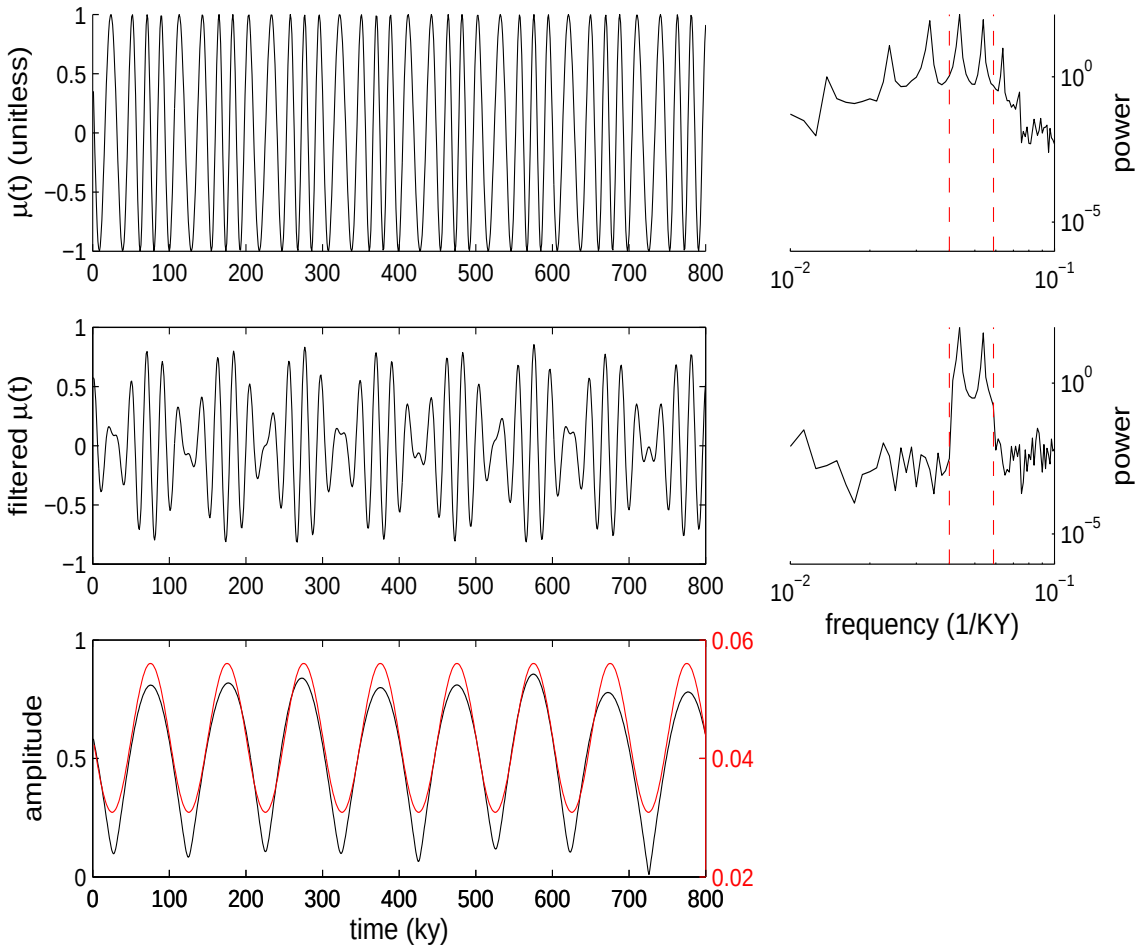

Figure 2-4: **Top left** the frequency modulated signal $\mu(t)$ given by Eq. 2.9. Note there is no amplitude modulation. **Top right** shows the periodogram of $\mu(t)$ with power concentrated at the carrier frequency of 1/23KY and side-bands at $1/23 \pm k/100KY$, $k = \{0, 1, 2...\}$. **Middle left** applying a narrow-band-pass filter to $\mu(t)$ gives $\tilde{\mu}(t)$ with amplitude modulation. **Middle right** shows the periodogram of $\tilde{\mu}(t)$. The pass-band filter cut-off frequencies at 1/23KY and 1/16KY are indicated by the vertical dashed lines. A small amount of white noise was added for plotting purposes. **Bottom** shows that the instantaneous amplitude of $\tilde{\mu}(t)$ (black) is strongly correlated with the instantaneous frequency of $\mu(t)$ (red).

section it is shown that, in direct analogy with the previous simple example, eccentricity amplitude modulation can be generated from precessional frequency modulation alone.

Figure 2-5 shows the frequency modulated precession signal $\sin \varpi$; note there is no eccentricity amplitude modulation. The periodogram of $\sin \varpi$ contains concentrations of energy at 1/23 and 1/19KY as well as concentrations of energy at a variety of side-

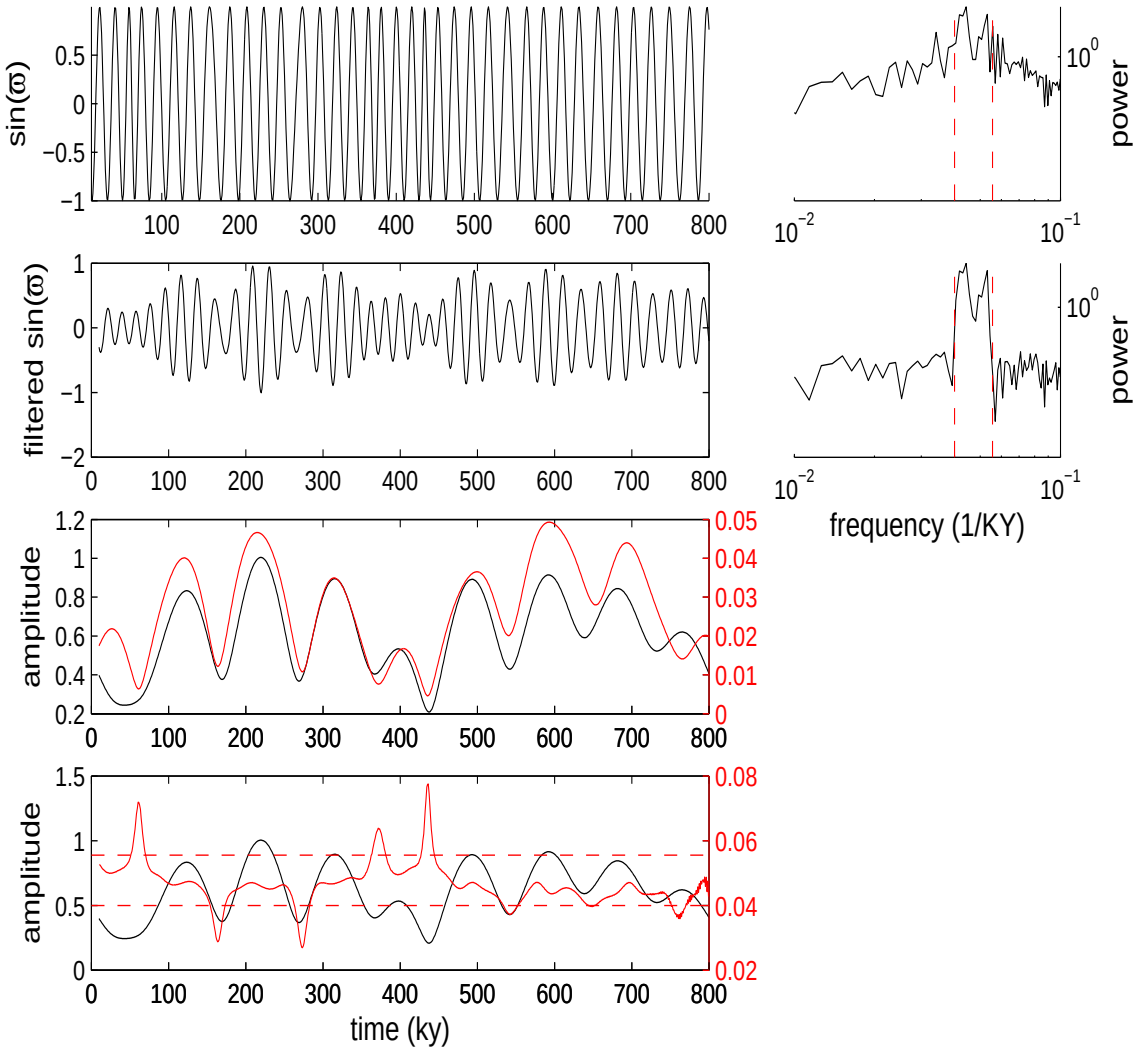

Figure 2-5: Similar to Figure 2-4 but now for the precession signal. **Top left** the precession signal $\sin \varpi$ without eccentricity amplitude modulation. **Top right** The periodogram of $\sin \varpi$ showing excesses of energy near 1/23 and 1/19KY but also significant energy in numerous side-bands. **Upper left** is $\sin \varpi$ after narrow-band-pass filtering, and **upper right** is the associated periodogram. The filtering cut-off frequency are indicated by the vertical dashed lines at 1/25 and 1/18KY. **Lower left** shows the strong similarity between the instantaneous amplitude of the filtered precession signal (black) and the eccentricity (red), each plotted on their own scales. **Bottom** is again the instantaneous amplitude (black) but also the instantaneous frequency (red) of the filtered precession signal. The horizontal dashed lines indicate the cut-off frequencies used for filtering the precession signal. Note that when the instantaneous frequency strays outside the cut-off frequencies, the amplitude of the filtered precession signal tends to be small.

bands. For the signal $\mu(t)$, the distribution of side-band energy was particularly simple [see Figure 2-4]; by contrast, the distribution of precession side-band energy is complicated by the more abrupt and episodic changes in the frequency of precession. Nonetheless, Figure 2-5 shows that after narrow-band-pass filtering $\sin\varpi$ between cut-off frequencies of 1/25 and 1/18KY, an eccentricity-like amplitude modulation appears.

The instantaneous amplitude of the filtered $\sin\varpi$ signal closely corresponds with the eccentricity variability with a cross-correlation of 0.87. A qualitative explanation for the close resemblance between the filtered signal's amplitude and the eccentricity is that during times of low eccentricity, precession tends to have significant deviations in instantaneous frequency [see Eq. 2.4]. These deviations in frequency manifest as the side-band energy in the periodogram of $sin(\varpi)$. The removal of this side-band energy by narrow-band-pass filtering also removes the energy associated with the anomalously high or low frequencies in $sin(\varpi)$, tending to give a reduced amplitude during times of low eccentricity. Thus the amplitude of the filtered precession variability corresponds in phase and magnitude with the eccentricity induced frequency modulations.

The further question arises of whether an eccentricity amplitude modulation can be built into a signal, absent any true precession energy. In Appendix C of Chapter 3, it is demonstrated that orbitally-tuning a noisy signal to precession and then narrow-band-pass filtering over the precession band does, in fact, generate a precession period signal with eccentricity-like amplitude modulation, consistent with the results of *Neeman* [1993]. Thus, contrary to assertions made elsewhere, it is concluded that the appearance of eccentricity-like amplitude modulation in orbitally-tuned and pass-band-filtered paleoclimate records does not provide evidence for orbital control.

In summary, it was shown that the frequency of the precession parameter undergoes large deviations when the eccentricity is small. It was also shown that narrow-band-pass filtering a frequency modulated signal can generate an amplitude modulation similar in period to the original frequency modulation. Because it is well established that orbital-tuning can build frequency modulation into a signal [e.g. *Shackleton et al*, 1995], it is expected and shown that eccentricity amplitude modulation will appear in records which are tuned to precession and then narrow-band-pass filtered. Thus, the presence of eccentricity amplitude modulation in records tuned to precession does not provide evidence for orbital climate control.

2.3 Rectification and precession signals in the climate system

The appearance of precession signals in orbitally-tuned records is somewhat suspect because of the ability to build-in concentrations of variability at the precession bands and to generate eccentricity-like amplitude modulation. However, it has been shown that even in the absence of orbital age-model assumptions, concentrations of precession period variability do appear in the $\delta^{18}O$ record [e.g. *Hays et al.*, 1976; also see Chapter 3]. In the following section, repeated verbatim from [*Huybers* and *Wunsch*, 2003], the origins of such precession period variability in the climate record are discussed in more detail.

The following is repeated verbatim from Huybers and Wunsch [2003]

Abstract: Precession of the equinoxes has no effect on the mean annual insolation, but does modulate the amplitude of the seasonal cycle. In a linear climate system, there would be no energy near the 21,000 year precession period. It is only when a non-linear mechanism rectifies the seasonal modulation that precession-period variability appears. Such rectification can arise from physical processes within the climate system, for example a dependence of ice cover only on summer maximum insolation. The possibility exists, however, that the seasonality inherent in many climate proxies will produce precession-period variability in the records independent of any precession-period variability in the climate. One must distinguish this "instrumental" effect from true climate responses. Careful examination of regions without seasonal cycles, for example the abyssal non-equatorial ocean, and the use of proxies with different seasonal responses, might permit separation of physical from instrumental effects.

2.3.1 Introduction

One of the most important elements in the discussion of climate change concerns the appearance in, and possible dominance by, Milankovitch cycles in paleoclimate records. Setting aside the 100 kyr band, whose relationship to Milankovitch forcing remains problematic [e.g *Roe and Allen*, 1999], the Milankovitch-forced energy is largely, but not wholly, contained within two bands around 41 kyr and 21 kyr—the obliquity and precessional bands respectively [*Bradley*, 1999; *Cronin*, 1999].

In particular, reports of strong precessional signals in various records are widespread;

among the most recent reports are *Lamy et al.* [1998] for deep-sea sediments, *Thaman et al.*. [2002] for monsoon strength, and *Bozzano et al.*. [2002] for atmospheric dust. Such signals are usually interpreted as demonstrating orbital-period climate variability [e.g., *Ruddiman and McIntyre*, 1981; *Imbrie et al.*, 1992]. Here we raise the question of whether these signals are due to subannual climate variability or, at least in part, are an artifact of the way in which climate signals are recorded.

2.3.2 Obtaining precessional rectification

Changes in Earth's obliquity alter the amplitude of the seasonal cycle and generate low-frequency shifts in the latitudinal distribution of insolation. Precessional changes also alter the seasonal cycle, but in contrast to obliquity, cause no change in annual average insolation at any latitude [*Rubincam*, 1994],. A general expression for insolation contains terms related to seasonal variability of the form,

$$\begin{aligned} \mathcal{F} &= a \sin\epsilon \sin M + b \sin(M - \varpi) + ... \\ &\equiv \mathcal{F}_1 + \mathcal{F}_2 + ... \end{aligned} \tag{2.10}$$

Here, M is the true anomaly, an angle increasing by 360° per year, ϵ is the obliquity, varying between 22° and 25° with a time scale of about 41 kyr; and ϖ is the angle between perihelion and the vernal equinox and varies with periods dominantly between 19 and 23 kyr. a, b are coefficients that are either constant or have even lower frequency dependencies.

Both terms $\mathcal{F}_{1,2}$ vary at periods of close to one year. $\mathcal{F}_1$ has an annual carrier frequency, $s_a = \dot{M}/2\pi$, the dot denoting the time derivative, and is amplitude modulated by obliquity at a frequency $s_\epsilon = \dot{\epsilon}/2\pi$. The amplitude modulation involves two combination frequencies $s_a \pm s_\epsilon \approx s_a$, which vanish when averaged over a tropical year. In $\mathcal{F}_2$, the frequency is $s_a - s_\varpi \approx s_a$; because $s_\varpi << s_a$, the forcing averages to zero over any integral multiple of durations $2\pi/(s_a - s_\varpi)$, that is over one anomalistic year. In the full insolation forcing ϵ also occurs independent of M, thus varying at low-frequencies, while all instances of ϖ appear in combination with M, thus varying at periods near one year.

How does one obtain a low frequency response to high frequency insolation variations? There are several possibilities. Suppose, following the very large literature on Milankovitch forcing, that the climate system responds primarily to summer in-

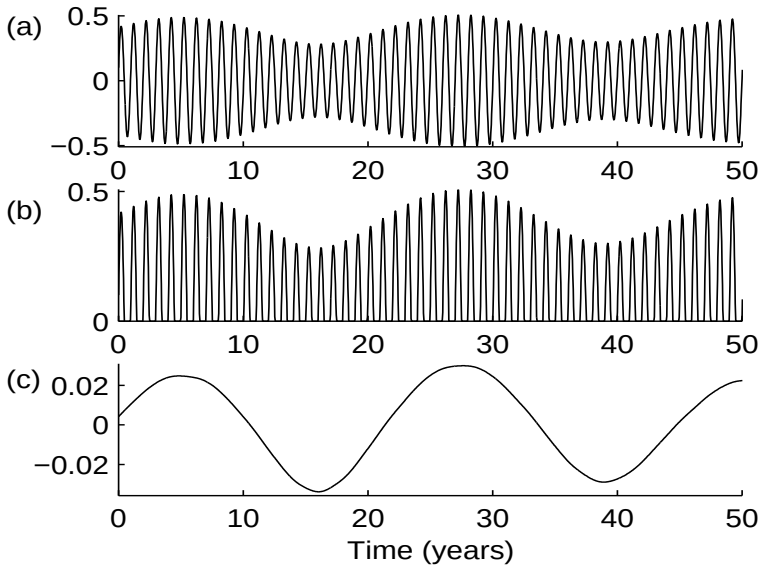

Figure 2-6: Production of low-frequency variability. (a), Simple amplitude-modulated signal of form (2.10) having no low frequency content. (b), Rectified signal according to (2.11) and then, (c), low pass filtered to leave only the envelope function. For visual clarity, the periods of the secular orbital terms are decreased by a factor of 1000 giving roughly 1/23 precession and 1/41 obliquity cycles per annual cycle.

solation. That is, simplifying slightly, let the climate system respond only when $\mathcal{F}$ is above some threshold, τ,

$$\begin{aligned} \mathcal{F}_r = &\quad |\mathcal{F}|^\nu, \quad \tau \leq \mathcal{F} \\ = &\quad 0, \quad \text{otherwise} \end{aligned} \tag{2.11}$$

The effect of Equation (2.11) on $\mathcal{F}$ is an example of what is called a νth-power-law device [*Davenport and Root*, 1958; *Middleton*, 1960]. General nonlinearities can be represented by superposition of devices with differing values of ν.

A simple example is given by taking $\tau = 0$, $\nu = 1$, which is a "half-wave rectifier"or "detector"[e.g., *Zimmerman and Mason*, 1959]; an example of its effects can be seen in Figure 2-6. The simple supposition that only positive values are important immediately, and drastically, changes the frequency content of the forcing. Figure 2-7 displays the periodogram of forcings (2.10) and (2.11). $\mathcal{F}_o$ has no energy below the annual cycle, while the rectified signal $\mathcal{F}_r$ does. We will call this "climate-system rectification"and there are many physical processes which can act this way [e.g., *Kim et al.*, 1998; *Clement et al.*, 2000].

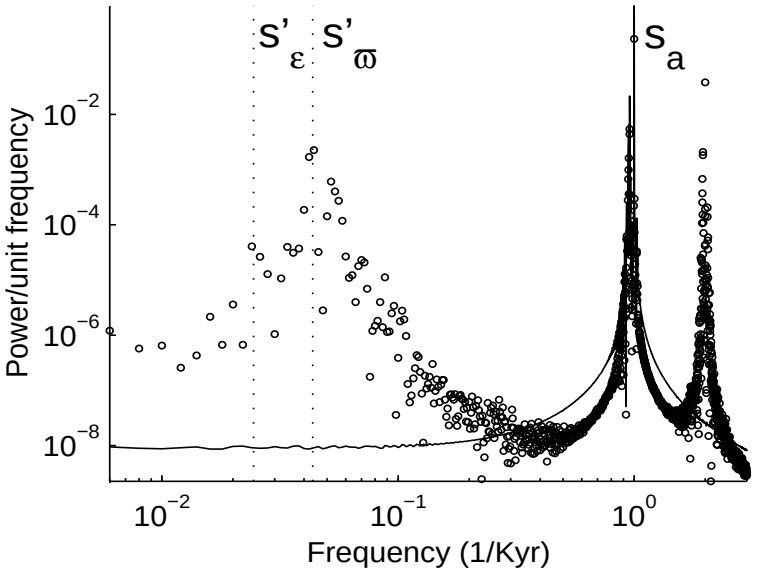

Figure 2-7: Periodograms of the original and rectified forcings. Solid line is from the original forcing (2.10) plus a small amount of white noise. The energy near the annual cycle, s_a, is split owing to modulation by the precession and obliquity terms, but there is no excess energy at the lower frequencies. Circles are the result after applying a half-wave rectifier to the signal. Now excess energy appears at the higher harmonics of s_a as well as the frequencies s'_ϖ and s'_ϵ where the primes indicate that the orbital terms have a 1000 fold decrease in period.

So far there is nothing new here. But consider that exactly the same low frequency effect can be produced by the recording devices. These recorders can represent anything that has a seasonality, including foraminifera that grow only during one season or month, or just grow more in summer than in winter, or a tracer laid down by a windfield direction confined primarily to one month or season. (Rectification of the annual cycle is not the same as its aliasing [*Wunsch*, 2000], which is a result of discrete sampling. Purely analogue devices, such as ordinary radio receivers, employ rectifiers.) That is to say, the most obvious representation of a seasonal growth, wind, or precipitation dependence in tracers or organisms will be the same form as Equation (2.11).

At least some of the inferred precessional signals are thus likely an artifact of seasonal biases in growth, wind, or temperature patterns, among other possibilities. Any recording medium, be it biological or physical, subject to an annual cycle, has to be examined for such rectification effects, and which could actually dominate the observed signals.

2.3.3 A more complete discussion

General analytical expressions, involving hypergeometric functions, are available for the response of rectifiers to a variety of inputs [*Davenport and Root*, 1958; *Middleton*, 1960]. Because there are many terms in $\mathcal{F}$, however, a discussion of its rectification is more complicated than can be obtained by examining only one or two carrier frequency contributions, and it is simpler to compute the results numerically. We therefore use estimates of the secular variability in Earth's orbital parameters [*Berger and Loutre*, 1992] along with a numerical code to estimate mean diurnal insolation (*J. Levine*, personal communication, 2003) at 65°N over the last 800 kyr. This representation is incomplete at the highest frequencies—not including diurnal variations nor other very high-frequency perturbations. It is adequate, nonetheless, to illustrate the influence of rectification on the annual cycle.

Owing to the vastly different periods between the annual variability and the secular modulating terms, it is impractical to plot the full time series of insolation over timescales of interest. Instead, Figure 2-8 shows insolation at 65°N plotted at the equinoxes and solstices. The date of the solstices and autumnal equinox, assuming the vernal equinox is fixed at March 20th, can vary substantially [*Vernekar*, 1972]. Over the last 1000 kyr, for example, the autumnal equinox occurred between September 5th and October 1st, depending on Earth's mean radial velocity, or equivalently, the eccentricity and phase of precession. The magnitude of equinoctial insolation depends only on eccentricity and precession, whereas solstice insolation at high-latitudes is primarily controlled by obliquity. The variability in the date and magnitude of these snapshots of mean diurnal insolation are indicative of the phase and amplitude modulation of the full annual cycle.

Application of the rectification device (2.11) to the insolation signals dramatically alters the low-frequency content of the insolation record. Figure (2-9) shows results using $\tau = 250$ Watts/m^2 and $\nu = 1$, where the parameters are largely arbitrary. Other choices of τ and ν would change the distribution of energy in the rectified signal, but the basic effect—transferring energy from the high to low frequencies—is robust. Apart from the concentration of energy in the obliquity and precession bands, the rectified insolation also has enhanced energy in a broad-band ranging from millennial to 100 kyr periods. One source of this energy appears to be interactions between the modulation terms; another is the presence of low-frequency obliquity energy which, after rectification, is transferred into higher harmonics. The second harmonic of

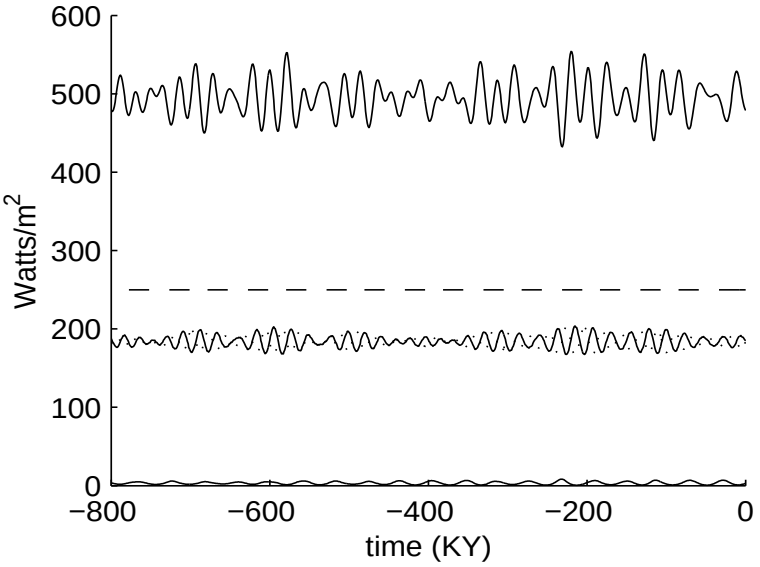

Figure 2-8: Mean diurnal insolation at 65° N. The full timeseries, sampled at 30 day intervals, oscillates too rapidly to be usefully plotted; instead snapshots of the insolation at the solstices and equinoxes are shown. Uppermost solid line is for the summer solstice, middle solid line is for the autumnal equinox, and near-zero solid line is at the winter solstice. The dotted line indicates the vernal equinox insolation. A similar plot appears in *Imbrie et al.* [1993], but there the vernal equinox and solstices are incorrectly assigned fixed dates. Horizontal dashed line indicates the lower level at which rectification is applied, denoted τ in Equation (2.11).

obliquity, 2/41 kyr, lies within the precession-band [*Huybers and Wunsch*, 2003] thus providing another potential source for precession-band energy.

2.3.4 Further considerations

Another small rectification effect exists for insolation. In Figure 2-8 it is evident that winter solstice insolation variations are attenuated as compared with those of the summer solstice. Above the Arctic or Antarctic circles, attenuation becomes "clipping"as insolation goes to zero during polar night. This polar clipping is a form of rectification and is solely due to geometry. The effects account for the higher harmonics in the insolation cycle shown in Figure (2-9), and the very slight excess in energy in the precession band. At higher latitudes, the geometric rectification is more pronounced, and Figure (2-9) shows a periodogram of the low-frequencies in insolation at 85°N calculated over the last 800 kyr. Concentrations of energy are apparent in both the obliquity and precession bands. Geometrical rectification is also

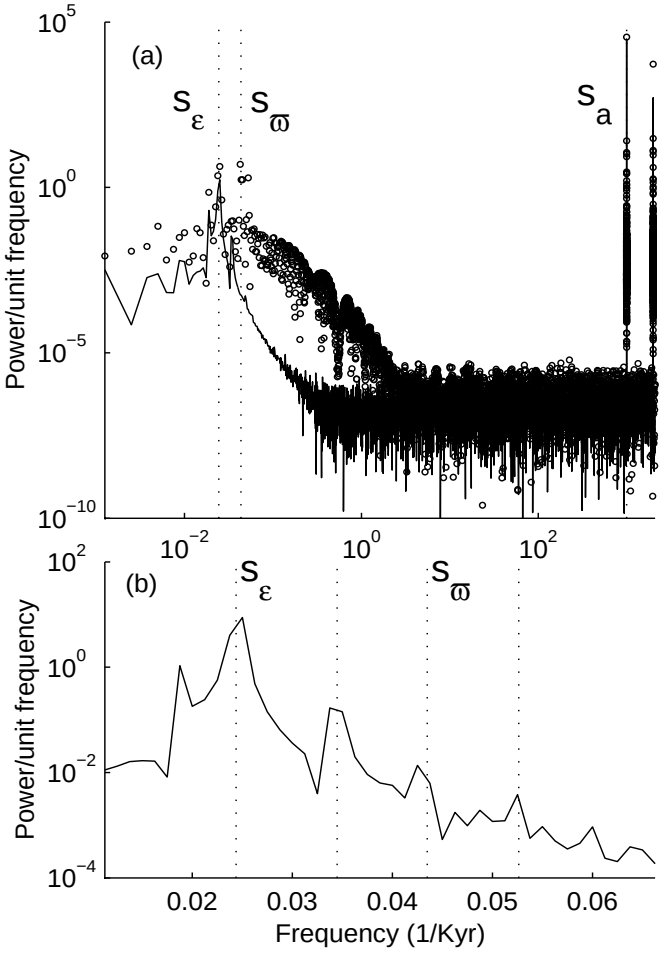

Figure 2-9: Periodograms of mean diurnal insolation plus a small amount of white noise. (a), Solid line is from insolation at 65°N, while circles are from insolation passed through a νth-law device with $\tau = 250$ Watts/m^2 and $\nu = 1$. After rectification, low frequency energy at the obliquity band (s_ϵ) is enhanced, and energy at the precession band (s_ϖ) now appears. The ordinate and abscissa are logarithmic. For plotting purposes, an exponentially diminishing number of periodogram estimates are shown for frequencies above 1/10 kyr except near the annual cycle and its first harmonic where full resolution is used—no significant structural changes result. (b), Periodogram of insolation at 85°N. Vertical lines from left to right are centered on the obliquity bands at 1/41 and a minor side-band at 1/29 kyr [*Melice et al.*, 2001] and precession at 1/23 and 1/19 kyr. The abscissa is linear, and for visual clarity, only the low-frequencies are shown. The seasonal cycle, s_a, is so much more powerful than any other insolation frequency (other than the diurnal) that its rectification is of greatest concern, but all frequencies are susceptible to such effects.

expected for the diurnal cycle, but we do not consider this higher frequency variability here.

Suppose a component of the apparent signal arises from the recorder rectification with amplitude a and in-phase with the precession angle, written as $x_1(t) = a\cos(\varpi)$; suppose too, that the climate system itself produces a rectified signal with phase, η, which is faithfully reproduced in a core record as $x_2(t) = b\cos(\varpi - \eta)$. Then omitting any stochastic component, the apparent signal at the precession frequency is,

$$\begin{aligned} x(t) &= a\cos(\varpi) + b\cos(\varpi - \eta) \\ &= (a^2 + b^2 + 2ab\cos\eta)^{1/2} \times \\ &\qquad \cos(\varpi - \tan^{-1}\{b\sin\eta/(a + b\cos\eta)\}), \end{aligned} \tag{2.12}$$

and one faces the problem of separating the recorder-rectified signal from that of the climate system. If another source is present due e.g., to geometrical rectification or higher harmonics of the obliquity energy, one has to separate a three-component vector sum.

There is one medium, the deep ocean (below about 300m, with the major exception of the equator) that typically displays no sign of seasonal signals in temperature or velocity. Measured variables reflecting only these physical processes, nonetheless having significant precessional-band signals, have a straightforward interpretation as showing rectification of the climate system, rather than that of the recording devices – assuming no seasonal cycles in the infalling nutrient supply to biological recorders.

The possibility of instrumental rectification renders the discussion of the relationship of proxies to climate variables a somewhat intricate one. In particular, one must carefully define "climate" change. Consider for example an earth in which hotter summers gave rise to a corresponding increase in precipitation, P. Suppose further that the increased P was exactly compensated by increased evaporation, E, during the colder winters. Then the anomaly of $P - E$ vanishes in the annual average, and there is no net climate change at low frequencies. Now suppose that increased precipitation and temperatures also lead to an increase in leaf mass of deciduous trees during the growing season and that all such leaves were shed during the autumn. Then a proxy based upon the annual mass of leaf generation would be rectified by the autumn shedding, and there would be a signal in the precession band that would be an incorrect measure of the annual average $P - E$. To the contrary however, if P, or E, by themselves are of interest, then the rectified leaf signal directly measures their low frequency content. Furthermore, leaf mass, with its influence on albedo and

evapotranspiration, is itself a climate variable, and the rectified leaf-mass signal could itself be regarded as real climate change. Evidently, one must specify in detail the particular physical variable that the proxy is intended to represent before it can be interpreted.

2.3.5 Conclusion

Our central point is that any precession-band energy appearing in climate time series requires the existence of a seasonal-cycle rectifier, and such rectifiers appear not only in the climate system itself, but also in the recording devices, both biological and physical. A similar phenomenon exists for the obliquity band, but analyzing this effect is more complex because obliquity band energy is also present in the forcing itself. To understand the origins of Milankovitch band energy in the climate record, one must apparently model the seasonal cycle in the recording instruments and correct for it in the climate variables.

2.4 Simplifications of insolation variability

To resolve the temporal variability of insolation requires a sampling interval of less than a day,[2] and for most paleoclimate contexts, extending over thousands of years — a prohibitively large data-set. Ninety such timeseries are required if one seeks two degree latitudinal resolution. Thus, for many applications, simplified versions of the insolation are instead used, often which aim to reduce the variability to a single timeseries requiring only a low sampling resolution. This over simplification inevitably enhances some modes of variability while diminishing or suppressing others. In this section some of the most common insolation simplifications are reviewed and compared with one another. In the next section a more complete description of the insolation is developed.

Spatial simplifications of insolation forcing usually take the form of choosing a particular latitude [e.g. *Milankovitch*, 1941], the difference between two latitudes [e.g. *Raymo and Nisancioglu*, 2003], or averaging over a hemisphere or the globe [e.g. *Berger*, 1978]. Common temporal simplification of the full forcing function are to

[2]Technically, because of the day-night clipping of insolation, a much shorter sampling interval is required to perfectly reconstruct the signal, but in practice hourly samples provide a good approximation.

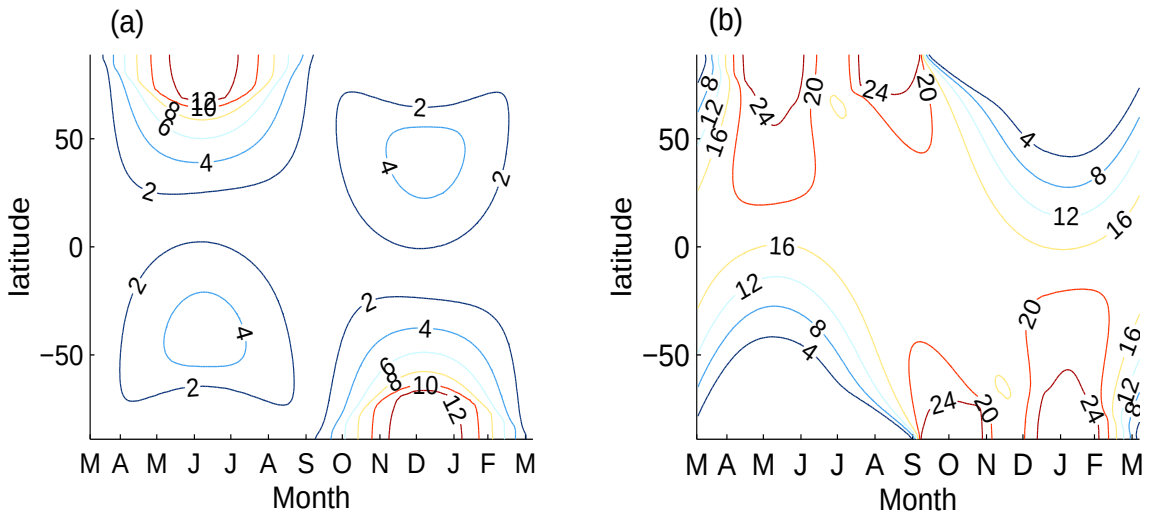

Figure 2-10: The root-mean-square insolation variability due to changes in **(a)** obliquity and **(b)** precession, shown as a function of latitude and day of year running from March 22nd (vernal equinox) to March 21st. Because the root-mean-square variability is only calculated on a single day of the year, it is rectified, and thus has precession period variability. Contour lines are labeled in W/m^2.

pick a particular solar-longitude, day of the year, or some interval of time or solar longitude [e.g. *Vernekar*, 1972]. Depending on the location and day selected, different modes of secular variability are more pronounced. Also note that the solar longitude and day of the year do not have a unique relationship [e.g. Figure 2-1; *Vernekar*, 1972; *Berger et al.*, 1993]. *Joussaume and Braconnot* [1997] show that paleoclimate simulations which do not take into account changes in the seasonal cycle can have biases of the same order as the simulated climate change.

Figure 2-10 shows the root-mean-square (rms) insolation variability due to obliquity and precessional variations, contoured as a function of latitude and day of the year. Insolation calculations are made using the orbital solution of *Berger and Loutre* [1992] and a program provided by *J. Levine* [personnel communication] which calculates insolation based on Earth's position and orientation relative to the sun. The program has been modified to run more efficiently and to calculate insolation either according to day of the year or to solar longitude. At the equinoxes, currently occurring on March 20th and September 22nd, earth's tilted spin axis is perpendicular to the direction of the sun, and obliquity has no effect on insolation. Insolation variations due to obliquity are the most pronounced during summer and have the opposite

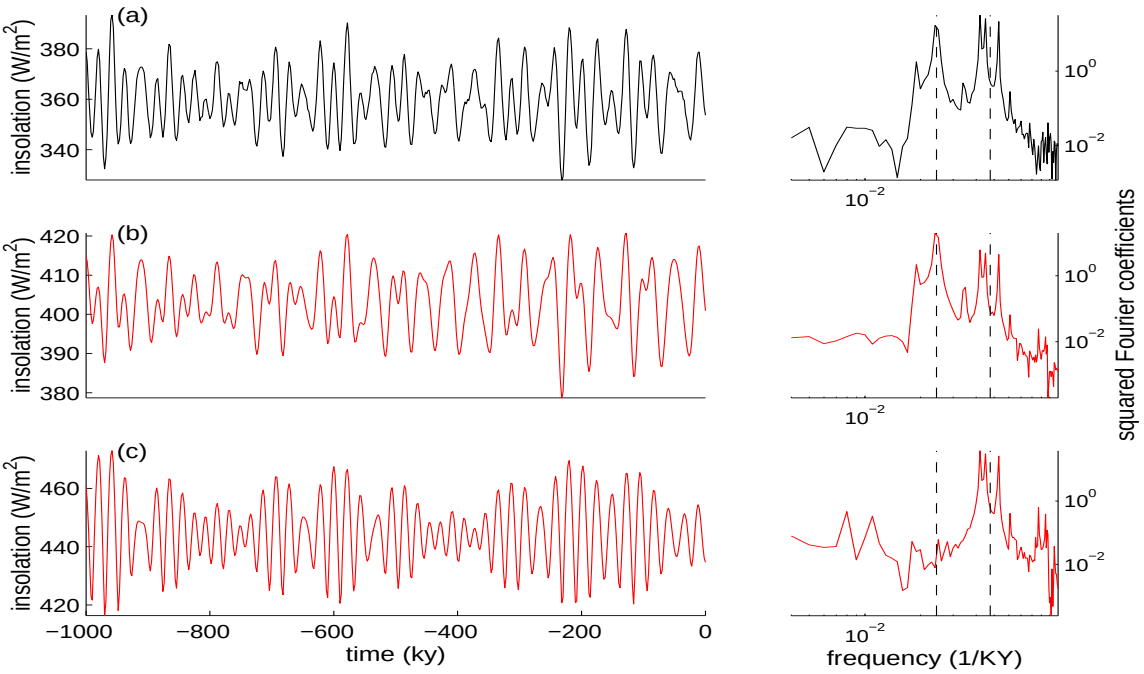

Figure 2-11: ((**a**) Astronomical and **(b)** caloric half-year insolation averaged for latitudes $\geq 60^\circ$ where averages are area weighted. The corresponding periodograms are plotted at right with vertical dashed lines at frequencies of 1/41KY (obliquity) and 1/21KY (precession). Note that calculating insolation only over half the year is a rectification which generates the precession period variability. In addition, the astronomical half-year insolation is averaged over a period which itself depends on precession. The caloric half-year and calendar half-year insolation (not shown) are both averaged over fixed periods and are very similar with a squared-cross-correlation greater than 0.99. **(c)** Caloric half-year insolation averaged between zero and 30°N along with its periodogram (right). At low-latitudes, the astronomical and caloric half-years are both dominated by precession and are very similar to one another.

sign during winter. At high-latitudes, increases in obliquity cause small decreases in winter insolation and larger increases in summer insolation, so that the net effect is to increase the annual insolation. At lower-latitudes, the net winter decrease in insolation due to obliquity has a greater magnitude than the summer increase, with the cross-over in seasonal influence occurring at 43° North and South. This cross-over can be derived from the insolation equations of *Rubincam* [1994] by omitting all the annual and higher frequency terms and solving for the zeros. Therefore, depending on the selected date and latitude, the variability due to obliquity or precession can vary substantially.

Rather than calculating insolation for a given day or solar longitude, it is possible

to average insolation over some portion of the year. For the case of half-year insolation, several possibilities exist: astronomical, calendar, and caloric half-year insolation (see Figure 2-11). (1) Astronomical half-year insolation is obtained by averaging between solar-longitudes, $\lambda = 0$ and $\lambda = \pi$ [e.g. *Vernekar*, 1972]. Although the seasons are strictly defined, the duration of the averaging period changes, according to the degree of eccentricity and the angle of perigee. The earliest and latest dates corresponding to the autumnal equinox ($\lambda = \pi$) are separated by a month.

(2) Calendar half-year insolation averages between two selected dates — usually vernal equinox and somewhere near the time variable autumnal equinox. The duration of the calendar half-year is fixed, but because the date of autumnal equinox is time-variable, it does not ensure a true winter or summer season. This prompted Milankovitch [1941] to introduce: (3) the caloric half-year which maintains equal durations between the summer and winter half-years, while maximizing the insolation contrast [e.g. *Milankovitch*, 1941]. *Vernekar* [1972] and *Berger* [1978] give good discussions of both astronomical and caloric half-year insolation. The astronomical half-year insolation has more precession variability than either the calendar or caloric half-year insolations owing to precession's influence on both the intensity of the insolation and period over which the insolation is averaged. It is also possible to average over some latitude band (see Figure 2-11); when the average is confined to only high or low latitudes, the variance and frequency structure of the signal changes only slightly.

There exists an endless number of possibilities regarding the temporal and spatial averaging of insolation. Various choices can be motivated by physical concepts, but in the absence of a general theory for how changes in radiation at the top of the atmosphere affect climate, many choices remain plausible but largely arbitrary. Furthermore, no low-frequency timeseries of insolation can represent how the secular changes in insolation affect both the seasonal and low-frequency changes in insolation. As the annual cycle is extremely powerful[3], this constitutes a major short-coming of traditional simplification of the insolation variability. In Chapter 1, it was shown how neglecting high-frequency variability could lead to incorrect power-law estimates; and in Section 2.3 it was shown how the proxy response to the annual cycle could be misinterpreted as low-frequency climate variability. For these reasons, a full representation of the seasonal and secular insolation variability is important for understanding the

[3]Consider that the annual range in Arctic temperatures is on the order of 50°C, roughly double the difference between mean temperatures during the Holocene and the Last Glacial Maximum calculated by *Dahl-Jensen et al.* [1998] using the GRIP borehole.

relationship between climate and orbital forcing.

2.5 A Compact representation of insolation

One alternative to simplifying the forcing is to determine an analytical expression for the full insolation variability. *Rubincam* [1994] and *B. Bills* [personal communication, unpublished] have derived general expressions for insolation as a function of the orbital parameters. These solutions provide useful insight into insolation variability, but involve summations over numerous basis functions, some of which require many terms to converge, making the results somewhat opaque. A complementary approach is to numerically solve for basis functions which are optimally efficient at explaining the variability. While lacking the elegance of an analytical solution, in practice this numerical estimate allows insolation to be accurately represented using a small number of functions, and is amendable to physical interpretation.

The goal is to find the simplest representation of insolation variability. Here I consider diurnally averaged insolation, which only varies meridionally. A full representation of diurnally averaged insolation, then, only requires latitude and time. One approach is to generate a matrix, $\mathbf{X}$, of insolation values with N rows of latitude and M columns of time. But as suggested when reviewing the common simplification of insolation forcing, the number of columns is prohibitive. To resolve both days and the longest major period in eccentricity variability (400KY) requires roughly 150 million time columns. If insolation is calculated at each latitude, the total number of values is roughly 30 billion. To reduce these sizes, a compact representation of the spatial and temporal variability is first presented, after which the various modes of insolation variability are interpreted.

While efforts are made to make the representation of insolation as compact and simple as possible, the following is a rather involved discussion of orthogonal decompositions using Legendre polynomials and singular value decompositions. The results are useful for interpreting the insolation variability, but none of the conclusions drawn in the following section are essential for understanding the remainder of the thesis. Thus the reader may find it useful to only skim the following sections.

2.5.1 Spatial variability

In Chapter 1, spherical harmonics were used to decompose temperature variability from the NCEP reanalysis. Since diurnally averaged insolation has no zonal structure, the one dimensional counter-part of spherical harmonics, the Legendre polynomials [e.g. *Jackson*, 1999], are a natural choice for spatial basis functions. The basis functions are chosen, rather than solved for, because in practice they prove to be both efficient descriptions and are readily interpretable as physical modes of insolation of forcing. The temporal basis functions will be solved for. Figure 2-12 shows the Legendre polynomials from order zero to three, $L_{(0-3)}$. Zero and even orders are symmetric, while the odd orders are anti-symmetric. For continuous functions the polynomial expansion can be carried to arbitrarily high orders of accuracy, but for discretely sampled functions there is a limit beyond which higher order polynomials vary too rapidly to be useful — in close analogy with the Nyquist frequency in Fourier analysis. Here, insolation is calculated at 1° intervals over the range $\{-89.5°, 89.5°\}$ and polynomials of up to order 40 give stable results.

To begin, two-dimensional slices of the insolation variability are considered: one slice is of the spatial and seasonal variability and another of the spatial and secular variability. Although both seasonal and secular variations are referenced to time, it proves useful to consider these variations as independent coordinates because of their vastly different timescales. Figure 2-13 shows the diurnally averaged insolation for the year of 10 KY BP contoured as a function of latitude and day. A matrix representation of this information can be written as $\mathbf{X}$, with $N = 180$ rows of latitude and $M = 365$ days of the year (matrices will always be printed in bold-face). To project $\mathbf{X}$ onto a set of Legendre polynomials, form another matrix L with N columns corresponding to polynomials 0 to $N - 1$ and $M = 180$ rows corresponding to latitude. Then,

$$\mathbf{P} = \mathbf{L}\mathbf{X}, \tag{2.13}$$

gives the loadings associated with each Legendre polynomial. By recombining the Legendre polynomials according to the loadings, $\mathbf{X}$ can be approximated,

$$\mathbf{X} \approx \mathbf{L}^T\mathbf{P} = \mathbf{L}^T\mathbf{L}\mathbf{X},$$

where the accuracy depends on the number polynomials included in $\mathbf{L}$ and how well these polynomials span the vector space of $\mathbf{X}$. As the Legendre polynomials are or-

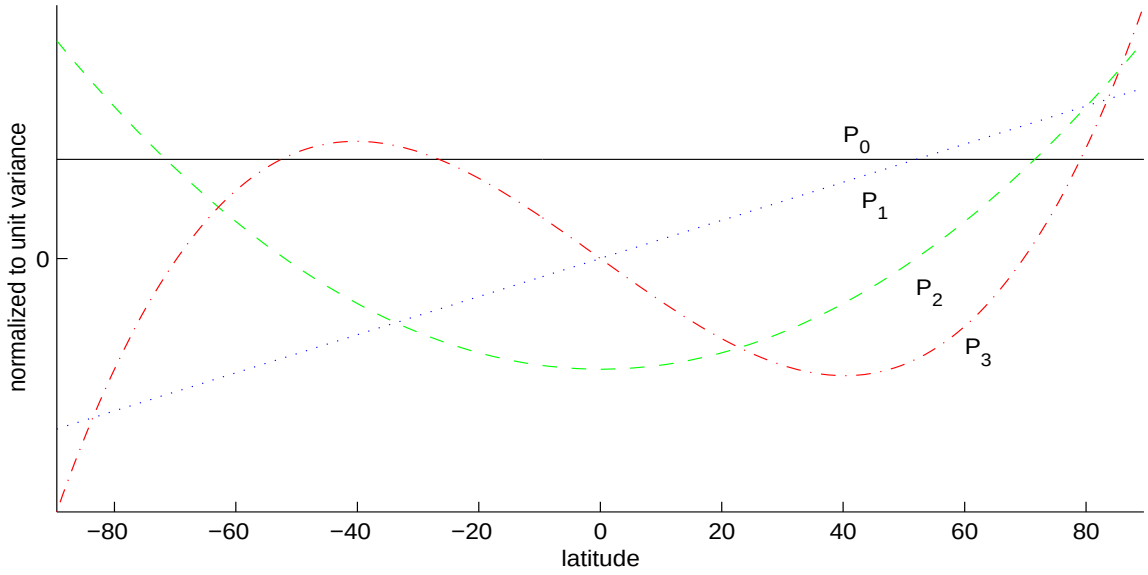

Figure 2-12: The Legendre polynomials from order zero to three, each normalized to unit variance. Note zero and even orders are symmetric, while the odd orders are anti-symmetric. P_0 alone has a non-zero mean and represents mean global changes in insolation; P_1 represents the inter-hemispheric gradient in insolation; P_2 indicates hemispherically symmetric differences between high-latitude and low-latitude insolation; and P_3 indicates hemispherically anti-symmetric differences between high-latitude and low-latitude insolation. Higher order polynomials account for only a small fraction of the variability and are not discussed.

thogonal, $\mathbf{L}^T\mathbf{L} = \mathbf{I}$, where $\mathbf{I}$ is the identity matrix. The utility of this decomposition is that $\mathbf{X}$ can be reconstructed to a high degree of accuracy using a small number of polynomials: on average, the first four explain 99.9% of the variance in diurnally averaged insolation, the first eight explain 99.9994% [see Figure 2-13]. The actual variance explained by each polynomial changes according to the day of the year. As might be expected, the larger inter-hemispheric insolation asymmetry during summer or winter makes the odd Legendre polynomials more important for explaining insolation variance, while during the equinoxes, the even polynomials describe more of the insolation variance. The diurnally averaged insolation calculations are weighted by the fraction of surface area they represent. All insolation calculations are made referenced to a vernal equinox fixed at March 20th. Note, this differs from the Gregorian calendar which has the vernal equinox occur on either March 20th or 21st so as to maintain an integer number of days in the year.

Having considered the decomposition of the seasonal-spatial variability, now at-

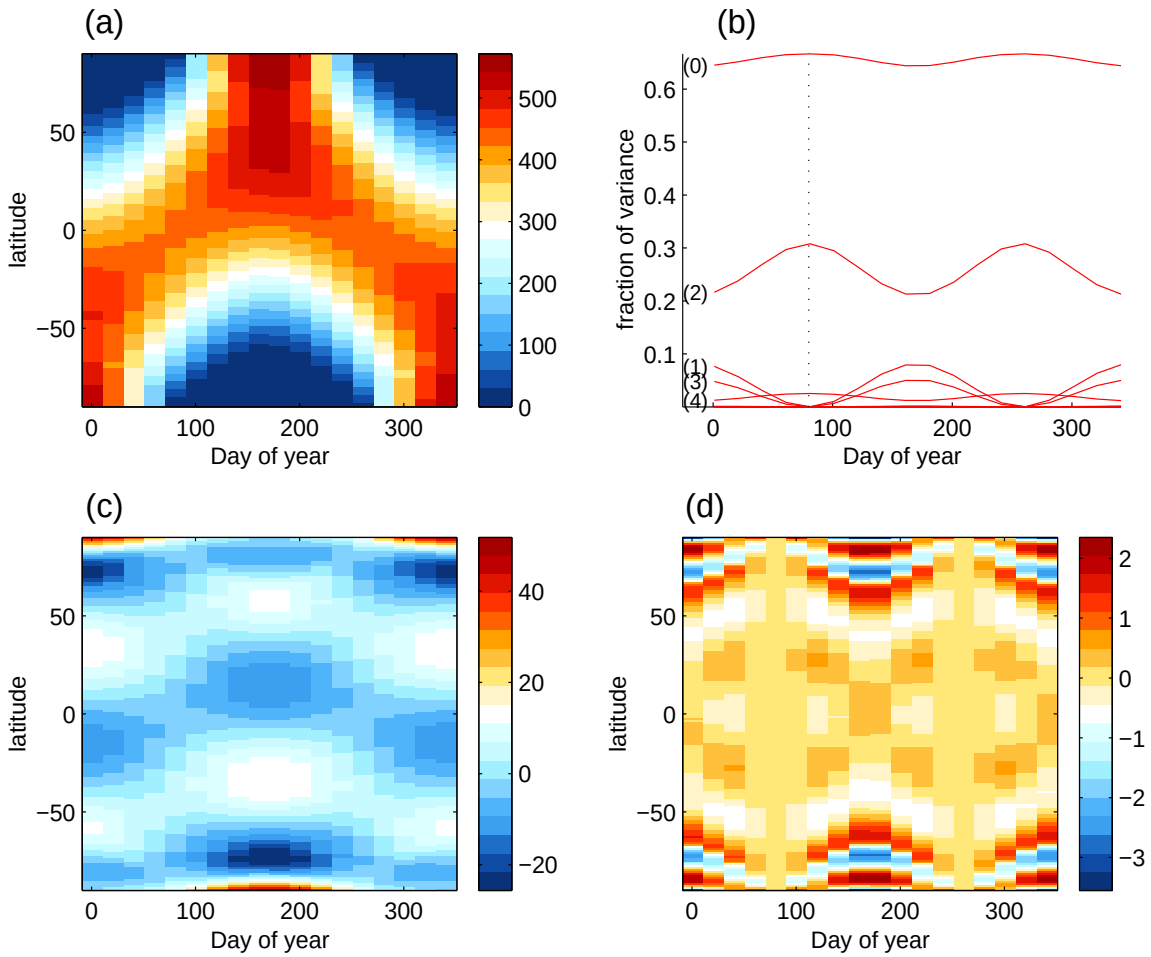

Figure 2-13: Regression of diurnally averaged insolation variability onto the Legendre polynomials. **a** Diurnally averaged insolation contoured in Watts per meters squared against latitude and day for 10 KY BP. **b** The fraction of the insolation variability explained by Legendre polynomials of order zero through four $L_{(0-4)}$ for each day of the year. By way of example, note that during the solstices, when insolation is meridionally symmetric, the fraction of variance explained by L_2 (symmetric) increases while $L_{(1,3)}$ (anti-symmetric) goes to zero. The vertical dotted line indicates the vernal equinox which, in the convention used here, always occurs on day 80 (March 20th). **c** shows residual insolation variability after subtracting the full calculated insolation quantities by the reconstruction using only $L_{(0-3)}$; **d** is the residual using $L_{(0-7)}$. $L_{(0-3)}$ explains 99.9% of the meridional insolation variability, while $L_{(0-7)}$ explains 99.9994%.

tention is turned to the secular-spatial variability. Figure 2-14 shows global insolation for a fixed day of the year, July 15th, over a period of 40KY and its representation using a small number of the leading Legendre polynomials. There is less overall variability to explain than in the seasonal case because, for example, mean spatial

insolation, L_0, only changes slightly depending on the precession and eccentricity, and the hemispheric gradient, L_1, varies in amplitude according to the obliquity but is always positive. The leading four Legendre polynomials explain 98% of this secular (i.e. long-term) variability, and the leading 8 explain 99.997%. Thus the Legendre polynomials provide an efficient description of the meridional insolation variability at seasonal and secular timescales.

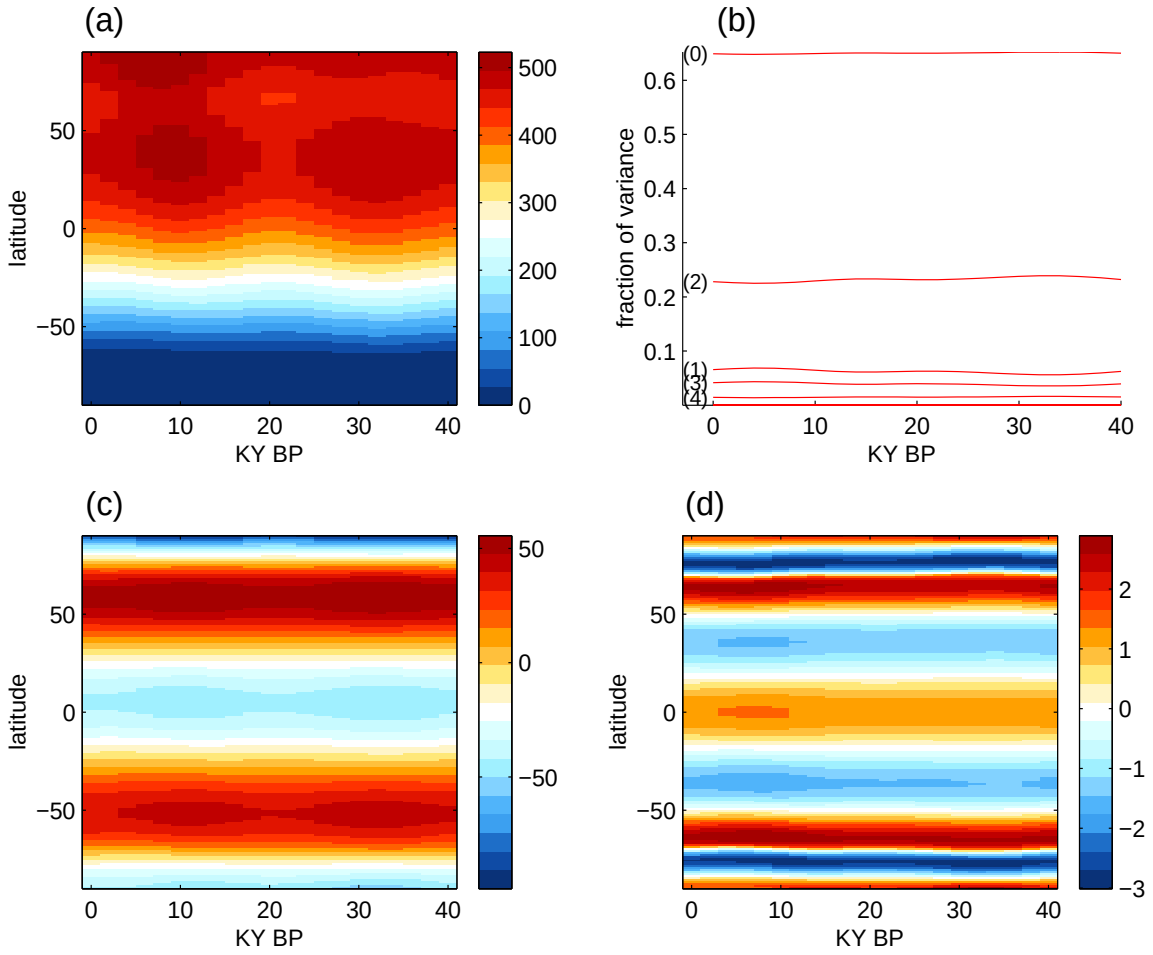

Figure 2-14: Similar to Figure 2-13 but now for a fixed day with time-steps in KY. **a** Average July 15th insolation in W/m^2 contoured against latitude and KY BP. **b** The fraction of the insolation variability explained by Legendre polynomials, $L_{(0-4)}$, for each KY BP. Variations in polynomial loadings are related to secular variations in earth's orbit, and are much less pronounced than for the annual variability. **c** shows residual insolation variability after subtracting the full calculated insolation quantities by the reconstruction using only $L_{(0-3)}$; **d** is the residual using $L_{(0-7)}$. $L_{(0-3)}$ explains 98% of the meridional insolation variability, while $L_{(0-7)}$ explains 99.997%.

2.5.2 Temporal variability

The time-varying weights associated with the n-th Legendre polynomial, P_n, (from Eq. 2.13) are of a length equal to the number of time-steps, which for most applications is still too large to be easily interpreted. The difference in timescales between seasonal and secular orbital variations suggests rearranging P_n into a matrix $\mathbf{P}_n$ with rows corresponding to days and columns corresponding to years. The secular changes in earth's orbit are smoothly varying (nearly band-limited), and with little loss of information only one year out of each KY needs to be recorded in the columns of $\mathbf{P}_n$. A basis set for $\mathbf{P}_n$ could be motivated through the knowledge that both the annual cycle and secular changes in Earth's orbit must be present. A somewhat more general approach, however, is to take the singular value decomposition [e.g. *Wunsch*, 1996; *von Storch and Zwiers*, 1999] of $\mathbf{P}_n$,

$$\mathbf{U}_n\mathbf{S}_n\mathbf{V}_n^T = \mathbf{P}_n.$$

Here $\mathbf{U}$ represents the daily variability while $\mathbf{V}$ represents inter-annual changes in insolation. This orthogonal decomposition is ordered such that the first row of $\mathbf{U}_n$, multiplied by the transpose of the first row of $\mathbf{V}_n$, together known as the first set of *singular vectors*, explains the largest fraction of variance in $\mathbf{P}_n$. The second set of singular vectors explains the largest possible fraction of the remaining variability in $\mathbf{P}_n$, and so on. All the variance will be explained when the number of pairs of singular vectors is less than or equal to the number of columns or rows (whichever is less) in $\mathbf{P}_n$. The fraction of variance explained by each pair of singular vectors is,

$$l_n^k = \frac{(\mathbf{S}_n^k)^2}{\sum_k (\mathbf{S}_n^k)^2},$$

where $\mathbf{S}_n$ is a diagonal matrix containing the *singular values*, and S_n^k is the singular value corresponding to the kth set of singular vectors.

2.5.3 A simple example

At this point it is useful to consider a simple example. Assume a fictional sun-earth system where the spatial distribution of diurnally averaged insolation is uniform, e.g. a cylinder whose axis is perpendicular to the orbital plane. In this case, only the Legendre polynomial L_0 is required, and the time-variable weightings are given by

$\mathbf{P}_0$. Further assume that the temporal variability in insolation is,

$$\mathbf{I}(d,y) = \left[\frac{1}{1-e(y)^2}\right]^2 \times \left[340 + 20\sin\left(\frac{2\pi d}{365}\right)\right], \tag{2.14}$$

where the seasonal cycle is a function of the day, d, and the amplitude is a function of the eccentricity, e, on year, y. Here, the year is approximated as having an integer number of days. The selected constants in Eq. 2.14 give values roughly corresponding to the seasonal variations in global mean insolation, measured in W/m^2. The eccentricity term in Eq 2.14 represents the secular insolation variability, while the sine term represents the seasonal variability.

Continuing with the simple example, $\mathbf{P}_0$(d,y)=$\mathbf{I}$(d,y) because insolation is spatially uniform. Furthermore, the singular value decomposition of $\mathbf{P}_0$ will only require a single pair of singular vectors with $\mathbf{U}\sim$ $(340+20\sin(\frac{2\pi d}{365}))$, $\mathbf{V}\sim$ $[1/(1-e(y)^2)]^2$, and a singular value $\mathbf{S}$= $\sum_y \sum_d I^2(d,y)$; the '$\sim$' means proportional to. Thus, insolation at any given latitude (ϕ), day (d), and year (y) can be calculated as,

$$\mathbf{I}(\phi,d,y) = \mathrm{L}_0(\phi)\ \mathbf{U}(d)\ \mathbf{S}\ \mathbf{V}^T(y).$$

Note that the variability in space, seasonal time, and secular time are divided between the Legendre polynomials, $\mathbf{U}$ singular vectors, and $\mathbf{V}$ singular vectors respectively. In this simplified case, the result is trivial, and there is little benefit to representing the insolation in terms of Legendre polynomials and singular vectors. However, for the real insolation variability, the Legendre/singular vector representation proves an efficient descriptions which provides real insight into the modes of insolation variability.

2.5.4 Interpretation

Returning now to the real earth-sun system, Figure 2-15 shows the fraction of variance explained by each set of singular vectors for each matrix of Legendre polynomials, $\mathbf{P}_n$. The leading three pairs of singular vectors explain over 99.99% percent of the variance in each $\mathbf{P}_n$. After the first, the singular values associated with each $\mathbf{P}_n$ come in pairs — that is, the second and third set of singular vectors explain nearly equal amounts of variance, likewise for the fourth and fifth, etc. Closer inspection of these paired singular vectors indicates that they are nearly identical, except for a 90° shift

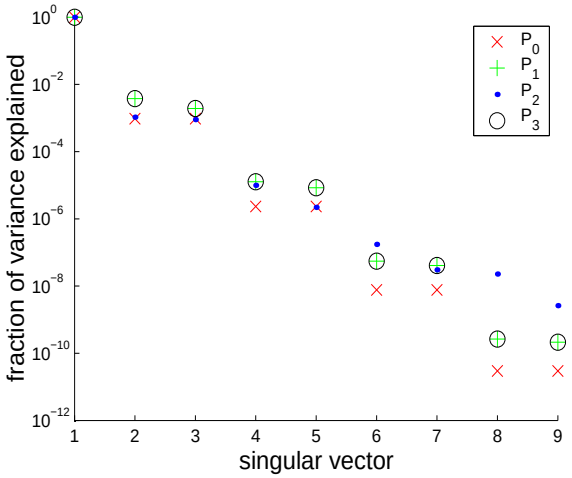

Figure 2-15: The variance explained by the leading singular vectors for each matrix of Legendre polynomial weightings, $\mathbf{P}_n$. In each case, the leading singular vector explains over 99% of the variability in the weightings — note the logarithmic scaling of the y-axis. The variance explained by higher order singular vectors comes in pairs, where each pair explains roughly 99% of the remaining variance. In this case, the pairings of explained variance indicates the presence of a traveling wave of insolation, due to the effects of precession on climate. Since the anomalistic year, controlled by precession, comes in and out of phase with the tropical year, which is controlled by obliquity, the precessional influence is manifested as a traveling wave, and is represented by two sets of singular vectors which are separated by 90° of phase.

in phase. This result implies the presence of a traveling wave present in the insolation variability. Because its phase shifts relative to the basic seasonal cycle, two sets of singular vectors are required to explain this wave, in direct analogy with adding a sine and cosine together to form a new signal with the same period but different phase. It is possible to describe this wave using a single set of complex singular vectors, by means of a Hilbert transform of $\mathbf{P}_n$ [e.g. *von Storch and Zwiers*, 1999], but for these purposes it is simpler to interpret the second and third sets of singular vectors together.

To understand the presence of this traveling wave, observe that Eq. 2.1 contains two different annual periods: λ_s and $\lambda_s - \varpi$. λ_s has a period of one *tropical* year (365.2422 days) and measures the mean interval between vernal equinoxes. Following the example of the Gregorian calendar, the insolation calculations used here define the vernal equinox as the 80th day of year, tying the seasonal phase to the vernal equinox and the tropical year. The $\lambda_s - \varpi$ period is associated with the *anomalistic* year (currently equal to 365.2422 days minus 1/21,000KY, or 365.2596 days) and

measures the time from one perihelion passage to another. Because insolation is calculated with respect to the tropical year, in the time it takes the angle of perigee, ϖ, to make a 360° rotation the anomalistic year will move in and out of phase with the tropical year, thus manifesting as a 21KY period traveling wave in the insolation calculations. *Thomson* [1995] has made the somewhat perplexing observation that temperatures in different cities around the world seem to follow one or the other of these annual cycles. Thus, this seemingly small difference in years appears to have real physical effects even on relatively short timescales.

This dual-period year effect is present in all insolation calculations, but only when the full annual cycle is resolved does it become obvious. When only a portion of the year is resolved, a significant fraction of the variability can be due to the anomalistic year coming in and out of phase with the tropical year. If only a portion of the annual cycle or a portion of the meridional variability is resolved, it is difficult to distinguish between a traveling wave, changes in mean annual insolation, and meridional shifts in insolation. Presumably, each of these redistributions of insolation will force different types of climatic responses, and it appears knowledge of the full insolation field is crucial when attempting to understanding the dynamical response to insolation forcing.

Figures 2-16 through 2-19 shows the leading three singular vectors associated with each matrix of Legendre polynomial loadings, $\mathbf{P}_n$. The singular vectors of the $\mathbf{P}_n$ describe how the spatial patterns of insolation vary at both seasonal and secular timescales. The singular vectors associated with the $\mathbf{U}$ describe the daily variations in insolation and are referred to as the *seasonal vectors*; while the $\mathbf{V}$ describe long-term changes in insolation and are called the *secular vectors*. For instance, variations in eccentricity cause changes in net annual insolation and are therefor associated with the secular vectors of $\mathbf{P}_0$ [see Figure 2-16]. The leading secular vector associated with $\mathbf{P}_0$, as originally computed, had a small component of precessional variability which accounted for less than 0.0001% of the spatially averaged insolation variance. To make the mean annual insolation variability easier to interpret [see Figure 2-16], this precessional variability was removed and placed in the precessional vectors. This was the only change made. For the decomposition of the other $\mathbf{P}_n$, $n > 0$, the secular variability in the leading set of singular vectors is determined by obliquity, and these singular vectors are therefor referred to as the *obliquity vectors*. The secular variability in the second and third sets of singular vectors are controlled by the climatic precession

and its 90° phase shift, $e\cos(\varpi)$, and are referred to as the *precession vectors*.

The seasonal obliquity vectors associated with even (symmetric) Legendre polynomials [see Figures 2-16 and 2-18] have a non-zero mean value indicative of changes in obliquity causing meridional redistributions of insolation. Conversely, changes in precession are independent of any annual mean variations at any latitude and thus the seasonal precession vectors are always zero-mean. It appears that the net insolation received by each hemisphere is equal as the seasonal vectors associated with all the odd (asymmetric) Legendre polynomials [e.g. Figures 2-17 and 2-19] are zero mean.

The precession vectors associated with odd (asymmetric) Legendre polynomials [see Figures 2-17 and 2-19] are doubly-periodic. To understand this, consider the case when aphelion occurs at the summer solstice. Then the argument of perigee is 90°, climatic precession is positive, and $\cos(90°) = 0$: thus, the only precessional contribution will come from the seasonal vector associated with the precession parameters. By Kepler's second law, being closer to the sun during Northern Hemisphere summer means the Earth will move more quickly, therefor reaching summer solstice prior to the average date of June 19th (depending on the magnitude of eccentricity). Summer solstice is a maximum in the inter-hemispheric gradient, and approaching it quickly results in an anomalously large insolation gradient for that period of the year. In addition, being closer to the sun during summer solstice increases the inter-hemispheric gradient in insolation. Because Earth reached the summer solstice quicker than usual, it also leaves more quickly, and by mid-July the precessional effect is negative. This negative trend continues, reaching a minima at the autumnal equinox. Note that adding this precessional seasonal vector to the obliquity vector yields seasonal variations which have both the summer solstice maximum and the autumnal equinox zero-crossing occurring earlier in the year. The cycle then repeats for the Northern hemisphere winter solstice, but now with a relatively slow Earth velocity, an anomalously large distance to the sun, and a change in sign of the insolation-gradient. These effects combine to create another oscillation with a maximum during the winter solstice, giving the doubly-periodic signal. The larger response during the autumnal equinox occurs because its date has the most variability, being furthest away from the fixed vernal equinox.

Paralleling the simple example given earlier, the insolation, I, is represented as

$$I(\phi, d, y) = \sum_{n=0}^{N} \mathbf{L}(\phi, n) \left(\sum_{m=1}^{M} \mathbf{U}_n(d, m)\mathbf{S}_n(m, m)\mathbf{V}_n(y, m) \right), \tag{2.15}$$

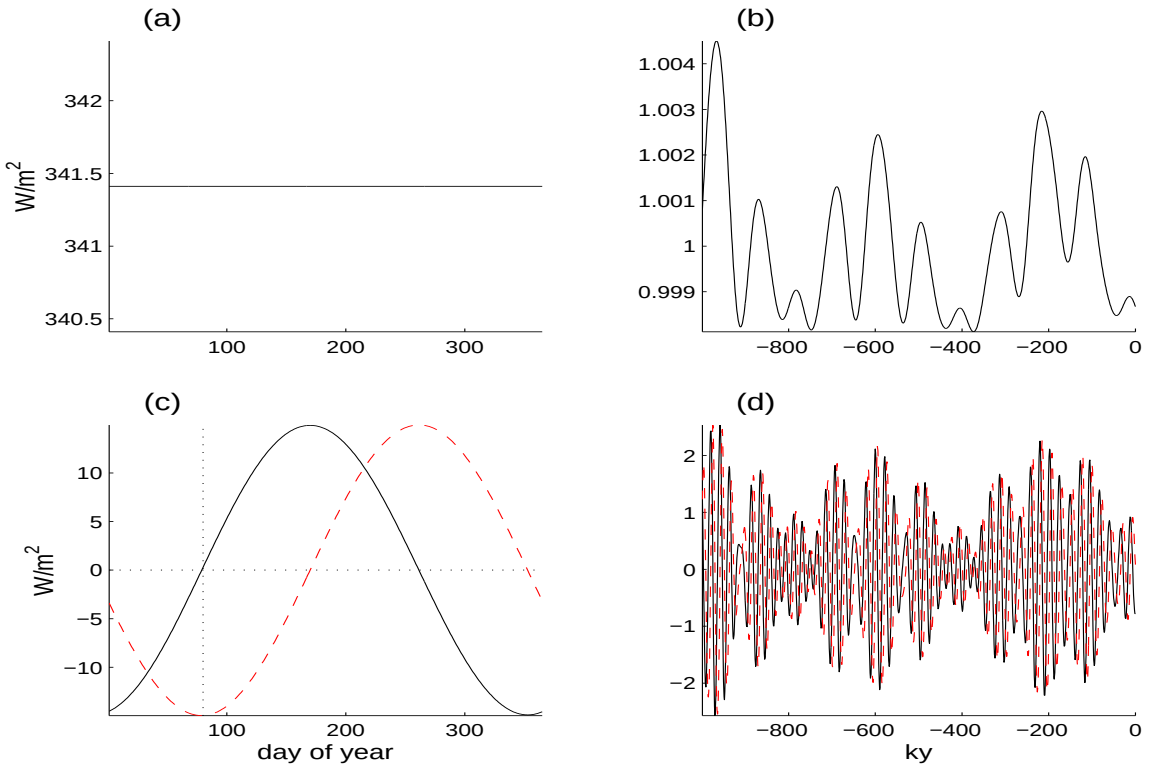

Figure 2-16: Singular value decomposition of $\mathbf{P}_0$ showing spatial average insolation variability over the last 1000 KY. The *seasonal* singular vectors (left) are scaled to units of W/m^2; the *secular* singular vectors (right) indicate the modulation of the mean and annual variability. **a,b:** The leading pair of singular vectors explain 99.8% of the spatial average insolation variance. **a,** the leading seasonal singular vectors represents the spatial and time average insolation over the last million years, 341.4 W/m^2; the solar constant is 1365 W/m^2. There is no seasonality associated with this mean value, thus the flat line. **b,** the secular variations in total annual insolation are only a function of eccentricity, scaling as $1/(1-e^2)^2$, and increasing by 0.65% from a minimum eccentricity, 0.005, to a maximum, 0.057. As discussed in the text, a slight modification was made to these singular vectors. **c,d:** the second and third sets of singular vectors, termed the *precession vectors*, show the anomalistic year coming in and out of phase with the tropical year and each account for 0.1% of the variance, almost all the variance not explained by the leading set of singular vectors. **c,** the seasonal precession vectors are a sine (solid) and cosine (dashed) pair with zero phase at the vernal equinox (the vertical dotted line at day 80, or March 20th) and can together be interpreted as a traveling wave. **d,** variations in eccentricity and argument of perigee control the amplitude and phase of this annual period wave in spatial average insolation. One secular precession vector is proportional to the precession parameter (solid); the other is phase shifted by 90°, and is proportional to $e\cos\varpi$ (dashed).

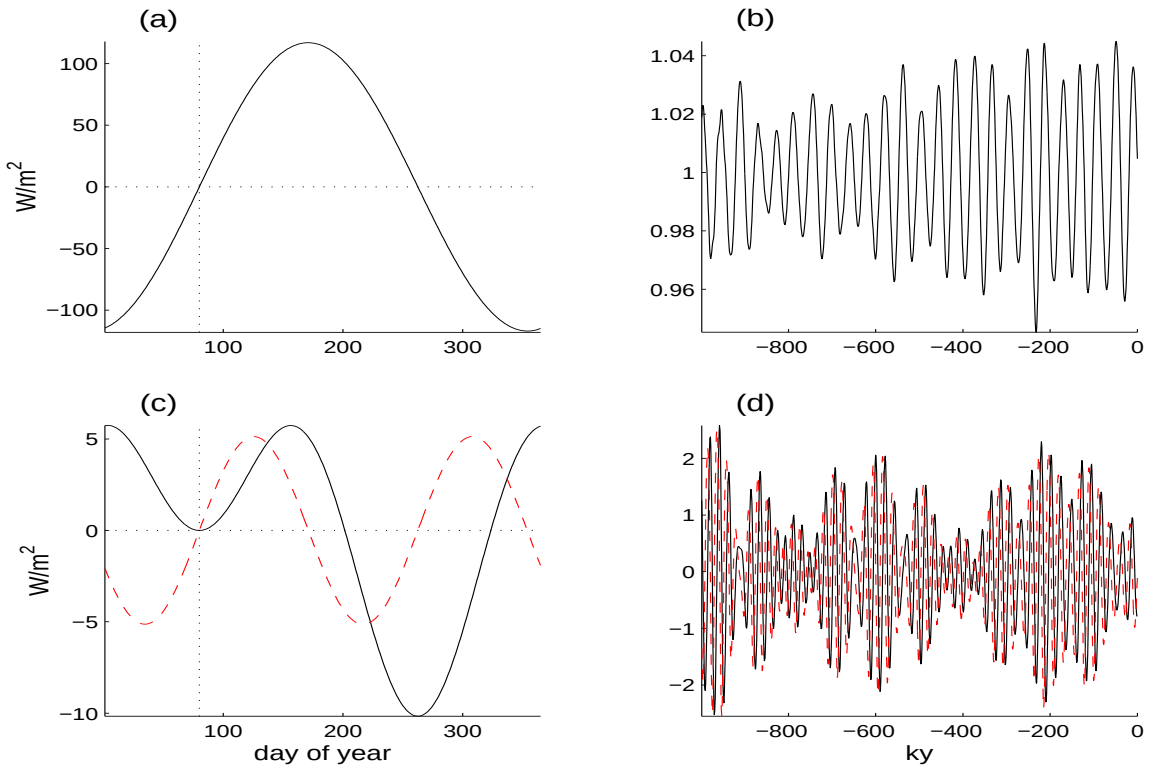

Figure 2-17: Similar to Figure 2-16 but for P_1 — the inter-hemispheric gradient in insolation. **a, b**: the leading set of singular vectors, termed the *obliquity* vectors, account for 99.4% of the variance in the insolation gradient. **a,** The leading seasonal obliquity vector is a sine wave with an annual period, amplitude of 110 W/m^2, and zero phase at the vernal equinox (vertical dotted line) — during the equinoxes there is no inter-hemispheric gradient in insolation. The seasonal obliquity vector is zero mean because changes in obliquity redistributes insolation between the hemispheres, but does not change global insolation values. **b**, the annual variability in insolation gradient is modulated by up to ±4% due to changes in obliquity. Because obliquity is always positive, the associated secular singular vector is also a positive function. **c,d:** The precessional vectors together explain 0.5% of the inter-hemispheric gradient. **c** The seasonal variability is mostly controlled by changes in the timing of the inter-hemispheric insolation gradient. As the vernal equinox is fixed to March 20th and, by definition, has no inter-hemispheric gradient in insolation its value must be zero. The doubly-periodic nature of the seasonal vectors and the large excursion near the autumnal equinox is explained in the text. **d** Changes in climatic precession can add or subtract up to 20 W/m^2 from the inter-hemispheric insolation gradient. Note the precession singular vectors are zero mean because precession variations do not affect annual mean insolation at any latitude.

and is a function of latitude (ϕ), the day (d), and the year (y). The inner summation is over the leading M singular vectors to obtain the weighting for the nth Legendre

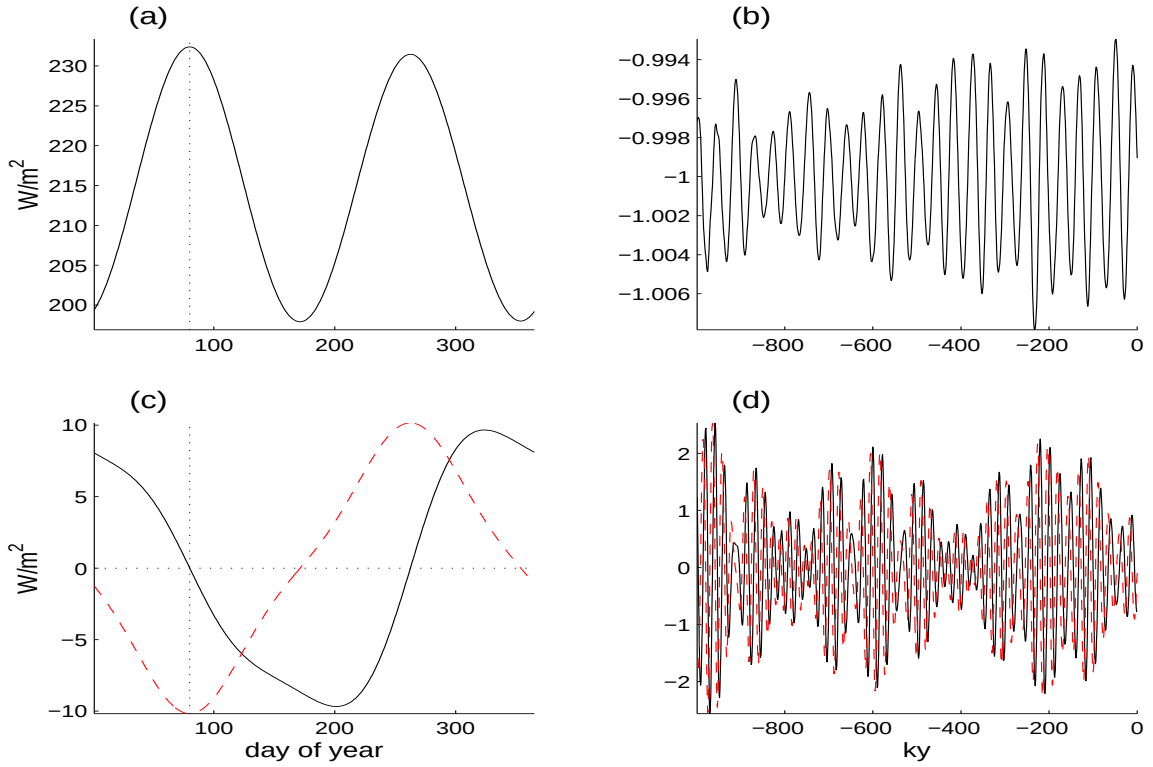

Figure 2-18: P_2 measures symmetric shifts of insolation from low-latitudes towards the high-latitudes ($> 52°$). **a,b** the leading set of singular vectors accounts for 99.8% of the variability in P_2 (0.0012% due to obliquity variability), and always contributes a negative value (note the secular obliquity vector is negative), primarily accounting for the increased angle of incidence at high-latitudes. **a,** The seasonal singular vector is proportional to a doubly-periodic cosine wave with zero phase at the vernal equinox plus a mean value of $215 W/m^2$. During the equinoxes insolation is at a maximum over the equator, thus the obliquity vectors make a maximal negative contribution. The double-period reflects the suns twice-annual zenith in the tropics. **b**, the secular obliquity vector is negative because an increase in obliquity causes greater inter-hemispheric asymmetry and less variance to be explained by the symmetric Legendre polynomial, P_2. **c,d** The precession vectors together explain 0.2% of the variance in P_2 and are nearly the negative of those associated with P_0. **c** When the Earth is closest to the sun during vernal equinox, that is $\cos(\varpi) = 1$), the earth receives roughly 10 W/m^2 more insolation at low-latitudes than at high latitudes. As is generally the case for the Legendre polynomials greater than zero, the seasonal precession vectors are not perfect harmonics because of the change in the timing of the seasons (i.e. frequency modulation) caused by precession and changes in eccentricity. **d** Precession can cause symmetric shifts in insolation from high to low latitudes with magnitudes as high as 20 W/m^2. These effects are purely seasonal, however, and average out in the annual mean.

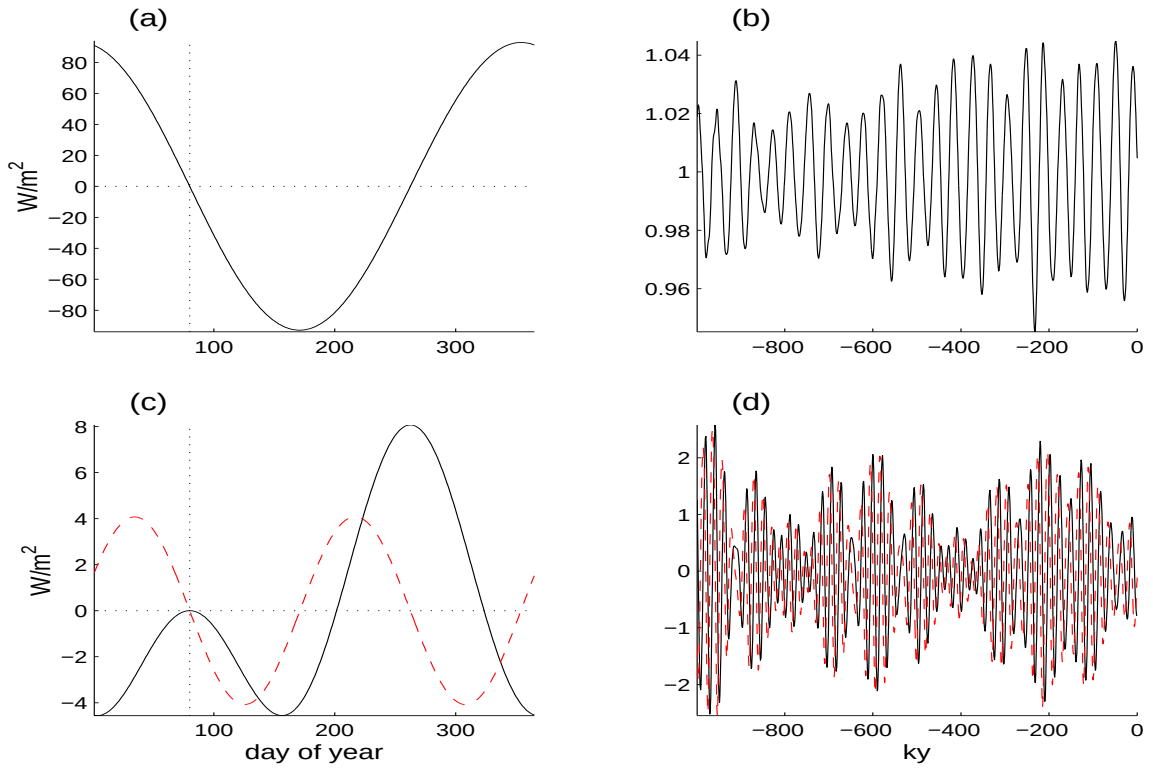

Figure 2-19: P_3 primarily describes shifts of insolation from the Northern mid-latitudes to the Southern mid-latitudes. This seasonal vectors are nearly the negative of those for P_1, suggesting that when the gradient in insolation is energized, so are the Northern mid-latitudes at the expense of the Southern mid-latitudes. **a, b** The obliquity vectors describe 99.4% of the variance. During Northern hemisphere summer this mode indicates there are $160 W/m^2$ more insolation at Northern than Southern mid-latitudes. Changes in obliquity will modulated this value by up to $\pm 4\%$. **c,d** The precessional vectors explain 0.5% of the insolation variability, and again have a doubly-periodic structure due to changes in the timing and amplitude of the seasons.

polynomial as a function of time. The $\mathbf{U}_n$ matrix represents the seasonal variability in the Legendre polynomials weights. When n is odd, the annual average $\mathbf{U}_n$ weights are zero mean, demonstrating that the net annual insolation received by each hemisphere is equal. The $\mathbf{V}_n$ matrix represents the secular variability in Legendre polynomial weights. The secular variations in $\mathbf{V}$ are composed of either eccentricity, obliquity, or precession signals depending on the n and m. The precession variability in V is zero-mean as there are no net annual changes in I resulting from precession. The leading four singular vectors (M=4) and four Legendre polynomials (N=4) are generally sufficient to reconstruct over 99% of the variability in I.

2.5.5 Take home messages

Any single timeseries of insolation can only represent a single spatial quantity (e.g. the value at a point, a mean, or a gradient) and a single time coordinate (a day of the year, or some average). The difficulty with using only one timeseries is that it is difficult to distinguish between changes in seasonality, the meridional distribution of insolation, or the mean value. From a physical point of view, a change in the seasonal timing of insolation is very different from a change in the latitudinal distribution of insolation, and the two should not be confused. Derived quantities, such as the insolation gradient between two latitudes, are useful but nonetheless incomplete representations of insolation variability — the inter-hemispheric gradient, L_1, accounts for less than 10% of the total spatial insolation variance. It is better to think of changes in the orbital parameters as causing changes in the relative weightings of meridional (the Legendre polynomials) and seasonal (annual or bi-annual cycles) modes of insolation variability. The compact representation of insolation developed here accurately represents the connection between changes in the orbital parameters and both seasonal and spatial modes of variability.

Each spatial model of variability has secular variability owing to multiple orbital parameters. The relative variance attributable to each orbital parameter is a function of the spatial mode and time of year considered. Arguments that attempt to rationalize the relative strengths of orbital variations, or the phase of precession variability, must consider both the spatial and temporal influence on the climatic quantity observed. Furthermore, the likelihood that time-varying climate signals are rectified by their recording devices adds another layer of complexity in interpreting proxy records of the climate. Thus, one should be wary of assuming a fixed ratio of orbital energies, or fixing the phase of the precessional variability, when investigating orbital climate change. Note that choosing a single timeseries of insolation does fix the relative amplitudes and phases. For applications where a small number of insolation timeseries is desirable, it appears better to follow the example of *Imbrie and Imbrie* [1980] and work directly with the obliquity and (phase variable) precession parameters.

Chapter 3

A Depth-Derived Age-Model and Nonlinear Climate Change

The material included in this chapter is reproduced verbatim from Huybers and Wunsch [2004]. In addition to the original paper, an appendix is included concerning the averaging of records whose relative ages are uncertain.

A chronology of glaciation, spanning the last 780,000 years, is estimated from 21 marine sediment cores using depth as a proxy for time. To avoid biasing this "depth-derived" age estimate, the depth-scale is first corrected for the effects of sediment compaction. To provide age uncertainty estimates, the spatial and temporal variability of marine sediment accumulation rates are estimated and modeled as an autocorrelated stochastic process. Depth-derived ages are estimated to be accurate to within $\pm 9,000$ years and within this uncertainty are consistent with the orbitally-tuned age estimates. Nonetheless, the remaining differences between the depth and orbitally-tuned chronologies produce important differences in the spectral domain. From the δ^{18}O record, using the depth-derived ages, we infer that there are weak nonlinearities involving the 100KY and obliquity frequency bands which generate interaction bands at sum and difference frequencies. If an orbitally-tuned age-model is instead applied, these interactions are suppressed, with the system appearing more nearly linear.

3.1 Introduction

Inference concerning past climate change relies heavily upon the assignment of ages to measurements and events recorded in marine and ice cores as well as to a variety of isolated markers in the geological record. Sedimentation and snow accumulation are analogous to strip-chart recorders, marking the past climate state in a large variety of physical variables. These records tend to be noisy and blurred by bioturbation and a variety of diffusive-like processes, [e.g. *Pestiaux and Berger*, 1984]. The major difficulty however, is that these strip-chart recorders run at irregular rates, stop completely, or even rewind and erase previous sections. If depth is taken as a simple proxy for time, irregularities in sedimentation stretch and squeeze the apparent time scale, and so distort the signals being sought. To the degree that the changes in rates are proportional to the signals themselves, one has a challenging signal demodulation problem. It is not an exaggeration to say that understanding and removing these age-depth (or age-model) errors is one of the most important of all problems facing the paleoclimate community. Timing accuracy is crucial to understanding the nature of climate variability and the underlying cause and effect. Here we attempt to understand the nature of some of these age-model errors, and to then apply that insight to construct a time scale for marine sediment cores spanning the last 780,000 years.

The currently favored method for estimating Pleistocene age is orbital-tuning [e.g. *Imbrie*, 1984; *Martinson et al.*, 1987; *Shackleton et al.*, 1990] wherein a constant phase relationship is assumed between paleo-climatic measurements and an insolation forcing based on Milankovitch theory [*Milankovitch*, 1941]. One of the well-known successes of orbital-tuning was the *Johnson* [1982], and later *Shackleton et al.* [1990], prediction of a Brunhes-Matuyama magnetic reversal (B-M) age older than previously estimated, an inference which was subsequently confirmed by argon-argon dating [e.g. *Singer and Pringle*, 1996]. A number of radiometric dates for termination 2 also support the orbital age-model [e.g. *Broecker et al.*, 1968].

Milankovitch theory however, has come under question [e.g. *Karner and Muller*, 2000; *Elkibbi and Rial*, 2001; *Wunsch*, 2003a] and radiometric ages conflicting with the orbital ages have also been reported: for termination 2 by *Henderson and Slowey* [2000], and *Gallup* [2002]; for terminations 3 by *Karner and Marra* [1998]; and for a variety of events by *Winograd et al.* [1992], among others. To understand long term climate change, it is necessary to resolve these conflicting age estimates. To avoid circular reasoning, an age-model devoid of orbital assumptions is needed.

As suggested by *Shaw* [1964], the age of geological events identifiable in multiple stratigraphies may be estimated using mean sediment accumulation rates, here termed "depth-derived" ages. The literature has numerous examples of depth-derived ages [e.g. *Shackleton and Opdyke* 1972, from 900 to 0 KY BP; *Hays et al.* 1976, 500-0 KY BP; *Williams* 1988, 1900-0 KY BP; *Martinson et al.* 1987, 300-0 KY BP; and *Raymo* 1997, 800-0 KY BP], but whose results have been inconclusive. The most comprehensive existing study, that by *Raymo* [1997], used 11 marine sediment cores. Owing to her inference of systematic core extension during recovery, she could not distinguish between the conflicting orbital and radiometric termination 2 age estimates.

This present study extends the depth-derived approach to 21 sediment cores, described below and, in what is a critical factor, accounts for the down-core trend in sediment compaction. An age uncertainty estimate for the depth-derived age-model is provided, in part, by modeling accumulation rate variability as an autocorrelated stochastic process. Within the estimated uncertainty, the depth-derived and orbital age-models are consistent with one another, but the depth-derived age-model implies nonlinear relationships between earth's orbital variations and the δ^{18}O climate proxy that are absent when the orbital age-models are applied.

3.2 Data

An ensemble of 26 δ^{18}O records from 21 separate coring sites are used in this study. The core sites are shown in Figure 3-1 and can be divided into four geographical regions: the North Atlantic, Eastern Equatorial Pacific, Equatorial Atlantic, and the Indian and Western Equatorial Pacific Oceans. Core site locations heavily favor the northern hemisphere. Four of the records are from piston cores (V22-174, V28-238, V28-239, and MD900963) while the remainder are composite records spliced together from multiple cores recovered by the Deep Sea Drilling Program (DSDP) or Ocean Drilling Program (ODP). For ODP and DSDP sites, the composite depth scale or, if available, the ODP revised composite depth scale, is used. Table 3.1 lists the pertinent statistics and a reference for each core.

All δ^{18}O records that were available to us, believed to be stratigraphically intact, and which extend through the B-M were included in this study. Use of planktic records, in addition to the benthic, allows for the inclusion of seven more sediment

Name	Reference	Species	$\bar{S}$	$\triangle t$	W. Dep	Lat	Lon
DSDP502T	*Prell*, 1982	P	1.9	6.5	3052	12N	79E
DSDP552MT	*Shackleton and Hall*, 1984	B	1.9	6.4	2301	56N	23W
DSDP607MT	*Ruddiman et al.*, 1989	B	4.0	3.5	3427	41N	33W
MD900963M	*Bassinot et al.*, 1994	P	4.6	2.3	2446	5N	74E
ODP659M	*Tiedemann et al.*, 1994	B	3.1	3.9	3070	18N	21W
ODP663	*de Menocal et al.*, unpublished	P	3.9	3.0	3706	1S	12W
ODP664M	*Raymo*, 1997	B	3.7	3.4	3806	0	23W
ODP677MT	*Shackleton et al.*, 1990	B,P	3.9	2.1,1.8	3461	1N	84W
ODP758MT	*Chen et al.*, 1995	B,P	1.6	6.5,6.7	2924	5N	90E
ODP806T	*Berger et al.*, 1994	B,P	2.0	4.8	2520	0	159E
ODP846MT	*Mix et al.*, 1995a	B	3.7	2.5	3461	3S	91W
ODP849MT	*Mix et al.*, 1995b	B	2.9	3.6	3296	0	111W
ODP851MT	*Ravelo and Shackleton*, 1995	P	2.0	5.0	3760	2S	110W
ODP925	*Bickert et al.*, 1997; *Curry and Cullen*, 1997.	B	3.7	2.2	3041	4N	43W
ODP927T	*Cullen et al.*, 1997 *Curry and Cullen*, 1997.	B,P	4.5	3.2,2.2	3315	6N	43W
ODP980T	*Flower*, 1999; *McManus et al.* 1999, 2002; *Oppo et al.* 1998, 2001.	B	12.3	1.6	2169	55N	17W
ODP982T	*Venz et al.*, 1999.	B,P	2.5	2.3,2.0	1134	57N	18W
ODP983	*Channell et al.*, 1997; *McManus et al.* 2003.	B	11.4	.9	1983	61N	22W
V22-174	*Thierstein et al.*, 1977	P	1.8	5.3	2630	10S	13W
V28-238MT	*Shackleton and Opdyke*, 1976	P	1.5	5.5	3120	1N	160E
V28-239M	*Shackleton and Opdyke*, 1976	P	0.9	5.6	3490	3N	159E

Table 3.1: The characteristics and primary references for each core. An 'M' appended to the core name indicates the B-M was identified via magnetic susceptibility measurements, and a 'T' indicates the availability of a published orbitally-tuned age-model. Columns from left to right display δ^{18}O species benthic (B) and/or planktic (P), the mean sediment accumulation rate ($\bar{S}$, cm/KY), the mean interval between δ^{18}O measurements ($\triangle t, KY$), water depth (meters), and the latitude and longitude of each core site.

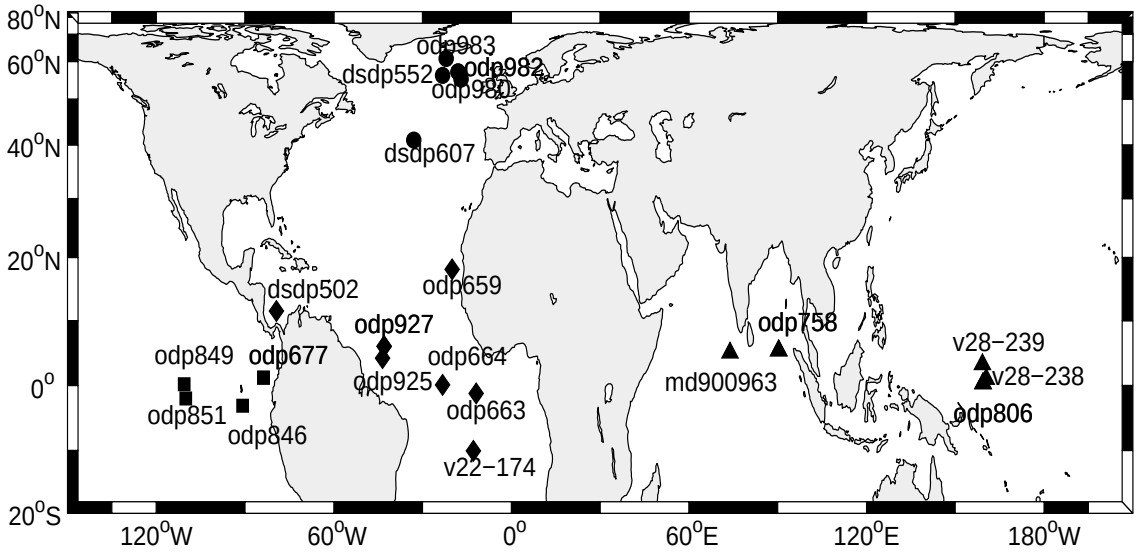

Figure 3-1: The locations of the records used in this study. Markings indicate geographic groupings: the North Atlantic (circles), Indian and Western Equatorial Pacific (triangles), Equatorial Atlantic (diamonds), and Eastern Equatorial Pacific Oceans (squares).

cores and decreases the uncertainty associated with the depth-derived age-model. The depth of the B-M was reported in the literature as identifiable via magnetic stratigraphy in 12 of the 21 cores, and these cores are indicated by an "M" appended to the name in Table 3.1. For the δ^{18}O records associated with these 12 cores, the B-M invariably occurs within δ^{18}O stage 19. Where the B-M transition is not identifiable, the depth of event 19.1 – the most negative δ^{18}O value in stage 19 – is instead used, and in all cases an age of 780 Kiloyears before present (KY BP) [*Singer and Pringle*, 1996, rounded to the nearest ten KY] is assigned.

At the outset, it is convenient to correct for the effects of compaction on the depth scale. Sediment compaction typically increases with depth [e.g. *Bahr et al.*, 2001] and thus systematically compresses a greater quantity of time into a given depth interval. Assuming that the estimated trends in porosity reflect inhomogeneities in relative compaction, we apply a correction based on conservation of dry sediment volume wherein the thickness of each sediment layer is adjusted so as to remove trends in porosity. Porosity trends are estimated by fitting a low order polynomial to porosity observations; for cores without observed porosity profiles – comprising 13 of the 21 cores – the mean down-core porosity trend from the observed porosity profiles is

instead used. While this method introduces an age-model uncertainty of up-to ±6KY, the alternative is an expected age-model bias of up-to 15 KY. See Appendix A for more details. All subsequent depth references are to this de-compacted scale. Note *Huybers* [2002] did not adequately account for the effects of compaction and thus arrived at older age estimates.

It is helpful to define some terminology used in estimating the depth-derived age-model. An "event" is a δ^{18}O feature whose depth can be uniquely identified within each δ^{18}O record. When an age is fixed to an event, it becomes an age control point (ACP). Two types of events are referred to, "stages" and "terminations." Stages are defined as local minima or maxima in the δ^{18}O record [*Prell et al.*, 1986] where the numbering system suggested by *Imbrie et al.* [1984] is used. All the stages referred to in this study have odd numbers after the decimal point, corresponding to low ice volume excursions in the δ^{18}O record. Terminations are defined as an abrupt shift from glacial to interglacial conditions [*Broecker*, 1984], where the assigned depth is the midpoint between the local δ^{18}O minimum and maximum. Figure 3-2 shows the eight termination mid-points and nine stages which were visually identified in each δ^{18}O record. For comparison purposes, figure 3-2 also shows these seventeen events identified on the SPECMAP δ^{18}O stack [*Imbrie et al.*, 1984].

A second, more objective, method of event correlation was also implemented using an automated cross-correlation maximization procedure. Within an expected error of 1KY, this algorithm, termed XCM, yielded event correlations which were identical to those determined from the visual procedure. This result gives some confidence in the ability to relate events in different δ^{18}O records. For more detail see Appendix B and *Huybers* [2002].

The choice of seventeen ACPs reflects a minimalist strategy for constraining the $\delta^{18}O$ record, especially when compared with the SPECMAP δ^{18}O stack which uses over 90 ACPs in the same 770KY interval. We do not use more ACPs for three reasons: (1) only a small decrease in age-model uncertainty would result (Section 4.1); (2) while more high-frequency structure in the composite δ^{18}O record is expected to be retained, false structure could be built into the averaged record by aligning noisy features; and (3) more ACPs are not expected to aid in resolving the spectra of higher-frequency processes because of the spectral smearing due to age-model uncertainty (Section 5.1).

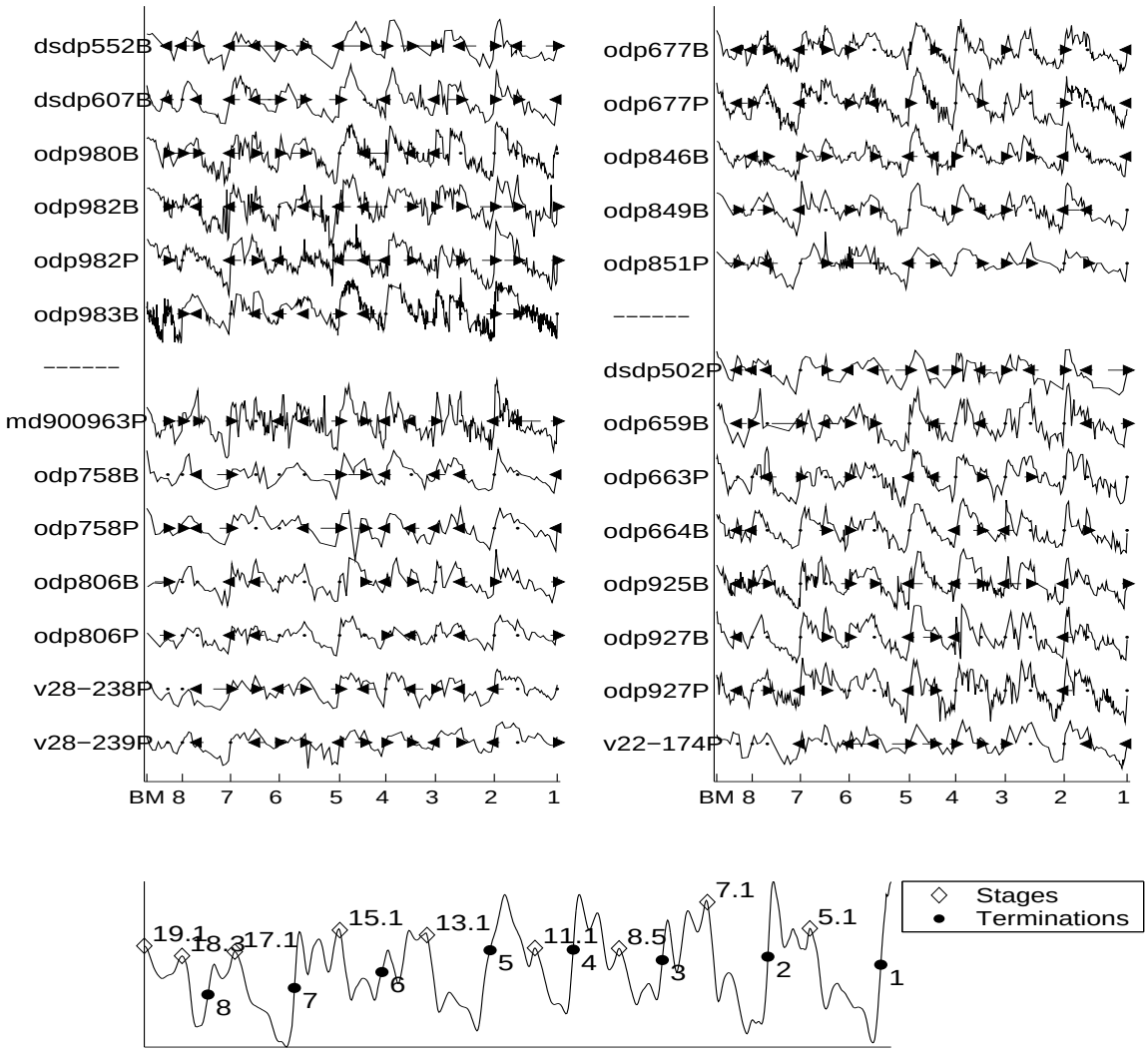

Figure 3-2: The δ^{18}O isotope records, grouped into the four geographic categories shown in Figure 3-1: the North Atlantic (top left), Eastern Equatorial Pacific (top right), Indian and Western Equatorial Pacific (bottom left), and Equatorial Atlantic Oceans (bottom right). As described in the text, simultaneity between all records is enforced at 17 isotopic events. The ordinate is labeled with the B-M boundary location and termination numbers. The abscissa is to scale, and the $\delta^{18}O$ records are vertically off-set from one another. The arrows at each event indicate how the age-model was adjusted from a linear age-depth relationship beginning with stage 18.3 and working toward stage 5.1. The letters B and P are appended to the record name to indicate it as benthic or planktic. Bottom panel is the SPECMAP δ^{18}O stack oriented such that upward indicates lighter δ^{18}O (inter-glacial). The SPECMAP stack is labeled with each of the 17 events for which ages are later estimated and the ordinate is arbitrary. Note that in this paper, time always increases to the right.

3.3 Time and sediment accumulation

3.3.1 A random walk model

To understand the relationships between age and depth, we need a model of sediment accumulation rates. Both are expected to have systematic and stochastic elements, the latter here modeled as a random walk. Let d_n be the depth of a layer of sediment in a core at timestep n. Then for a unit time step, $\triangle t$, d_n increases as,

$$d_{n+1} = d_n + \triangle t\bar{S} + \triangle t S'_n + W_n, \tag{3.1}$$

where $\bar{S}$ is the mean sediment accumulation rate, S'_n is the zero-mean stochastic contribution, and W_n is a systematic term. Dividing by $\bar{S}$ converts the change in depth for each increment to a true time increment plus two anomaly terms,

$$t'_{n+1} = t'_n + \triangle t + \triangle t\frac{S'_n}{\bar{S}} + \frac{W_n}{\bar{S}}, \tag{3.2}$$

where $t'_n = d_n/\bar{S}$, is the linear age estimate. W_n is treated here primarily as the sediment compaction affect – see Appendix A – although long-term variation in bio-productivity, terrigenous discharge, dust transport, and coring artifacts are also implicated. We focus first on the random element.

The simplest case is when S'_n is a white noise process, $< S'_n S'_m >= 0$, $n \neq m$ (brackets, $< \cdot >$, denote an ensemble average) and the variance of the difference between the apparent and true time grows linearly on average [*Feller*, 1966],

$$< (t'_n - n\triangle t)^2 >= n\triangle t\frac{\sigma^2}{\bar{S}^2}. \tag{3.3}$$

where $\sigma^2 = \left\langle S'^2_n \right\rangle$. Following *Moore and Thomson* [1991] and *Wunsch* [2000], we term the variance growth rate the "jitter,"

$$J = \left(\frac{\sigma}{\bar{S}}\right)^2, \tag{3.4}$$

an appropriate measure when only one δ^{18}O event is constrained to a known age. If the duration of the temporal random walk is fixed by introducing a second ACP at $t = N\Delta t$, the expected variance between the two fixed points behaves as a "Brownian bridge" process. Following *Odell* [1975] and *Bhattacharya and Waymire* [1990], the

Brownian bridge analogue of Eq. 3.3 is,

$$< (t'_n - n\triangle t)^2 >= n\triangle t J \left(1 - \frac{n}{N}\right), \qquad 0 \leq n \leq N \tag{3.5}$$

where N is the total number of time steps between the 2-ACPs. Age variance is then zero at the two end points, with a maximum at the midpoint. Integrating, and comparing Eqs. 3.3 and 3.5, shows that the inclusion of a second ACP results in a three-fold reduction in mean age variance.

3.3.2 Determining the stochastic element

To estimate the character and degree of jitter in deep sea sediment cores, it is useful to construct some simple age-models. Rather than using the mixed stage and termination notation, each event is assigned a number, $1 \leq k \leq 17$, running in temporal sequence from termination 1 to stage 19.1. Mean accumulation rates in core j between events 17 (stage 19.1) and 13 (termination 7) can be estimated as,

$$\bar{S}_j^{(1)} = \frac{d_{j,17} - d_{j,13}}{160}, \tag{3.6}$$

where $d_{j,k}$ is the depth of event k, and 160 KY is roughly the duration between events 17 and 13. If event 1 is pinned to an age of 10.6KY before present (BP), the ages of events 1 through 13 are then estimated as

$$A_{j,k}^{(1)} = \frac{d_{j,k} - d_{j,1}}{\bar{S}_j^{(1)}} + 10.6, \qquad 1 \leq k \leq 13, \tag{3.7}$$

where the superscript indicates the use of one ACP. If a second ACP at the B-M transition is incorporated, an age-model may be expressed as,

$$\begin{aligned} \bar{S}_j^{(2)} &= \frac{d_{j,17} - d_{j,1}}{780 - 10.6}, \\ A_{j,k}^{(2)} &= \frac{d_{j,k} - d_{j,1}}{\bar{S}_j^{(2)}} + 10.6, \qquad 1 \leq k \leq 17. \end{aligned} \tag{3.8}$$

where 780 KY BP is the age of B-M transition.

Calculation of the variance in age estimates for each event permits comparison with the random walk models of sediment accumulation. First, the mean age of each

event is determined by averaging over all cores,

$$\bar{A}_k^{(i)} = \frac{1}{21}\sum_{j=1}^{21} A_{j,k}^{(i)}, \tag{3.9}$$

for both the i =1 and $i = 2$ ACP cases. When planktic and benthic δ^{18}O records are available within the same core, only the benthic record is used. The age variance can then be estimated as,

$$v_k^{(i)} = \frac{1}{20}\sum_{j=1}^{21}(A_{j,k}^{(i)} - \bar{A}_k^{(i)})^2, \qquad 1 \le k \le 17. \tag{3.10}$$

Figure 3-3 shows the calculated age variances, $v_k^{(i)}$ $i = 1, 2$. As expected, $v_k^{(1)}$ increases with the elapsed time from event one, t, and $v_k^{(2)}$ has a Brownian bridge character. Also shown are the simple random walk and Brownian bridge models as determined from Eqs 3.3 and 3.5 with $J = 10$ in both cases. Were the model adequate, a single value of the jitter should be applicable to modeling both $v_k^{(1)}$ and $v_k^{(2)}$, but it is evident from Figure 3-3 that $J = 10$ under-estimates the variance of $v^{(1)}$ and over-estimates that of $v^{(2)}$. Eq. 3.3 also predicts $v_k^{(1)}$ is proportional to t, but it appears more nearly proportional to t^2 and is thus inconsistent with the hypothesis of a simple random walk in sediment accumulation. Some other effect is required to explain the result.

3.3.3 Sediment accumulation with autocovariance

A generalization of the simple random walk to a correlated random walk is capable of accounting for the observed quadratic growth in the $v^{(1)}$ age variance. This generalization is plausible because sediment accumulation rates are themselves climate variables and can be expected to have a structured frequency spectrum implying temporal autocorrelation. To proceed, it is first necessary to adopt an age-model estimated independent of accumulation rates.

The Devils Hole record is devoid of orbital assumptions [*Winograd et al.*, 1992] and has a radiometric age-model with uncertainties ranging from ±10KY at its oldest time, 519 KY BP, to ±2KY at its youngest, 140 KY BP. A complication, however, is that the Devils Hole record is, in places, offset from the marine δ^{18}O by up to 10 to 15 KY and is thus not suitable for directly dating the marine δ^{18}O records [*Wino-*

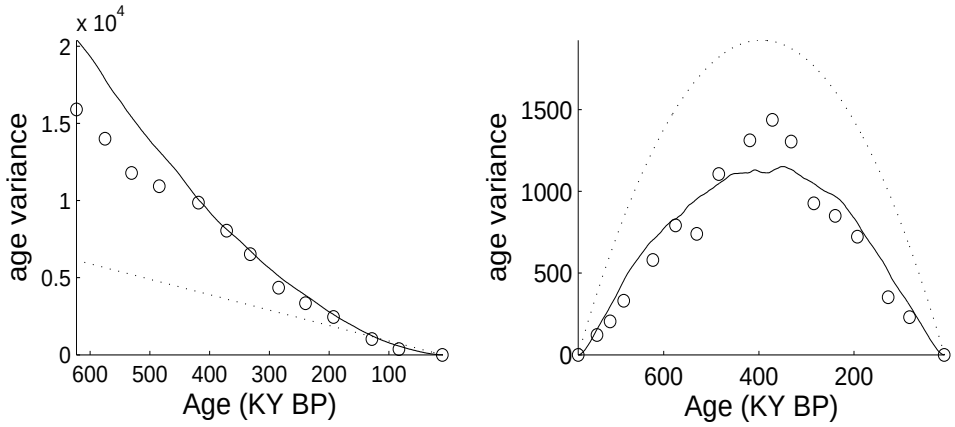

Figure 3-3: The observed age variance (circles), and simple models of age variance using correlated (solid line) and un-correlated (dotted lines) sediment accumulation rates. Both the one ACP (left) and two ACP (right) cases are shown with a simple random walk using $J = 10$ and a correlated random walk using $J = 0.5$ and $s_o = 1/40$. The simple random walk respectively under- and over-estimates the age variance, while the correlated random walk is similar to the calculated variance.

grad et al., 1997; *Herbert et al.*, 2001]. In estimating marine sediment accumulation rates, only the duration between events needs to be equal, and we assume that the relative timing between the marine and Devils Hole δ^{18}O records is constant during most intervals. Acknowledging that this fixed-lag assumption probably breaks down during glacial maxima and terminations, the marine $A^{(2)}$ age-models are none the less adjusted to maximize the squared zero-lag cross-correlation between the marine and Devils Hole δ^{18}O records using the XCM algorithm (see Appendix B). The derivative of depth relative the adjusted $A^{(2)}$ age-models then provide estimates of accumulation rates.

For the purpose of comparison, accumulation rates were also estimated from the orbitally derived age-models provided by other authors, as indicated in Table 1. Figure 3-4 shows the power density spectral estimates of sediment accumulation rates using the multitaper method [*Thompson*, 1990] with both the Devils Hole and the published orbital age-models. Both spectra may be characterized as,

$$\Phi(s, s_0) = \frac{1}{s^2 + s_o^2}, \tag{3.11}$$

where Φ is the power density and s the frequency. Such a relationship is consistent with an autoregressive process of order 1 (AR(1)), and implies a minus two power law

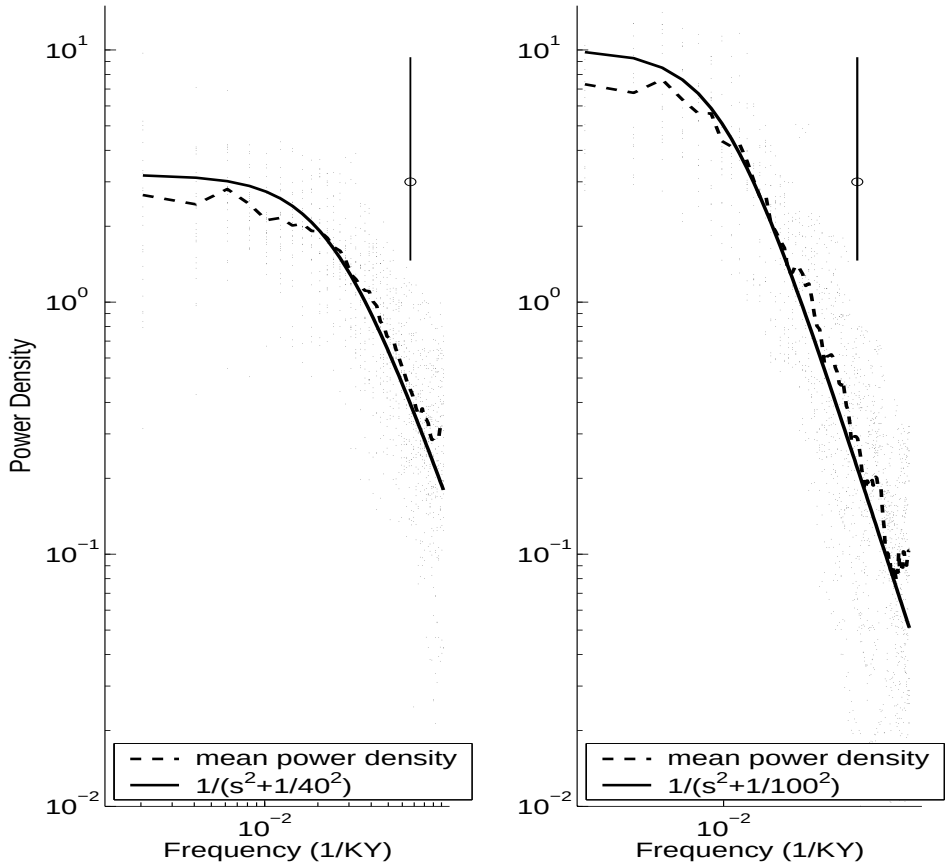

Figure 3-4: The multitaper spectral estimate of sediment accumulation rates for each record (dots), the mean from all the spectral estimates (dashed line), and an approximate spectral fit (solid line). Left panel is the analysis using the Devils Hole age-model, and the right panel is from the orbital age-models. Vertical bars indicate the approximate 95% confidence interval for the estimates from individual records (dots).

relationship for frequencies above s_o, with white noise at the lowest frequencies. The Devils Hole age-model gives $s_o \approx 1/40$KY, but the orbital age-models are consistent with the result of *Mix et al.* [1995] with $s_o \approx 1/100$KY. This difference in shape is likely due to errors in one or both of the age-models. The scope of the spectral damage owing to jitter is unclear, but as discussed later, either value of s_o gives a parameterization of accumulation rate variations consistent with the observed $v^{(1)}$ and $v^{(2)}$ age variances.

To estimate the uncertainty in ages due to accumulation rate variability, it is simplest to generate ensemble members from the stochastic accumulation model and calculate derived statistics from them. A synthetic accumulation rate with specified

jitter (J) and power density (Φ) can be generated as,

$$S(t) = \Im^{-1}\{\hat{\eta}\sqrt{J\Phi'(s, 1/40)}\} + 1, \tag{3.12}$$

where $\Im^{-1}$ is the inverse Fourier transform, $\hat{\eta}$ is the Fourier transform of a white noise process, and $\Phi'(s, s_0) = \Phi(s, s_o) / \sum \Phi(s, s_0)$ where the sum is over all frequencies. Summing the accumulation rate gives a depth profile, $d(t) = \sum S(t)$, with the specified autocorrelation and jitter. By generating a large number of synthetic depth profiles and converting each to age with Eq. 3.7, a least squares best fit was sought between the observed and modeled $v_k^{(1)}$, $1 \leq k \leq 13$, distribution by varying the jitter in Eq. 3.12. A best fit was achieved with $J = 0.5$, and the resulting modeled $v^{(1)}$ and $v^{(2)}$ are shown in Figure 3-3. The autocorrelated random walk model reproduces the quadratic growth in $v^{(1)}$ and a single value of the jitter fits both the calculated $v^{(1)}$ and $v^{(2)}$ age variances. Further tests (not shown) indicate the autocorrelated random walk is equally consistent when greater numbers of age control points are used, and we will assume the same value of J is appropriate for our 17-ACP model (see Figure 3-7). If $s_o = 1/100$KY, corresponding to the orbitally-tuned accumulation estimates, the observations are fit equally well using a smaller value of J; with this method one cannot distinguish between the Devils Hole and orbital age-model accumulation rate estimates in the marine cores.

3.4 The depth-derived age-model

An age-model based on a single linear age-depth relationship will be stretched or squeezed by every variation in sediment accumulation and each coring artifact. We seek to mitigate these age-model errors by using multiple age-depth relationships. Table 3.2 indicates the $A_{j,k}^{(2)}$ event ages for each record along with the averages, $\bar{A}_k^{(2)}$. An age-model based on these mean event ages, using all 17 events and termed the "depth-derived age-model," may be expressed as,

$$A_j^{(17)} = \frac{\bar{A}_k^{(2)} - \bar{A}_{k-1}^{(2)}}{d_{j,k} - d_{j,k-1}} d_j + \bar{A}_{k-1}^{(2)}, \qquad \begin{array}{l} d_{j,k-1} \leq d_j \leq d_{j,k}, \\ 1 \leq j \leq 21, \\ 2 \leq k \leq 17. \end{array} \tag{3.13}$$

event	17	16	15	14	13	12	11	10	9	8	7	6	5	4	3	2	1
	19.1	18.3	VIII	17.1	VII	15.1	VI	13.11	V	11.1	IV	8.5	III	7.1	II	5.1	I
dsdp502P	780	730	695	660	601	560	510	435	395	342	327	260	220	157	102	49	11
dsdp552B	780	734	693	677	576	519	505	474	362	321	293	265	253	176	122	63	11
dsdp607B	780	730	703	n/a	586	510	488	454	408	361	311	259	206	184	128	91	11
md900963P	780	751	735	715	663	619	563	496	446	412	365	310	278	234	160	73	11
odp659B	780	723	702	673	664	595	558	519	456	389	345	285	237	189	123	73	11
odp663P	780	737	710	664	612	567	534	489	415	356	319	278	230	194	126	86	11
odp664B	780	728	693	660	599	564	527	480	411	368	321	288	228	177	118	82	11
odp677B	780	735	699	680	604	562	526	476	413	378	333	283	244	195	143	96	11
odp677P	780	723	702	676	603	555	527	470	412	368	330	287	243	191	142	99	11
odp758B	780	739	714	679	642	598	558	512	475	458	409	357	293	235	170	123	11
odp758P	780	746	725	691	649	602	562	508	477	450	404	341	290	236	170	128	11
odp806B	780	765	733	709	641	578	530	478	411	370	325	284	235	175	117	73	11
odp806P	780	756	730	705	635	572	528	485	419	367	334	276	232	174	115	72	11
odp846B	780	737	697	676	622	592	552	514	433	378	347	296	256	215	144	99	11
odp849B	780	751	721	712	642	596	558	518	450	404	372	314	276	228	136	82	11
odp851P	780	765	734	687	626	594	484	437	359	328	286	249	213	187	125	87	11
odp925B	780	735	715	698	633	581	553	515	424	379	329	306	231	191	119	75	11
odp927B	780	734	706	680	622	580	542	496	421	395	350	298	255	205	125	84	11
odp927P	780	732	704	688	619	582	542	496	423	386	342	293	248	203	125	84	11
odp980B	780	748	737	726	647	605	568	546	481	397	359	296	238	192	126	83	11
odp982B	780	750	723	684	611	576	529	453	366	286	245	210	170	132	95	78	11
odp982P	780	751	720	693	611	576	522	470	362	289	244	210	164	133	93	74	11
odp983B	780	738	721	686	621	562	504	449	396	328	289	244	198	151	102	80	11
v22-174P	780	736	707	679	612	565	490	433	400	375	346	305	269	224	158	106	11
v28-238P	780	741	718	684	654	615	561	530	481	415	375	305	266	213	133	86	11
v28-239P	780	738	712	672	605	541	506	465	393	363	329	287	236	196	123	78	11
mean age	780	741	713	685	623	576	532	485	419	372	332	284	239	192	129	85	11
uncertainty	3	5	7	8	9	10	11	11	11	11	10	10	9	8	7	6	1
SPECMAP	731	711	693	668	621	574	531	481	423	368	337	287	244	194	128	80	11
ODP677B	784	743	709	690	620	574	531	482	417	382	335	283	243	200	129	73	11
Devils Hole							519	461	416	383	340	287	251	195	142	81	
Vostok (GT-4)										383	327	277	240	202	133	85	15

Table 3.2: The $A^{(2)}$ age estimate (KY BP) for each event in each δ^{18}O record, and the mean age of each event along with its estimated uncertainty (±KY). The events numbers are listed at top along with the associated stage (Arabic) and termination (Roman) numbers. For comparison, the orbitally-tuned SPECMAP stack [*Imbrie et al.*, 1984], orbitally-tuned benthic ODP677 [*Shackleton et al.*, 1990], radiometric Devils Hole [*Winograd et al.*, 1997], and Vostok GT-4 deuterium age estimates [*Petit et al.*, 1999] are also shown.

For each record, j, age is linearly interpolated with depth, d_j, between each pair of ACPs, $k-1$ and k, yielding a piecewise linear age-model. $A_j^{(17)}$ is our best-estimate of the core ages.

3.4.1 Uncertainty analysis

There are at least five sources of error in the $A^{(17)}$ age-model: non-simultaneity between isotopic events, uncertainty in identifying the depth of each event, variations in accumulation rates, post-depositional processes, and uncertainty in the age of the B-M. Each source of error is considered in turn, and a Monte Carlo method is applied in conjunction with the stochastic sediment accumulation model to assess the overall uncertainty.

Simultaneity (1) The ocean mixing times for the δ^{18}O signal can range out to 1000 years and longer [*Wunsch*, 2003c]. Imposing simultaneity between δ^{18}O events, if

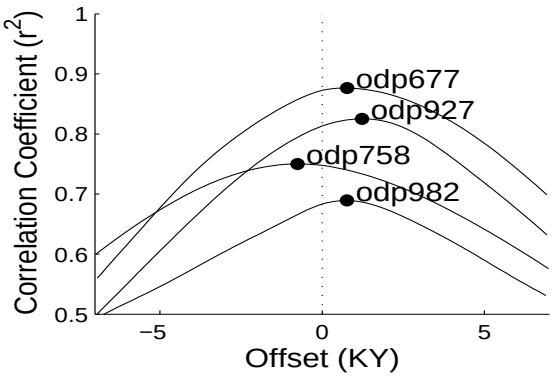

Figure 3-5: Lagged cross-correlation between sets of benthic and planktic δ^{18}O records measured in the same core. Positive values indicate a benthic lead.

correct, de-blurs this mixing effect. To account for the ocean mixing time, a random variable with a ±1KY standard deviation is added to the δ^{18}O event ages in the stochastic sediment accumulation simulation.

(2) This study incorporates benthic and planktic foraminiferal species over a wide geographic range. Foraminiferal δ^{18}O responds to both the temperature and δ^{18}O of their environments [e.g. *Schrag et al.*, 1996], and these environmental values likely fluctuate asynchronously and spatially heterogeneously. The presence of systematic offsets between benthic and planktic records can be estimated by means of a lagged cross-correlation when both species are measured in the same core. Figure 3-5 shows that the five benthic and planktic δ^{18}O pairs used here have a maximum cross-correlation at positions within a 1KY lag; a 1KY error is included in the stochastic accumulation model. More localized offsets between benthic and planktic records may occur in parts of the isotopic sequence, but we find no obvious pattern; if present, these localized offsets are apparently secondary to uncertainties associated with event identification.

Identification Owing to machine error in measuring δ^{18}O, finite sampling resolution, and bioturbational blurring, events are only identifiable to within a finite depth range [*Pisias*, 1984; *Huybers*, 2002]. For the mean accumulation rates of the cores sampled here, we estimate the depth uncertainty translates to approximately ±4KY. Larger errors are incurred if δ^{18}O events are misidentified, but we do not account for this possibility.

Accumulation Rate Variations (1) Core-site variations in accumulation rate will introduce errors in linear age-depth relationships, as discussed in Section 3.3.3. Averaging multiple age-depth realizations, to the degree that they are independent, reduces this uncertainty. An empirical orthogonal functions (EOF, or "singular vectors") analysis [e.g. *Wunsch*, 1996; *von Storch and Zwiers*, 1999] of accumulation rate variability, as estimated using $A^{(17)}$, indicates there are about 11 degrees of freedom in accumulation rate variations, and thus also in the age estimates.

(2) Trends in global mean accumulation rates, as monitored at these 21 core sites, could bias the depth-derived age-model. Spectra from both Devils Hole and from orbitally-tuned chronologies, however, show low frequency white noise behavior (Figure 3-4) precluding long period global variations in accumulation. In agreement with this inference, *Lyle* [2003] found no evidence for spatially coherent long-period trends in Pacific carbonate accumulation during the Pleistocene. Thus, no uncertainties due to trends in accumulation are incorporated into the model.

(3) Porosity is itself a climate variable and is known to change with other components of climate system, [*Herbert and Mayer*, 1991; *Hagelberg et al.*, 1995]. While random variations in porosity are implicitly accounted for in (2) above, climatically induced quasi-periodic age errors could contribute to the nonlinear and/or non-Gaussian structure of the δ^{18}O signal discussed below in Section 3.5 [see also *Herbert*, 1994]. Changes in porosity are often linked with changes in organic and calcium carbonate deposition [*Herbert and Mayer*, 1991], and, it is likely that porosity-climate biases tend to cancel out when one aggregates cores from different ocean basins, owing to the opposite response of Pacific and Atlantic carbonate cycles. Furthermore, spectral estimates of sediment accumulation rate variations using the orbital age-models (see Figure 3-4) show a smooth red-noise trend both on a site-by-site basis and in the mean. This result indicates the absence of strong quasi-periodic variations in total accumulation rates, or alternatively that such variability is not resolved by orbital age-estimates. In Section 5.3 we further evaluate the potential these quasi-periodic variations have to influence our results.

Post-depositional Effects (1) Appendix A compares $A^{(17)}$ with a similar age-model in which compaction is not accounted for. The latter displays a bias, with ages, on average, 10KY older than the compaction-corrected age-model, but tapering to zero at the fixed end-points. Two sources of error exist in the compaction correction. First, scatter in the porosity measurements introduces uncertainty in determining

the trend toward lower porosity with depth. Second, a larger source of uncertainty results from the absence of porosity measurements for 13 of the records, requiring an indirect compaction correction as discussed in Appendix A. The combined compaction correction uncertainty averages ±5KY, and is listed for each event in Table 3 of Appendix A. While large, this uncertainty is preferable to an age-model bias which is expected to average 10KY. In future work, the de-compaction uncertainty could be reduced by using more porosity measurements or, possibly, by accounting for differential compaction according to sediment composition.

(2) The effects of coring on a sediment column are a further source of uncertainty for the depth-derived age-model. Most of the records used here are from the advanced piston corer of the Ocean Drilling Program (ODP-APC) which uses a rigid-drill pipe and a stationary piston in extracting cores. This drilling method reduces age-depth uncertainties related to over-sampling, a common problem for conventional non-rigid piston-corers, and related to under-sampling, a common problem for gravity-corers [*Skinner and McCave*, 2003]. A remaining problem, however, is that the depth-scale of cores obtained with the ODP-APC are typically stretched due to elastic rebound of the sediment after the core is recovered [*MacKillop et al.*, 1995; and *Moran*, 1997]. The degree of rebound depends on sediment lithology and is likely to be heterogeneous. The high-frequency variations and down-core trends in age-depth relationships caused by sediment rebound are effectively folded into the previous estimates of accumulation rate variability and trends in sediment compaction. Because we seek only to estimate an age-model, it is not necessary to disentangle these in-situ and post-coring sources of uncertainty.

Brunhes-Matuyama Reversal *Singer and Pringle* [1996] estimate that the age of the B-M is radiometrically constrained to within ±2KY. The depth of the reversal however, is not always clearly identifiable [*Tauxe et al.*, 1996] and thus another uncertainty of ±4KY is added.

Monte Carlo Analysis The combined uncertainties associated with the depth-derived age-model are incorporated into a stochastic age-depth model and estimated with a Monte Carlo analysis. All errors, except those associated with the compaction correction and accumulation rate variations, are modeled as independent realizations of a zero-mean Gaussian distribution. The expected squared error in the $\bar{A}_k^{(17)}$ age

estimates is then,

$$< e_k^2 >= \frac{1}{21} 4^2 + 1^2 + 1^2 + 2^2 \Big|_{k=17}, \; 1 \leq k \leq 17. \tag{3.14}$$

The first term on the right is the event-depth determination error, assumed to be independent in each core and hence divided by the number of cores, 21. The second and third terms are the benthic/planktic timing error and the ocean signal propagation times. The last term is the estimated radiometric age error applied only for $k = 17$, the Brunhes-Matuyama. Apart from the depth determination error, each error is likely to be correlated between cores, and thus not effectively reduced by averaging.

The compaction correction uncertainty, denoted c_k, is strongly correlated between events, biasing the entire age-model toward either younger or older ages. Realizations of c_k are thus generated by multiplying the expected uncertainty structure (see Table 3 of Appendix A) by single a value drawn from a zero-mean unit standard deviation Gaussian distribution.

To account for the effects of jitter, a depth profile is generated according to Eq. 3.12 with $J = 0.5$ and $s_o = 1/40$KY. This depth profile nominally spans events 1 (10.6KY BP) to 17 (780KY BP), and has a true age, t, associated with each depth. Seventeen depths are identified such that,

$$t(d_k) = \bar{A}_k \qquad 1 \leq k \leq 17, \tag{3.15}$$

where each d_k represents the depth of a synthetic-event and $\bar{A}_k$ are the fixed values estimated in Eq. 3.9. Applying Eq. 3.8, the depth profile is linearly converted to age yielding a jittered age estimate for each synthetic-event. This process is repeated 11 times, corresponding to the approximately 11 degrees of freedom in accumulation rate estimates. Averaging over each of the synthetic records, j, yields a mean jittered age estimate,

$$\bar{A}'_k = \left(\frac{1}{11} \sum_{j=1}^{11} A'_{j,k} \right) + e_k + c_k, \qquad 1 \leq k \leq 17, \tag{3.16}$$

to which the additional e_k and c_k error realizations are added.

Applying Eq. 3.13 to Eq. 3.16 generates a single stochastic depth-derived age-model realization. The root-mean-square (rms) age deviation of numerous stochastic model realizations are used to estimate the expected $A^{(17)}$ age-model uncertainty. As shown in Figure 3-7, each event is a local minimum in uncertainty and events

are spanned by short Brownian bridges. The event uncertainties are also tabulated in Table 3.2 and have a mean of ±9KY. As the magnitude of the short Brownian bridges is on the order of ±1KY and there are approximately 11 independent age-depth relationships, additional ACPs and independent age-depth relationships would only marginally reduce the uncertainty of this age-model. Compared to the expected accuracy of most geochronological markers, particularly between the B-M and termination 2, the $A^{(17)}$ depth-derived age-model has good age control.

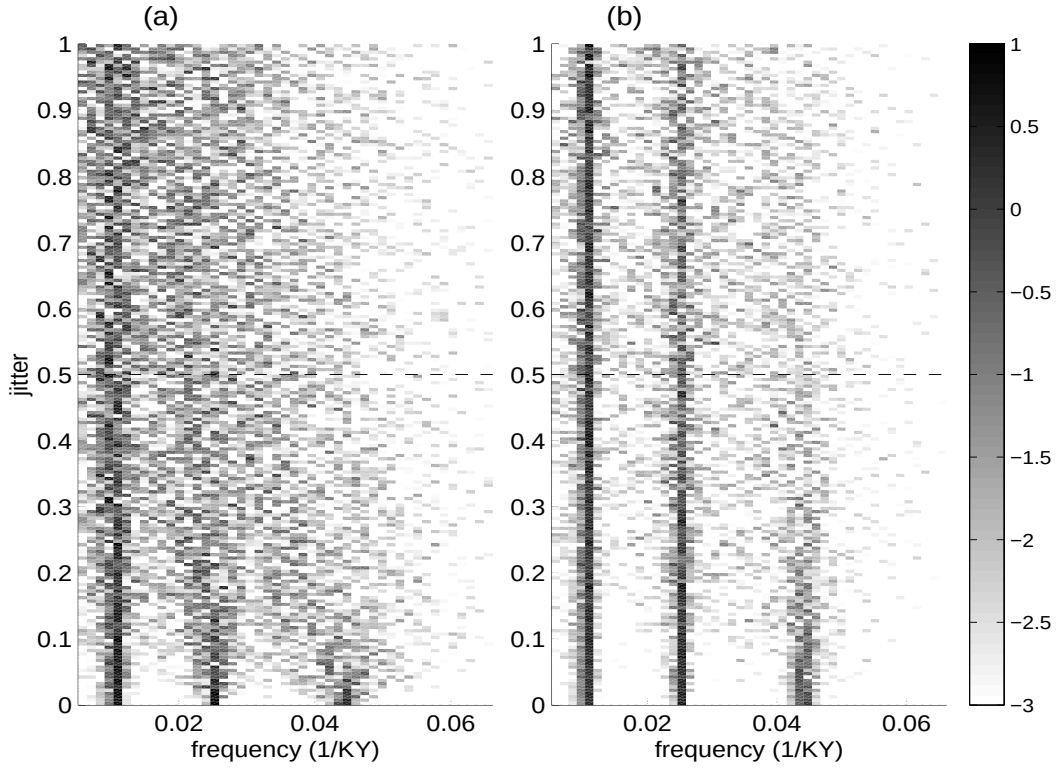

Figure 3-6: The impact of age-model jitter on the power spectrum of a harmonic processes, $\mathcal{H}$ (Eq. 3.17). Shading indicates the logarithm of the power estimate plotted against frequency (1/KY) and the degree of jitter where $s_o = 1/40$KY (see Eq. 3.11). Both plots show spectra of $\mathcal{H}$ after distorting its timescale according to the specified jitter: (a) has errors as expected for a single age-depth relationship, while (b) has errors as expected for the depth-derived age-model. The degree of jitter expected in a real core is 0.5, and is indicated by the horizontal dashed line. In (a) only the 100KY band can be distinguished, while (b) retains good resolution of the 100KY and 41KY bands and a semblance of the 23KY band.

In Section 5.1 the depth-derived age-model is used in estimating the spectra of $\delta^{18}O$ records. It is expected that higher frequency processes will, in general, be more susceptible to age-model jitter [*Moore and Thomson*, 1991; *McMillan et al.* 2002].

To gain a sense of the influence jitter will have on spectral estimates, consider the harmonic process,

$$\mathcal{H}(t) = \cos(2\pi t/100) + \cos(2\pi t/41) + \cos(2\pi t/23). \tag{3.17}$$

Figure 3-6 shows successive periodograms of $\mathcal{H}(t')$, where time, t, is stretched and squeezed to t' using an increasingly large jitter. Jitter is modeled as realizations of Eq 3.16 with J increasing from zero to one and $s_o = 1/40$KY (see Eq. 3.11). For comparison, periodograms of $\mathcal{H}(t')$ are also shown with the jitter expected for a single age-depth relationship, i.e. Eq 3.16 with $e_k = 0$ and without the summation. For a single age-depth relationship, the 100KY variability is poorly resolved, and the higher frequency variability is smeared into a red-noise back-ground. The depth-derived age-model does considerably better at resolving the 100KY and 41KY (obliquity) variability, but none the less has significant spectral smearing associated with the 23KY variability. Thus, if present, excess precession band variability is expected to be poorly resolved.

3.4.2 Comparison with other age-models

The $A^{(17)}$ age-model makes no assumptions about orbital control of climate, and thus provides independent age estimates to compare against the orbitally-tuned chronologies. Figure 3-7 shows the difference between $A^{(17)}$ and the orbitally derived age-models for the SPECMAP stack [*Imbrie et al.*, 1984] and the ODP677 benthic δ^{18}O record [*Shackleton et al.*, 1990]. The SPECMAP orbital age estimates beyond 625KY BP are generally considered too young—due to an incorrect B-M age [e.g. *Shackleton et al.*, 1990; *Singer and Pringle*, 1996], and ages beyond termination 7 for SPECMAP are adopted from the orbitally-tuned ODP677 chronology. There are up-to 2 KY differences between termination ages listed in *Imbrie et al.* [1984] and in Table 3.2 due to our use of the δ^{18}O midpoint in defining termination depths; also note there are typographical errors for the termination 5 and 7 ages in the *Imbrie et al.* [1984] table. Using the Table 3.2 ages, the root-mean-square (rms) event age discrepancies between the depth and orbital age-models are 3KY (SPECMAP) and 5KY (ODP677). Considering $A^{(17)}$ has an estimated uncertainty of ±9KY and SPECMAP one of ±5KY, the depth-derived chronology is consistent with the orbitally derived age estimates.

The depth-derived age estimate for termination 2 closely agrees with the orbitally-

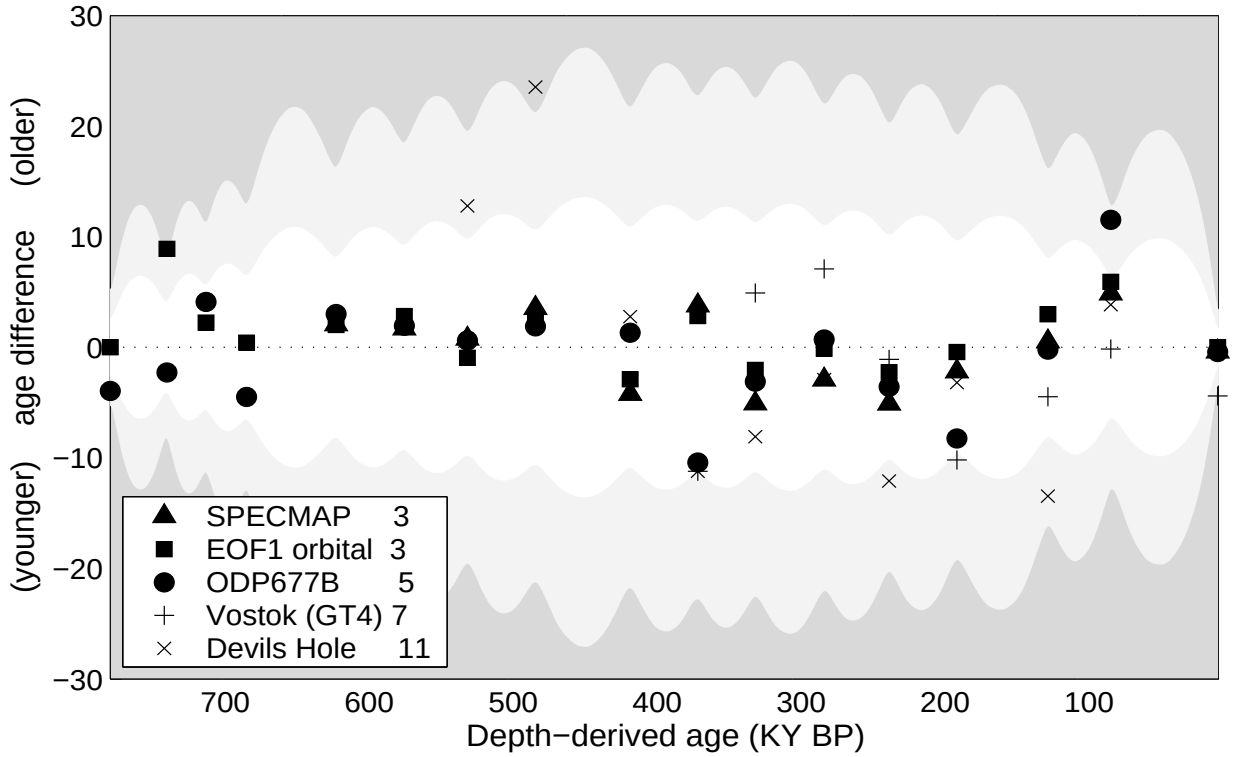

Figure 3-7: The $A^{(17)}$ depth-derived age-model relative to other δ^{18}O age-models. Negative values indicate the depth-derived age-model is relatively younger. Root-mean-square age-model differences are listed in the legend. Depth-derived ages are most consistent with the orbitally-derived age-estimates. The inner and outer gray clouds respectively indicate the one and two standard deviation depth-derived age-model uncertainty. Within two standard deviations, all age-models are consistent with the depth-derived ages.

derived age estimates (128KY BP), thus supporting the younger termination 2 radiometric age estimates [e.g. *Broecker*, 1968; *Bard*, 1990] over the older ages [e.g. *Gallup*, 2002; *Henderson and Slowey*, 2000]. Note, however, this conclusion is directly dependent upon the compaction correction which shifts the mean termination 2 age from 139 to 129KY BP (see Table 3 in Appendix A; at termination 2 uncertainties in the compaction correction are about ±4KY.) Using a depth-tuning approach, but not correcting for compaction, *Raymo* [1997] estimated an age of 136KY BP for termination 2 and concluded this age was anomalously old due to sediment extension in the upper core. In general, however, the magnitude of sediment extension is expected to increase down-core because of the greater changes in effective stress [*Moran*, 1995; *MacKillop et al.*, 1995]. Acting alone, greater extension with depth will give anomalously young ages. Anomalously old ages are more readily explained by a down-core increase in compaction. Because compaction is partially plastic [*Moran*, 1995], the post-coring sediment rebound does not fully compensate for compaction. If uncorrected, this residual trend in compaction leads to the anomalously old termination 2 ages (see Table 3).

Figure 3-7 also compares the Vostok deuterium (δD) ages [*Petit et al.*, 1999, GT-4 ice age] with the $\bar{A}^{(17)}$ event ages. Clearly, the δD of Antarctic ice (Vostok) and δ^{18}O need not have a simple relationship with marine foraminiferal δ^{18}O records. Nonetheless, the rms age deviation between GT-4 and $\bar{A}^{(17)}$ is only 6KY (events 2 through 8 only), and is within the expected uncertainty of the depth-derived age-model. More striking in Fig. $3-7$ is the tendency of some of the Devils Hole event dates to differ markedly from those of the deep-sea cores—beyond the one-sigma error estimates of both data types. Devils Hole has an rms age deviation with $\bar{A}^{(17)}$ (events 2 through 11) of 11KY where the depth-derived chronology is relatively younger between terminations 2 and 5, and older beyond termination 5. One should not infer from this result that either is incorrect: as noted, there is no necessity in the climate system for open ocean changes to be contemporaneous with those near-shore or over continents [*Winograd et al.*, 1997].

Of the available Pleistocene age-models, $\bar{A}^{(17)}$ most closely accords with the orbitally-tuned age estimates. Because the orbital and depth-derived age-models were estimated using completely independent assumptions, their approximate accord encourages the belief that there is real skill in both of them. Nonetheless, as we will see, the differences between them have important consequences for the interpretation of

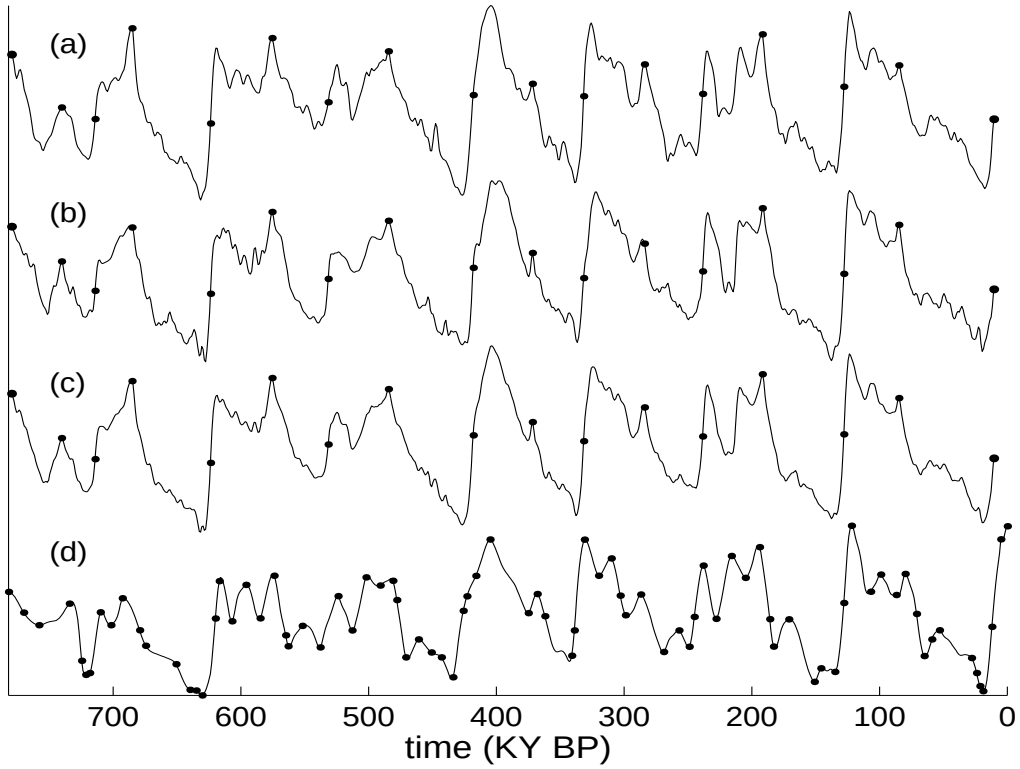

Figure 3-8: (a) The leading empirical orthogonal function of the five best resolved planktic records (EOFp) and (b) the five best resolved benthic records (EOFb). The squared cross-correlation between EOFb and EOFp is 0.89. (c) The leading EOF of both the best resolved benthic and planktic records (EOF1); each EOF is on the depth-derived age-model. (d) The SPECMAP stack on its orbitally-tuned age-model. The squared cross-correlation between the SPECMAP stack and EOF1 is 0.68, slightly higher than the correlation between SPECMAP and either EOFb or EOFp. Dots indicate the location of ACPs used for the depth-derived and SPECMAP stack age-models.

the climate record.

3.5 The δ^{18}O signal and nonlinear climate change

We now turn our attention away from the age-models and toward the δ^{18}O signal itself. To extract a well resolved and representative signal from the ensemble of 26 δ^{18}O records, the leading empirical orthogonal function (EOF1) is calculated from the five planktic and five benthic records with an accumulation rate of 3cm/KY or greater and the smallest available mean sampling interval (see Table 3.1). EOF1 explains 78% of the $\delta^{18}O$ variance and represents an almost uniformly weighted average of the ten

best-resolved δ^{18}O records, thus making it similar to a mean or "stacked" record. For comparison, the leading EOFs of the five best resolved benthic records (EOFb) and planktic records (EOFp) are also calculated (see Figure 3-8). EOFb and EOFp are very similar to EOF1: each has a squared cross-correlation with EOF1 of 0.97. The squared cross-correlation between EOFp and EOFb is 0.89, indicating the ubiquity of the oceanic $\delta^{18}O$ signal. Given these high correlations, it is not surprising that the spectral description of EOF1 presented in the following sections also holds for EOFb and EOFp.

Figure 3-8 shows EOF1 from $A^{(17)}$ and the SPECMAP δ^{18}O stack [*Imbrie et al.*, 1984] on its orbitally-tuned age-model. The SPECMAP age-model was constructed by imposing a constant phase relationship between the obliquity and precessional orbital parameters and the respective frequency bands in five separate δ^{18}O records [*Imbrie et al.*, 1984]. The five orbitally tuned δ^{18}O records were then averaged to form the stack. The initial discussion here compares EOF1 with the SPECMAP stack; afterward, for purposes of comparison, an orbitally-tuned version of EOF1 is also investigated.

The ten δ^{18}O records used in EOF1 are independent of the five SPECMAP stack records, yet the isotopic variations in the SPECMAP stack and EOF1 are strongly similar in timing, number, and amplitude. That there is only a 3KY rms age-model difference between the SPECMAP stack and EOF1 is rather remarkable. When pinned to their respective independent age-models, the squared correlation between EOF1 and SPECMAP is 0.68. This is a higher correlation than between the exclusively planktic SPECMAP stack and EOFp — even when the single high-latitude planktic record from ODP982 is excluded from EOFp.

3.5.1 The spectral description of the δ^{18}O record

The spectral distribution of the SPECMAP stack, shown in Figure 3-9, has a power law relationship with frequency, s^{-q}, $q \approx 2.7$ and spectral peaks lying above the approximate 95% level-of-no-significance in the 1/100, 1/41 (obliquity), 1/23 and 1/18KY (precession) bands relative to the background continuum. Bands are defined as the interval $\pm$1/400KY about the central frequency. The SPECMAP distribution of energy has been widely accepted as accurately representing long-period δ^{18}O variability [e.g. *Imbrie et al.*, 1993], with the spectral peaks in the obliquity and precession bands commonly interpreted as showing linear responses to the respec-

tive orbital variations [e.g. *Hagelberg et al.*, 1991]. Of course, this obliquity and precession prominence is assumed in the orbital-tuning. Note in particular that the energy fraction lying in the obliquity and precessional bands is a small fraction of the record total. The origins of the 100KY band variability are much more contentious owing to the paucity of insolation forcing in this band. Climatic resonance, nonlinear climatic response, and additional forcing mechanisms have all been postulated as explanations for the 100KY-band variability (for a review see *Elkibbi and Rial*, 2001). *Roe and Allen* [1999] point out the difficulty in differentiating among these competing 100KY-band orbital theories, and there is some doubt whether an orbital relationship exists at all [*Wunsch*, 2003a].

The depth-derived age-model provides a somewhat different perspective on δ^{18}O variability. The periodogram of EOF1, shown in Figure 3-9, has a power law, like that of the SPECMAP stack, with $q \approx 2.7$. But unlike the SPECMAP result six, rather than four, spectral bands are above the approximate 95% level-of-no-significance at 1/100, 1/70, 1/41, 1/29, 1/23, and 1/18KY. A simple relationship between the central frequencies, $s\,(n)$, of these bands is,

$$s(n) = \frac{1}{41} + \frac{n}{100}, \qquad -1 \leq n \leq 3. \tag{3.18}$$

$s(n)$ is written in terms of the 1/41KY band (obliquity) rather than the 1/23 or 1/18 bands (precession) because the 1/41KY band accounts for a greater fraction of the δ^{18}O variability.

The energy in the 1/100, 1/41 ($n = 0$), 1/23 and 1/18KY ($n = 2, 3$) bands has been much discussed. Excess energy near 1/70 and 1/29KY has also been noted in the literature [e.g. *Nobes et al.*, 1991; *Yiou et al.*, 1991; *Bolton and Maasch*, 1995; *Mix et al.*, 1995]. The simple rule embodied in Eq. 3.18 is strongly suggestive of a spectral structure resulting from a weak nonlinear interaction of the obliquity band with the 100KY band. The conventional interpretation, referred to as the "pacemaker" hypothesis [*Hays et al.*, 1976], requires that the timing of the very energetic quasi-100KY variability be controlled by the weaker high frequency elements. Here, it appears that the most energetic bands (100KY, 41KY) interact to produce sum and difference frequencies, as is typical of a weakly nonlinear system. A complication of the conclusion is the possibility that the enhanced precession band energy is due, all or in part, to overtones of the obliquity band response.

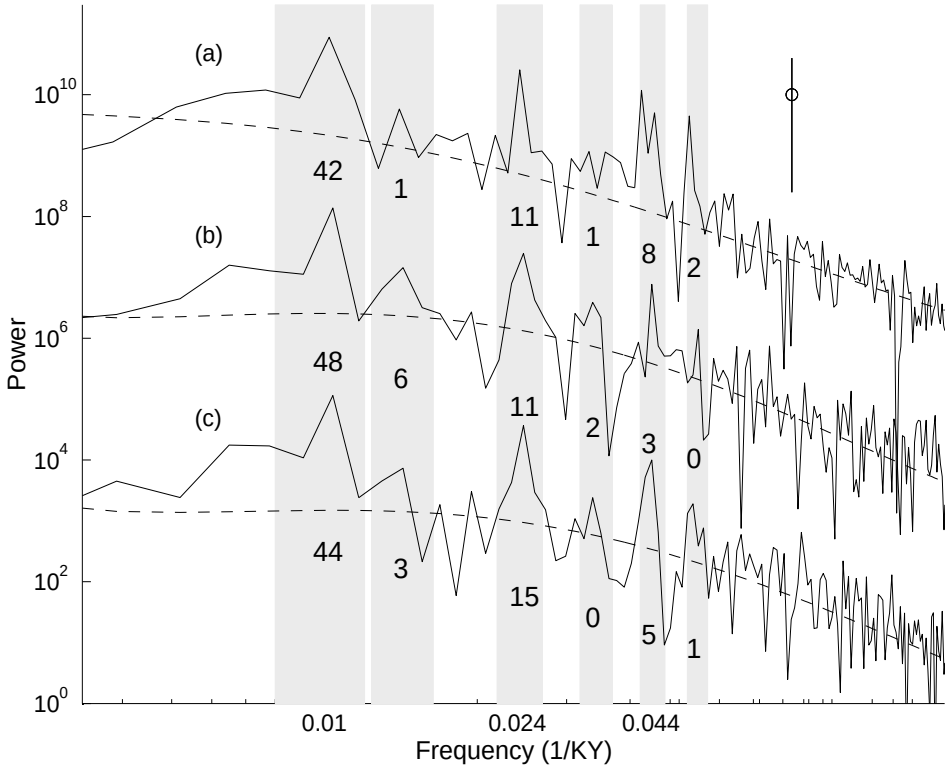

Figure 3-9: Periodograms are (a) SPECMAP, (b) EOF1, and (c) the orbitally-tuned EOF1. For presentation purposes each periodogram, after the first, is shifted downward by two orders of magnitude. Dashed lines are 3rd order polynomials fit to the noise background of each periodogram. Numbers within each band (1/100, 1/70, 1/41, 1/29, 1/23, and 1/18KY) are the energy above the background noise level as a fraction of the entire spectrum. The approximate 95% confidence interval (from χ^2 with two degrees-of-freedom) is indicated by the vertical bar in the upper right hand corner; the open circle represents the expected background level.

3.5.2 Higher-order spectral analysis

A higher-order statistic, the auto-bicoherence, aids in distinguishing the behaviors of EOF1 and the SPECMAP stack age-model. The 95% level-of-no-significance for auto-bicoherence—computed by Monte Carlo methods for Gaussian red noise with a power law of minus two—is 0.7 along the diagonal ($s_1 = s_2$) and 0.55 off the diagonal ($s_1 \neq s_2$). Appendix D discusses the auto-bicoherence test in more detail. Before examining auto-bicoherence in the δ^{18}O records, the nature of the possible forcing is investigated using a test signal,

$$T(t) = \theta(t) + p(t), \tag{3.19}$$

where θ is obliquity and p is precession as calculated by *Berger and Loutre* [1992]. Both components of $T(t)$ are normalized to have unit standard deviation and zero mean. Because the origins of the 100KY band are so uncertain, no corresponding forcing term is included. The completely deterministic $T(t)$ displays a number of significant auto-bicoherencies (see Figure 3-11) related to the amplitude and frequency modulations inherent to these orbital parameters [e.g. *Hinnov*, 2000]. The strong auto-bicoherence at (1/41,1/41) highlights the potentially ambiguous origins of the precession band; that is, the first harmonic of obliquity (2/41KY) and the precession band (1/23 to 1/18) overlap. Note that a rectification of the annual cycle is required for long-term precessional variability to appear in a record [*Rubincam*, 1994; *Huybers and Wunsch*, 2003], and that such rectification is also expected to generate harmonics of the obliquity energy.

Significant auto-bicoherence can indicate the presence of a nonlinearity in a record, or that the distribution is non-Gaussian, or both (nonlinear records are usually non-Gaussian). Here, $T(t)$ is non-Gaussian (it is deterministic). The distribution of the δ^{18}O record — shown as a histogram of δ^{18}O measurements from the 26 records shown in Table 1 — appears in Figure 3-10. The δ^{18}O signal has a skewness of -0.1 and a kurtosis of 2.5, clearly indicating its non-Gaussian nature and as with $T(t)$, interpretation of the auto-bicoherence must account for this fact.

The auto-bicoherences of EOF1 and the SPECMAP stack are shown in Figure 3-11. The SPECMAP estimate displays significant auto-bicoherence at frequency pairs (1/70,1/70), (1/70,1/41), and (1/41,1/29), a pattern which resembles that of $T(t)$, on which the chronology of SPECMAP is based. The SPECMAP auto-bicoherencies

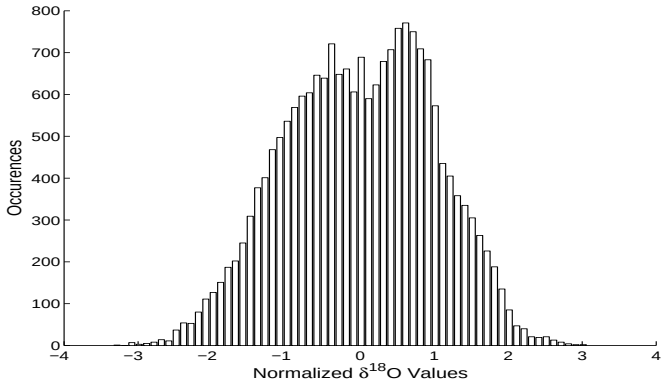

Figure 3-10: Histogram of δ^{18}O measurements between 10 to 780KY BP from the 26 records listed in Table 1.

which are most emphasized however, involve the 1/70 and 1/29KY bands, and unlike EOF1, these bands display no significant concentrations of energy. *Hagelberg et al.* [1991] also find evidence of a (1/80, 1/41) auto-bicoherence in the orbitally-tuned ODP 677 benthic and planktic δ^{18}O records, which given the coarseness of their frequency resolution, is indistinguishable from the SPECMAP (1/70, 1/41) pair.

EOF1 displays a gridded pattern of auto-bicoherencies: all combinations of frequencies in Eq. 3.18 with integers $-1 \leq n \leq 2$ are coincident with significant local maxima in auto-bicoherence except for $(1/29, 1/29)$ and $(1/23, 1/23)$. Whether the auto-bicoherence arises from non-Gaussian statistics in the forcing, or nonlinearity in the response, its distinct frequency structure supports the inference of weak inter-band interaction within the climate system. The absence of bicoherence at the strongest precession band $(1/23, 1/23)$ points to obliquity's central role in this coupling.

3.5.3 The importance of age-models

There are important differences between EOF1 and the SPECMAP $\delta^{18}O$ stack: SPECMAP has more than three times the energy concentrated within the precession band but no discernible concentration of energy at 1/70 and 1/27KY; furthermore the auto-bicoherent features are significantly different. The small amount of precession band energy in EOF1 may be a result of age-model jitter (see Figure 3-6). We attribute the remaining differences to the orbital tuning of the SPECMAP age-model; support for this hypothesis is provided by considering the effects of jittering SPECMAP and orbitally-tuning EOF1.

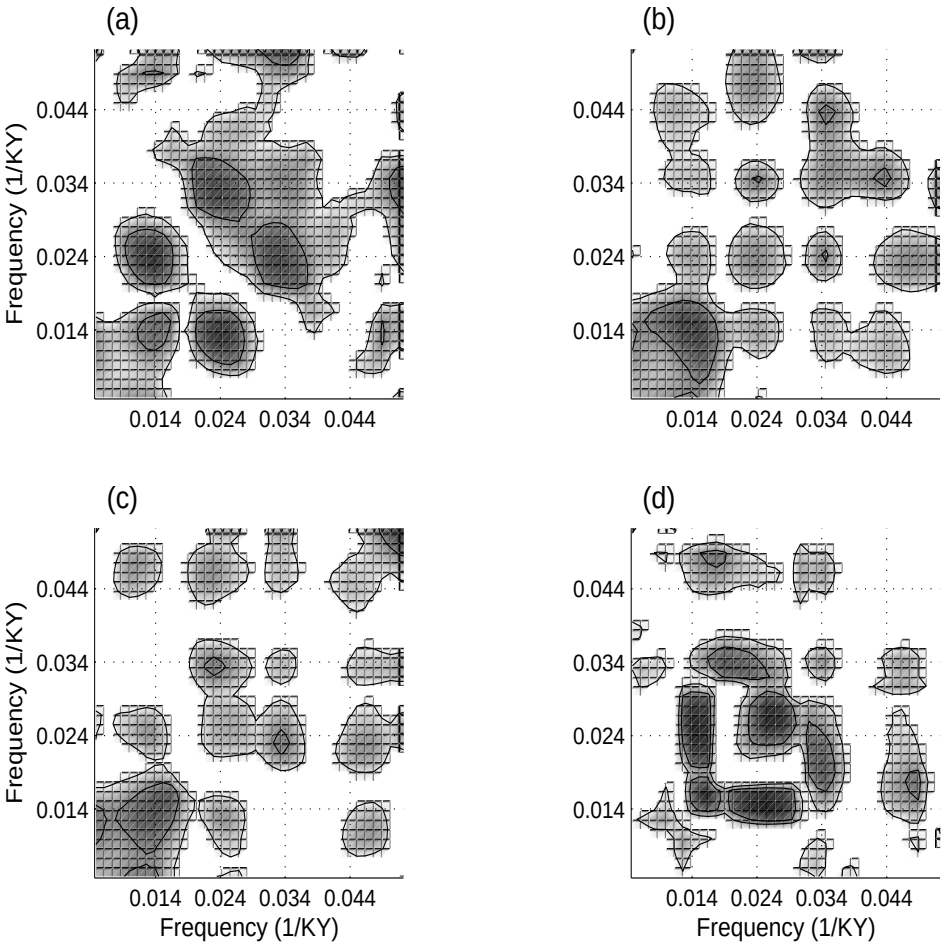

Figure 3-11: Auto-bicoherence of (a) SPECMAP, (b) EOF1, (c) orbitally-tuned EOF1, and (d) the orbital test signal, $T(t)$. The tick marks on the frequency axes are given by Eq. 3.18. Contour intervals are at 0.5 and 0.7 — respectively the 95% level-of-no-significance for off-diagonal and diagonal features.

Monte Carlo simulations indicate that random age-model errors tend to diminish both concentrations of spectral energy and auto-bicoherence, making such errors an unlikely explanation for the structure in EOF1. Quasi-periodic age-model errors, however, can create spurious structure in spectral estimates [see Section 4.1; *Herbert*, 1994]. To examine this possibility, the spectral and auto-bicoherence structures of SPECMAP were examined after distorting the age-model using periodic and quasi-periodic functions. The most relevant results occur for 100KY periodic distortions of the SPECMAP age-model, yielding significant concentrations of energy at the 1/70 and 1/27KY bands. Similarly, distorting SPECMAP ages in proportion to the $\delta^{18}O$ signal yields a concentration of energy at 1/70KY. All of these age-model errors, however, tend to decrease auto-bicoherence without making the pattern appear more like that of EOF1.

On the other hand, in Appendix C, we show that the orbital tuning of EOF1 makes its spectra and auto-bicoherence pattern appear more similar to the SPECMAP stack. It is further demonstrated, using synthetic signals, that orbital tuning tends to suppress evidence of weak nonlinearity in a record, by shifting energy out of overtone and interaction bands and into the Milankovitch bands. We thus conclude that orbital tuning tends to suppress evidence of real nonlinearity in the $\delta^{18}O$ record.

3.6 Conclusions

Age-models assigned to paleo-climatic records strongly influence the inferences drawn about past climate behavior. Variations in sediment accumulation rate cause errors in linear age-depth models, so that a simple linear age-depth relationship is often not sufficiently accurate to yield meaningful results. Use of orbital-tuning to remove these age-model errors, however, suppresses evidence of nonlinearity at low frequencies in the system.

An alternative to orbital-tuning is to estimate sediment core age using spatial mean sediment accumulation rates, and in conjunction with an important compaction correction, this alternative is used at 21 core sites to construct a depth-derived age-model spanning the last 780KY. The observed error in linear age-depth relationships is modeled as an autocorrelated stochastic process, and the $A^{(17)}$ age-model is estimated to be accurate to within ±9KY. The depth-derived ages make no assumptions regarding orbital control, but agree with the orbitally-tuned age-models to within

±5KY, and thus within the error limits are consistent with one another. The remaining discrepancies, however, have important consequences.

Spectral analysis of EOF1, using the $A^{(17)}$ age-model, indicates significant spectral energy at combination tones of the 1/100KY and obliquity bands. There is also significant auto-bicoherence between each of these bands in EOF1, all of which indicates a weakly nonlinear climatic response to obliquity forcing interacting with the quasi-100KY variability. These results may aid in differentiating between the various mechanisms proposed to explain glacial inter-glacial climate variability.

3.7 Appendix

3.7.1 Compaction correction

Sediment compaction is, to first order, a function of pressure and lithology [e.g. *Athy*, 1930; *Baldwin and Butler*, 1984]; factors such as time, temperature, and porewater chemistry [e.g. *Tada*, 1991] are generally secondary. Because pressure increases with depth, systematic down-core compaction is expected, and this phenomenon is observed in a wide variety of marine cores [e.g. *Baldwin and Butler*, 1984; *Bahr et al.*, 2001]. Post-coring sediment rebound partially compensates for in-situ compaction, but because compaction is more plastic at higher pressure [e.g. *Moran*, 1995], residual down-core trends towards greater compaction are retained. Variations in lithology can also modify the compaction profile, for instance clay deposited above limestone can lead to reduced compaction with depth [e.g. *Schwarzacher*, 1975], but there is no reason to expect such structures to be systematically present in the global array of cores studied here. Climatically driven quasi-periodic changes in compaction are addressed in Sections 4.1 and 5.3.

The effect of compaction on linear age-depth relationships is discussed qualitatively by *Hays et al.* [1976], *Williams et al.* [1988], and *Raymo* [1997]. Here, a quantitative age correction function is developed for gross trends in compaction and then applied to the depth-scale of each core. *Athy* [1930] first showed an increasing load on porous sediment results in pore water draining from the sediment matrix and an exponentially decreasing porosity. Porosity, ϕ, is the fraction of sediment volume occupied by water,

$$\phi = 1 - \frac{\rho}{\rho_{\mathrm{d}}}, \tag{3.20}$$

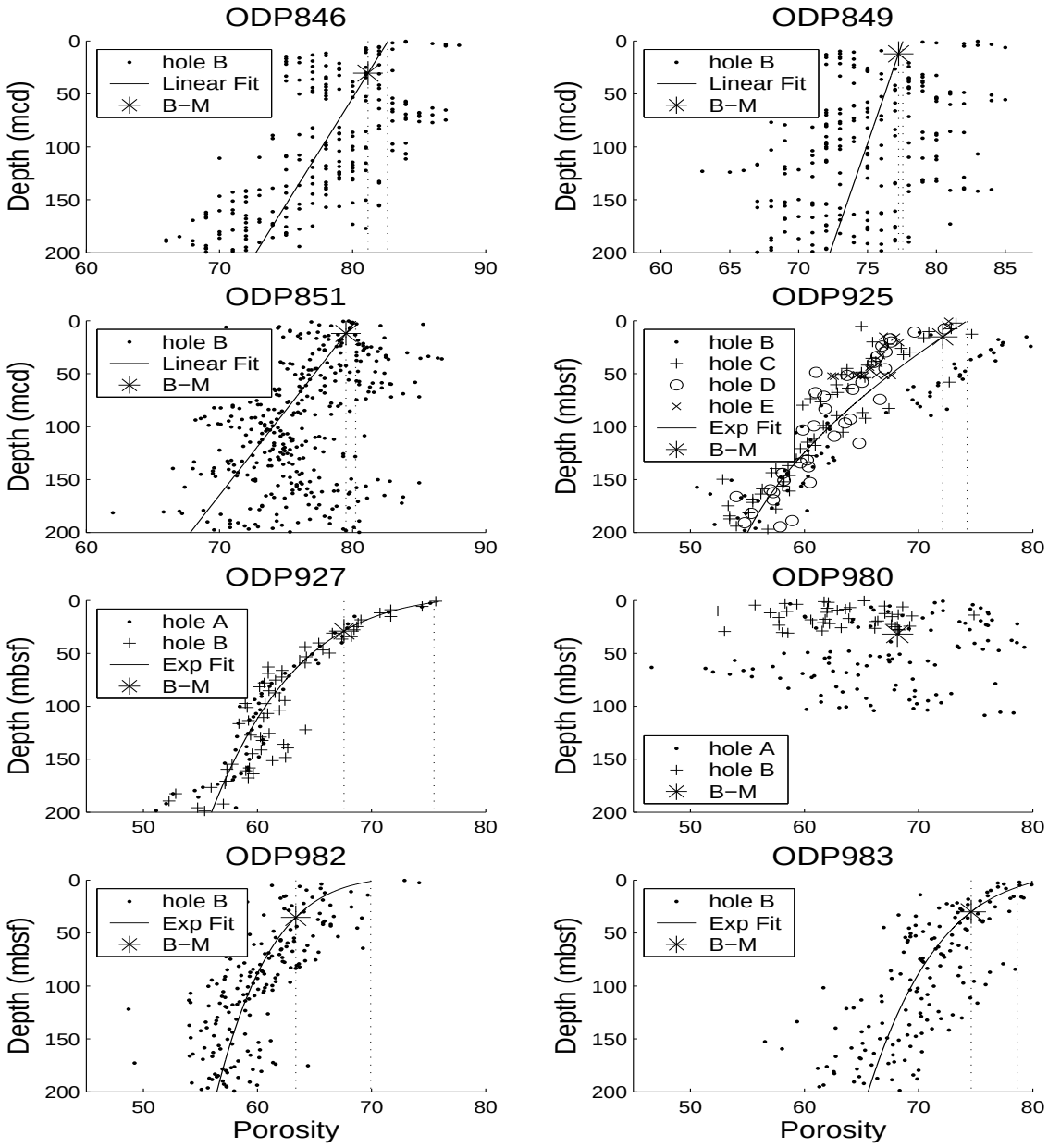

Figure 3-12: Changing porosity with depth in ODP cores from the E. Equatorial Pacific, Ceara Rise, and N. Atlantic. An exponential curve or straight line (whichever is better) was fit to each porosity profile, except for ODP980 which showed no distinct pattern. The vertical dotted lines bound the change in porosity between Termination 1 and the B-M.

where ρ is the bulk density, and ρ_{d} is the dry density.

Given a functional relationship between depth and porosity, it is possible to estimate the effects of compaction on a linear age-model. Take $h = 0$ and $t = 0$ as the sediment height and date of the B-M magnetic reversal. Sediment accumulates at a rate S so that,

$$h = \int_0^t S(t)dt, \tag{3.21}$$

and without compaction, the final height would be, $H = \bar{S}T$. $\bar{S}$ is the mean accumulation rate, H and T are the final-time values of h and t.

If compaction is assumed to result solely in the upward expulsion of pore water [e.g. *Berner*, 1980], the compacted and un-compacted sediment column heights are related by,

$$h = \int_0^{h'} \frac{1-\phi'}{1-\phi} dh', \tag{3.22}$$

where primes indicate the compacted quantity. For the moment, assume post-depositional compaction is present, but accumulation rates are constant. Then, if age is taken to be linear with depth between $h = 0$ and $h = H$, an error is incurred as,

$$\delta t = t' - t = T\left(\frac{h}{H} - \frac{h'}{H'}\right). \tag{3.23}$$

The age error is zero at the top, $h = H, h' = H'$, and bottom, $h = h' = 0$, but between these fixed points errors occur to the degree that h' is a nonlinear function of time. If compaction increases with depth, as expected, a layer of sediment between the top and bottom has $h/H > h'/H'$, $\delta t > 0$, and compacted age estimates which are erroneously old.

To illustrate the possible effects of compaction on an age-model, assume that ϕ is constant and that compaction occurs at a linear rate with depth, c, such that $\phi' = \phi - c(H' - h')$. Inserting this porosity relationship into Eq. 3.22 and integrating yields

$$h = h' + \frac{ch'}{(1-\phi)}\left(H' - \frac{h'}{2}\right). \tag{3.24}$$

Substituting Eq. 3.24 into Eq. 3.23 and writing $h' = Ht'/T'$ gives,

$$\delta t = t'\left(\frac{1-\phi+cH'(1-t'/(2T))}{1-\phi+cH'/2} - 1\right). \tag{3.25}$$

Plausible values for Eq. 3.25 are $\phi = 0.7$, c =.001m/m, H' =30m, and T =800KY,

yielding a maximum age-offset, $\delta t = 9$KY at 400KY BP. Eq. 3.25 shows that offsets toward older ages will increase with greater porosity, compaction, and accumulation rate.

Figure 3-12 shows the porosity profile plotted against depth for eight ODP cores located in the eastern equatorial Pacific [ODP846, 849, and 851; Leg 138 ODP Initial Reports CD-ROM], Ceara Rise [ODP925 and 927; Leg 154 Log and Core Data CD-ROM, Borehole Research Group, LDO], and the N. Atlantic regions [ODP980, 982, and 983; Leg 162 Log and Core Data CD-ROM, Borehole Research Group, LDO] measured using gravimetric techniques [*Boyce*, 1976]. The Eastern Equatorial Pacific group shows a general trend of decreasing porosity with depth superimposed on a large degree of scatter where the scatter is in-part attributable to variations in lithology, coring effects, and measurement error.

For the eight cores in which data are available, porosity trends are estimated from 400 meters below the sea floor to the core top. For the Eastern Equatorial Pacific cores, a line is fit to each porosity profile, and for the Ceara Rise and North Atlantic cores a second order exponential is used. ODP980 was alone in showing no discernible trend. Assuming that the estimated trends in porosity reflect inhomogeneities in relative compaction, we apply a compaction correction based on conservation of dry sediment volume [e.g. *Berner*, 1980],

$$h(1-\phi) = h'(1-\phi'). \tag{3.26}$$

Here, the thickness of a compacted sediment layer, h', is adjusted to thickness, h, by adjusting the down-core trend in porosity, $\phi'(h')$, to a constant value, ϕ. Note, the depth-derived ages are insensitive to the choice of reference porosity, ϕ, because they are pinned to a constant age at termination 1 and the B-M.

Although it is highly likely that trends in compaction exists at all, or most, of the core sites [e.g. *Bahr et al.*, 2001], the compaction correction has considerable uncertainty for the thirteen sites at which porosity measurements are not available. Standard decompaction formula are only applicable at depths well below that of the B-M [*Baldwin and Butler*, 1984; *Bahr et al.*, 2001] (greater than 200m), and we choose to use the mean of the seven identified porosity trends (see Fig. 3-12) as the basis for decompacting the remaining fourteen cores according to Eq. 3.26, to include ODP980. To estimate the associated uncertainty, each of the fourteen cores are also decompacted using the individual porosity-depth trends, yielding seven estimates of

event	17	16	15	14	13	12	11	10	9	8	7	6	5	4	3	2	1
	19.1	18.3	VIII	17.1	VII	15.1	VI	13.11	V	11.1	IV	8.5	III	7.1	II	5.1	I
dsdp502P	0	2	4	5	8	9	10	11	12	12	12	11	10	8	6	3	0
dsdp552B	0	2	4	5	8	10	10	11	12	12	11	11	11	9	7	4	0
dsdp607B	0	3	5	7	11	14	15	16	17	17	17	17	15	14	11	8	0
md900963P	0	2	3	5	8	11	13	16	17	18	19	19	18	17	14	8	0
odp659B	0	3	4	6	6	9	11	12	13	14	15	14	13	12	9	5	0
odp663P	0	3	5	7	10	12	14	15	17	17	17	17	16	15	11	8	0
odp664B	0	3	6	7	11	12	14	15	16	17	17	17	15	13	10	7	0
odp677B	0	3	5	6	10	12	14	15	17	17	17	17	16	14	12	9	0
odp677P	0	4	5	7	10	13	14	15	17	17	17	17	16	14	12	9	0
odp758B	0	2	3	4	6	7	8	9	10	10	10	11	10	9	8	6	0
odp758P	0	2	2	4	5	7	8	9	10	10	10	10	10	9	8	6	0
odp806B	0	1	2	4	7	9	10	11	12	13	13	12	11	10	7	5	0
odp806P	0	1	3	4	7	9	10	11	12	12	12	12	11	9	7	4	0
odp846B	0	2	3	3	5	5	6	7	7	7	7	7	7	6	4	3	0
odp849B	0	0	1	1	1	2	2	2	2	2	2	2	2	2	1	1	0
odp851P	0	0	1	2	3	3	4	4	4	4	4	4	3	3	2	2	0
odp925B	0	5	7	9	15	20	22	24	29	30	30	30	28	26	20	13	0
odp927B	0	5	7	10	14	17	20	22	25	26	27	27	26	24	18	14	0
odp927P	0	5	7	9	15	17	20	22	26	26	27	27	26	24	18	14	0
odp980B	0	3	4	5	12	15	17	19	22	25	25	25	24	22	17	12	0
odp982B	0	2	3	5	8	9	10	12	13	12	12	11	10	8	6	5	0
odp982P	0	1	3	4	7	9	10	11	13	12	12	11	10	8	6	5	0
odp983B	0	5	6	10	16	21	25	28	30	31	31	30	28	24	19	15	0
v22-174P	0	2	3	5	7	8	10	11	11	11	11	11	11	10	8	6	0
v28-238P	0	2	3	4	5	6	8	9	10	10	11	10	10	9	6	4	0
v28-239P	0	1	2	3	5	6	6	7	7	7	7	7	6	6	4	2	0
mean	0	3	4	5	8	10	12	13	15	15	15	15	14	13	10	7	0
σ	0	1	2	2	3	4	4	5	5	6	6	6	5	5	4	3	0

Table 3.3: The de-compacted age corrections in KY applied to each core where all age corrections produce a relatively younger age-model. Event numbers are listed at top along with the associated stage (Arabic) and termination (Roman) numbers. At bottom are the mean correction and the associated uncertainty. The applied corrections are a continuous function of depth, but are listed only at the 17 selected events.

decompacted depth. Age is then estimated from each realization of the decompacted depth-scale according to Eq 3.13, and the standard deviation of these ages is taken as the estimated uncertainty.

Table 3.3 lists the age correction resulting from de-compaction at each event for each δ^{18}O record and the uncertainty in the mean age off-set. All corrections make the δ^{18}O events relatively younger and range from zero at the endpoints to 15 KY at 350KY BP. While uncertainties range up-to 6 KY, they are always less than half the magnitude of the estimated bias, and thus decompaction is inferred to significantly improve the accuracy of the depth-derived age estimates.

3.7.2 The XCM tuning algorithm

A simple and repeatable algorithm, termed XCM (cross-correlation maximizer), is used for objective tuning. In common with most such methods [e.g. *Martinson et al.*, 1982; *Bruggerman*, 1992; *Lisiecki and Lisiecki*, 2002], the algorithm adjusts the timescale of a record, $\psi(t')$, in relation to a target record, $\tau(t)$, while seeking to

maximize a given quantity; in this case, the squared cross-correlation coefficient

$$r^2 = \left(\frac{\sum_t \psi(t' + \mu(t'))\tau(t)}{\sqrt{\sum_t \psi(t' + \mu(t'))^2}\sqrt{\sum_t \tau(t)^2}} \right)^2 . \tag{3.27}$$

Here $\mu(t')$ is the time adjustment function. For the applications presented in this paper, $\tau\,(t')$ and $\psi(t')$ are discretely sampled at 1-KY intervals and age control points (ACPs) are assigned to $\psi(t')$ at specified intervals. A simulated annealing optimization method [*Press et al.*, 1999] is then applied to estimate the arrangement of ACPs which maximizes the cross-correlation. To prevent unrealistic changes in implied accumulation rates, XCM may be constrained to not stretch or squeeze time beyond a specified factor. The final control-point arrangement provides a piecewise linear approximation to $\mu(t')$. It should be noted that XCM may significantly increase the cross-correlation between two records without there being any true relationship (see Appendix C).

Most tuning algorithms employ narrow-band-pass filtering to isolate the Milankovitch band of interest. A difficulty with this approach is that even slight errors in the preliminary age-model can smear spectral energy across the entire frequency range [e.g. *Martinson et al.*, 1987]. This mistiming results in a form of aliasing of the spectral power, and like all aliasing, no filter can undo it. Thus we have chosen not to filter records prior to tuning, and instead use what is termed the direct response approach [*Martinson et al.*, 1987].

3.7.3 The impact of orbital-tuning

If climate linearly responds to insolation variations, one would expect the modulation structure of the forcing to be at least qualitatively mimicked in the response. If one seeks to tune to precession, this assumption is immediately complicated by the requirement for a rectifier to be present [*Rubincam*, 1984; *Huybers and Wunsch*, 2003]. Nonetheless, assuming some climatic response to insolation forcing, a multitude of methods have been used to orbitally-tune paleo-climatic records. The criteria generally used to assess the accuracy of an orbitally-tuned timescale [e.g. *Imbrie et al.*, 1984; *Bruggerman*, 1992; *Shackleton et al.*, 1995] are that geochronological data should be respected within their estimated accuracies, sedimentation rates remain plausible, variance should become concentrated at the Milankovitch frequencies with

a high coherency between the orbital signal and the data, and – what is often referred to as the clinching argument – similar amplitude modulation should appear in the Milankovitch derived insolation functions and in the orbitally-tuned result.

To comply with the criteria for a successful orbital-tuning result, the XCM algorithm is constrained to not stretch or squeeze a record by more than a factor of four, thus keeping accumulation rates within plausible levels. Considering the difficulty of determining geochronological dates in the interval between termination two (approximately 130KY BP) and the Brunhes-Matuyama (B-M) boundary (approximately 780KY BP), it seems unlikely the available geochronological constraints would conflict with most tuning results. Three signals are selected to demonstrate the impact of orbital-tuning: EOF1, white-noise, and a weakly nonlinear signal.

EOF1

The selected target curve for orbitally-tuning EOF1 is,

$$\tau(t) = \sqrt{.2}\theta'(t) + \sqrt{.8}p'(t). \tag{3.28}$$

The primes indicate the phases of obliquity and precession are each phase-lagged assuming a linear response with a time constant of 17KY, consistent with the orbital target curves of *Imbrie et al.* [1984]. Rather than iteratively tuning to precession and obliquity respectively, as done by the SPECMAP group, the two parameters are combined into a single target curve, $\tau(t)$, with precession accounting for 80% of the total variance. ACPs are assigned to the $A^{(17)}$ age-model every eight KY, and XCM was used to maximize the cross-correlation between EOF1 and $\tau(t)$.

The difference between the $A^{(17)}$ and the fully orbitally-tuned EOF1 age-model is shown in Figure 3-7. Not surprisingly, orbital-tuning brings $A^{(17)}$ into close agreement with the SPECMAP and orbital ODP677 age-models. The periodogram (Figure 3-9c) and auto-bicoherence (Figure 3-11c) of the orbitally-tuned EOF1 now resemble those from SPECMAP. In particular, orbital-tuning enhances the obliquity and precession peaks in EOF1 while diminishing the 1/29 and 1/70KY spectral peaks and making the (1/70,1/29) and (1/41,1/41KY) auto-bicoherence appear insignificant. The spectrum of EOF1 is sensitive to the process of orbital-tuning, and assuming a linear response to obliquity and precession imposes a behavior consistent with the SPECMAP analysis.

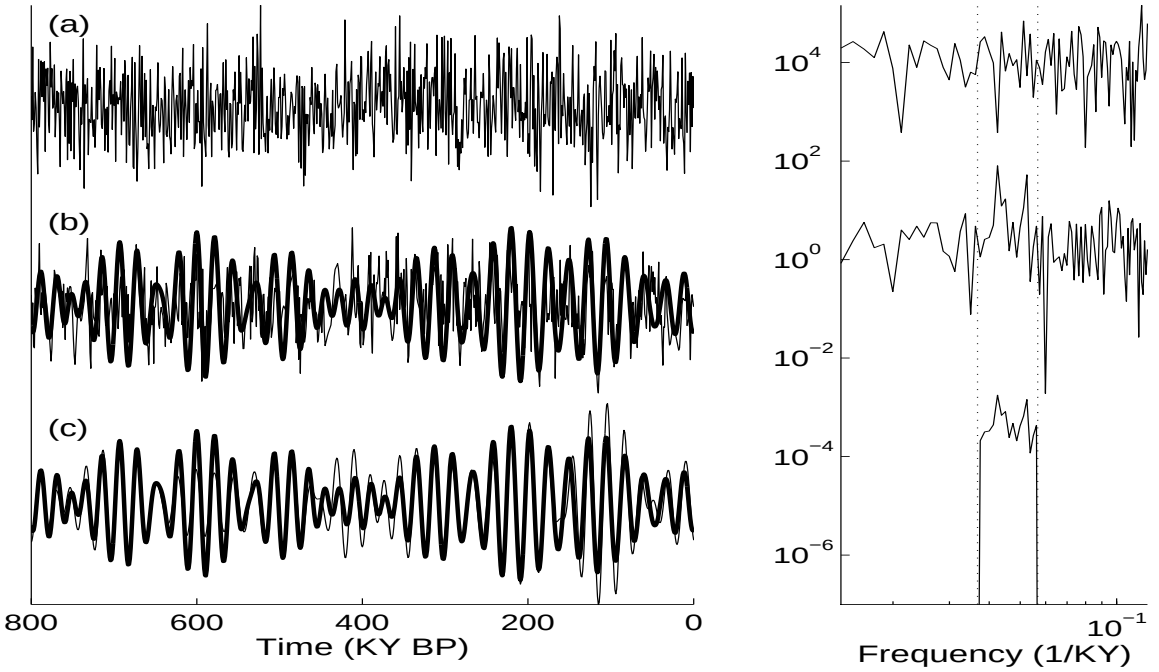

Figure 3-13: Results from the orbital tuning of white noise. Top left panel shows time series of white noise. Middle left panel shows the precession curve (thick line) and same white noise process tuned to precession (thin line). Lower left panel displays the band-pass filtered, tuned white noise (thin line), and the precession curve. Note that the band-pass filtered white noise shows an amplitude modulation similar to the precession curve. Right panel displays the power density spectra of the original white noise (top), of the tuned white noise (middle) and of the band-pass filtered tuned white noise (bottom). These spectra are displaced in the vertical by a factor of 10^4 for visual clarity, and the vertical dotted lines delineate the precession band, 1/23 to 1/18 KY.

Noise

It is also useful to investigate signals with known statistical properties. We begin with a white noise Gaussian distributed process, $\psi(t')$, and tune it to the precession parameter [*Berger and Loutre*, 1992] over a 800KY period. A typical realization of XCM tuning is presented in Figure 3-13 where the squared cross-correlation is increased from zero to 0.19. Consistent with the results of *Neeman* [1993], a concentration of variance at the triplet of precessional peaks occurs, coherence in the precession band is greater than 0.9 (0.65 is the approximate 95% level-of-no-significance), and both amplitude and frequency modulation similar to the precession parameter appears — completely spuriously. When band-pass filtered, the imposed frequency modulations

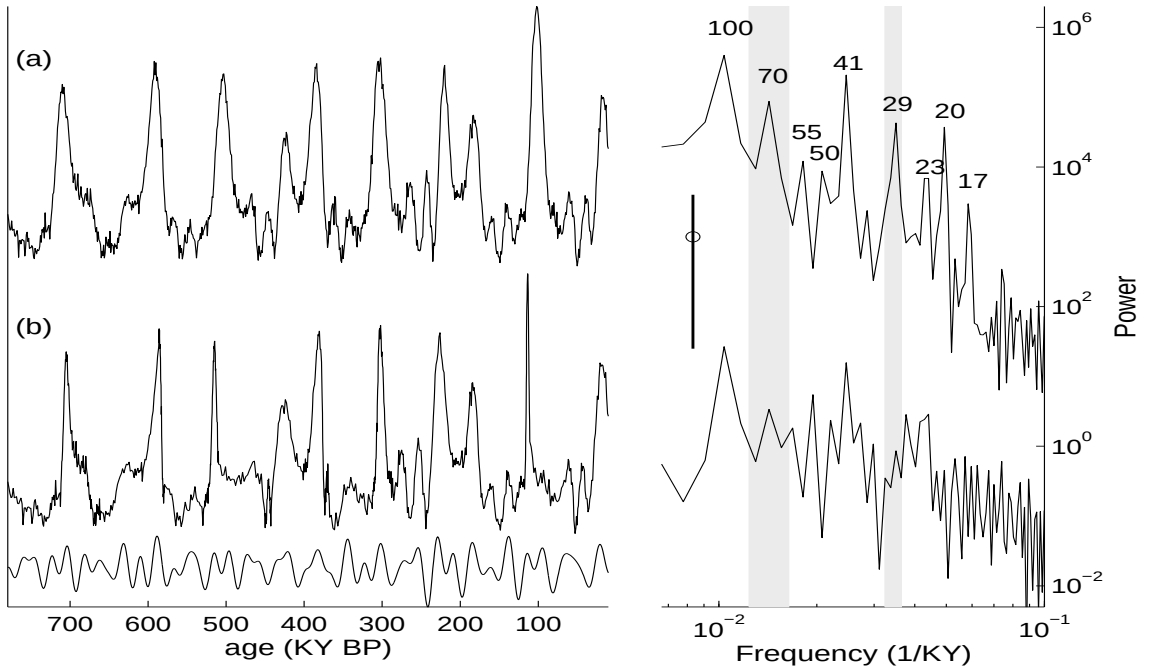

Figure 3-14: (a) The orbital signal $\psi(t)$ from Eq 3.29 (left) and its associated periodogram (right). The linear components of $\psi(t)$ give spectral peaks at 1/100; 1/55, a side-band of obliquity; and 1/41KY, the main obliquity band. The nonlinear components give spectral peaks at 1/70, the 1/100-1/41 combination tone; 1/50, the 2/100 overtone; 1/29, the 1/100+1/41 combination tone; 1/23, an interaction tone; 1/21, the 2/41 overtone; and 1/17KY, another interaction tone. (b) After a small degree of orbital-tuning, assuming a linear response to obliquity and precession (bottom curve), the signal is visually similar but the periodogram has concentrations of energy primarily at the 100KY, obliquity, and precession bands. The approximate 95% confidence interval for red-noise is indicated by the vertical bar.

produce the visual amplitude modulation in the tuned signal [see *Huybers*, 2002]. Similar results hold when red-noise, rather than white-noise, is orbitally-tuned. Thus precession-like amplitude modulation in an orbitally-tuned record does not guarantee the accuracy of an age-model.

A nonlinear signal

Finally, the observations regarding EOF1 in Section 5 motivate investigation of another signal,

$$\psi(t) = 2\cos(2\pi t/100) + \theta(t) + 0.5\left(\cos(2\pi t/100) + \theta(t)\right)^2, \tag{3.29}$$

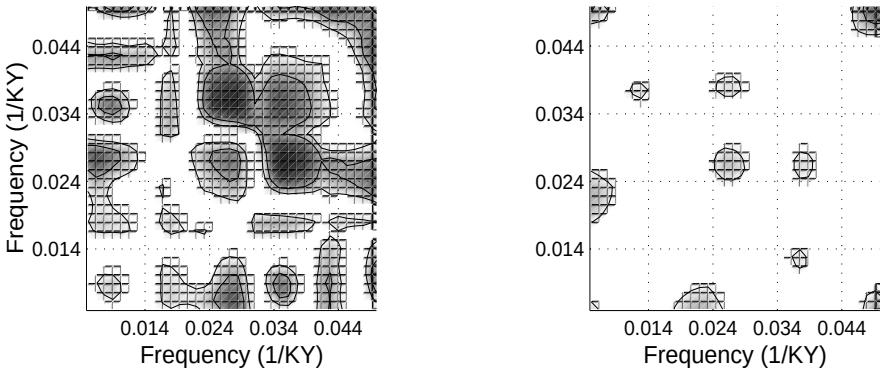

Figure 3-15: The auto-bicoherence of $\psi(t)$ before (left) and after (right) orbital-tuning. Significant auto-bicoherence is indicated by light-shading for the off-diagonal and dark-shading for the on-diagonal.

involving linear and nonlinear contributions from a 100KY harmonic and zero-mean unit variance obliquity variability. The relative amplitudes are selected to reflect the distribution of variance observed in EOF1, and for statistical stability, a small amount of white noise is added. As evident from the periodogram in Figure 3-15, the nonlinearity generates variability at a number of combination and over-tones. A potentially confusing result is that energy appears at the first overtone of the main obliquity band 1/21KY, and, because of the frequency and amplitude modulation inherent to obliquity, at interaction bands of 1/23 and 1/17KY. Without knowing the form of $\psi(t)$, a triplet of spectral peaks at these frequencies could readily be mistaken for evidence of precession variability.

Figure 3-14 also shows $\psi(t')$ after orbital-tuning to the target curve, $\tau(t)$, given in Eq. 3.28. Typical results increase the squared cross-correlation between the target curve and ψ from 0.1 to 0.25. After tuning, the nonlinear spectral peaks are suppressed while precession period variability is enhanced. Similarly, figure 3-15 shows that the auto-bicoherent structure of $\psi(t)$ is almost totally obscured by the orbital-tuning, all of which indicates that orbital-tuning will suppress evidence of real nonlinearity.

3.7.4 Auto-bicoherence

A test for quadratic coupling was presented by *Hasselmann et al.* [1963] and used to evaluate weak nonlinearities in shallow water wave propagation. When two harmon-

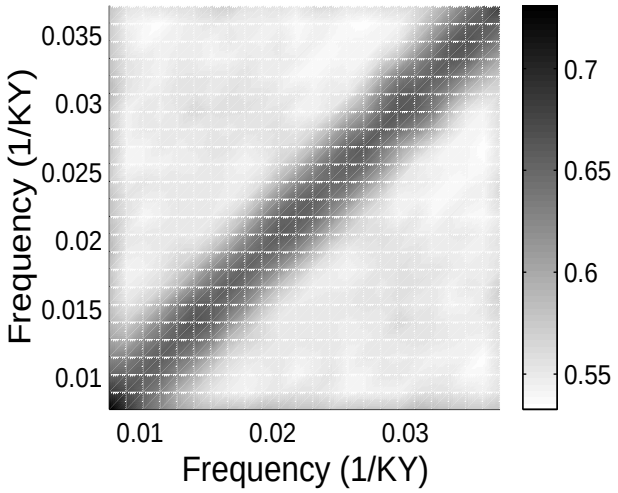

Figure 3-16: Results of a Monte Carlo estimate indicating the approximate level below which 95% of auto-bicoherence estimates, made using Gaussian red noise, are expected to occur by chance. The results are symmetric about the diagonal, and values are about .55 for $k \neq l$ and .7 for $k = l$.

ics are coupled so as to modulate one another, a third harmonic with a particular frequency and phase is expected,

$$S(t) = e^{2\pi i f_k t + \phi_k} e^{2\pi i f_l t + \phi_l} = e^{2\pi i (f_k + f_l) t + \phi_k + \phi_l}.$$

To test for this relationship define the bispectrum as

$$B_{k,l} = < \hat{S}_k \hat{S}_l \hat{S}^*_{k+l} >$$

where $\hat{S}_k$ is the discrete Fourier transform of $S(t)$ at frequency k, S^* is the conjugate ($S^*_{k+l} = S_{-k-l}$), and $<>$ indicates the expected value. Unless $\phi_{k+l} = -(\phi_k + \phi_l)$, $B(k,l)$ will be complex. The magnitude of $B(k,l)$ depends on both the magnitude of the complex Fourier coefficients, $|\hat{S}_k||\hat{S}_l||\hat{S}_{k+l}|$, and the stability of the phase relationship between the coefficients; i.e. for random phasing $< \hat{S}_k \hat{S}_l \hat{S}_{k+l} >= 0$. The auto-bicoherence is defined as,

$$C_{k,l} = \frac{< \hat{S}_k \hat{S}_l \hat{S}_{k+l} >}{< |\hat{S}_k||\hat{S}_l||\hat{S}_{k+l}| >}$$

where the denominator represents $B(k,l)$ for the case of perfect phase coherence, and $0 \leq C_{k,l} \leq 1$. The expected value of the auto-bicoherence is estimated here by adapting the bispectral routine presented by *Muller and MacDonald* [2000]. The algorithm consists of subtracting the mean value of $S(t)$, applying a Hanning window, and estimating the auto-bicoherence as

$$C_{k,l} = \frac{|\sum_{k-2}^{k+2}\sum_{l-2}^{l+2} a_{k,l}\hat{S}_k\hat{S}_l\hat{S}_{k+l}|}{\sum_{k-2}^{k+2}\sum_{l-2}^{l+2} a_{k,l}|\hat{S}_k||\hat{S}_l||\hat{S}_{k+l}|},$$
$$a_{k+n,l+m} = \frac{1}{\sqrt{(k-n)^2+(l-m)^2}}, \quad n,m \in \{-2,-1,1,2\}, \quad a_{k,l} = 1,$$

where $a_{k,l}$ is a weighting coefficient. A Monte Carlo method was used to estimate uncertainty levels for auto-bicoherence computed according to the above algorithm. Figure 3-16 shows the approximate 95% level-of-no-significance to reject the null hypothesis of Gaussian distributed red noise; levels are roughly .55 for $k \neq l$ and .7 for $k = l$. A significant auto-bicoherence can also indicate the presence of a non-Gaussian signal, thus care is required in interpreting the result.

3.7.5 Averaging Geophysical Records with Uncertain Age-Models

This final appendix in Chapter 3 was not included in the original paper of Huybers and Wunsch [2004].

An understanding of the impacts of age-model error in geophysical analysis is emerging [e.g. *Moore and Thomson*, 1991; *McMillan et al.*, 2002], but there remains a strong potential for bias in statistical tests which do not account for age-model errors or assumptions built into the age estimate. In Chapter 3, for example, it was shown that a narrow-band spectral peak subject to random age-model error (jitter) has a substantial fraction of its narrow-band energy dispersed over a wide frequency range. In this note, the influence of jitter on averaging, or stacking, geophysical records is explored. Forming an averaged record is useful for suppressing noise and enhancing the signal common to a number of records[1] [e.g. for the marine $\delta^{18}O$ record, *Imbrie et al.* 1984; *Karner et al.*, 2002; *Huybers and Wunsch*, 2004]. However, when the relative ages have errors — referred to as synchronization jitter — both the noise

[1]The use of empirical orthogonal functions to extract the δ^{18}O signal common to numerous records [e.g. *Huybers and Wunsch*, 2004] gives a weighted average which, in practice, is similar to the more common simple average in that the weights were found to be all of the same sign and of similar magnitude.

and the signal will be suppressed. Note that synchronization uncertainty is not the same as age-model uncertainty — the relative ages of two records could be perfectly synchronized without knowing the absolute timing.

In Chapter 3, records were synchronized by identifying common $\delta^{18}O$ events and enforcing simultaneity. This synchronization is inevitably uncertain, owing to difficulty in identifying the depth of events and to the growth of age-model uncertainty away from the identified events. Once ages are assigned to these events, they are termed Age Control Points (ACPs). The use of seventeen ACPs reflects a minimalist strategy in constructing an averaged record, particularly when compared with the 90 ACPs employed in constraining the SPECMAP δ^{18}O over the same 770KY interval.

A minimalist ACP strategy is useful for guarding against artificially building structure into the average δ^{18}O time-series. That is, if peaks and troughs are aligned in a noisy time-series, the average signal can show spurious structure. On the other hand, insufficiently synchronizing time-series prior to averaging, suppresses the signal common to each of the records. Thus one wants to use a sufficient number of ACPs to minimize suppression of the signal, but also few enough ACPs to guard against building spurious structure into a record. The best number of ACPs will depend on the noise, signal structure, age-model uncertainty, and intended use of a given record. Nonetheless, it is possible to come to some general conclusions regarding averaging in the presence of synchronization jitter. These conclusions are then applied to the specific case of the marine $\delta^{18}O$ record.

Understanding how errors in synchronization influence averaged records directly relates to the interpretation of EOF1, presented in Chapter 3. In Chapter 3 it is argued that the difference between the SPECMAP stack and EOF1 can be accounted for on the basis of age-model discrepancies. As support, it was shown that orbitally-tuning EOF1 makes the resulting time-series appear more similar to the SPECMAP stack. Developing a depth-derived stack with a greater number of ACPs will permit further evaluation of whether the discrepancies between EOF1 and the SPECMAP stack owe to age-model differences, or if they are also influenced by the fewer number of ACPs used in constructing EOF1.

Furthermore, Chapters 4 and 5 argue that the simplest interpretation of EOF1 is that obliquity paces the glacial cycles. The nonlinear coherence calculated between the orbital parameters and EOF1 in chapter 4 is a function of the timing of the glacial terminations. As there exists an ACP at each glacial termination in EOF1, adding

more ACPs will not change the termination timing nor the nonlinear coherence. In chapter 5, however, a simple model is fit to the entire EOF1 time-series. It is expected that adding more ACPs will make the substage variability in EOF1 more pronounced, and this could influence the model fit to the observations.

An analytical expression

To demonstrate the effects of averaging imperfectly synchronized records, consider a set of time-series composed of a signal, Φ, plus an independent, normally distributed noise term, η_n,

$$y_n(t+\epsilon_n) \quad = \quad \Phi(t+\epsilon_n) + \eta_n(t+\epsilon_n) \qquad n = \{1, 2, ...N\}. \tag{3.30}$$

The synchronization error, ϵ_n, is modeled as an independent random variable drawn from a normal distribution. While the use of a constant time-shift to model the synchronization jitter is simplistic (one expects time-variable synchronization errors), this form permits an analytical solution whose utility is later demonstrated under more realistic conditions. Averaging the realization of $y_n(t+\epsilon_n)$ yields,

$$a(t) \quad = \quad \frac{1}{N}\sum_{n=1}^{N} y(t+\epsilon_n). \tag{3.31}$$

Absent age-model errors ($\epsilon_n = 0$), the expected variance of $a(t)$ is

$$< a^2 > \quad = \quad \Phi^2 + \frac{\nu}{N}, \tag{3.32}$$

where ν is the variance associated with $\eta(t)$. The important point is that the signal variance is unaffected by the averaging, while the noise variance decreases by a factor $1/N$. However, if age-model errors are present, the variance of the signal will also be suppressed.

Figure 3-17 shows an example where $y(t)$ is taken to be a signal whose spectral energy is inversely proportional to frequency (i.e. a red spectrum) containing no noise and sampled at 1 kiloyear (KY) intervals. $a(t)$ is realized by averaging ten time-shifted realization of $y(t)$ where the synchronization jitter, ϵ, has a standard deviation of 2KY. It is visually evident that $a(t)$ is a smoothed version of $y(t)$. To better quantify this smoothing effect, Figure 3-17 also shows the spectral power density estimates associated with a and y. The ratio of the spectra associated with a and y is called

the gain, and shows that for frequencies greater than 1/10KY, a has less than half the spectral energy of y. Next, an analytical expression is derived which relates the gain to the frequency, synchronization jitter, and number of records averaged.

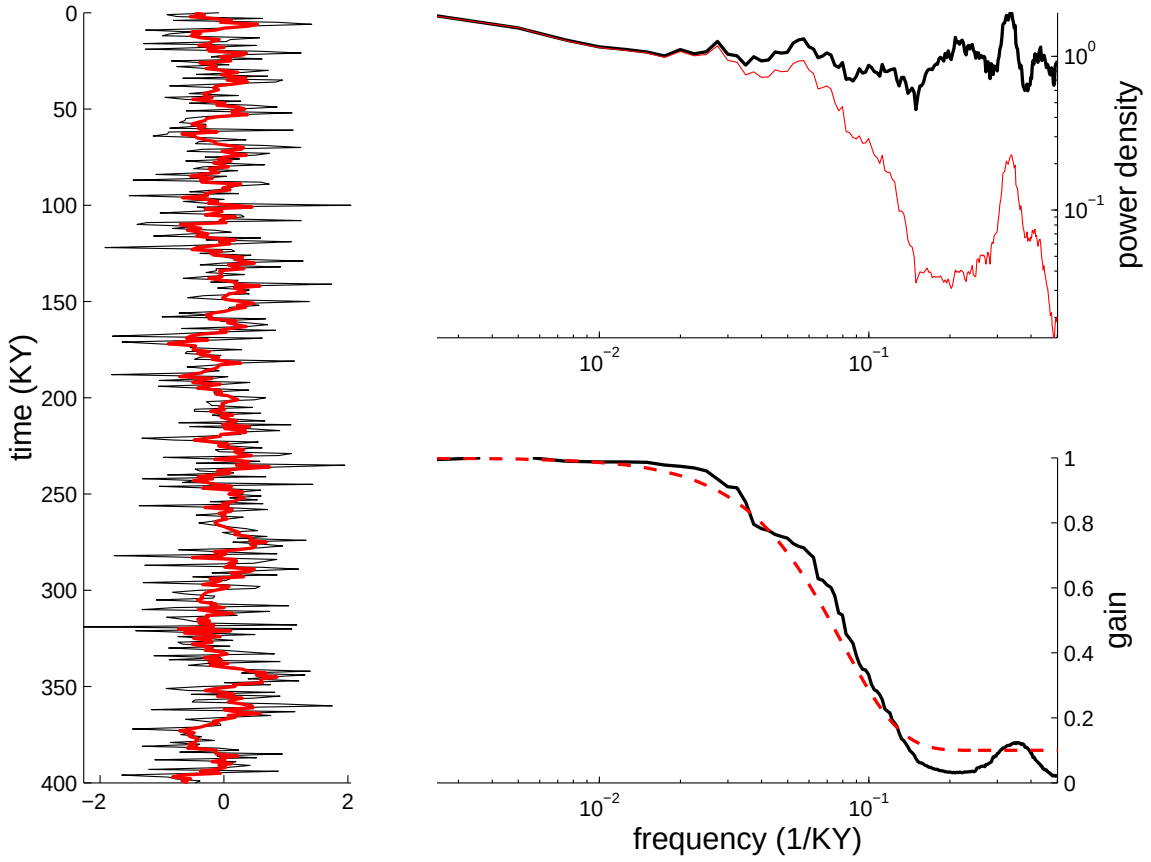

Figure 3-17: **Left**, a signal (y_n, black line) and the average of ten time-shifted (jittered) realizations of y_n (red line). The jitter has a standard deviation of 2KY. **Top right**, the multi-taper power density spectra of the signal (black) and its jittered averaged (red) showing reduced energy at high frequencies. **Bottom right**, the gain (black line) computed as the ratio of energy between the signal and its jittered average. Also shown is the analytically derived expected gain (red dashed line).

To proceed, we take the Fourier transform of 3.31,

$$\hat{a}(s) = \frac{1}{N}\sum_{n=1}^{N}\left(\hat{\Phi}(s) + \eta_n(s)\right)e^{-i2\pi s\epsilon_n}, \tag{3.33}$$

where s is the frequency and $e^{-i2\pi s\epsilon_n}$ translates the age errors in y_n into frequency dependent phase-shifts [see *Bracewell*, 2000]. Because $\eta(s)$ has a uniformly distributed phase, the further randomization does not alter its distribution. As might be ex-

pected, uncorrelated white noise is equivalently suppressed when averaging synchronized or unsynchronized records. The important point is that the signal term in Eq. 3.33 is multiplied by $e^{-i2\pi s\epsilon_n}$, indicating that some phase randomization of the signal will take place. The resulting amount of signal suppression can be written as a spectral gain function,

$$\hat{g}(s) = \left| \frac{1}{N} \sum_{n=1}^{N} e^{-i2\pi s\epsilon_n} \right|^2, \tag{3.34}$$

where $|.|$ indicate the absolute magnitude. This gain function relates the spectra of the original and averaged signals,

$$|\hat{a}|^2 = \hat{g}|\hat{y}|^2.$$

As the simplest case, consider averaging two records (N=2). Then the gain function can be written as,

$$\begin{aligned} \hat{g}(s) &= \frac{1}{4}(e^{-i2\pi s\epsilon_1} + e^{-i2\pi s\epsilon_2}) \times (e^{i2\pi s\epsilon_1} + e^{i2\pi s\epsilon_2}) \\ &= \frac{1}{2} + \frac{1}{2}\cos\left(2\pi s(\epsilon_2 - \epsilon_1)\right) \end{aligned}$$

In terms of the original standard deviation associated with the ϵ, the probability density function (PDF) of $\epsilon_2 - \epsilon_1$ is,

$$p(x) = \frac{1}{2\sigma\sqrt{\pi}}\, e^{-x^2/(4\sigma^2)}. \tag{3.35}$$

Thus, the expected value of the gain function is,

$$< \hat{g}(s) >= \frac{1}{2} + \int_{-\infty}^{+\infty} \frac{1}{4\sigma\sqrt{\pi}} e^{-x^2/(4\sigma^2)} \cos(2\pi sx). \tag{3.36}$$

This expression can be evaluated using an identity [Beyer, 1991, p272],

$$\int_{-\infty}^{+\infty} e^{-bx^2} \cos(cx)dx = \frac{\sqrt{\pi}}{2b}\, e^{-c^2/(4b^2)}, \quad (bc \neq 0), \tag{3.37}$$

so that,

$$< \hat{g}(s) >= \frac{1}{2} e^{-(2\pi s\sigma)^2} + \frac{1}{2}. \tag{3.38}$$

The expected gains when $N = \{3, 4, 5...\}$ are obtained using a similar approach, and

by induction, the solution to Eq 3.36 is

$$< \hat{g}(s) >= \left(1 - \frac{1}{N}\right) e^{-(2\pi s\sigma)^2} + \frac{1}{N}. \tag{3.39}$$

As a check, the above solution was found to be consistent with Monte Carlo results over a wide parameter range to within a standard deviation of 10^{-5}.

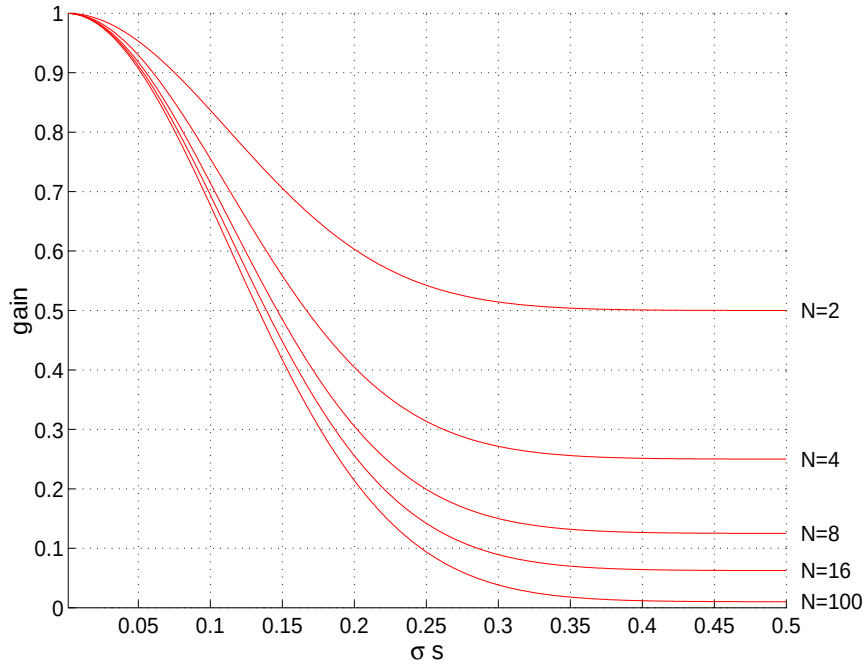

Figure 3-18: The expected gain, Eq 3.39, plotted against frequency, s, times the standard deviation of the relative age-model jitter, σ. Plots are for averaging $N = 2, 4, 8$, and 16 records. The gain scales equivalently with both σ and s ($\sigma s \sim \sqrt{-\ln g}$) so that it is more general to plot the gain against σs. For small σs the gain approaches one, while for large σs the gain asymptotes to $1/N$ — the expected behavior for perfect synchronization and complete phase randomization respectively.

The expected spectral power of the averaged signal is

$$< |\hat{y}(s)|^2 >=< \hat{g}(s) > |\hat{\Phi}(s)|^2 + \frac{\nu}{N}. \tag{3.40}$$

This expression can be connected with with Eq 3.32 using the Parseval relationship [e.g. *Bracewell*, 2000]. The gain function is plotted for various N in Figure 3-18. At high-frequencies and high standard-deviations, $< \hat{g}(s) >$ asymptotes to $1/N$ so that both the signal and noise are equally suppressed. This can be understood in that a phase-randomized signal behaves like Gaussian noise. At low-frequencies and small

errors, $< \hat{g}(s) >$ tends to 1 so that little signal suppression occurs. As a rule of thumb, stacking errors are expected to attenuate more than half the energy of frequencies above $(10\sigma)^{-1}$ where σ is the standard deviation in the stacking synchronization.

Averaging marine $\delta^{18}O$ records

To better evaluate the effects of synchronization jitter on averaged marine $\delta^{18}O$ records, it is useful to identify more than the seventeen ACPs used in EOF1. Thirteen additional ACPs are identified which, following the decimal notation employed by *Imbrie et al.* [1984], are labeled 3.1, 3.3, 5.3, 6.5, 7.3, 8.3, 9.1, 11.3, 12.31, 13.13, 14.3, 15.3, and 16.3. Figure 3-19 shows the SPECMAP stack labeled with all thirty of the ACPs employed in this study. An increase in the number of ACPs is expected to decrease the synchronization jitter. The amount of decrease will depend on how well events can be identified and how quickly age-model errors grow away from the ACPs. Given the inevitable presence of noise, there is some limit to how well records can be synchronized, but at present, there is little theory to guide one in determining the degree of synchronization uncertainty. Synchronization uncertainty is further discussed in the last section.

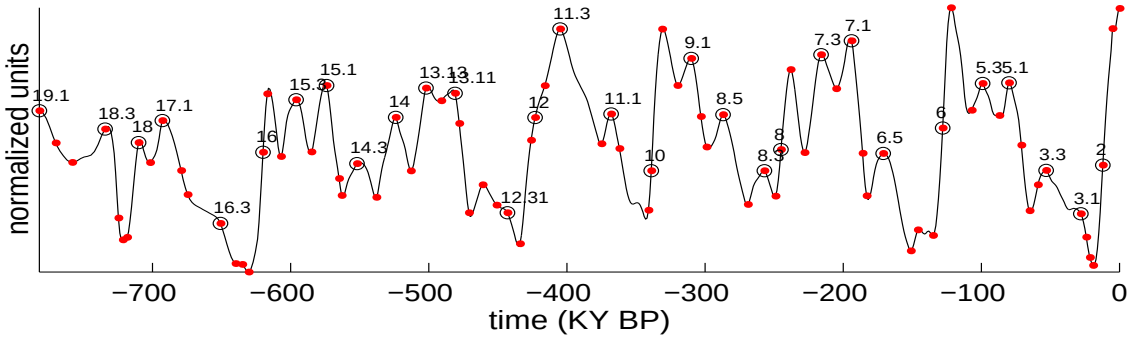

Figure 3-19: The SPECMAP $\delta^{18}O$ stack [*Imbrie et al.*, 1984] with each of its ACPs labeled as red dots. The thirty ACPs used to construct the high-resolution EOF1 are indicated by black circles and are numbered according the decimal notation used for the SPECMAP stack. Time goes from left to right and the units are normalized.

In Chapter 3, seventeen events were identified in the depth-domain in each of twenty-seven δ^{18}O records. In this case, not all records are of sufficient resolution to permit identification of the additional thirteen events. Instead, only the four highest resolution tropical planktic records are used. The use of tropical planktic records follows that of the SPECMAP stack, but were benthic or high-latitude records instead

used, the results are not expected to change. These planktic $\delta^{18}O$ records have a mean sampling interval of no greater than 2.5KY and are distributed across the equatorial oceans at core sites MD900963, ODP663, ODP677, and ODP927. A map of core locations is shown in Chapter 3, Figure 3-1. Figure 3-20 shows the four $\delta^{18}O$ time-series along with each of the identified ACP.

The introduction of additional ACPs provides for a new age-model estimate, referred to as $A^{(30)}$. The values of the thirteen additional ACPs in $A^{(30)}$ are estimated by averaging the $A^{(17)}$ age estimates obtained from each of the four planktic records. This is in direct analogy to how $A^{(17)}$ was estimated from $A^{(2)}$, and the interested reader is referred to Chapter 3 for more detail. Another age-model is employed, $A^{(9)}$, which is similar to $A^{(17)}$, but only has ACPs at the terminations and stage 19.1. The four age-models used here, $A^{(2)}$, $A^{(9)}$, $A^{(17)}$, and $A^{(30)}$ give a mean spacing between ACPs of roughly 800, 100, 50, and 25KY respectively. The four planktic $\delta^{18}O$ records are averaged using each of the four age-models yielding records M2, M9, M17, and M30 — results are shown in Figure 3-20.

As expected, the averages made with fewer ACPs have less high-frequency variability. For example, substages 5.1 and 5.3 (near 85 and 100KY BP respectively) are absent from M2 and M9. As there is good physical evidence that sea-level was anomalously high during substages 5.1 and 5.3 [e.g. *Broecker et al.*, 1968; *Bard et al.*, 1990], it is reasonable to infer that the global planktic δ^{18}O signal should show local minima at these substages. Furthermore, substages 5.1 and 5.3 are absent from M2 and M9, but identifiable in the individual planktic $\delta^{18}O$ records, suggesting that M2 and M9 both suppress variability at periods of 20KY and less because of synchronization errors.

The introduction of eight further ACPs, including one at substage 5.1, gives M17. M17 shows small minima near substages 5.1 and 5.3 and, relative to M9, a variety of other more distinct isotopic excursions. The addition of a further thirteen ACPs gives M30, as shown in Figure 3-20. substages 5.1 and 5.3 and other isotopic excursion are somewhat more distinct than in M17, but there is evidence that a point of diminishing returns has been reached. The squared-cross-correlation between M2 and M9 is 0.60, and between M9 and M17 is 0.90, showing that the addition of ACPs will affect the variability in M2 and M9. However, the squared-cross-correlation between M17 and M30 is 0.98 (they are nearly identical), showing that the addition of ACPs to $A^{(17)}$ has little affect on the overall variability in M17. Furthermore, the spectral

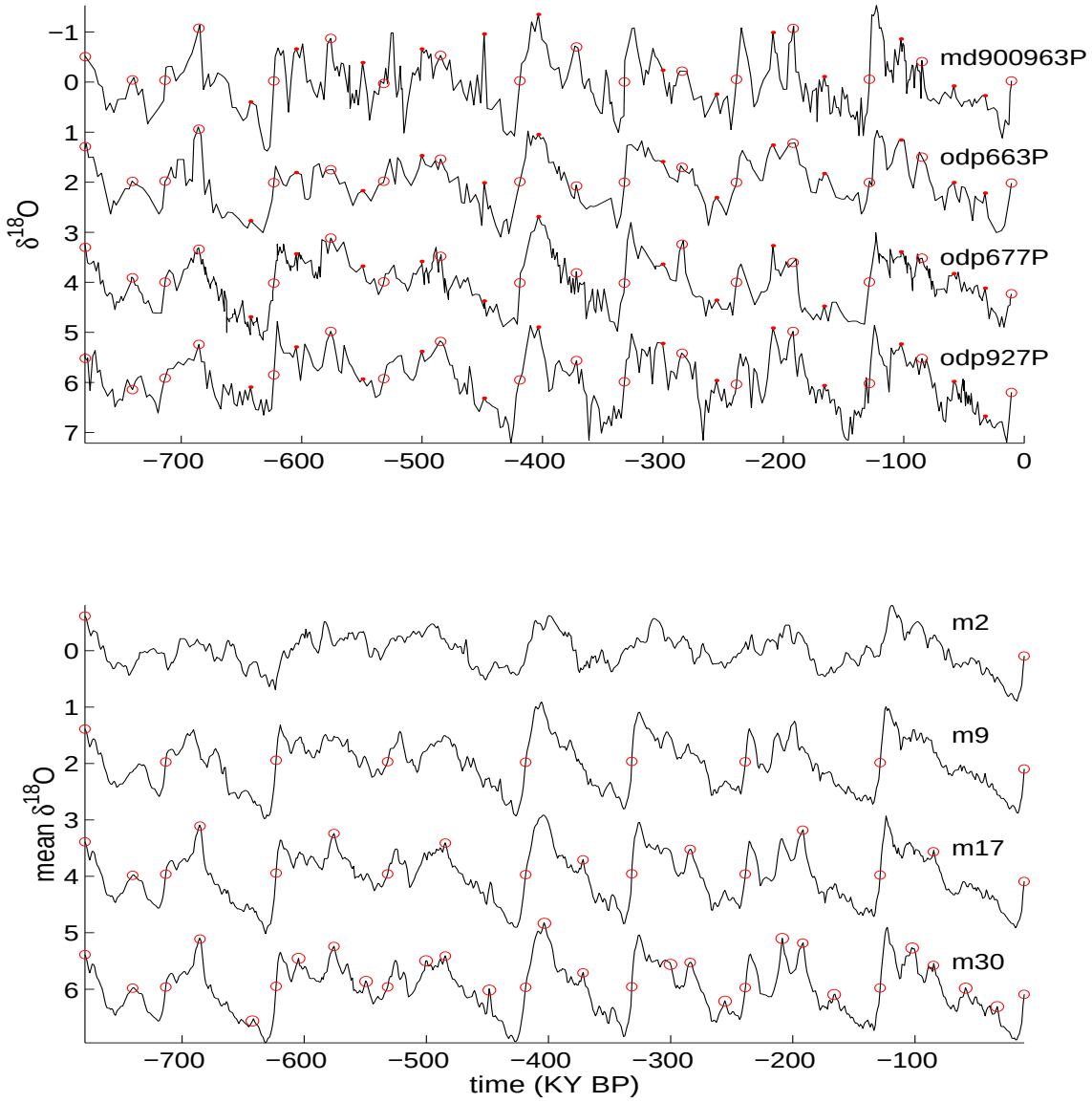

Figure 3-20: **Top**, Planktic $\delta^{18}O$ records pinned to the $A^{(30)}$ age-model. Open red circle indicate ACPs used in $A^{(17)}$, while the red dots indicate the thirteen additional ACPs. **Bottom**, The average of the four records when constrained by $A^{(2)}$, $A^{(9)}$, $A^{(17)}$, and $A^{(30)}$, termed M2, M9, M17, and M30 respectively. The ACPs used for each average are indicated by the open circles. The squared cross-correlation between M2 and M9 is 0.60, between M9 and M17 is 0.90, and between M17 and M30 is 0.98. So while there are appreciable differences between M2, M9, and M17, the very high correlation between M17 and M30 suggests a point of diminishing returns has been reached in using more than 17 ACPs.

estimates (Figure 3-21 and auto-bicoherence patterns (not shown) associated with M17 and M30 are virtually indistinguishable. Given the small change between M17

and M30, it is expected that the addition of more ACPs would not affect the spectra or auto-bicoherence estimates associated with the estimated average δ^{18}O variability.

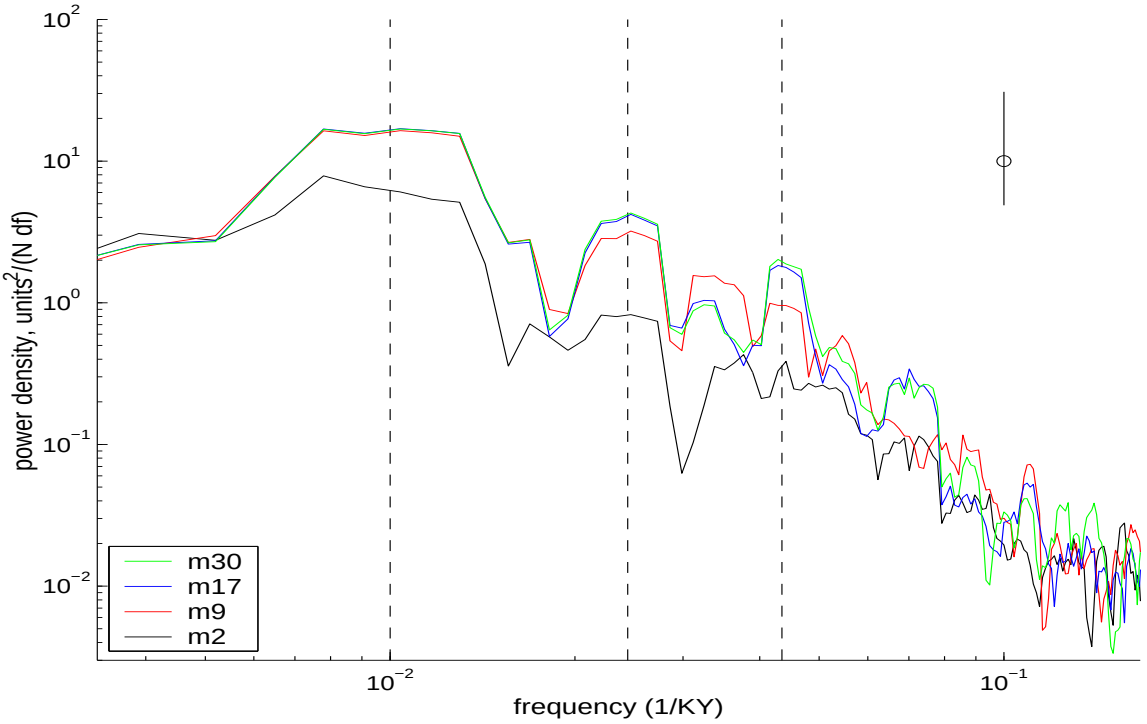

Figure 3-21: Multi-taper spectral estimates of the averaged $\delta^{18}O$ records shown in Figure 3-20 using 3 windows. In general, fewer numbers of ACPs gives a reduced spectral power.

A further test was made to determine if the differences between M17 and M30 might influence the parameter estimates for the simple model introduced in Chapter 5. Using the simulated annealing approach described in Chapter 5, the maximum cross-correlation between model results and both M17 and M30 was found to occur for the same parameters. That is, the simple model results are insensitive to the addition of further ACPs to M17. It is concluded that spacing ACPs by roughly 50KY is sufficient for accurately representing the late-Pleistocene δ^{18}O variability at time-scales of 20KY and longer. Considering the similarity of M17 and M30 results, Occam's Razor suggests using $A^{(17)}$. In cases where it is important to resolve individual events (e.g. substages 5.1, 5.2 and 5.3, 5.3), the use of slightly more ACPs would be preferable.

Comparing analytical results against observations

In this final section a comparison is made between the analytical results from Section 3.7.5 and the observational results from Section 3.7.5. In deriving the expected gain (Eq .3.39), the simplifying assumption was made that synchronization jitter could be modeled as a constant off-set in time. In reality, the accuracy of the synchronization between geophysical records is expected to be time-variable and depend on the distribution of ACPs and how the accuracy of the linear age-depth assumption. Furthermore, to apply Eq 3.39 to interpreting averaged $\delta^{18}O$ records, one requires an independent estimate of the uncertainty in synchronization.

For M2, the jitter is estimated using the $A^{(2)}$ ages for the 30 identified events in each of the four records. For example, the termination 2 ages according to $A^{(2)}$ are 160, 126, 142, and 125KY BP, giving a standard deviation of $\pm$16KY. Similarly, standard deviations are calculated for each of the 30 identified events and then averaged to estimate the over-all synchronization jitter; for M2 this is $\pm$17KY. The same technique is used to estimate the synchronization jitter for M9 and M17 using $A^{(9)}$ and $A^{(17)}$ respectively, yielding estimates of $\pm$5KY and $\pm$1.5KY. The M30 synchronization jitter must be estimated separately because in $A^{30)}$ all the identified events have been forced to coincide. The range of plausible M30 jitter values is bounded by the M17 jitter and zero. Fortunately, at the frequency bands of interests, the results are largely insensitive to what jitter is selected for M30, and for simplicity, a value of $\pm$1KY is adopted for the M30 jitter. Figure 3-22 shows the three gain ratios computed using Eq. 3.39 with N=4 and the respective estimates of the synchronization jitter.

Now we turn to the averaged $\delta^{18}O$ records themselves. Without knowledge of the true $\delta^{18}O$ spectrum, it is not possible to compute the gain of the spectral estimates shown in Figure 3-21. It is, however, possible to compute the relative gain between different spectra. Because M30 is presumably closest to the true $\delta^{18}O$ spectrum, it will be used to compute the relative gain associated with M2, M9, and M17. Another consideration is that the $\delta^{18}O$ records are expected to have a significant noise component, so that computing the expected gain of the whole spectrum would require an accurate understanding of the noise structure. To side-step this issue, it is assumed that at the most significant spectral peaks, the noise component is negligible. Thus, the gain will only be computed at bands centered on frequencies of 1/100KY, 1/41KY, and 1/23KY using a bandwidth of $\pm$1/400KY. Figure 3-22 shows the spectral energy in M2, M9, and M17 at these bands after normalizing by

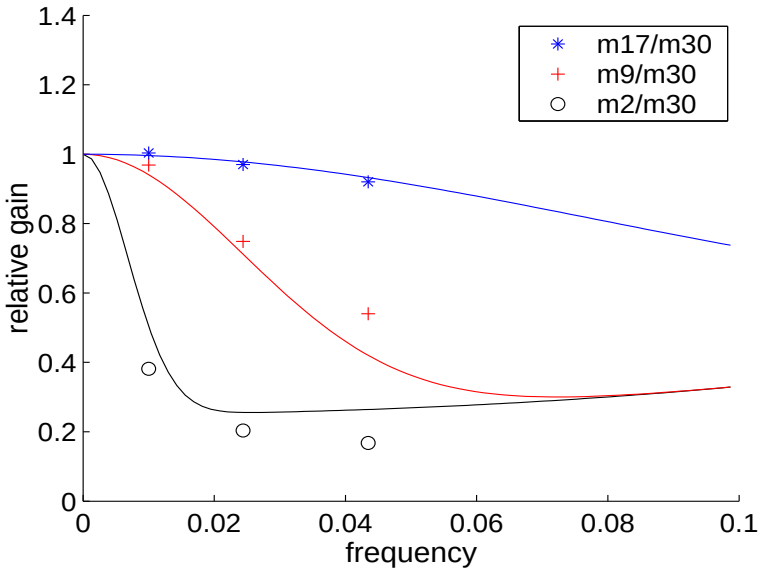

Figure 3-22: The ratio of energy between M30 and the other averaged records — M2, M9, and M17. Marks are the ratio of energy at bands centered at 1/100, 1/41, and 1/23KY derived from the averaged $\delta^{18}O$ records, and lines are the expected ratio of energy based on analytical results. Analytical results are from Eq. 3.39 using estimates of synchronization jitters of ±17KY for M2, ±5KY for M9, ±1.5KY for M17, and ±1KY for M30. The good correspondence between the observed and expected ratios indicates the applicability of the analytical gain function to marine $\delta^{18}O$ records. The correspondence also suggests that the energy in the identified spectral bands is common to each of the four planktic records shown in Figure 3-20.

the narrow-band energy in M30.

The analytically derived ratio of gains corresponds well with the marine $\delta^{18}O$ ratios. This correspondence indicates that the analytical gain function is applicable for use with the marine $\delta^{18}O$ records and may be appropriate for other geophysical records derived from marine and ice-cores. The correspondence between the analytical and observational results also supports the assumption that the spectral energy centered at 1/100, 1/41, and 1/23KY is common to each of the planktic marine $\delta^{18}O$ records.

Chapter 4

Are the Glacial Cycles Paced by Orbital Variations?

In the previous chapter, a significant nonlinear coupling was found between the 1/100KY and 1/41KY bands of climate variability, suggesting some relationship between the glacial cycles and obliquity. This chapter uses hypothesis testing procedures to further explore the relationship between glacial cycles and orbital forcing. Of the three orbital parameters, the obliquity results are the most conclusive. A phase coupling between terminations and maxima in obliquity is found to be significant at the 5% level. From this phase-coupling, it is inferred that deglaciations are triggered by shifts in insolation owing to change in obliquity. The largest insolation shifts related to increasing obliquity are greater high-latitude insolation, greater seasonality, and a reduced annual average hemispheric insolation gradient. Glacial cycles span either two or three obliquity cycles, giving an average duration of 100KY. Tests of the coupling between precession and the glacial cycles are inconclusive due to an age-model uncertainty approaching half a precession cycle. Many models call on the eccentricity amplitude modulation of precession to pace the ice-ages. It is shown that eccentricity maxima lag terminations and drift in timing, making eccentricity an unlikely pacing mechanism for the ice-ages. The simplest supposition supported by the observations appears to be that obliquity variations pace the glacial cycles.

4.1 Introduction

The cause of the quasi-100KY climate variability remains uncertain due to an over-abundance of plausible explanations [e.g. *Roe and Allen*, 1999]. The contending explanations for the quasi-100KY variability can be divided into two categories: those which are wholly internal to the climate system [e.g. *Ghil*, 1994; *Saltzman*, 2002; *Wunsch*, 2003a], and those which call upon orbital forcing [e.g. *Hays et al.*, 1976]. The latter can be further divided according to orbital parameter. Eccentricity [e.g. *Benzi et al.*, 1982; *Rial*, 1999] has the virtue of varying at 100KY period (although the 400KY variability is stronger), but the insolation changes this causes are only on the order of a few W/m^2 and are probably too small to be of much climatic relevance. The climatic precession variability has a much larger signal, with seasonal changes in global insolation of up to 30 W/m^2. The most widely accepted version of the orbital forcing of the glacial cycles is that a nonlinear response to the precession forcing demodulates the eccentricity envelope and generates a roughly 100KY timescale [*Imbrie et al.*, 1993]. Note that this is a two-fold nonlinearity: first, a nonlinear seasonal response must generate the precession period variability (see Chapter 2), and second, some longer timescale nonlinearity generates a climatic eccentricity response. Obliquity has played a more obscure role in theories of the glacial cycles, largely because it is not obvious how a forcing dominated by 41KY variability can be related to a roughly 100KY climatic signal. Unlike the climatic precession, the amplitude and frequency modulation of obliquity are small, but it has none-the-less been suggested that these modulations are related to the 100KY glacial cycles [*Liu et al.*, 1998]. In the following chapter a new model is introduced which suggests a mechanism for phase-locking the glacial cycles to changes in Earth's obliquity.

In searching for the cause of the quasi-100KY variability, the marine Pleistocene $\delta^{18}O$ record has been examined using a wide variety of statistical tests. Most commonly employed are Fourier based spectral techniques [e.g. Hays et al, 1976] and cross-spectral techniques [e.g *Imbrie et al.*, 1992], but also non-Fourier methods such as wavelet analysis [e.g. *Bolton and Maasch*, 1995]. However, in so much as a relationship exists between glacial cycles and obliquity or precession variability, it is necessarily nonlinear. This excludes many of the simplest and most powerful tools available for testing the relationship between two signals.

Higher order spectral analysis [e.g. *Hagelberg*, 1991; *Wara et al.*, 2000] is a useful tool for exploring possible nonlinear coupling in the climate record. To date, however,

results are inconclusive regarding the degree to which orbital variations are related to the 100KY variability. For instance, *Muller and MacDonald* [2000] use higher order spectral analysis techniques to argue against a causal link between precession variability and the ice-ages. In Chapter 3 a nonlinear coupling between the 100KY and 41KY variability was identified using both spectral and bispectral techniques, but it was not possible to distinguish between orbital control of the 100KY variability and a weak nonlinear coupling between obliquity and an independent 100KY variability. Despite the large literature analyzing the 100KY variability, it has not been established whether or not orbital variations somehow control the glacial cycles.

The depth-derived age-model developed in Chapter 3 provides a new opportunity to apply hypothesis testing procedures [e.g. *Devore*, 2000, or any standard statistics textbook] to the question of whether glacial cycles are coupled with orbital variations. The important features of the depth-derived age-model are its independence from orbital assumption, good age-control, and uncertainty estimates, all of which are crucial for conducting a rigorous test of the orbital hypothesis of glacial variability. The relationship between orbital variability and the glacial cycles is analyzed using the generalized *phase-coupling* between glacial terminations and the orbital parameters. The method involves estimating the distribution of orbital phases relative to the glacial terminations, and determining the degree to which the phase distribution is distinguishable from chance. Whereas higher order spectral analysis techniques are well suited to identifying weak nonlinear coupling in a system, the generalized phase coupling approach is better able to identify coupling in fully nonlinear systems. The magnitude and abruptness of the glacial terminations suggests the presence of strong nonlinearity in the climate system and motivates use of a generalized phase coupling analysis. Similar approaches to studying nonlinear coupling in timeseries have been successfully applied in a wide range of contexts including physics, chemistry, biology, and the social sciences; for an overview, see *Rosenblum and Pikovsky*, [2003].

At the outset, it is important to note the small number of observations we are dealing with — there are seven or eight (depending on how you count) glacial terminations during the late Pleistocene. This small population could render the test results inconclusive or sensitive to the particular assumptions employed. In seeking to make the results of the test as general as possible, a range of plausible formulations of the hypotheses are investigated to determine the sensitivity of the result to the methodology employed. Of course, this work does not exhaust the statistical tests

that might be made, and is therefore best viewed as an installment towards a more rigorous test of the orbital theory of climate change.

4.2 Features of an orbital hypothesis

To test the relationship between the glacial cycles and orbital variability, one seeks a hypothesis which is general enough to encompass many of the possible climatic responses to insolation forcing, yet specific enough to permit testing. Generality is necessary because there are numerous mechanisms which might link climate and orbital variability. Milankovitch [1941] hypothesized that increases in Northern Hemisphere summer insolation would lead to deglaciations, thus setting the phase of the glacial cycles. Another possibility is that high-latitude insolation increases North Atlantic sea-ice, reduces atmospheric moisture, and eventually starves the Northern Hemisphere glaciers [*Gildor and Tziperman*, 2000]. A related mechanism for starving glaciers is to decrease the meridional moisture flux by decreasing obliquity [*Raymo and Nisancioglu*, 2003]. As a final example, consider that during the last deglaciation, Antarctic temperatures warmed roughly three kiloyears prior to Greenland temperatures [e.g. *Imbrie et al.*, 1993; *Blunier and Brook*, 2001; *Wunsch*, 2003c], suggesting that southern hemisphere insolation might also play a role in pacing the glacial cycles.

Given the variety of plausible insolation forcing mechanisms, the hypothesis should not be restricted to a single orbital configuration when testing whether the glacial cycles are paced by orbital variations. That is, not simply whether high-latitude Northern Hemisphere summer insolation controls the glacial cycles, but also insolation gradients, Southern Hemisphere insolation, winter insolation, etc. As discussed in Chapter 2, the orbital elements of eccentricity, obliquity, and precession control the long-term evolution of each mode of insolation forcing. By testing for a relationship between the glacial cycles and each orbital parameter individually, this *omnibus* test is generalized to all long-term variations in modes of insolation variability.

To make a statistical test possible, it is necessary to demand consistency in the dynamics associated with each glacial cycle. A statistical test is not possible if each glacial cycle is permitted to have a different relationship with the insolation forcing. The hypothesis used here will assume a fixed relationship between the glacial cycles and orbital variability over the record duration.

It is also important for the hypothesis to depend on quantities which can be ac-

curately identified. It is straight-forward to identify the Earth's orbital configuration at any given point in time over the last ten million years [e.g. *Laskar*, 1993]. It is more challenging to identify the Earth's climate state at a given time. For the glacial variability, terminations are focused on because their magnitude makes for easy identification and their abruptness permits more precise determination of the timing. The timing of terminations is estimated from the depth-derived age-model presented in Chapter 3; it is no exaggeration to say that the use of an age-model independent of orbital assumptions is crucial for making a test of the coupling between terminations and orbital variability. Orbital-tuning attempts to drive energy into the orbital-bands; one way to do this is to align the termination with times when the climate response to orbital variability is also increasing. It is therefore expected, and found to be the case in Monte Carlo experiments (not shown), that the termination ages of orbitally-tuned records are preferentially aligned to be in-phase with the orbital variability. For similar reasons, and again found to be the case in Monte Carlo simulations, narrow-pass-band filtering over the orbital bands will produce signals which are biased towards being in-phase with the terminations.

This test focuses on the orbital configuration during a termination occur, rather than the climate state during daring a particular orbital configurations. For eccentricity, the distinction is a small one, as there is a nearly one to one correspondence between local maxima and glacial terminations. For obliquity and precession, however, the distinction is more important as terminations only occur every two or three obliquity cycles and every four or five precession cycles [e.g. *Raymo*, 1997]. The assumption is that the climate of the last 650KY may somehow skip beats in responding to the orbital forcing. Examples of such nonlinear phase-locking are well known in many biological and physical contexts; for a good introduction see *Pikovsky et al.* [2001]. Chapter 5 discusses nonlinear phase-locking of the climate system with orbital variations in more detail.

It should be noted that the more signals which are tested in relation to the terminations, the higher the chance of obtaining at least one false positive. For this reason, only those parameters are considered which cause significant long-term shifts or modulations in the insolation forcing. Other forms of orbital variability which are not included in the test, but which have been postulated to be responsible for the glacial cycles are variations in the orbital plane [*Muller and MacDonald*, 2000], frequency modulation of the obliquity, [*Liu*, 1998], and frequency modulation of the

eccentricity [*Rial*, 1999]. If one did test the timing of the glacial terminations against each orbital parameter, their frequency and amplitude modulations, and variations in the orbital plane this would comprise some ten tests, and there are probably more. Given such a large number of tests, it should be expected that at least one of the tests would give a result significant at the 10% level, even if the orbital variations are wholly independent of the terminations. Given sufficient data, it would be possible to carry out a multivariate test to simultaneously test several parameters. However, given the small number of glacial cycles, it is important to keep the hypothesis test confined to the most likely orbital suspects.

4.2.1 Identifying glacial terminations

As noted above, glacial terminations provide clear markers for defining the phase of the glacial cycles. Terminations have been qualitatively defined as abrupt shifts in the marine $\delta^{18}O$ record [*Broecker*, 1984], suggesting that a quantitative definition should be formulated using the rate of change of $\delta^{18}O$. Figure 4-1 shows the histogram of rates of change in EOF1 over the last 650KY. Because EOF1 is linearly related to $\delta^{18}O$, the relative distribution of the rates of change will be the same. The age estimates are from the depth-derived age-model discussed in Chapter 3. The distribution of EOF1 indicates that ice-volume is usually slowly increasing, while the presence of a long positive tail indicates less frequent but more rapid melting events which are identified with the glacial terminations. There is also a significant temperature component to the $\delta^{18}O$ variability recorded in EOF1 [e.g. *Lea et al.*, 2000], so that the rapid events identified in EOF1 cannot be interpreted as ice-volume changes alone.

Here, terminations are defined as instances when EOF1 rises faster than two standard deviation of the distribution. To more precisely specify the timing, the initiation of a termination is defined by when the rate of sea-level change first exceeds the two standard deviation threshold. To prevent short-lived climate events and noise from falsely appearing as termination events, EOF1 was first lightly smoothed using a three point triangular window. The termination initiation time is defined as the zero phase point for each glacial cycle, and the identified terminations are shown along with EOF1 in Figure 4-2. Only the last 650KY of the climate record is examined as this period corresponds to the interval in which quasi-100KY glacial variability predominates [e.g. *Schmieder et al.*, 2000]. There are some indicators that quasi-100KY glacial variability is also present at earlier periods in the climate record [e.g.

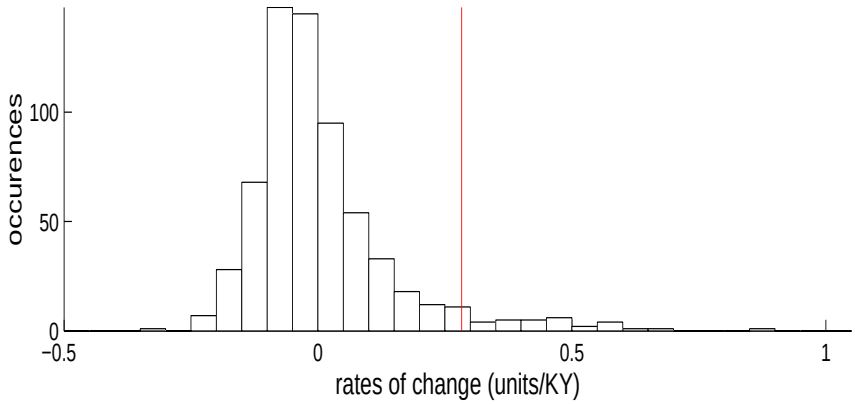

Figure 4-1: The normalized distribution of the rate of change of EOF1 over the last 650KY (black). The bulk of the distribution is weakly negative, but note the long tail extending into rapid increases in EOF1. The vertical line indicates the two standard deviation level above which terminations are defined to occur.

Beaufort, 1994], but these periods are not covered by the depth-derived age-model and are thus outside the scope of this study.

By convention, there are seven terminations identified in the $\delta^{18}O$ record over the last 650KY [see Chapter 3], and these same features are identified by the two standard deviation criterion. An additional event also meets the termination criterion during stage 7, near 210KY BP. This additional event occurs roughly 30KY after what is conventionally called termination three; to distinguish the two, termination three is labeled 3b while the additional event is labeled termination 3a. It is possible to exclude either event 3a or 3b by employing more elaborate rules for identifying terminations. Examples are: requiring the preceding maximum in ice-volume to be above some threshold or requiring terminations to be spaced by some number of years. But adding such a rule to exclude a single event is ad hoc, and instead all eight events are treated as glacial terminations. Reassuringly, the test results are not sensitive to whether 3a or 3b are included or not. It is also worth noting that the model results of *Paillard* [1998] reproduce the timing of each glacial termination in a robust fashion, except for that of termination 3 which is sensitive to the model parameterization and occurs at either event 3a or 3b. It is possible that termination 3 is split between two distinct time intervals.

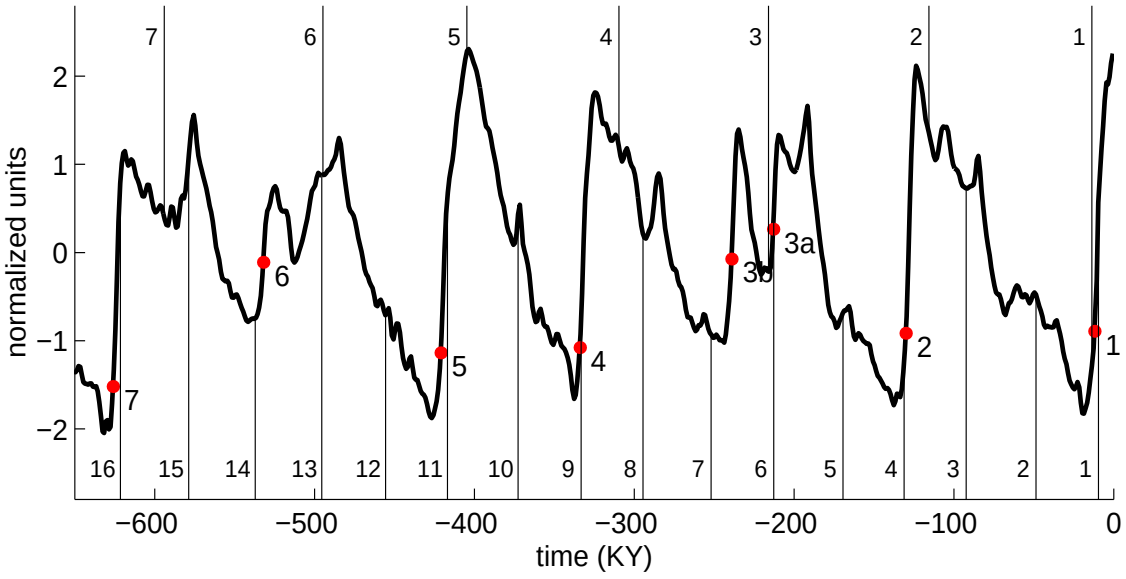

Figure 4-2: The relationship between terminations and orbital variability. Plotted is EOF1 with filled dots indicating the termination initiation times. Vertical lines indicate local maxima in eccentricity (top) and obliquity (bottom), and are counted starting from near termination one. Precession maxima occur too often to be usefully plotted.

4.2.2 Orbital phase

The climatic precession parameter and earth's obliquity vary smoothly and quasi-periodically in time [e.g. *Hinnov*, 2000], making the time-varying phase of each parameter simple to estimate, for instance using a Hilbert transform method [e.g. *Bracewell*, 2000]. Eccentricity is not amenable to the Hilbert transform method as the phase is poorly defined when the Earth's orbit is nearly circular. Thus it is most straight forward to define the local maximum in each orbital parameter as being zero-phase. Between local maxima, the phase is linearly interpolated with time so that a full 360° revolution occurs between each maximum. However, the phase of the orbital parameters during terminations will not be so simple to calculate due to frequency modulation effects and the more abrupt changes in eccentricity. A more general approach is to identify the two local maxima nearest to T_n, where the closest is denoted $M1_n$ and the next closest as $M2_n$. Assuming the signal is not severely frequency modulated, $M1_n$ and $M2_n$ will bracket T_n, and the phase is calculated as

$$\phi_n = \frac{|T_n - M1_n|}{M2_n - M1_n} \times 360^\circ \qquad\qquad n = \{1, 2...N\}, \tag{4.1}$$

Term.	7	6	5	4	3b	3a	2	1
Age	-626	-532	-421	-334	-239	-213	-130	-12
σ	9	10	11	11	10	12	8	2
Δ^p	5	4	-7	-1	-3	-7	3	1
Δ^θ	5	-5	4	1	-13	0	-1	3
Δ^e	32	37	16	25	23	-3	14	-2
ϕ^p	60	50	-130	-10	-50	-120	50	10
ϕ^θ	40	-40	40	10	-120	0	-10	20
ϕ^e	120	140	70	90	90	-10	50	-10

Table 4.1: The timing and phasing of orbital variations relative termination initiation times. Listed are the termination number, the initiation time for each termination in kiloyears, and the one standard deviation timing uncertainty, also in kiloyears. Δ is the timing difference in KY between the termination time and the nearest local maximum for each orbital parameter; subscripts p, θ, and e refer to precession, obliquity, and eccentricity respectively. ϕ is the phase of each orbital parameter at the termination time listed in degrees. Positive Δ and ϕ indicate that the nearest maxima in the orbital parameter lags the termination.

So defined, the phase estimates for obliquity and precession are very similar to those obtained using the Hilbert transform. The timing of the local maxima for obliquity and eccentricity over the last 650KY are shown in Figure 4-2; precession varies too rapidly to be usefully plotted.

As discussed in Chapter 2, the precession parameter is defined as $p = e \sin \varpi$, where e is the eccentricity and ϖ is the angle between perihelion and vernal equinox. So defined, increases in precession lead to greater insolation during Northern high-latitude summer and lower insolation during winter. Increases in obliquity cause greater annual average insolation at high-latitudes (the increase in summer more than compensates for the decrease in winter high-latitude insolation) and lower annual average hemispheric insolation gradients. Finally, zero phase in eccentricity means the Earth receives maximum annual average insolation and the seasonal effects of precession are largest. Thus defined, when each of the orbital parameters are near zero phase, the orbital configuration gives anomalously high Northern hemisphere summer insolation, the configuration *Milankovitch* [1941] postulated would cause glacial terminations.

While all calculations will be made using the orbital phase, it is sometimes clearer to discuss differences between orbital maxima and terminations in units of time. Because the orbital parameters are frequency modulated, there is no constant mapping between phase and time. However, the orbital variations are close to being periodic,

and an approximate translation of time into phase can be made using the average period between local maximum in the orbital parameters over the last 650KY. These are: 96.7 KY/360° for eccentricity, 40.8 KY/360° for obliquity, and 22.0 KY/360° for precession.

Table 4.1 lists the time between each termination and the nearest maximum for each orbital parameter, denoted by $\Delta^{p,\theta,e}$ for precession, obliquity, and eccentricity and by Δ for all three. Also listed are the phase of each orbital parameter relative to the initiation of each termination, denoted by ϕ. Figure 4-3 shows this same information visually. There are some notable features. The plus and minus one standard deviation age-model uncertainty is of the same order as half a precession cycle. Thus it is expected that age-model uncertainty will overwhelm our ability to determine the phasing between precession and the terminations.

A rough test of the significance of the obliquity phasing can be made by noting that seven of the eight Δ^{θ} are contained within ±10KY of each termination. The probability of having seven or more of the Δ^{θ} results cluster into either one or the other half of the phase space, assuming a uniform phase distribution, is 0.07. This statistical sketch suggests that a more careful analysis may show that the clustering of the obliquity phases is significant.

Finally, the eccentricity Δ^{e} shows a distinct trend of about -6KY per 100KY, suggesting that the average time between eccentricity maxima is shorter than the average glacial cycle. One might expect that the phasing of the precession would also influence the climate response to eccentricity, but note that the drift in the relative timing of eccentricity maxima and terminations in 650KY is over 30KY, or well over a precession cycle. From a physical view point, it seems difficult to reconcile orbital pacing of the glacial cycles with this drift in Δ^{e}.

4.2.3 Nonlinear coherence (Rayleigh's R)

In this section a statistic is introduced under the name of nonlinear coherence. It has recently come to the author's attention that this statistic is known as Rayleigh's R [see Upton and Fingleton, 1989]. In the following, the term nonlinear coherence is synonymous with Rayleigh's R.

An accurate measure of the phase relationship between terminations and orbital variations should account for the periodic nature of phase measurements. For example, the standard deviation is a poor candidate because a ϕ which hovered near ±180°

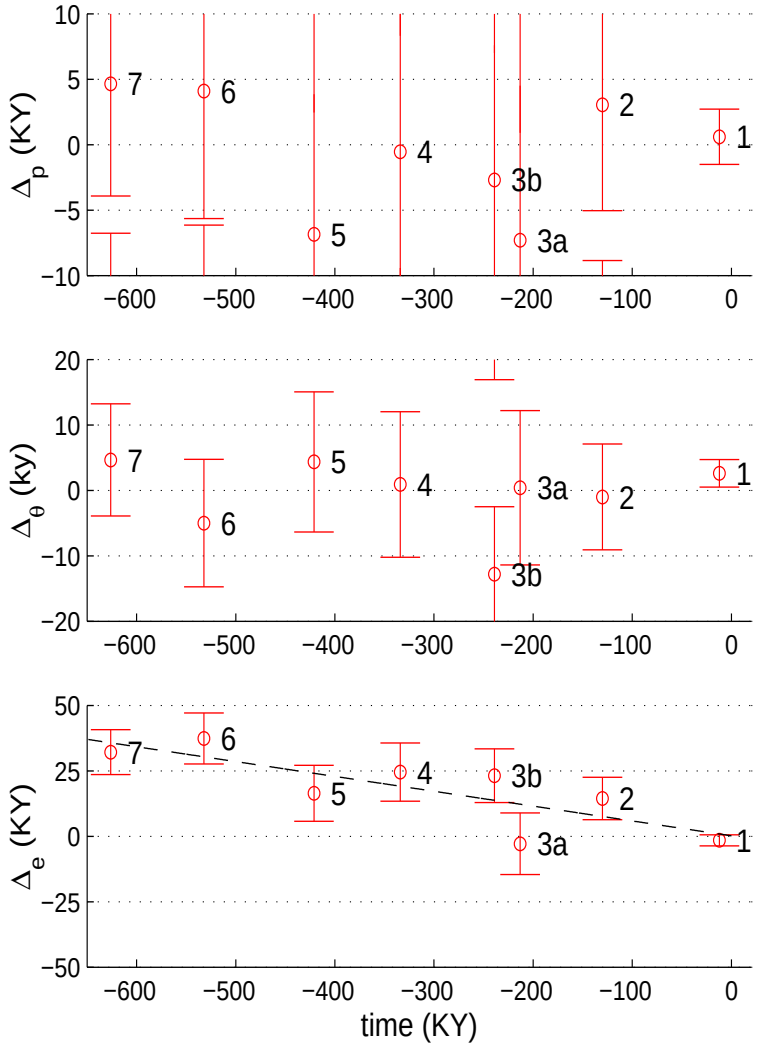

Figure 4-3: Similar to Table 4.1, the timing of terminations relative to local maxima in precession (top, Δ^p), obliquity (middle, Δ^θ), and eccentricity (bottom, Δ^e) in KY. Positive values indicate the maximum in the orbital parameter lags the termination. Termination numbers are listed for each estimate along with vertical bars indicating the one standard deviation age-model uncertainty. Note that the scaling of the y-axis is plus and minus roughly half the period of each orbital parameter and that uncertainty bars wrap around. A least-squares fit of the trend in Δ^e is indicated by the dashed line; it has a slope of -6KY/100KY.

could have nearly constant phasing, but nonetheless a large standard deviation. Another statistic, the root mean square deviation of ϕ, is also a poor choice because it requires one to select a reference phase from which to measure the deviation, thus biasing the test towards a single orbital configuration. Furthermore, standard coherence tests, which do account for periodic phases, are only applicable between identical frequency bands. To test for a nonlinear coupling, it will be necessary to compare the relative phasing between processes which have energy concentrated at different frequency bands.

Tass et al. [1998] introduced a measure of nonlinear phase coupling based on the normalized Shannon entropy of the phase distribution. While useful in some contexts, this test requires a large number of measurements for the results to be accurate, and thus cannot be applied in this case where only eight measurements are available. Another drawback is the lack of analytical methods for evaluating the significance of the Shannon entropy, making Monte Carlo techniques necessary. This state of affairs motivates the introduction of a statistic, termed the *nonlinear coherence*,

$$c = \frac{1}{N}\left|\sum_{n=1}^{N} \cos\phi_n + i\sin\phi_n\right|. \tag{4.2}$$

Here ϕ_n is the phase of the orbital variability relative to the nth termination, N is the total number of phase estimates, and $|.|$ indicates the magnitude of a complex quantity. Eq 4.2 provides a measure of the phase clustering between a quasi-periodic process and some other series of events which are localized in time but are not necessarily periodic or even quasi-periodic. As written, the nonlinear coherence estimate weights each phase equally, but were it decided that some events are more important than others, the estimate could be modified to include a set of weights. An more detailed discussion of the nonlinear coherence, its relationship with the linear coherence, and its probability distribution is given in Appendix 4.6.1.

4.3 Lessons from the Titius-Bode "Law"

Before discussing the significance of the observed phasing between orbital variations and the terminations, it is useful to consider the case of the Titius-Bode law. This empirical relationship describes the approximate regularity in the distance of the planets of our solar system from the sun and has been the subject of much attention

in the statistical [e.g. *Good*, 1969; *Efron*, 1971] and astrophysical communities [e.g. *Murray and Dermott*, 1999; *Lynch*, 2003]. *Lynch* [2003] wrote the law as,

$$r_\eta = 0.4 + 0.3^\eta \qquad \eta = -\infty, 0, 1, 2, 3....,$$

where r is the distance from the sun (measured using the semi-major axis), η is an index referring to the planets, and the constants (0.4 and 0.3) were chosen to minimize the least squares differences between r and the planets' semi-major axis. The choice of indexing and the associated least squares best fit changes slightly from author to author. The law played an important role in the discovery of Uranus (η=6) by Herschel in 1781, and the largest asteroid, Ceres (η=3), by Piazzi in 1801. However, for Neptune (η=7) there is a poor fit, and for Pluto (η=8) the law breaks down completely. The use of $-\infty$ in the sequence for η and the inclusion of an asteroid, albeit a big one, also seems arbitrary. As put by *Efron* [1971], "For a statistician, fitting a three-parameter curve of uncertain form to ten points with three exceptions certainly brings one to the far edge of the known world.".

In terms of hypothesis testing, the Titius-Bode law and the orbital theory of the ice-ages share much in common. 1) The hypothesized relationships are largely empirical[1]. 2) Neither result has been shown to arise solely as a consequence of the governing dynamical laws. Because of (1) and (2), the significance of the relationship depends on the aesthetic judgment of what constitutes a *simple* explanation of the observations. 3) Both hypotheses have a small sample number – seven or eight terminations and ten *planets* – making judgment regarding significance difficult. The small sample size makes the power of the test small, as later discussed in further detail. Finally (4), both have made predictions which were subsequently confirmed. That is, the accurate prediction of the Brunhes-Matuyama magnetic reversal date [*Johnson*, 1982; *Shackleton et al.*, 1990] and the accord between depth-derived and orbitally-derived ages gives partial confirmation of the orbital theory of climate change. Note, however, that the obliquity and precession bands of variability are used for orbital age estimates, and the orbital age estimates are largely independent of the quasi-100KY variability[2]. It appears no predications for the origins of the quasi-100KY variability

[1]Milankovitch predicted orbital control of ice-ages, but at the period of obliquity. Recognition of the quasi-100KY timescale of the ice-ages came with observations made in marine cores and radiometric dating of coral high-stands.

[2]In orbitally-tuning ODP677 and predicting the age of the Brunhes-Matuyama magnetic reversal, *Shackleton et al.* [1990] used the results of *Imbrie and Imbrie*'s [1980] model which has energy

have been subsequently confirmed.

Statistical tests of the significance of the Titius-Bode laws have widely varying results. *Good* [1969] finds a probability of about 130 to 1 that the law is not a mere accident, while *Efron* [1971], replying to *Good*'s article, finds a probability of about one to one. The large difference in probability is mostly due to differences in the null-hypotheses. Debate over a suitable null-hypothesis for the Titius-Bode law continues [e.g. *Hayes and Tremaine*, 1998; *Lynch*, 2003]. The lesson appears to be that, in seeking a test of the orbital theory of glaciation, one needs to account for the range of plausible formulations of the hypothesis test.

4.4 Testing the orbital hypotheses

Prior to discussing the hypothesis tests themselves, it is useful to review the terminology which will be used in articulating the design and results of the hypothesis test [see e.g. *Devore*, 2000]. The *significance level* of a statistical hypothesis test is the probability of wrongly rejecting the null hypothesis (H_0) when it is true and is denoted as α. The *critical value* for a hypothesis test is the value of the observed test statistic at which H_0 is rejected. In this case, the test statistic is the nonlinear coherence between the glacial terminations and an orbital parameter. The set of test statistic values for which H_0 is rejected is called the *rejection region*.

The ability to reject H_0 is not sufficient for establishing the credibility of the alternate hypothesis (H_1). One also needs to know the likelihood of rejecting H_0 when it is in fact false, and this is termed the *power*, as denoted by $1 - \beta$. An optimal statistical test will minimize α and β. If α plus β equal one, the test is insensitive to whether H_0 is true or false, and the results are meaningless. As one is usually more concerned with falsely accepting a hypothesis (H_0), the significance level is typically prescribed and the associated β is computed. Here a significance level of $\alpha = 0.05$ is used, and the β depends on the probability density functions (PDFs) of the alternate hypothesis. The power of the test will be considered in detail only when the null-hypothesis can be rejected.

concentrated near 1/100KY frequencies. This 1/100KY variability is seen to be incidental in that *Johnsen* [1982] had previously predicted the age of the Brunhes-Matuyama magnetic reversal without using a model with 1/100KY variability.

4.4.1 The null-hypotheses

A hypothesis test is conducted for each of the three orbital parameters where the null-hypotheses are

$\mathbf{H}_0^p$, glacial terminations are independent of the phase of precession

$\mathbf{H}_0^e$, glacial terminations are independent of the phase of eccentricity

$\mathbf{H}_0^\theta$, glacial terminations are independent of the phase of obliquity

To proceed it is necessary to translate the $\mathrm{H}_0^{p,e,\theta}$ into PDFs of nonlinear coherence. In estimating these PDFs, one could assume that the phase between orbital variations and the terminations is uniformly distributed. Although this uniform assumption would be simple, it is also most likely incorrect in that it requires the interval between consecutive terminations to be uniformly distributed between zero and infinity. Instead, it appears that ice-sheets have an intrinsic timescale associated with growth and collapse [e.g. *Imbrie et al.*, 1993; *Marshall and Clark*, 2002], and a null-hypothesis is developed with incorporates a plausible timescale for glacial variability.

The simple stochastic glacial model introduced by *Wunsch* [2003b] is used as the basis for estimating the PDF associated with the H_0. The stochastic model postulates a random walk in ice-volume,

$$\begin{aligned} V_t &= V_{t-1} + a\eta_t + b, \\ &\quad \text{if } V_t < 0,\ V_t = 0, \\ &\quad \text{if } V_t > \xi,\ V_t = 0, \end{aligned} \tag{4.3}$$

where V is ice-volume, t is a discrete time measured in one KY intervals, η_t is a zero-mean white noise process, and a, b, and ξ are constants. The noise term, η, is independent and normally distributed so that the expected variance, $< (a\eta)^2 >$, is a^2 where a is chosen as two. So that no particular sequence of termination times is made more likely, the initial ice-volume is set to a random value between 0 and ξ with uniform probability.

For a simple random walk, the variance of the timeseries is expected to grow linearly in time at a rate controlled by a. However, Eq. 4.4 incorporates two threshold conditions which modify the behavior of this random walk. First, a barrier is imposed at zero ice-volume so that values of V_t which are less than zero are reset to zero.

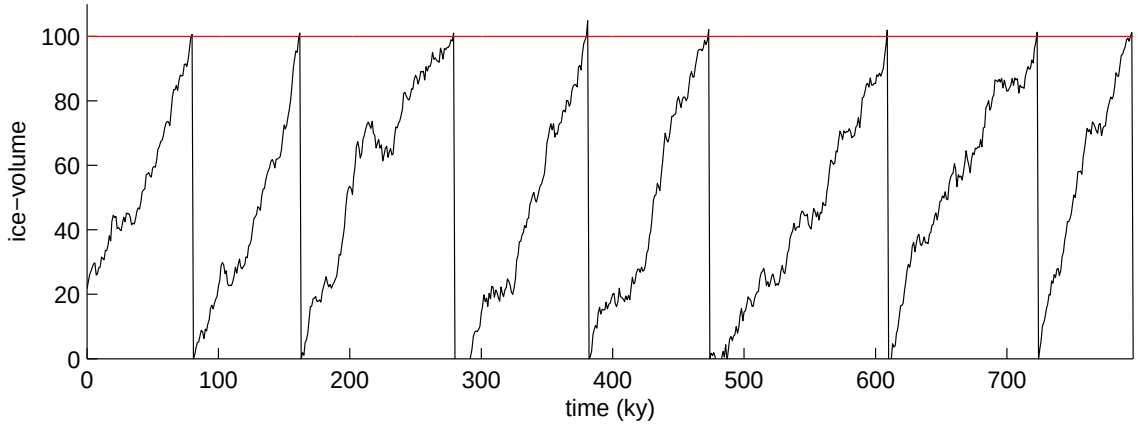

Figure 4-4: A realization of the random walk model of ice-volume (Eq. 4.4). The selected parameterizations are a noise amplitude of a=2, a drift of b=1, and an ice-volume threshold of ξ=100. Terminations are triggered once the threshold (indicated by the horizontal red line) is crossed. All units are normalized.

Second, a collapse threshold is imposed at ξ above which ice-volume is also reset to zero. The nth crossing of this threshold is identified with the triggering time, T_n. *Wunsch* [2003b] added an additional stochastic term to the collapse threshold, but here ξ is simply taken to be constant at a value of 100. A drift term, not in the original model, of $b = 1$ is included to provide a bias toward accumulation. A similar bias is observed in the histogram of the rates of change of EOF1 shown in Figure 4-3. Without this bias the distribution of termination intervals is similar to a Poisson process where long intervals of more than 200KY are common. The positive bias towards accumulation makes terminations occur at a more regular rate; if there was no noise, the terminations would be periodic at 100KY. A realization of the model output is shown in Figure 4-4.

The threshold crossing statistics of V_t could be computed analytically using the theory of Brownian motion with reflecting and absorbing barriers [e.g. *Feller*, 1957], but such an approach is not pursued here. Rather, it suffices to derive the pertinent statistics associated with V_t using a Monte Carlo approach. To obtain a single realization of the nonlinear coherence associated with H_0, first a sequence of eight glacial termination are generated using the stochastic glacial model, in analogy with the values listed in Table 4.1. Next, the relative phasing between the terminations and each orbital parameter is calculated using Eq. 4.1. Finally, the nonlinear coherence is computed from each set of eight phases using Eq. 4.2. Fifty-thousand Monte Carlo

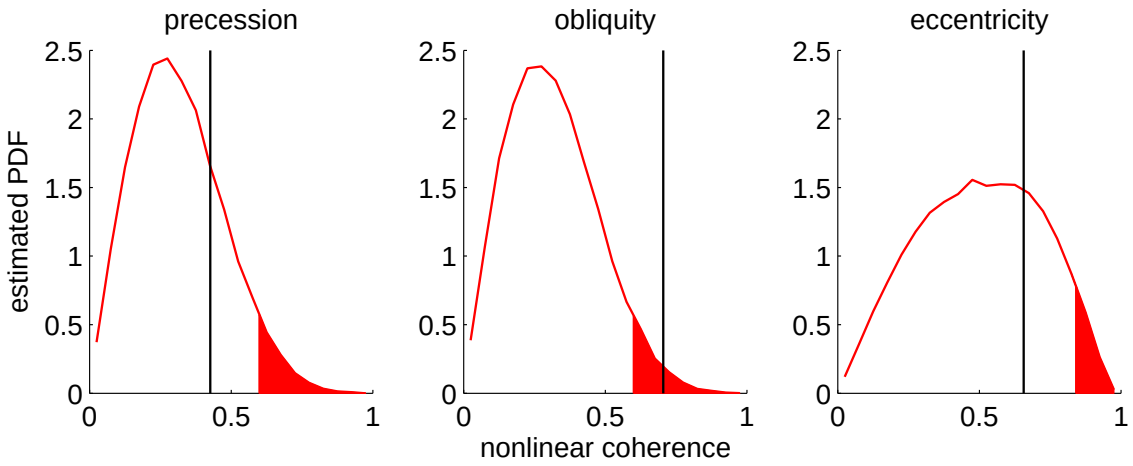

Figure 4-5: From left to right are the null-hypothesis PDFs associated with precession, obliquity, and eccentricity. The vertical bar indicates the estimated nonlinear coherence, and shading indicates the $\alpha = 0.05$ rejection region for the null-hypothesis of no connection between the parameter and the timing of the terminations. The critical value (v) and nonlinear coherence (c) with EOF1 are ($v = 0.6$,$c = 0.43$) for precession, ($v = 0.6$,$c = 0.7$) for obliquity, and ($v = 0.84$, $c = 0.66$) for eccentricity. Only obliquity has a nonlinear coherence greater than its critical value so that the obliquity null-hypothesis alone is rejected.

realizations of nonlinear coherence are used.

The PDFs associated with the $H_0^{p,e,\theta}$ are estimated by sorting fifty-thousand Monte Carlo realizations of the nonlinear coherence for each orbital parameter into twenty bins centered on $\{0.025, 0.05...0.975\}$ and then normalizing the histogram area to one. Critical values are estimated by finding the nonlinear coherence above which 5% of the Monte Carlo realizations reside. The resulting PDFs and critical values are shown in Figure 4-5 and tabulated in Table 4.2. Only the obliquity null-hypothesis, H_0^{θ}, can be rejected as the obliquity nonlinear coherence (0.70) is greater than the obliquity critical value (0.60). Thus a significant coupling exists between obliquity and the glacial terminations at the 5% level. In fact, the likelihood of obtaining such an obliquity nonlinear coherence by chance alone is one in a hundred. Furthermore, it is estimated that the power of the obliquity test is 0.58; see Appendix 4.6.2 for further discussion of how the power of the test was calculated and how it should be interpreted.

	c	v	β
precession,	0.43	0.60	—
obliquity,	0.70	0.60	0.42
eccentricity,	0.66	0.84	—

Table 4.2: Summary results of the hypothesis test. From left to right, columns refer to the nonlinear coherence between orbital variations and the terminations (c); the nonlinear coherence critical values (v) for an $\alpha = 0.05$ significance level; and the probability of making a Type II error, β.

4.4.2 Discussion

A natural question is why H_0^θ (that glacial cycles are independent of obliquity) is rejected, while H_0^p and H_0^e are not rejected. The first and simplest reason is that the obliquity nonlinear coherence with the terminations (0.70) is higher than that of precession (0.43) or eccentricity (0.66). The second reason is that the obliquity critical value (0.60) is lower than that of eccentricity (0.84). To address why there is a difference in the critical values, one must consider the glacial timescale built into the random walk glacial model.

Figure 4-6 shows a histogram of the duration between threshold crossings derived from a long run of the stochastic ice-volume model. The mean time between consecutive terminations is 100KY with an approximately normal distribution and ±20KY standard deviation, whose spread agrees with other estimates of the deviation in glacial cycle length [*Raymo*, 1997]. Note if the bias term, $b = 1$, were not included in Eq 4.3 the distribution would more resemble a Poisson distribution. The magnitude of this standard deviation suggests that the relative phasing between terminations and obliquity will be nearly uniform, while the relative phasing between terminations and eccentricity will be more structured. In general, the more structured the phase distribution, the higher the expected nonlinear coherence. Thus, the requirements for establishing a significant phase coupling between eccentricity and the terminations (i.e. the critical value) is higher because eccentricity has a timescale similar to the terminations.

The above discussion may seem to turn the argument on its head: typically, a similarity between timescales is cited as evidence for a relationship between two phenomena. But consider a counter example in which two unrelated signals are both periodic at 100KY. Then, the relative phasing at the first event must also be the relative phasing at all subsequent events. In this case, even though the signals

are unrelated, there is only one degree of freedom in the system and a nonlinear coherence of one is assured. Oppositely, when two signals have differing periods and are unrelated (barring the case of one signal being a harmonic of the other) one expects the phase to be more uniformly distributed and the nonlinear coherence to be lower. The average duration between eccentricity maxima is similar to average duration between terminations resulting in fewer DOF and a higher critical value relative the obliquity test.

There are also some qualitative observations which argue against a coupling between eccentricity and the glacial cycles. First, the most significant band of variability in eccentricity is near 1/400KY, but a concentration of 1/400KY variability is absent from Pleistocene climate variability [e.g. *Imbrie et al.*, 1993]. Second, terminations lead eccentricity maxima by an average of 20KY, or 68°. This indicates that terminations would have to be triggered by moderate values of eccentricity. It would seem more physical for glacial termination to be triggered during maximum rather than intermediate values of the eccentricity. That the lead is equivalent to a full precession cycle is also important, as this argues against glacial pacing by the eccentricity amplitude modulation of the climatic precession. Third, there is a trend whereby eccentricity maxima lag terminations by smaller values as time progresses. The change in lag averages 6KY per 100KY (see Figure 4-3), and it is difficult to conceive of physical mechanisms which would drift in this way. Finally, the eccentricity variations only cause weak changes in insolation forcing. Taken together with the inability to reject H_0^e, these observations make eccentricity appear an unlikely candidate for pacing the ice-ages.

A second question is whether excluding either of the termination 3 events would change the obliquity test results? Figure 4-2 and Table 4.1 shows that termination 3a contributes to obliquity's high nonlinear coherence; if it is excluded, the nonlinear coherence decreases from 0.70 to 0.66. Decreasing the number of terminations from seven to eight also increases the critical value from 0.60 to 0.64. Thus the nonlinear coherence remains greater than the critical values so that the null hypothesis would still be rejected and the results unchanged.

In Section 4.3 the difficulty of testing the significance of the Titius-Bode "Law" was discussed. In particular, it appeared that test results were sensitive to the null-hypothesis used in testing the Titius-Bode "Law". This raises the final question considered here; how robust are the obliquity test results to modifications of the

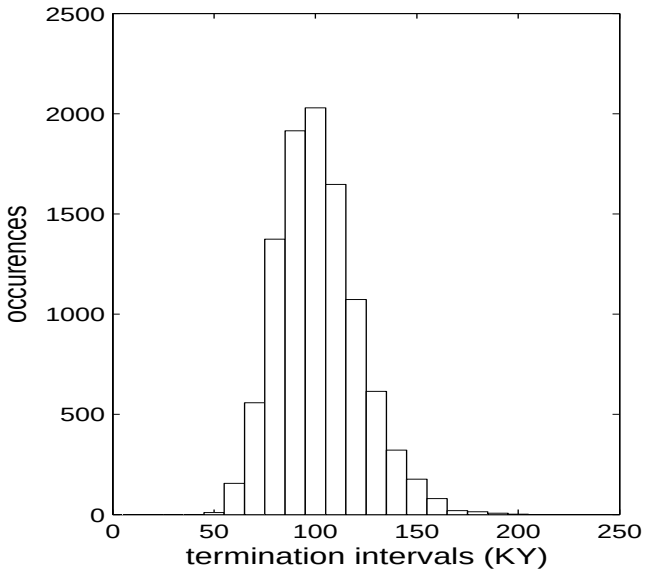

Figure 4-6: A histogram of the time between consecutive terminations derived from the random walk ice-volume model (Eq. 4.4). The selected parameterizations are a noise amplitude a=2, a drift b=1, and an ice-volume threshold ξ=100. The mean interval between terminations is 100KY with a $\pm 20KY$ standard deviation. The distribution is close to Gaussian but with a slightly elongated tail towards longer intervals.

null-hypothesis? To answer this question, it is useful to investigate whether some other plausible formulation of H_0^{θ} would increase the critical value above 0.70. One approach ($H_0^{\theta\prime}$) is to phase randomize EOF1, identify terminations in the phase randomized record, and compute the newly realized nonlinear coherence. A more sophisticated approach, which accounts for the non-Gaussian distribution of EOF1, is to use the phase shuffling algorithm of *Schreiber and Schmitz* [2000]. Experiments were also performed in which the non-Gaussian distribution of the rates of change of EOF1 was preserved. In all cases, the PDF resulting from these phase randomized approaches was qualitatively very similar to the PDF associated with the random walk accumulation mode (H_0^{θ}) and the obliquity null-hypothesis was invariably rejected. Assuming a uniform phase distribution between obliquity and terminations also leads to rejection of the null-hypothesis.

Another approach to exploring whether the obliquity null-hypothesis can be rejected is to build other simple models, akin to the random walk ice-volume model presented earlier. A simple model was formulated ($H_0^{\theta\prime\prime}$) which requires terminations to follow a Poisson distribution. Pursuing the idea that termination identification

times could be biased by the existence of a linear response to orbital forcing, obliquity variability was superimposed on the results of the Poisson model prior to identifying termination initiation times. It is found that $H_0^{\theta''}$ can be rejected at the 5% significance level even when the obliquity variability is made to account for an unreasonably large 40% of the total record variance. On the basis of three separate formulations, it is concluded that the null-hypothesis of no coupling between terminations and the obliquity variability can be safely rejected. It should, however, be noted that this result does not constitute proof of the obliquity pacing theory. For proof, one wants an ironclad physical mechanism, a much stronger statistical test, or preferably both.

4.5 Obliquity pacing of the glacial cycles

Having identified obliquity as significantly associated with the glacial terminations, it remains to identify a physical mechanism by which changes in obliquity could pace the glacial cycles. There are some clues. The mean phase of obliquity during termination initiation is $6 \pm 53°$. From this phasing it can be inferred that terminations are triggered by an insolation forcing related to a high obliquity orbital state. Candidate modes of insolation forcing are increased annual average high-latitude insolation, increased seasonality, a reduced summer hemispheric gradient, or an increased winter hemispheric gradient. Note that the hypothesis test did not presuppose a particular orbital configuration. That the sense of obliquity phasing during the glacial terminations lends itself to a simple physical interpretation (it would be more difficult to rationalize low obliquity causing glacial termination) provides additional, independent support to the inference of obliquity pacing of the glacial cycles.

The obliquity pacing of the glacial cycles implies that terminations only occur every second or third obliquity cycle, where the average of the 2×40 and 3×40KY cycles gives the 100KY variability. This is similar to the suggestion of *Imbrie et al.* [1991] and *Ridgwell et al.* [1999] that terminations occur every fourth or fifth precession cycle. Figure 4-7 shows a histogram of the elapsed time between multiples of orbital maxima over the last 650KY: the duration between every fourth or fifth precession cycle has a broad distribution with a peak near 90KY, eccentricity maxima are spaced at a nearly constant 100KY interval, and every second or third obliquity cycles have a bimodal distribution. The distribution of the terminations is also bimodal, in keeping with the hypothesis test results that obliquity paces the

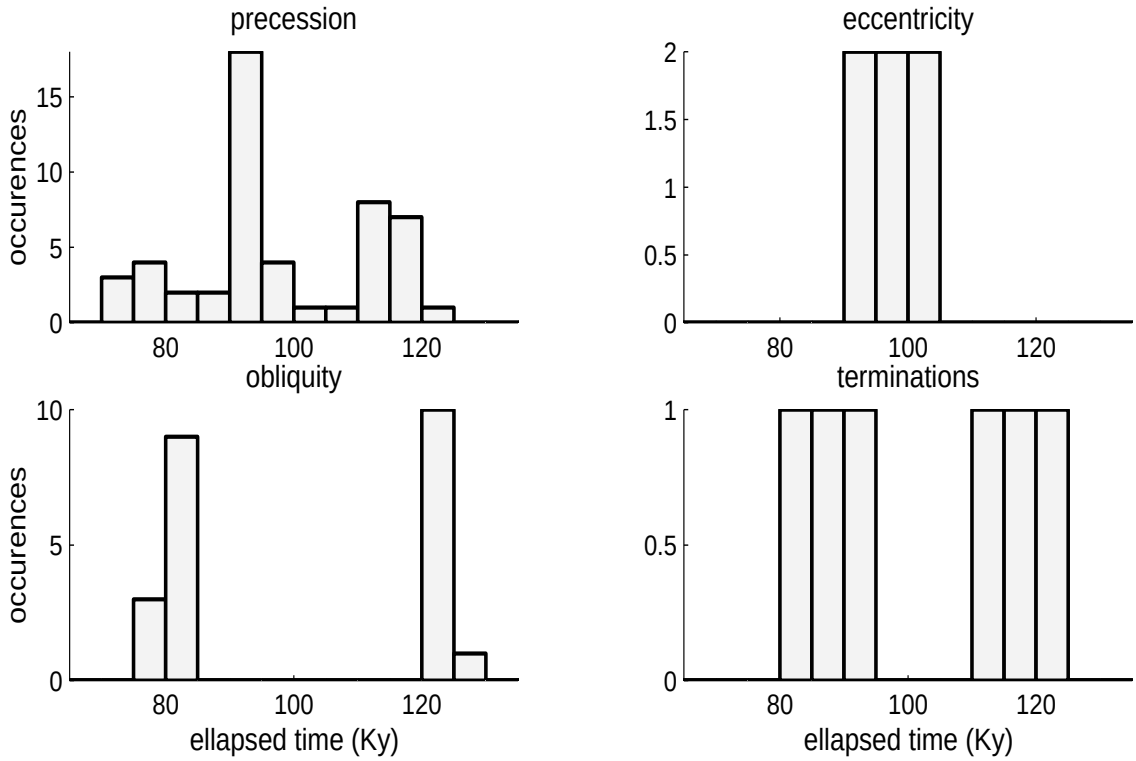

Figure 4-7: Histograms of the elapsed time between the orbital parameter maxima and terminations for the period -650 to 0 KY. Histograms are of the time between every fourth or fifth precession maxima (top left), each successive eccentricity maxima (top right), every second or third obliquity cycle (bottom left), and each successive termination where event 3b has been excluded (bottom right). Both obliquity and the intervals between terminations show a distinct bimodal pattern. As discussed in the text, the termination bimodality is somewhat less evident when event 3b is included. Note the scaling of the y-axis changes between plots.

glacial cycles. Termination intervals are calculated excluding termination 3b (see Figure 4-2) on the basis that termination 3 is a split event which should only be counted once. If termination 3a is instead excluded, the bimodal structure of the termination intervals is less obvious but still present. Although these histograms provide a simple argument for obliquity pacing of the glacial cycles, the distribution of termination intervals is estimated from only six realizations, and is thus only a rough indicator of the true probability distribution. From the histograms one can only conclude that the apparent bimodal structure of the glacial cycle durations is consistent with obliquity pacing — the nonlinear coherence results are stronger.

Ridgwell et al. [1999] also considered the obliquity pacing of glacial cycles, but

rejected this mechanism on the basis that obliquity paced glacial cycles would have a spectrum inconsistent with that of the SPECMAP $\delta^{18}O$ stack [*Imbrie*, 1984]. Their obliquity paced spectrum does, however, agree with the periodogram of EOF1 (see Chapter 3), further supporting the hypothesis of obliquity pacing of the glacial cycles. As discussed in Chapter 3, orbital-tuning tends to mask the coupling between obliquity and the glacial cycles, potentially explaining why the spectrum of the SPECMAP $\delta^{18}O$ stack does not show signs of obliquity pacing. In Chapter 5 obliquity pacing of the glacial cycles is further investigated using a variety of simple models.

Summarizing the results of the orbital pacing hypothesis test, it is found that the precession and eccentricity nonlinear coherencies cannot be distinguished from chance. Only the obliquity nonlinear coherence is found to have a significant relationship with glacial terminations, and this under a range of plausible formulations of the test. The simplest supposition supported by the observations appears to be that terminations are triggered by high obliquity states, and that obliquity is the pacemaker of the ice ages.

These results are an initial attempt at making a rigorous test of the orbital theory of climate change. Given the continuing proliferation of theories involving the glacial cycles, it is foreseen that further work will be undertaken in differentiating between the various proposed mechanism for the glacial cycles. Further efforts might employ further radiometric age-control, other climate proxies, longer records, or different measures of the coupling between orbital variations and the glacial cycles. Differing results would suggest that the hypotheses presented here do not span the set of plausible formulations, while concurrence would support the notion of obliquity pacing of the glacial cycles.

4.6 Appendix

4.6.1 Linear and nonlinear coherence

As defined within the main text of the chapter [see Eq 4.2], the nonlinear coherence is

$$c = \frac{1}{N}\left|\sum_{n=1}^{N} \cos\phi_n + i\sin\phi_n\right|, \tag{4.4}$$

where ϕ_n is the phase of a periodic or quasi-periodic signal relative the nth event identified in another signal. N is the total number of phase estimates, and $|.|$ indicates

the magnitude of a complex quantity. Eq 4.2 has a form similar to standard linear coherence estimates [e.g. *Priestley*, 1984]. For comparison purposes, consider the linear coherence estimate,

$$c' = \left(\sum_{n=1}^{N} a_n^2 \sum_{n=1}^{N} b_n^2 \right)^{-\frac{1}{2}} \times \left| \sum_{n=1}^{N} a_n b_n (\cos \phi_n + i \sin \phi_n) \right|. \tag{4.5}$$

Here ϕ_n is the phase between nth set of harmonics, where the harmonics must be of equal frequency. Note that unlike the nonlinear coherence, the linear coherence weights each ϕ_n term according to the amplitude associated with each of the harmonics, here denoted as a_n and b_n. In the case that both a_n and b_n are constant (a and b need not be equal), the linear coherence estimate reduces to the same form as the nonlinear coherence estimate.

The maximum value of both c and c' is one, occurring when ϕ is a constant; the minimum value is zero, occurring when the sum of the vectors exactly cancel. Even when the true coherence is zero, however, it is unlikely for the estimated coherence to be zero, given a finite number of observations. While it is possible to correct for this bias, it is easier to account for this effect when determining significance levels, and the latter approach is adopted here. Table 4.2 lists the estimated nonlinear coherence of each orbital parameter with the glacial terminations.

The similarity between the nonlinear and linear coherence estimates suggests that they will have similar distributions. *Amos and Koopman* [1963] have derived an expression for the probability density function (PDF) associated the linear coherence estimates under the assumptions that the phase estimates are independent and uniformly distributed. Figure 4-8 shows how the cumulative density functions (CDFs) for linear coherence varies with increasing degrees of freedom (DOF), i.e. increasing independent phase estimates. The CDF of the nonlinear coherence is estimated using a Monte Carlo approach. A single Monte Carlo realization is made by computing the nonlinear coherence of N randomly selected phases distributed uniformly on the interval $-180°$ to $180°$. A histogram of nonlinear coherence is generated from 10^5 Monte Carlo realizations whose area is normalized to one. The cumulative sum of this histogram of nonlinear coherence the provides an estimate of the nonlinear coherence CDF and results are shown in Figure 4-8 along with the linear CDFs.

A small systematic offset exists between the linear and nonlinear coherence CDFs but which diminishes with increasing DOF. This discrepancy presumably arises be-

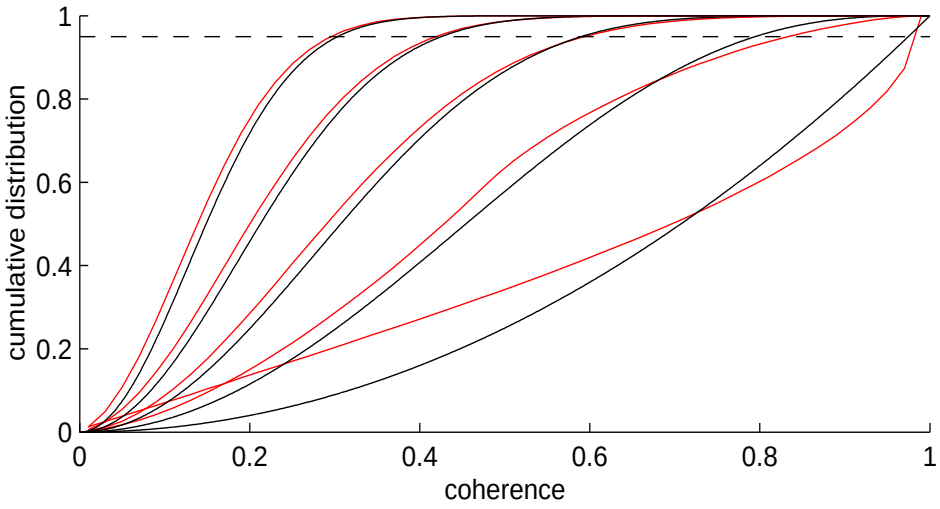

Figure 4-8: The cumulative density function (CDF) for linear coherence (black) from the analytical results of *Amos and Koopman* [1963] and nonlinear coherence (red) estimated using a Monte Carlo method as described in the text. From left to right the pairs of linear and nonlinear CDFs are for 32, 16, 8, 4, and 2 degrees of freedom. Results assume the phase is uniformly distributed. The nonlinear coherence CDFs tend to be shifted toward lower values, but for greater degrees of freedom this difference becomes small. The vertical dashed line indicates the 95% confidence level above which the null-hypothesis of a uniform phase distribution can be rejected.

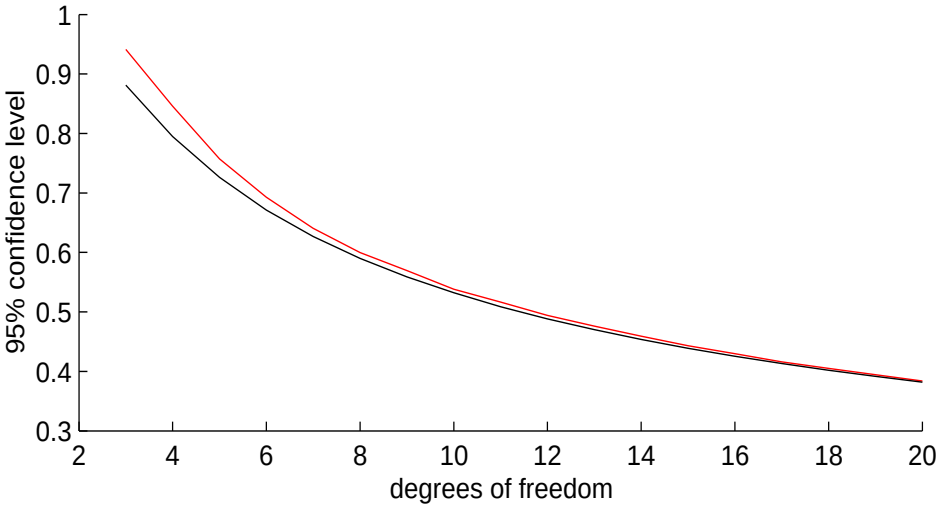

Figure 4-9: The 95% confidence level for linear coherence (black) and nonlinear coherence (red) as a function of the degrees of freedom (DOF). For large DOF the difference between the difference between linear and nonlinear coherence becomes negligible.

cause of the weighting terms included in estimating c' (Eq 4.5) but which are not present in the expression for c (Eq. 4.2). Figure 4-9 shows the 95% confidence level plotted as a function of DOF for the linear and nonlinear coherence where the nonlinear coherence confidence level is estimated using the Monte Carlo approach previously described. At eight DOF there is only a 0.01 difference between the linear and nonlinear 95% confidence levels. At sixteen DOF this difference is less than 0.005. This results suggests that for sufficiently large DOF, the analytical results of *Amos and Koopman* [1963] can be used to judge the significance of nonlinear coherence estimates, assuming uniformly distributed and independent phases. However, because the nonlinear coherence estimates made here have only eight degrees of freedom, Monte Carlo techniques are used to estimate the PDF of nonlinear coherence.

The linear coherence is typically computed over a range of frequencies. One of the useful features of such a calculation is that one obtains a sense of the behavior of the coherence statistic. For instance, one would generally be hesitant to conclude much from a coherence which has a large variance and shows little structure. As another example, if one thought two records were unrelated and yet found what appeared to be significant coherence, it would be prudent to perhaps explore the coherence estimate using more or less DOF, perhaps a different record interval, or data from other sources. Similarly, to get a sense for the behavior of the nonlinear coherence estimate it is useful to calculate the nonlinear coherence of the glacial terminations with a range of periodic signals with differing frequencies.

The timing of the glacial terminations are listed in Table 4.1, and the timing of the nth termination will be designated as T_n. The periodic signal can be written as

$$x(t) = \cos(wt + \alpha),$$

where w is the circular frequency and α is a phase constant. It is possible to compute the nonlinear coherence by calculating the phase at the terminations times,

$$\phi_n = wT_n + \alpha,$$

and substituting into Eq. 4.2.

Figure 4-10 shows the spectrum of 400 nonlinear coherence estimates computed between T_n and a periodic signals with frequencies ranging from 1/10KY to 1/2KY with a 1/1000KY bandwidth spacing. This range of frequencies is selected because

at frequencies above 1/10KY there is no known orbital pacing of the glacial cycles and 1/2KY is the Nyquist frequency associated with a one KY sampling interval. The level below which 95% of the nonlinear coherence estimates fall is 0.58, in good agreement with the Monte Carlo and analytically derived 95% confidence levels. This correspondence between multiple estimates supports the accuracy of the confidence level estimates and indicates that the T_n are not an unusual case.

The distribution of the spectrum of nonlinear coherence estimates provides a basis for judging the significance of the orbital nonlinear coherence estimates. The orbital nonlinear coherence between the T_n and precession is 0.43, 0.66 for eccentricity, and 0.70 for obliquity. Figure 4-10 shows that 100 out of 400 nonlinear coherence estimates exceed 0.43, 10 out of 400 exceed 0.66, and only 3 out of 400 exceed 0.70. Thus precession appears to be unrelated to the terminations, the significance of the eccentricity nonlinear coherence is somewhat ambiguous, and obliquity appears to be highly coherent. The significance of each of these nonlinear coherence results is more formally considered in section 4.5.

There are some similarities between the assessment of phase coupling presented here, and the paper by *Rahmstorf* [2003] which calls attention to how the Dansgaard-Oeschger events are spaced by roughly integer multiples of 1500 years. At some level both studies seek to quantify the regularity in reoccurrence times of events. There are, however, two important differences. First, *Rahmstorf* [2003] never quantitatively assesses the likelihood of finding the regularity in the Dansgaard-Oeschger events as a function of chance. Second, the regularity of the glacial cycles are compared with the long-term variations in modes of insolation forcing, while the regularity in the Dansgaard-Oeschger events are not associated with any known forcing. The latter situation is not unlike finding a very large nonlinear coherence between terminations and some arbitrary periodic signal and attempting to ascertain its physical significance — a much more demanding task.

4.6.2 The power of the obliquity test

The ability to reject H_0^θ is not sufficient for establishing the credibility of an obliquity pacing of the glacial cycles. One also requires some knowledge of the probability of making a Type II error; that is, the probability of not rejecting H_0^θ when H_0^θ is false. To illustrate this point, consider the case when the probability of making a Type I error is $\alpha = 0.05$, and the probability of making a Type II error is $\beta = 0.95$. Then

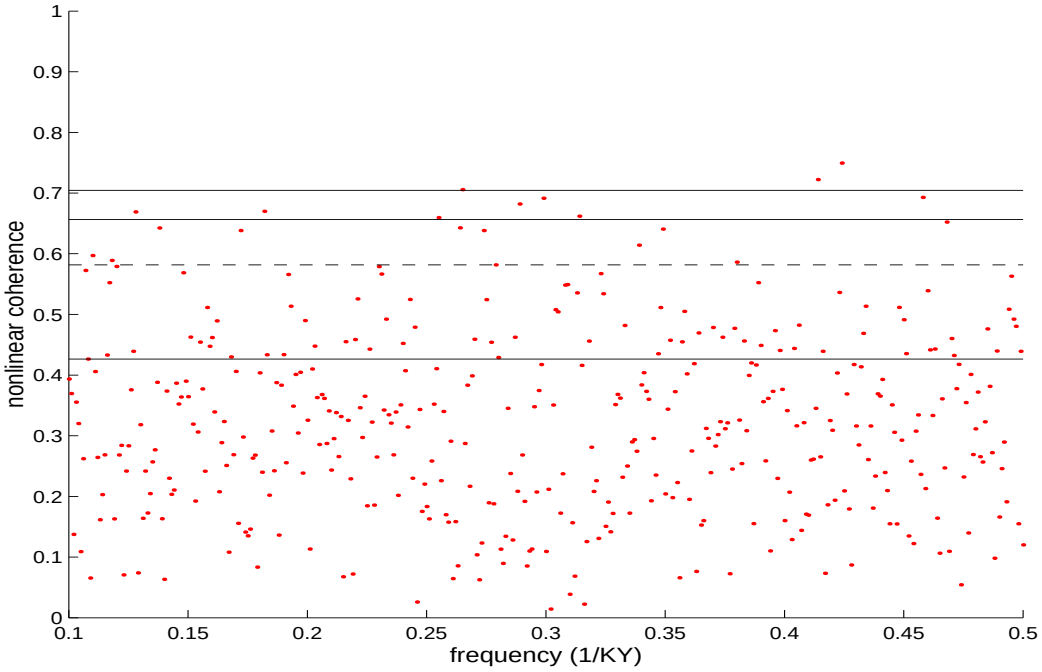

Figure 4-10: The nonlinear coherence between the glacial terminations and a periodic signal as a function of frequency (dots). The solid horizontal lines from top to bottom are the nonlinear coherence between the glacial terminations and obliquity (0.70), eccentricity (0.66), and precession (0.43). The horizontal dashed line indicates the level above which 5% of the nonlinear coherence estimates happen to fall (0.58), in close agreement with the Monte Carlo and analytically derived confidence level estimates for eight degrees of freedom.

there is a 95% chance of accepting the null-hypothesis when it is either true or false, and the test is wholly insensitivity to the truth. Thus, in determining whether the glacial cycles are paced by obliquity, it is necessary to estimate how unlikely it is to have made a Type II error; that is, the power of the test, $P = 1 - \beta$. Consult any standard statistical text book for more detail regarding hypothesis testing and power [e.g. *Devore*, 2000].

The alternate hypothesis used to estimate the power of the obliquity test is

$\mathbf{H}_1^{\theta}$, glacial terminations occur near a fixed phase of obliquity.

The fixed phase condition in H_1^{p} includes any climate response to insolation forcing which results in the timing of glacial terminations being tied to a particular tile of the Earth's axis. This phenomenon is referred to as orbital pacing [e.g. *Hays* et al, 1976], and includes both the case of glacial cycles resulting from the orbital forcing and the case of glacial cycles existing as a free oscillation within the climate system but which

are phase-locked with the orbital forcing. This obliquity pacing hypothesis is a subset of the fourth *Milankovitch hypothesis* listed by *Wunsch* [2004, submitted]. The exact phasing of the Earth's precession in H_1^θ is left intentionally vague as there could be natural variability in the obliquity phase which triggers a glacial termination.

It is necessary to translate H_1^θ into a PDF of nonlinear coherence. Absent age-model errors and natural variability in the phase at which terminations are triggered, the nonlinear coherence associated with H_1^θ would be constant at one. Accounting for this triggering uncertainty and age-model error, a realization of the nth termination time is

$$T_n = M_n + \epsilon_n + \sigma_n \qquad\qquad n = \{1, 2...8\}. \tag{4.6}$$

Here M_m is the time associated with the obliquity maximum closest to the estimated age of T_n. For example, Table 4.1 for the T_n and time between each termination and the nearest obliquity maximum gives $M_1 = -10KY$ and $M_2 = -129KY$. That the M_n are taken as maxima in obliquity, rather than some other fixed phase, does not affect the hypothesis results because nonlinear coherence is insensitive to the reference phase. That is, the nonlinear coherence associated with $\{\phi_1, \phi_2...\phi_N\}$ and $\{\phi_1 + \alpha, \phi_2 + \alpha...\phi_N + \alpha\}$ is the same. Only the scatter associated with the phase decreases the nonlinear coherence.

The next term on the right hand side of Eq. 4.6, ϵ_n, represents the age-model uncertainty. Termination age uncertainty translates into uncertainty in the timing between terminations and orbital variations. To simulate the ϵ_n, age-model perturbations are made according to the red-noise algorithm discussed in Chapter 3. The one standard deviation age uncertainty estimates are listed in Table 4.1 for each termination. A further source of uncertainty arises in the identification of when a termination first begins, and this is accounted for by additional $\pm$1KY uncertainty added to the ϵ_n realizations. The final term in Eq. 4.6, σ_n, owes to natural variability in the initiation time of each termination and is termed the triggering uncertainty. For simplicity, it is initially assumed that the σ_n are zero.

Because there is the possibility that the ϵ_n plus σ_n terms are larger than half an obliquity cycle, the obliquity maximum closest to T_n need not be M_n. To account for this effect, $M1_n$ is defined as the obliquity maximum closest to T_n and $M2_n$ as the next closest, and the phase, ϕ_n, is estimated using Eq. 4.1. Substituting sets of ϕ_n for $n = \{1, 2, 3...8\}$ into Eq. 4.2 gives a single realization of the nonlinear coherence, c. Fifty thousand Monte Carlo realizations of c are used to estimate the

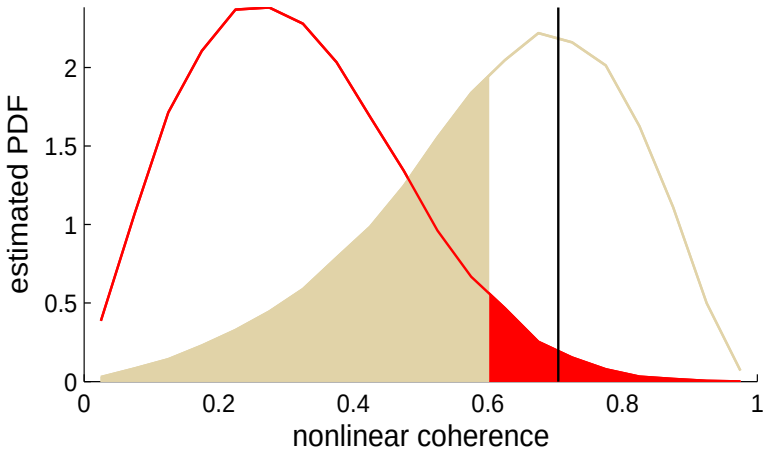

Figure 4-11: The PDFs associated with H_0^θ (red) and H_1^θ (brown). The probability of committing a Type I error is $\alpha = 0.05$ (red shading). The probability of committing a Type II error is $\beta = 0.42$ (brown shading), and thus the power of the test is $P = 058$.

PDF associated with H_1^θ, and results are shown in Figure 4-11. Having fixed the probability of committing a Type I error at $\alpha = 0.05$, it is found the probability of committing a Type II error is $\beta = 0.42$. Thus the power of the test is $P = 0.58$. This result can be interpreted as indicating that, given H_1^θ is true, the odds are better than half that H_0^θ will be rejected at the 95% confidence level using the available data. The power of the test can be increased if more glacial terminations events are identified (perhaps at times prior to the Mid-Pleistocene Transition) or by decreasing the uncertainty in the timing of the glacial terminations.

Chapter 5

A Simple Deterministic Model of the Glacial Cycles

From the hypothesis tests conducted in Chapter 4, it was concluded that glacial terminations are triggered by obliquity forcing of the climate system at above the 95% confidence level. These statistical results show that obliquity probably paces the glacial cycles, but this raises numerous other more physical questions. Some of the most important questions are why glacial terminations are only triggered every second or third obliquity cycle? Is precession variability also necessary to explain the glacial cycles? And what causes the onset of strong, roughly 100KY variability around 650KY ago? This chapter explores these questions using simple deterministic climate models. As noted in discussing the continuum of climate variability in Chapter 2, one would also do well to approach the climate question assuming a purely stochastic behavior. There is an adage that if a physical phenomena is possible, somewhere and to some extent, it probably occurs so that the climate system is probably partly deterministic and partly stochastic. It is anticipated that eventually the question will turn from whether the climate is deterministic or stochastic to one of quantifying how much and when.

Regardless of whether the simple models used to describe glacial variability are deterministic or stochastic, it should be noted that they are only descriptions of the climate variability, not theories of climate variability. A theory of climate would explain the descriptions codified in these simple models. Nonetheless, it is an interesting game to see how well one can describe climate variability using as simple a model as possible. At the least, remembering a simple model is easier than remem-

bering a sequence of unrelated events. There is the further hope that a simple climate description will ultimately lead to a deeper understanding of the climate itself; for example, that the dynamics embodied in a simple climate model will correspond with the dynamics governing the climate. There is little reassurance, however, that the dynamics of a low order system will correspond with the diffusive, turbulent, and highly complex climate system. With these caveats in mind, the thesis now turns towards describing the Pleistocene glacial variability using simple models.

5.1 Introduction

A complete theory of paleoclimate variability should be three dimensional, time dependent, and explicitly represent the oceans, atmospheres, cryosphere, lithosphere, biosphere, and chemosphere. An economic and political model might even be included for anthropogenic influences on climate. In principle, such a climate system model could account for all the features of the past geologic record and might predict the future climate state. Apart from the practical considerations involved in the running of such an enormous model, there are also more fundamental problems. These include poorly constrained external forcing variability due to solar luminosity variations, volcanic activity, mountain building, and the opening and closing of seaways. Even the Milankovitch forcing has important uncertainties due to the influence of earth's climate state on the obliquity [e.g. *Bills*, 1994] as well as the limitations in calculating past and future orbits imposed by the chaotic nature of the solar system [*Laskar*, 1989]. Another class of uncertainties arises from small-scale processes which, at some level, must be parameterized. Such processes include cloud micro-physics and ocean mixing, and whose aggregate affects can have a strong influence on the climate state. There is a further possibility that the basic evolution of the climate state is sensitive to perturbations ranging from slight changes in external forcing to fluctuations in small-scale processes [e.g. *Lorenz*, 1963].

Saltzman [2002] pointed out that in paleoclimate studies the rates of change of ice volume, deep ocean state, and geochemical inventories are of the same order as the dissipative rates, thus requiring the consideration of nonequilibrium dynamics. A major obstacle is that these rates of changes are too small to be measured or calculated using current physical models because of uncertainties in flux parameterizations. For instance, the last glacial termination involved approximately 5×10^{15}kg of ice melting

per year, with an associated sea-level rise of less than 5cm per year [*Fairbanks*, 1989]. To account for this small rise in sea-level requires accounting for the residual difference between evaporation, precipitation, melt, and freezing — and is a truly difficult task. Similar considerations hold if one seeks to account for the flux of energy into and out of the oceans or ice-sheets during terminations which amount to roughly 10 W/m^2 [*Saltzman*, 1983]. Furthermore there is a significant *drift* associated with many climate models [e.g. *Shackley et al.*, 1999] which is also on the same order as many of the paleoclimate variations.

The uncertainties owing to model drift and the physical parameterizations are major hindrances in accurately calculating the slow evolution of the climate state, suggesting that we are far from being able to deduce climate variability from first principles. Another approach is to infer the behavior of the climate system through a combination of observational analysis, physical reasoning, and simplified numerical modeling. In this case, the numerical models are not deduced from first principles, but rather incorporate plausible assumptions regarding the behavior of the climate system. Simple models are useful for demonstrating how the interaction of various mechanisms could give rise to the observed phenomena. While one does not expect any simple model to provide definitive proof for the origins of the ice-ages, they can demonstrate the likelihood of a given set of mechanisms. *Saltzman* [2002] outlined three rules by which such simple models should be developed and assessed. (1.) The model results should be robust in that they can survive small changes in parameters and acceptable levels of noise. (2.) A maximum amount of the structure in the observations should be deducible from the model using a minimum number of free parameters and a minimum level of prescribed noise. Finally (3), the model should make predictions which can be tested.

The second rule *Saltzman* [2002] outlined for assessing simple models implies that it is desirable to minimize the stochastic elements of a model. Whether the absence of prescribed noise is in fact desirable is debatable; for example, the simple stochastic sea surface temperature model of *Hasselmann* [1976] provides insight into many features of SST variability that a deterministic model would be hard pressed to reproduce. Each of the models considered in this chapter have a deterministic response to insolation forcing, but it is important to point out that exploring stochastic models would provide a complementary approach. One could add a deterministic orbital forcing to an otherwise stochastic model and find what level of orbital control is necessary to

make the model consistent with the observations. As an example, the threshold in the random walk model presented in Chapter 4 could be varied according to Earth's obliquity. This approach would probably prove useful in distinguishing the degree to which the long-term evolution of the climate is deterministic or stochastic, but such a stochastic approach is not further pursued at this time.

The strategy pursued here in developing a simple deterministic models of the glacial cycles is to analyze the ways in which some other models successfully reproduce elements of the glacial climate variability. I focus on the model by *Imbrie and Imbrie* [1980] because of its simplicity, and the model by *Paillard* [1998] because of the excellent fit it achieves with late Pleistocene $\delta^{18}O$ observations. Some common features are found between both of these models which do not appear to have been previously discussed. These features, along with the earlier tests of the coupling between orbital variations and ice-volume changes (see Chapters 3 and 4) suggest some important characteristics which a qualitative model of the glacial cycles should incorporate. A simple nonlinear system is presented which, using only a small number of degrees of freedom, reproduces many of the salient features of the ice-ages to include the timing and amplitude of the terminations as well as the spectral and auto-bicoherence patterns similar to those observed for the $\delta^{18}O$ EOF1 record. Recall that in Chapter 4 terminations were found to be triggered by high obliquity states. This nonlinear coupling will, in part, guide the discussion of the simple models.

5.2 The Imbrie model

One of the first simple models of orbital control of the ice-ages was presented by *Imbrie and Imbrie* [1980]. They argued that the geologic proxies for ice-volume clearly indicate the presence of an orbital influence on climate [e.g. *Hays et al.*, 1976], and that a major opportunity was at hand to begin researching the physical mechanisms by which the climate responds to orbital forcing. Several prior studies had investigated the link between climate and orbital forcing using radiation balance models [*Pollard*, 1976; *Weertman*, 1976; *Suarez and Held*, 1979] or time-dependent models [*Calder*, 1979] but here the model of *Imbrie and Imbrie* [1980] is focused on because of its simplicity, skill, and influence on subsequent work. The model of *Imbrie and Imbrie* [1980] will be referred to simply as the Imbrie model.

The Imbrie model states that changes in ice-volume are negatively proportional

to the total ice-volume, V, and the solar forcing, $\mathcal{F}$. Written here in discrete form the Imbrie model is,

$$V_t = V_{t-1} - \frac{\mathcal{F} + V_t}{T} \qquad T = \begin{cases} T_1 & \text{if } \mathcal{F} + V \leq 0 \\ T_2 & \text{if } \mathcal{F} + V > 0. \end{cases} \tag{5.1}$$

where T is a time-constant which switches between T_1 and T_2 depending on $\mathcal{F}$. $\mathcal{F}$ is nondimensionalized orbital forcing so that the units of the right hand side term are in ice-volume per KY. When $\mathcal{F} + V$ is greater than zero the time-constant will be T_2, otherwise it is T_1. By choosing $T_2 < T_1$, the system will tend to undergo rapid deglaciations followed by slow reglaciation. When the time-constants are appropriately tuned, this asymmetry causes variability at periods lower than those present in $\mathcal{F}$, specifically with a concentration of energy at 100KY periods.

Imbrie and Imbrie [1980] develop their model in analogy to heating a fluid, and write Eq 5-1 using temperature rather than ice-volume. A problem with this analogy is that when *Imbrie and Imbrie* [1980] discuss the results in terms of ice-volume, it requires the implicit assumption that temperature and ice-volume are perfectly anti-correlated. *Lea et al.* [2000] have provided evidence that tropical sea surface temperatures leads ice-volume variability by more than 3KY, making it important to specify which climate variable one is dealing with. This raises a further important point in the interpretation of EOF1, which is sensitive to both temperature and ice-volume. Here, for simplicity, EOF1 is interpreted as indicating changes in ice-volume with the understanding that there is also a temperature influence. This short-coming in interpretation could be addressed in future work by developing a simple model which predicts both temperature and ice-volume, thus providing a forward model of $\delta^{18}O$ variations. Another possibility is to work with estimates of the $\delta^{18}O$ of sea-water, but these measurements are much more sparse and currently have large uncertainties relative the $\delta^{18}O$ of calcite measurements [*D. Lea* personal communication] making it seem more prudent to use EOF1.

In Chapter 2 it was shown that the spatial and temporal variability in insolation can be expressed in terms of Legendre polynomials, annual and biannual periodic functions, obliquity, climatic precession, and eccentricity. The long-term shifts and modulations in insolation are primarily a function of obliquity and precession. Following *Imbrie and Imbrie* [1980], a simplified forcing for the climate models can be

generated as the linear sum of obliquity and a given phase of precession,

$$\mathcal{F} =< \theta > +(1+\alpha) < e\sin(\varpi - \phi) >, \tag{5.2}$$

where $< . >$ indicates that the obliquity, θ, and precession, $e\sin(\varpi)$, signals are normalized to zero mean and unit variance. The ratio of the variances between obliquity and precession is controlled by α, while the phase of precession is controlled by ϕ. The obliquity contribution in Eq. 5.2 is identified with changes in seasonality as well as lower frequency shifts in hemispheric insolation gradients. The precession variability is exclusively associated with changes in seasonality. Eq. 5.2 should be thought of as representing a combination of spatial and seasonal modes of insolation forcing. The primary virtue of Eq. 5.2 is that it has only two adjustable parameters. A drawback is that the direct inclusion of precessional variability assumes the presence of some nonlinear seasonal response in the climate system (see Chapter 2), and this blurs the distinction between climate model and forcing. Furthermore, in forcing a model with Eq 5.2 the assumption is being made that the stochastic variability is not important. In subsequent sections the influence of stochastic elements on simple climate models is discussed further.

5.2.1 Fitting to EOF1

The Imbrie model has four degrees of freedom: two for the timescales and two for insolation forcing. *Imbrie and Imbrie* [1980] searched for a best fit between their model output and a set of radiometrically dated $\delta^{18}O$ records extending between zero to 130KY BP using a coarse grid search technique. They found optimal output for an ablation time-constant $T_2 = 10.6KY$, accumulation time-constant $T_1 = 42.5KY$, precessional phase $\phi = 16°$, and insolation ratio of $\alpha = -2$. It appears *Imbrie and Imbrie* [1980] define ϖ as the angle between vernal equinox and aphelion, rather than the more standard definition employing perihelion [e.g. *Vernekar*, 1972; *Berger and Loutre*, 1992], so that negative α and $\phi = 16°$ indicates a July perihelion. This inference was checked by simulating Figure 3 in *Imbrie and Imbrie* [1980]. In this thesis, ϖ is always defined relative perihelion.

As the Imbrie model was originally tuned using data only over approximately the last 250KY, it is useful to repeat the exercise using the longer and better resolved EOF1 record. An exhaustive search of all combinations of plausible parameters can

easily be made because the Imbrie model has a small number of adjustable parameters. However, in anticipation of discussing models with more adjustable parameters, a simulated annealing search algorithm [e.g. *Press et al.*, 1999] is instead used. Simulated annealing is a Monte Carlo method which works in analogy with the slow cooling of a liquid from a hot and disordered state to a cool, crystallized state. If the adjustable parameters are considered molecules, and the misfit between model output and observations interpreted as energy, the cooled crystallized state corresponds to a minima in molecular energy or a local minima in the cost function.

The search domain for parameter values is restricted to one significant figure. This gives a dramatic reduction in the number of possible values — if the search is restricted to values between one and a hundred, there are only nineteen possible values, $\{1, 2...9, 10, 20...100\}$. Note, however, there are still an infinity of numbers with one significant figure between zero and one. Apart from making the parameter space easier to search, there are other advantages to restricting the search domain to one significant figure. The Imbrie model, and other models considered later, all represent drastic simplifications of the dynamics governing climate variability. If the behavior of the model is sensitive to the second or higher significant figures in a parameter value, it is less likely to represent a physically meaningful solution. One hopes to find a model which is robust to minor perturbations as this aids in identifying mechanisms likely to control climate. It should be kept in mind, however, that parameterizations with only one significant figure can still lead to results sensitive to minor perturbations — they are only less likely to be sensitive. Furthermore, the climate system could itself be sensitive to minor perturbations; for instance, the glacial cycles could be chaotic in nature. The development and fitting of a simple model to observations is as much an art as a science, and there is no foolproof method for determining the adequacy of a given model or the accuracy of the parameterizations. Rather, insight into the adequacy of a given model requires careful consideration of the assumption, comparison of the results against independent observations as well as the results of other competing models.

The Imbrie model is initially fit to EOF1 over a search range with timescales T_1 and T_2 ranging from 1 to 120KY, a precessional phase ϕ between 10° and 360°, and an obliquity to precession ratio α of -1 to 5. Values of $\alpha < -1$ are not permitted as these are redundant for values of ϕ differing by $\pm 180°$. As discussed in Chapter 4, only the last 650KY of EOF1 are used for fitting the models, as this is the portion which clearly

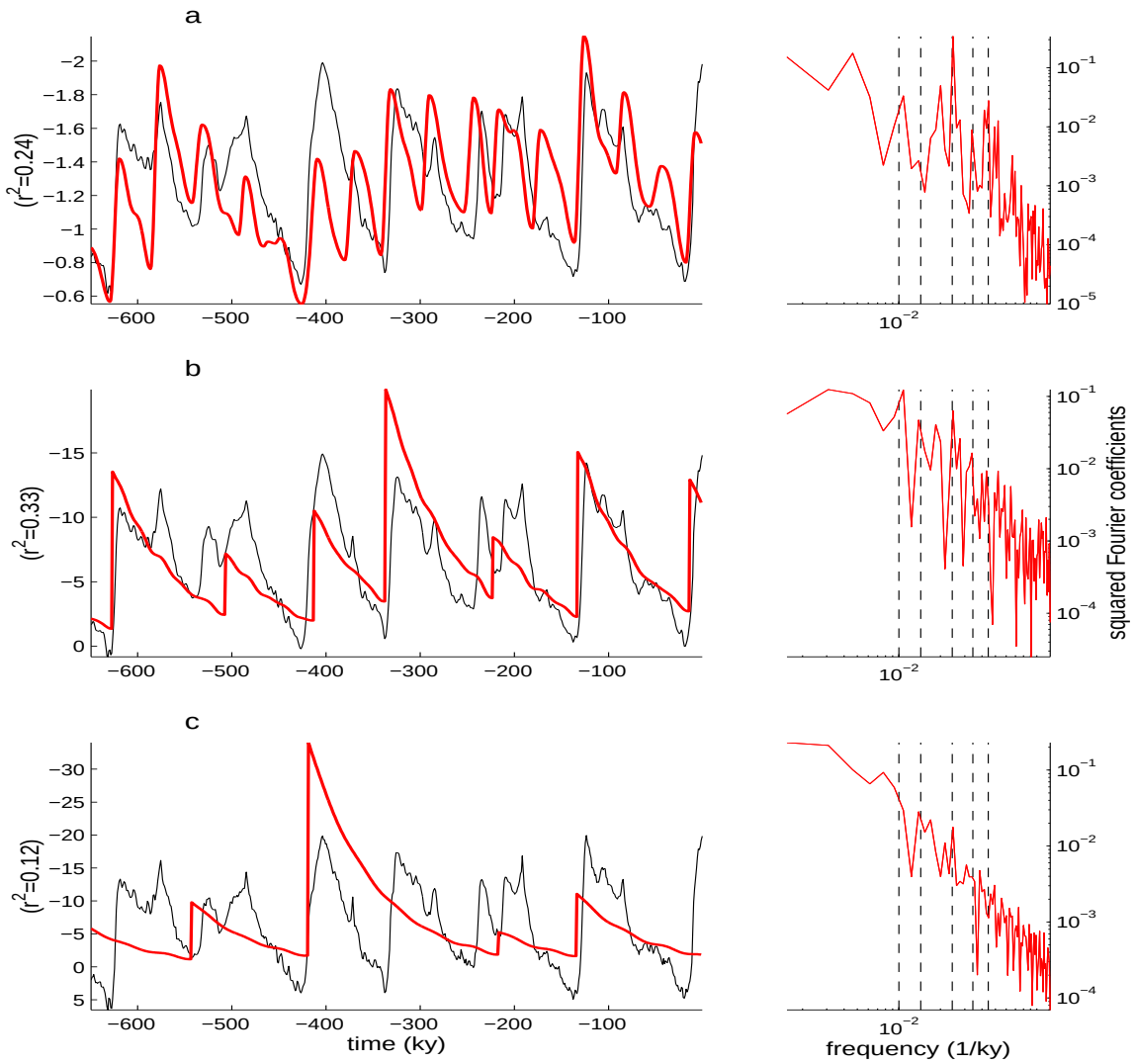

Figure 5-1: Results from the Imbrie model (red) after adjusting the free parameters to maximize the cross-correlations with EOF1 (black) over the last 650KY. EOF1 is scaled to the model output. **a** shows the best fit achieved when both obliquity and precession are included in the forcing, but requiring the ablation timescale to be longer than 1KY. **b** is the best fit when ablation timescales are permitted to be arbitrarily small, here a best fit is achieved for T_2=0.05KY. **c** shows the best fit when the model is forced only by obliquity variability, again using very rapid ablation. The squared-cross-correlations between model results and EOF1 are shown at left. Although difficult to see on this plot, the terminations in EOF1 occur over a period of roughly 10KY. At right are periodograms of the model results with vertical dashed lines indicates bands centered on 1/100, 1/70, 1/41, 1/29, and 1/23KY —- the bands of energy which exceed the 95% confidence level in EOF1.

shows 100KY variability; prior to 650KY BP, the glacial cycles have less low-frequency variability [e.g. *Raymo and Nisancioglu*, 2003]. To help ensure that the estimated parameters are the best global fit, rather than a localized feature in parameter space, the annealing algorithm is initiated at random locations in parameter space. For the Imbrie model, regardless of where the search is initialized, the same solution is consistently arrived at, suggesting it is globally the best fit for a one significant figure set of parameterizations.

The values which maximize the cross-correlation between EOF1 and the model results are $T_1 = 90KY$, $T_2 = 10KY$, $\phi = 60°$, and $\alpha = -0.09$ yielding a squared-cross-correlation of 0.24. Relative to the original fit by *Imbrie and Imbrie* [1980], the reglaciation timescale derived from the fit to EOF1 is closer to observations, the obliquity variability is seen to be more important, but the squared-cross-correlation is nearly the same. The squared-cross-correlation between model and output will also be referred to as the fraction of variance described by the model. The significance of the variance described and robustness of the parameterization should be greater because the duration of EOF1 is three times that of the observations used by *Imbrie and Imbrie* [1980]. The new fit is shown in Figure 5-1.

To gauge how sensitive the results of the Imbrie model are to the exact parameterizations, a series of perturbation experiments are carried out. The squared-cross-correlation between model results and EOF1 is computed as a function of a single varying parameter while holding the others fixed at the optimal values determined using the simulated annealing method. Results are shown in Figure 5-2. As expected for a successful optimal fit of the model to observations, the largest cross-correlation is achieved when no perturbations are made to the model. The timescales are adjusted over a range of 10 and 200KY for T_1, and 1 and 20KY for T_2. The Imbrie model is most sensitive to making the accumulation timescale short (small values of T_1), dropping the squared-cross-correlation by a factor of four. The precessional phase of the insolation forcing was varied from 10° to 360° and the ratio of precession to obliquity energy was varied from zero ($\alpha = -1$) to three ($\alpha = 2$). Smallest correlations occur when the precession phase is changed by 180°, giving the equivalent of anomalously large Southern Hemisphere summer insolation. Overall, the cross-correlation between the Imbrie model results and EOF1 vary smoothly with changes in its parameterization. Even for large changes, the Imbrie model retains some correlation with EOF1 showing that the Imbrie model is fairly robust to perturbations in the

parameterizations.

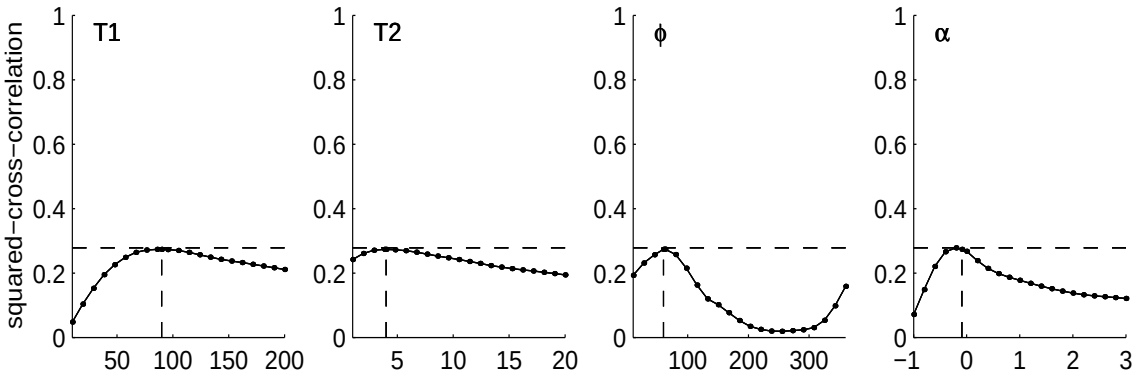

Figure 5-2: Model sensitivity to parameter perturbations. Starting from the best fit, the squared-cross-correlation between model results and EOF1 are computed over the last 650KY as a function of one of the parameters while holding the others fixed. From left to right are the $T1$ and $T2$ measured in KY, ϕ the precessional phase measured in degrees, and α which controls the ratio of obliquity to precession energy; minus one is no precession, zero is equal parts precession and obliquity.

5.2.2 A new source of low-frequency variability

A second fitting exercise was also conducted, this time allowing the ablation time-constant to become arbitrarily small. The variance described by the model now increases from 0.25 to 0.33 for a fit of $T_1 = 70KY$, $T_2 = 0.05KY$, $\phi = 90°$, and $\alpha = 1$. This result suggests that very rapid terminations are better able to describe the timing and amplitude of the climate events recorded in EOF1. Taken literally, an ablation timescale on the order of 50 years is unphysical, but there is a lesson to be learned from this fit. Imbrie and Imbrie [1980] interpret the difference between time-constants as indicating the degree of nonlinearity in the system — were the time-constants equal, the system would be linear. The very rapid terminations required by the small values of T_2 suggest the presence of some strongly nonlinear mechanism operating during glacial terminations. While the simplicity of the Imbrie model is appealing, it appears that capturing such strongly nonlinear behavior requires pushing the ablation timescale to an extreme case. Glacial terminations typically occur over a period 10KY [e.g. *Imbrie et al*, 1992], the 50 year timescale parameterized for T_2 is interpreted as the attempt of a weakly nonlinear model to capture processes which are in fact strongly nonlinear.

A final fitting exercise was conducted to see how much of the variability in EOF1 can be described as the response of the Imbrie model to obliquity forcing alone, i.e. setting $\alpha = -1$ in Eq. 5.2. Such a simplified insolation function has a number of advantages. First, it eliminates two degrees of freedom associated with α and ϕ, so that model results are less dependent on tuning. Second, as discussed in Chapters 2 and 3, there are a large number of uncertainties associated with interpreting the response of the climate system to the precessional modulation of the insolation forcing. Obliquity variability is more straight-forward in that its phase is fixed and obliquity period variability is directly present in the insolation forcing. Finally, as shown in Chapter 4, there is a significant phase coupling between glacial terminations and obliquity, making it interesting to explore how much of the glacial variability can be described as a response to obliquity forcing alone.

To distinguish the various forcing scenarios, parameterizations corresponding to combined obliquity and precession forcing are referred to as $\mathcal{F}_{op}$, while those corresponding to obliquity forcing only are referred to as $\mathcal{F}_o$. The best $\mathcal{F}_o$ fit of the Imbrie model to EOF1 occurs for $T_1 = 90KY$ and $T_2 = 0.1KY$, and describes 0.12 of the variance in EOF1. For these parameterization, the Imbrie model behaves in a manner qualitatively similar to the random walk model introduced in Chapter 4. Both slowly accumulate ice and then, once a threshold is crossed, rapidly terminate; differences are that the Imbrie model threshold varies according to obliquity and is completely deterministic.

Figure 5-1 shows that the $\mathcal{F}_{op}$ parameterizations result in model output which has a deficit of 100KY variability and too much energy at 400KY periods. In this parameter range, as explained by *Imbrie and Imbrie* [1980], the 100KY variability is attributed to the demodulation of the eccentricity envelope of the precession parameter, which itself has weak 100KY variability and much stronger 400KY variability (see Chapter 2). When rapid and strongly nonlinear glacial terminations are permitted, a new source of low-frequency variability is found in the model. The timescale of reglaciation now itself generates low-frequency variations. That is, in the Imbrie model with very rapid terminations, it takes more than 40KY to regrow ice-sheets large enough that the threshold criterion for melting is again crossed. In this view, the basic 100KY period is set by the growth timescale of large ice-sheets while the triggering of the terminations is controlled by the local maxima in the insolation forcing. This mechanism is highlighted by completely removing the precession pe-

riod variability from the forcing function of the Imbrie model. If permitted to have abrupt terminations, the Imbrie model can generate low-frequency variability when forced by obliquity alone. This slow regrowth mechanism will be incorporated into a new model, inspired by the Imbrie model, but better suited to generating glacial cycles using a slow increase in ice-volume followed by a rapid and strongly nonlinear termination.

5.3 The Paillard model

Paillard's [1998] model is interesting to study on two accounts: first it is able to reproduce the glacial cycles in striking detail, second it posits a series of rules by which the climate system might behave. Insomuch as the rules appear to work, it is useful to see if some further physical meaning can be derived from them. *Paillard* states that the threshold model was inspired by a simple ocean circulation model and that the climate system generally appears to have thresholds, but the connection between this model, ocean circulation, and the ice-ages is not discussed in further detail. Building from the results in the previous section, this section explores the question of why the Paillard model works as well as it does.

The Paillard model can be written in discrete from as

$$V_{t+1} = V_t + \frac{V_R - V_t}{T_R} - \frac{\mathcal{F}'}{T_{\mathcal{F}}}, \tag{5.3}$$

$$R = \begin{cases} i & \text{if } \mathcal{F}' > F_1 \text{ and } R' = G, \\ g & \text{if } \mathcal{F}' < F_0 \text{ and } R' = i, \\ G & \text{if } V > 1, \end{cases}$$

$$V_R = \begin{cases} 0 & \text{if } R = i, \\ 1 & \text{if } R = g, \\ 1 & \text{if } R = G, \end{cases}$$

$$T_R = \begin{cases} T_i & \text{if } R = i, \\ T_g & \text{if } R = g, \\ T_G & \text{if } R = G, \end{cases}$$

$$\mathcal{F}' = \left\langle \mathcal{F} + \sqrt{4a^2 + \mathcal{F}^2} \right\rangle. \tag{5.4}$$

The model states that changes in ice-volume are proportional to the difference between a reference ice-volume (V_R) and current ice-volume (V_t) minus a forcing proportional to a rectified insolation function ($\mathcal{F}'$). $\mathcal{F}'$ is normalized so that the right hand term in Eq. 5.4 is in units of ice-volume per KY. The reference ice-volume and timescale (T_R) change depending on the glacial state (R) which can be: interglacial ($R = i$), mild glacial ($R = g$), or full glacial ($R = G$). Transitions from states G to i occur when the rectified insolation ($\mathcal{F}'$) is greater than the threshold value F_1, from i to g when $\mathcal{F}'$ is less than the threshold value F_0, and from g to G when the normalized ice-volume exceeds one. No other state transitions are permitted, so that the model cycles through the *i-g-G* sequence at a rate determined by the intervals between which $\mathcal{F}'$ crosses the insolation thresholds and by the time-constants which regulate how quickly ice-volume increases. The requirement for a sufficient amount of ice-volume to accumulate prior to a terminations is reminiscent of the Imbrie model behavior when parameterized to have very rapid ablation events. That is, the rate of ice accumulation is again regulating the duration of the glacial cycles.

Paillard [1998] presents model results with respect to insolation at 65°N, but also notes that the use of different high-latitude summer insolation curves give similar results. The choice of the insolation forcing function lends additional degrees of freedom in the model, and to make these specific the insolation forcing function presented by *Imbrie and Imbrie* [1980] (Eq 5.2) is used. The Paillard model also employs a rectification of the insolation forcing which is rationalized on the basis that, empirically, ice-volume is less sensitive to insolation forcing during *colder* periods. Such rectifications of the low-frequency variability associated with orbital variations should, ideally, be included directly in the model as this would aid in distinguishing between the forcing and climatic response, and this representation is easily achieved by substituting Eq. 5.5 into Eq. 5.4. This additional nonlinear transformation of the forcing function is important for obtaining a good fit between model output and observations. Without such rectification, the best fit obtained between the model results and EOF1, estimated from numerous simulated annealing runs, was a squared-cross-correlation of 0.55. Conversely, using this additional degrees of freedom in the forcing function consistently yielded squared-cross-correlations above 0.7.

It is useful to consider the influence of the insolation rectification on the behavior of the *Paillard* model in some more detail. The form of the rectification function in Eq 5.4 shows that as a approaches infinity there is no rectification effect. Conversely,

when a is zero the insolation signal would be fully rectified, except that subsequently the insolation is then normalized to zero-mean and unit variance. This last normalization operation is important. Setting the forcing function to zero-mean after rectification generates a forcing distribution which is usually weakly negative, but with bursts towards strongly positive values. Thus the rectified forcing distribution is qualitatively similar to the histogram of the rate of change of EOF1 (see Figure 4-1). Apparently, the nonlinear transformation of the insolation conditions the distribution of the forcing to be similar to the distribution of the rate of change of ice volume. In particular, the rectified insolation will contribute to slow accumulation in ice-volume and rapid ablation.

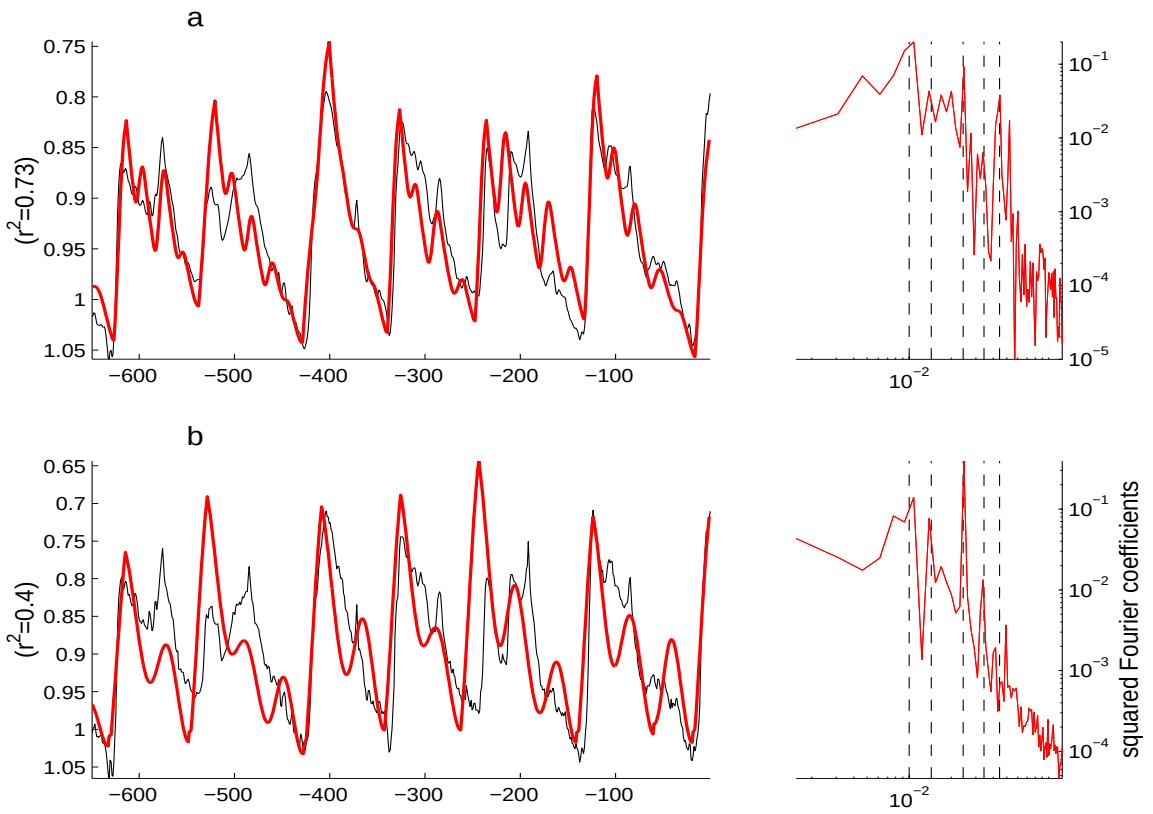

Figure 5-3: Results of the Paillard model (red) after adjusting the free parameters to maximize the cross-correlations with EOF1 (black) over the last 650KY. **a** shows the fit achieved when both obliquity and precession are included in the forcing, while **b** uses only obliquity forcing. At left the squared-cross-correlation is listed. Also shown at right are the periodograms of the model results. The vertical dashed lines are at frequencies of 1/100, 1/70, 1/41, 1/29, and 1/23KY and indicate the significant bands of energy found in EOF1. For the obliquity forcing only results, the Paillard model shows excesses of energy near each of these bands.

There are twelve degrees of freedom in the Paillard model: three for insolation, four time-constants, three rules for switching between climate states, and two reference ice-volume states (one reference state is not counted because the normalization of the model output is arbitrary). Using the simulated annealing technique previously discussed, a search was made for the parameterizations which maximize the correlation with EOF1. A maximum squared-cross-correlation of 0.73 was achieved for $F_0 = -0.8$, $F_1 = -0.006$, $T_i = 80$KY, $T_g = 30$KY, $T_G = 60$KY, $T_{\mathcal{F}'} = 200$KY, $a = 4$, $\phi = 100°$, and $\alpha = 3$. The fit with the observations is shown in Figure 5-3 along with the periodogram of the model results. The Paillard model's success at fitting EOF1 lies in reproducing the timing and amplitude of each glacial cycle as well as some of the fine scale structure. Similar to the Imbrie model, the periodogram shows a red-noise background with concentrations of variability near 1/100KY, the obliquity (1/41), and precession bands (1/23, 1/19). There are no concentrations of variability at the 1/70 or 1/29KY periods, as were observed for EOF1 and discussed in detail in Chapter 3.

The Paillard model achieves an excellent fit with EOF1, but given the relatively large number of degrees of freedom, it is difficult to distinguish whether the model is skillful or simply a clever match between two signals. One measure of skill is to compare the degrees of freedom in the model to the degrees of freedom in the record it seeks to fit. Counting the degrees of freedom in EOF1 is somewhat subjective. As a lower limit one might count each glacial cycle and conclude there are seven degrees of freedom. Reproducing seven events hardly seems skillful given the twelve degrees of freedom in the model. Another count, however, might include both the amplitude and timing of each termination as well as more detailed structure such as plateaus during stage five and local maxima during stage seven, giving roughly four degrees of freedom per glacial cycle and over twenty in total. In this view, roughly twenty degrees of freedom are accurately rendered using a model with twelve degrees of freedom. Such an arbitrary count is not conclusive, but for the time being I proceed under the assumption that the Paillard model has some real skill.

The sensitivity of the model results to changes in parameterizations can be estimated by perturbing each parameter while keeping the others fixed. The squared-cross-correlation between the Paillard model and EOF1 is shown as a function of parameter perturbation in Figure 5-4. Unlike the smoothly varying cross-correlations found for the Imbrie model, the Paillard model exhibits rapid transitions in cross-

correlation, probably related to changes in the crossing of one or more the thresholds prescribed by the model. The Paillard model shows strong sensitivity to adjustments in most parameters, with the notable exception of T_G which can apparently take on nearly any value without affecting the results. Thus the number of degrees of freedom counted for the Paillard model is decreased by one to eleven.

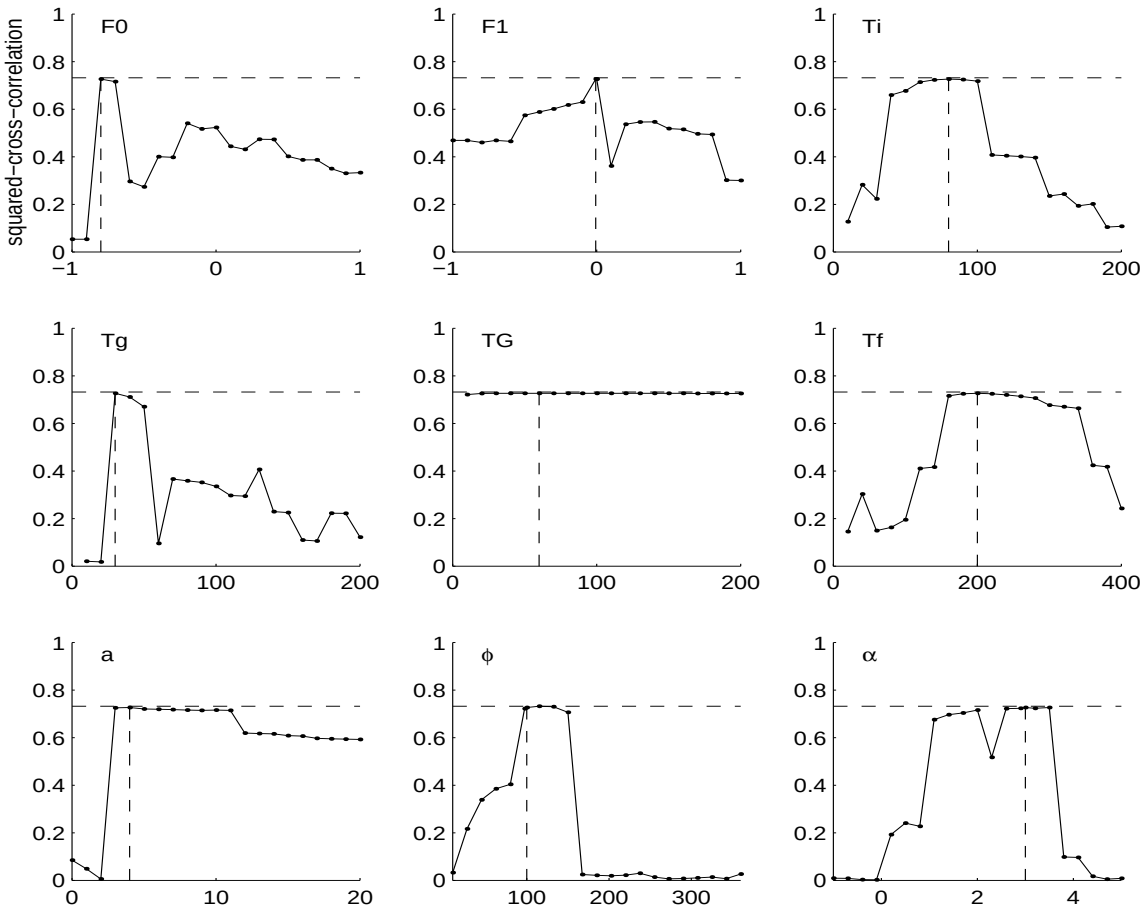

Figure 5-4: Similar to Figure 5-2, but now for the Paillard model's sensitivity to parameter perturbations. Starting from the best fit, the cross-correlation between model results and EOF1 is computed over the last 650KY after varying one of the parameters over a range of plausible values while holding the other fixed. From left to right are $\mathcal{F}_o$ and $\mathcal{F}_{op}$ which are threshold for the insolation forcing, Ti, Tg, TG and Tf, which are time constants measured in KY, a which is a rectification parameters, and ϕ and α which control precessional phase and amplitude. Apparently there is no model sensitivity to TG, thus the degrees of freedom in the Paillard model should be reduced by one.

That the Paillard model has an intrinsic timescale, set by the thresholds and time-constants, suggests that it can generate 100KY variability when forced by a variety of

quasi-periodic signals. It is interesting to see whether the Paillard model can generate a credible fit with EOF1 when forced by obliquity alone. The Imbrie model was able to generate a low-frequency climate response when forced by obliquity alone, but the overall fit with the observations was poor. Now, a simulated annealing fit of the Paillard model with EOF1 yields a squared-cross-correlation of 0.4 for parameter values of $F_0 = 0.3$, $F_1 = -0.2$, $T_i = 70$KY, $T_g = 40$KY, $T_G = 20$KY, $T_f = 200$KY, and $a = 20$, where there are two less degrees of freedom because precession is excluded. Judging the significance of the 0.4 squared-cross-correlation is nontrivial because it involves estimating the probability distribution associated with all models which might have been built using ten degrees of freedom [see e.g. *Efron*, 1971]. It is later shown [see Table 5.1] that this correlation appears to be insignificant when compared with correlations achieved by other simple models.

As shown in Figure 5-3, the Paillard model still reproduces the basic 100KY structure observed in EOF1 when forced only by obliquity. The periodogram of the obliquity Paillard model results shows concentrations of energy near the obliquity and the 1/100KY bands, although the obliquity band appears too energetic relative to the 100KY band. More interesting is that the model results show energy near the 1/70, 1/29, and 1/23KY bands, consistent with the periodogram of EOF1. While no claim is made that the fit between EOF1 and the obliquity Paillard model is significant, it does serve to demonstrate that obliquity forcing alone can yield a *good* fit with the glacial cycles and produce the combination tones involving the 1/100 and 1/41KY bands of variability consistent with EOF1 [see Chapter 3].

5.4 A new model

It is useful to summarize those elements which appear to be important for constructing a skillful simple model of the glacial cycles. These elements are first qualitatively discussed, after which a new simple model is constructed.

5.4.1 Qualitative features

1. Coupling of termination with orbital variations: In Chapter 4 it was found that obliquity and glacial terminations appear to be nonlinearly coupled. In particular, terminations appear to be triggered by high values of obliquity. In the Imbrie model terminations tend to occur during a positive phase of the obliquity

forcing because melting only occurs when insolation forcing is greater than negative ice-volume. Similarly, in the Paillard model the switch from a full glacial to an interglacial only occurs when insolation surpasses some threshold. Thus it seems that tying the triggering of a termination to changes in the Earth's orbit and/or orientation is an effective means of setting the phase of the glacial cycles.

2. Slow accumulation: Terminations only occur every second or third obliquity cycle, suggesting the presence a climatic timescale longer than the obliquity period. Earlier it was shown that the Imbrie model can generate a long timescale response by slowly reaccumulating sufficient ice-volume for an ablation event to occur. Similarly, the Paillard model transitions from a glacial to full glacial state only after sufficient ice-volume has accumulated, and this typically requires a period of two or three obliquity cycles. Thus one means of generating a long timescale response is to specify an amount of ice-volume required for a termination to occur and employ a relatively slow accumulation rate.

3. Episodic reglaciation: Apart from the basic structure of rapid ablation and slow accumulation, one also observes significant kinks in the reglaciation process. That is, reglaciation seems to proceed episodically. The reglaciation after termination two provides a good example where ice-volume appears to plateau during substages five and four before bottoming out towards the Last Glacial Maximum. The plateaus are further punctuated by local maxima, but which are smaller features than the general plateau structure. These plateaus are some of the best constrained aspects of ice-volume change, being unambiguously recorded in the coral terraces of uplifting topography [e.g. at Barbados, *Broecker*, 1968; *Gallup*, 2002]. The Paillard model goes further in mimicking the detailed features in the $\delta^{18}O$ record than does the Imbrie model. It achieves this more detailed structure by specifying climatic states so that the model output tends to re-glaciate in a series of steps. It is thus desirable for a model not to monotonically reglaciate, but rather to have a sequence of reglaciation episodes, perhaps paced by either orbital or stochastic variations.

4. Memory: The Paillard model cycles through a fixed sequence of states, requiring the system to remember its past state. The case of the Imbrie model is more involved. First, one of the major problems with the parameterization of the Imbrie model shown in Figure 5-1b and c is that terminations occur in a single timestep. This means that

the size of the terminations are related to the time-stepping used in integrating the model. Thus the Imbrie model, as presented here, might better be thought of as a map which describes how ice-volume at one instant is related to ice-volume 1KY later. Without very rapid melting, the terminations in the Imbrie model would abort as soon as the threshold condition is crossed. If the ablation events in the Imbrie model incorporated a time delayed state dependence, termination could continue beyond this threshold crossing without resorting to such rapid timescales.

5.4.2 A quantitative expression

Each of the features discussed in the previous section can be incorporated into a simple, deterministic model using only a handful of adjustable parameters. Written in discrete form the model is

$$V_t = V_{t-1} - V_{t-L}^P \times \frac{b - \mathcal{F}}{T} \qquad P = \begin{cases} 0 & \text{if } \mathcal{F} < b \\ p & \text{if } \mathcal{F} > b. \end{cases} \tag{5.5}$$

Here V is ice-volume, L is a time-lag, T is a time-constant, b is a threshold which also gives a bias towards positive accumulation, and P is an exponent whose value depends on whether the model is accumulating or ablating. When $b > \mathcal{F}$, $P = 0$, making accumulation linearly dependent on insolation anomalies. Ablation occurs when the forcing is greater than the accumulation bias, and now P is some positive integer (recall, all parameters are chosen to have only one significant figure), making the rate partially dependent on ice-volume L years ago. If V_t is less than zero, it is reset to zero on the physical grounds that one cannot have negative ice-volume. $\mathcal{F}$ is given by Eq 5.2, and represents anomalies in modes of insolation forcing. If precessional effects are included in $\mathcal{F}$, the model has six degrees of freedom; otherwise, if only obliquity forcing is used, it has four. To distinguish the model given by Eq 5.5 from the Imbrie and Paillard models, it will be referred to as the *new model*.

Though the notation is more cumbersome, it is possible to write Eq 5.5 so that the value of P remains fixed. First define $\gamma = (b - \mathcal{F})/T$ so that the model may be written as

$$V_t = V_{t-1} - \gamma V_{t-L}^{p(|\gamma|+\gamma)/2},$$

where $|.|$ indicates the absolute value. The exponent of V_{t-L} goes to zero when $\gamma < 0$, and equals p for $\gamma \geq 0$, thus playing the same role as the conditionality, but not

requiring any rules for switching the exponent.

It proves convenient to define the units of this model to be the ice-volume equivalent of a hundred meters of ice-volume. By this definition, one hectometer (hm) represents an important threshold in the model system. When lagged ice-volume is less than one hm, the ablation term, V^P_{t-L}, is small and little melting occurs, while values greater than one hm can induce rapid ablation. For a glacial termination to occur in the new model, two conditions must be met: the ice-volume must exceed one hm and the orbital forcing must induce a melting state. When one hm of ice-volume accumulates more slowly than the period between orbital melting states, the basic period of the glacial cycles will be controlled by the accumulation rate.

The formulation of Eq 5.5 bears two important parallels with the much more sophisticated thermomechanical ice-sheet model of *Marshall and Clark* [2002]. First, the results from the thermomechanical ice-sheet model indicate that thermal enabling of basal flow is an important feedback controlling the deglaciation of North American ice-sheets, and that this basal warming requires the presence of thick, high-elevation ice-sheets. As noted, the new simple model also requires sufficient ice-volume for a deglaciation to occur. A second parallel is that basal temperatures in *Marshall and Clark*'s model lag surface temperatures by 10KY. The parameter L in Eq. 5.5 can thus be thought of as the timescale for heat to penetrate from the surface of an ice-sheet to its base. There are, however, some unresolved differences. *Marshall and Clark* [2002] conclude that at large sizes ice-sheets become independent of the orbital forcing and affect their own demise. The results of Chapter 4 imply the opposite, that the initiation of deglaciation are triggered by high obliquity states, but the physical mechanism which ties obliquity to the triggering of terminations is unclear. One possibility is that increased high-latitude insolation causes surface melting of the ice-sheet, and the associated run-off aids in lubricating basal slippage. More work should be undertaken to determine the extent to which orbital variations could influence the results of *Marshall and Clark*'s model and the extent to which Eq. 5.5 is a faithful simplification of the model physics, but which is beyond the scope of this thesis.

Using the simulated annealing algorithm, a best fit is achieved between the model results and observations for a time constant $T = 80KY$, accumulation bias $b = 1$, power $n = 8$, lag $L = 9ky$, precessional phase $\phi = 100°$, and insolation ratio $\alpha = 0.04$; yielding a squared-cross-correlation of 0.60. If the model is forced only by obliquity variability, the best fit occurs for $t = 90KY$, $b = 0.9$, $n = 9$, and $L =$

$9KY$; and achieves a squared cross-correlation between model results and observations of 0.43. The meaning of this correlation will become more clear when the model results are compared with one another. Figure 5-5 shows the model results for the $\mathcal{F}_{op}$ (obliquity and precession) and $\mathcal{F}_o$ (obliquity only) forcing cases, as well as the associated periodograms.

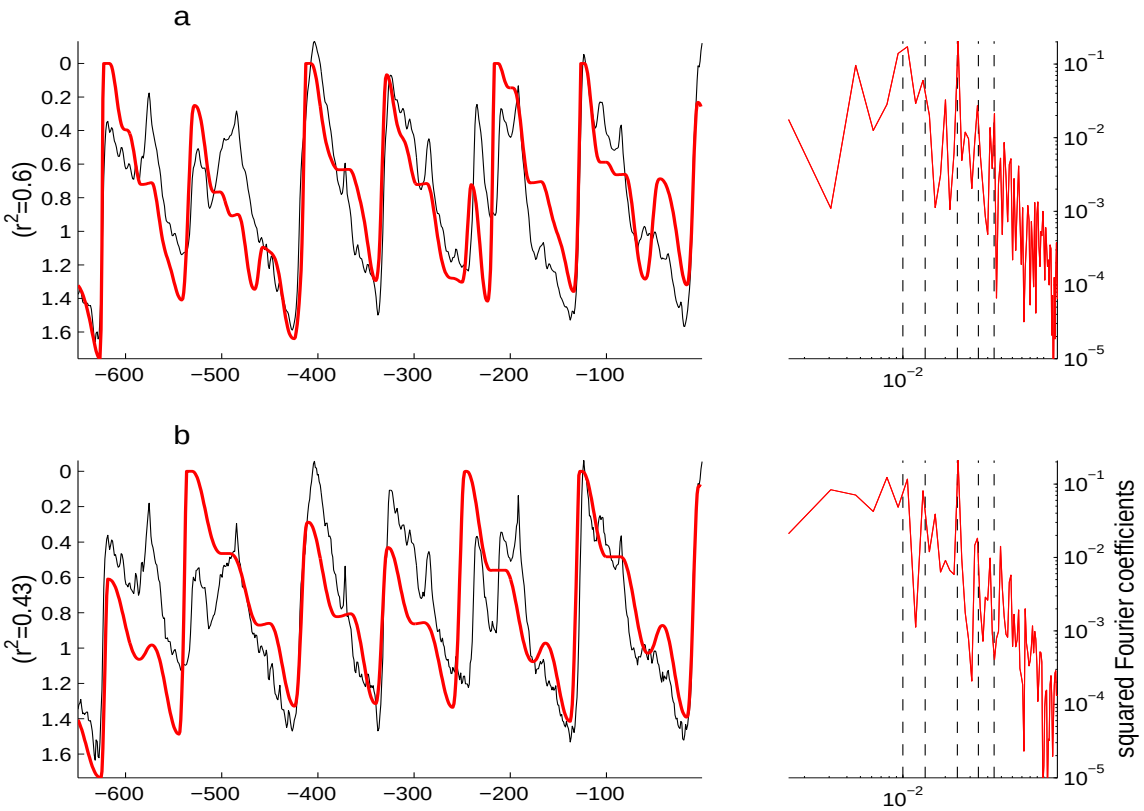

Figure 5-5: Model results (red, thick line) where parameters are chosen to maximize the cross-correlation with EOF1 (black, think line) **a** Model results using an orbital forcing comprised of obliquity and precessional variations ($\mathcal{F}_{op}$) along with the periodogram of the model results. **b** Results when the model is only forced by obliquity ($\mathcal{F}_o$). The vertical dashed lines at right indicate frequencies of 1/100, 1/70, 1/41, 1/27, and 1/23KY. Concentrations of variability exist at bands near each of the indicated frequencies for both model results a and b.

5.5 Robustness

In the introduction of this chapter, one of the guidelines for assessing simple models was that the results should be robust to small changes in parameters and acceptable

levels of noise. What constitutes small and acceptable is largely open to interpretation; but it is useful to draw some comparisons between each models behavior when the parameters are perturbed.

5.5.1 Initial conditions

Figure 5-6 shows that for the $\mathcal{F}_{op}$ parameterizations (including precession and obliquity) each model becomes phase-locked with the forcing independent of initial conditions. This behavior is important because it indicates the models have finite memory and are controlled solely by external forcing once the initial transients damp out. This behavior simplifies the analysis of the records and prevents the initial conditions from entering as a degree of freedom in model behavior. All model runs shown in this thesis are started at least 500KY prior to the period analyzed. This is a large enough lead time to ensure that the initial conditions are unimportant, with the exception of when the new model is in a chaotic regime, as discussed in a later section.

5.5.2 Parameterizations

The sensitivity of the Imbrie and Paillard model results to changes in parameterization were discussed earlier (see Figures 5-2 and 5-4). Figure 5-7 shows that the sensitivity of the new model to perturbations. Changes in the time-constant, the time-lag, and the forcing function of the new model all strongly influence the cross-correlation between EOF1 and model results. Generally speaking, the Imbrie model is least sensitive to perturbation in the parameters, followed by the Paillard model, and then the new model. According to the rules of the simple model building game outlined by *Saltzman* [2002] the new model must be discounted to some degree due to the sensitivity of the results to small perturbations. Later, the model is shown to be capable of chaotic behavior, and it is not surprising that small changes in its parameterization can cause large changes in its behavior.

Just as model robustness to small changes in parameterizations is desirable in terms of achieving a simple result, so is robustness to perturbations in the forcing function. It is expected that the external climate forcing contains not only low-frequency shifts, but also relatively rapid perturbations due to solar variability, cosmic dust, and high frequency perturbations to the earth's orbit [e.g. *Muller and MacDonald*, 2000]. Internal variability should also be expected in the form of changes in albedo (e.g.

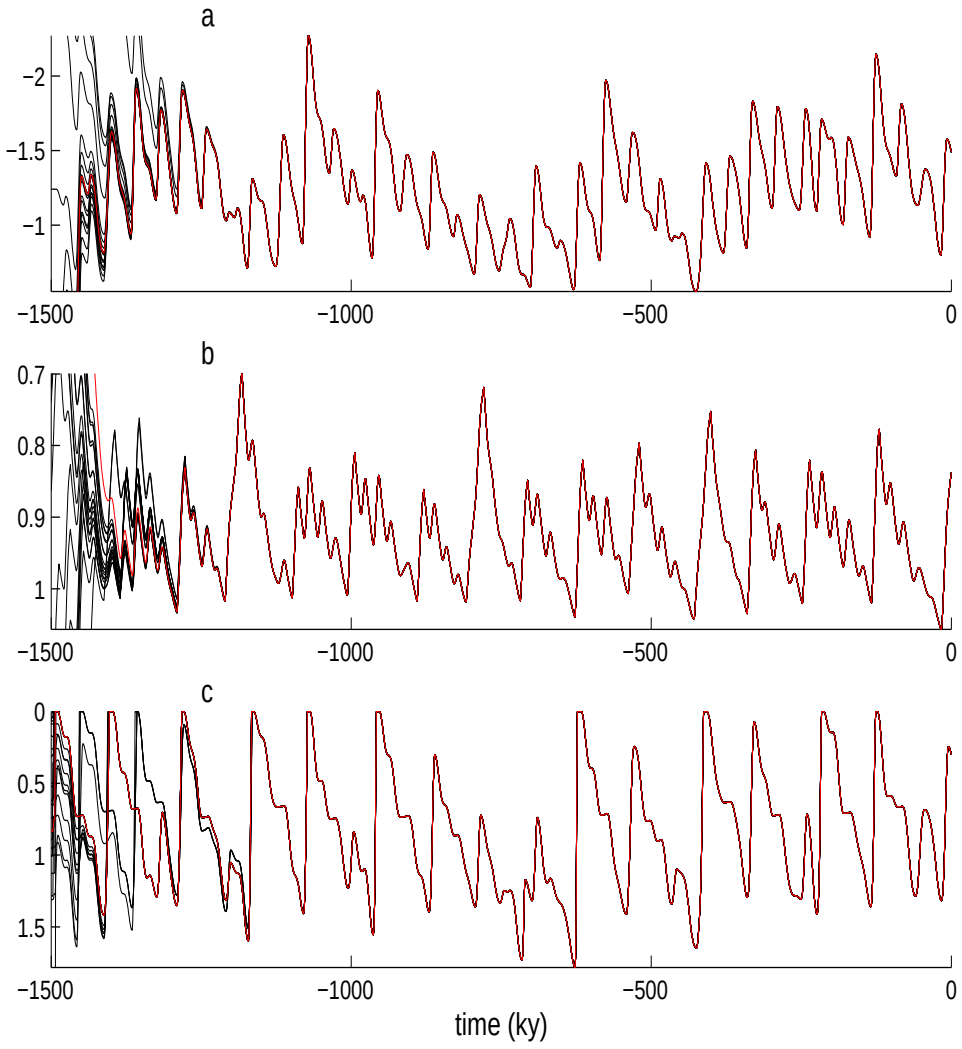

Figure 5-6: Sample trajectories of each model using randomized initial conditions: **a** the Imbrie model, **b** Paillard mode, and **c** the new model. Each of the models converge onto a single trajectory. The last realization from each model is plotted in red.

clouds, sea-ice, and snow cover variability), variations in atmospheric composition and aerosol loading (e.g. dust, forest fires, and volcanic eruptions), and variations in the atmospheric and oceanic fluxes of moisture and heat, to name but a few of the expected sources of variability. Figure 5-8 shows how the squared-cross-correlation between model results and EOF1 falls off with the addition of increasing amounts of band-limited white noise to the insolation forcing. Plotted are the average squared-cross-correlation between EOF1 and a hundred model results obtained from random realizations of the forcing with the prescribed noise level. The sensitivity to noise

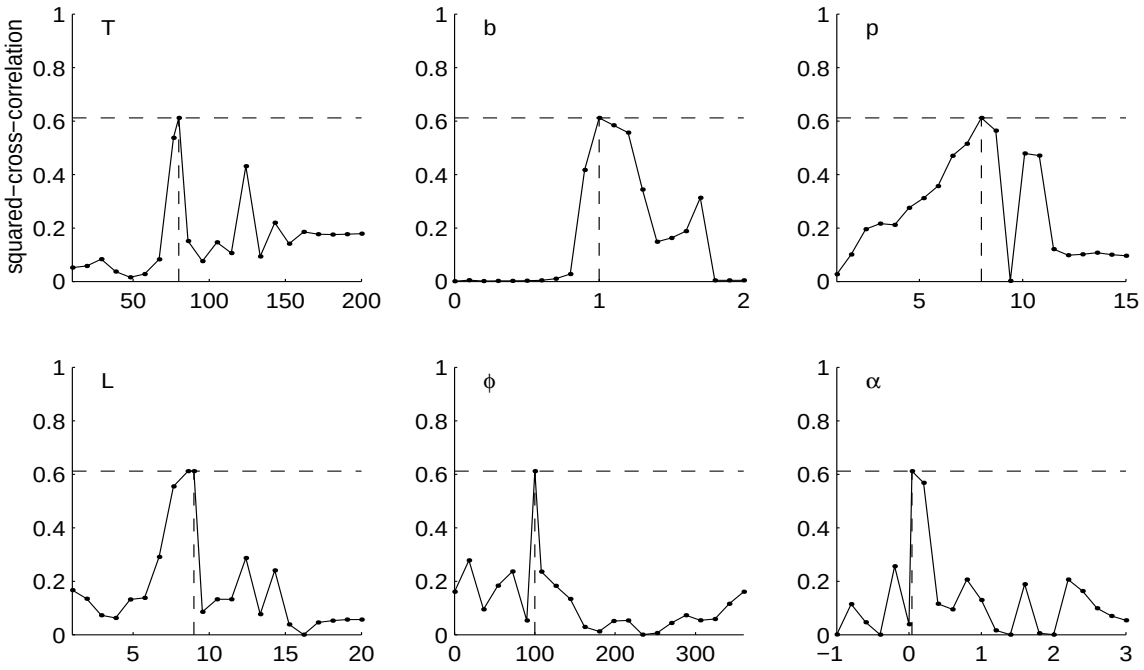

Figure 5-7: Similar to Figures 5-2 and 5-4, but now the sensitivity of the squared-cross-correlation between the new model and EOF1 to parameter perturbations. Starting from the best fit, the cross-correlation between model results and EOF1 is computed over the last 650KY after varying one of the parameters over a range of plausible values while holding the other fixed. From left to right are the time-constant T measured in KY, the accumulation bias b, the power-law exponent n, the time-lag L measured in KY, and the precessional phase ϕ and amplitude α.

initially appears to scale with the degrees of freedom available to each model. Thus, while the unperturbed Paillard model results describe the most variance, when the fraction of noise to orbital forcing variance is 0.1, all three models have an average squared-cross-correlation with EOF1 of roughly 0.3. By the time the noise variance equals the insolation forcing variance, all the models describe only a minor fraction of EOF1 with the new model preforming the worst. The forcing perturbation results indicate that the skill of these models strongly depends on how important stochastic variability is at long timescales.

In calculating the response of the simple models to stochastic forcing perturbations, it is assumed the system is discrete and the perturbations are uncorrelated, thus corresponding to the Ito calculus. For a discussion of Ito versus other forms of calculus see *Penland* [2003]. A more detailed investigation would incorporate the likely time-correlated nature of the stochastic perturbations, the continuous (i.e. not

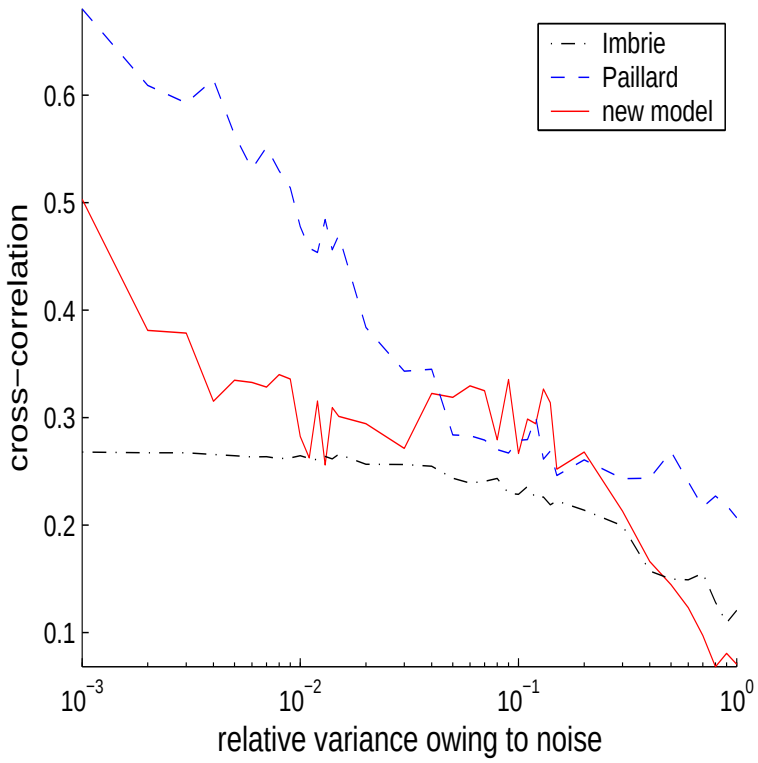

Figure 5-8: Model sensitivity to the addition of band-limited white noise to the forcing. Plotted is the squared-cross-correlation between the model results and EOF1 using the $\mathcal{F}_{op}$ parameterizations. The x-axis indicates the ratio of noise to orbital forcing variance — a value of one indicates equal noise and insolation variance. Note the x-axis is logarithmic. Each value is the average of a hundred noisy model runs. Results assume a discrete system corresponding to the Ito calculus.

discrete) nature of ice-volume variability, and possibly such factors as the integrated response of the climate system to higher-frequency annual or even diurnal insolation variability. The more simple stochastic response calculated here suffices to make the point that the response of these models critically depends on the degree of stochastic variability. If at timescales of tens of thousands of years, most of the climate system is controlled by low-frequency insolation forcing, then the results of these simple models can be interpreted at face value. Indeed, the coupling of obliquity with the terminations provides evidence that low-frequency shifts in insolation are important for controlling the long-term evolution of the climate system. On the other hand, the presence of precession band variability in a variety of climate indicators indicates the importance of the annual cycle (see the discussion regarding rectification in Chapter 2), and suggests that high-frequency variability also contributes to long-term cli-

mate change. Separating the stochastic from the deterministically forced components of climate variability remains a challenging problem in dynamical paleoclimatology.

5.5.3 Other measures of robustness

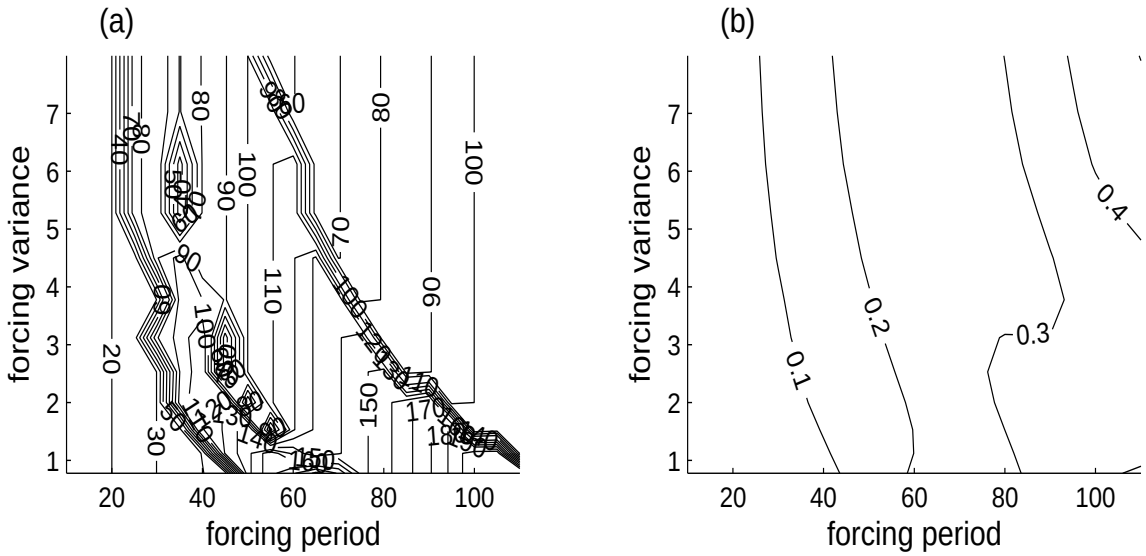

Figure 5-9: Model response to periodic forcing. **a** The period associated with the most energetic model response is contoured against the forcing variance and forcing period. **b** The variance of the model response contoured against the forcing variance and period. All model runs have 1KY time-steps for 5000KY.

In interpreting the model's sensitivity to perturbations, a distinction should be made between the sensitivity of a particular model realization to perturbations in the forcing, and the sensitivity of the underlying mechanisms to these same perturbations. For instance, the incorrect timing of a termination is quite different than the absence of 100KY variability. In any model with thresholds, one can expect realizations of the model to markedly differ when changes in parameterizations or the introduction of noise cause the threshold crossings to change. In the new model it is evident that threshold crossings are sensitive to the parameterizations. As the cross-correlation between model results and EOF1 heavily depends on the timing of the terminations, the incorrect timing of a single event will generally make it appear that the model's skill is significantly diminished. For these reasons phase-free statistics, such as the periodogram, can lend valuable insight into the robustness of the underlying model behavior.

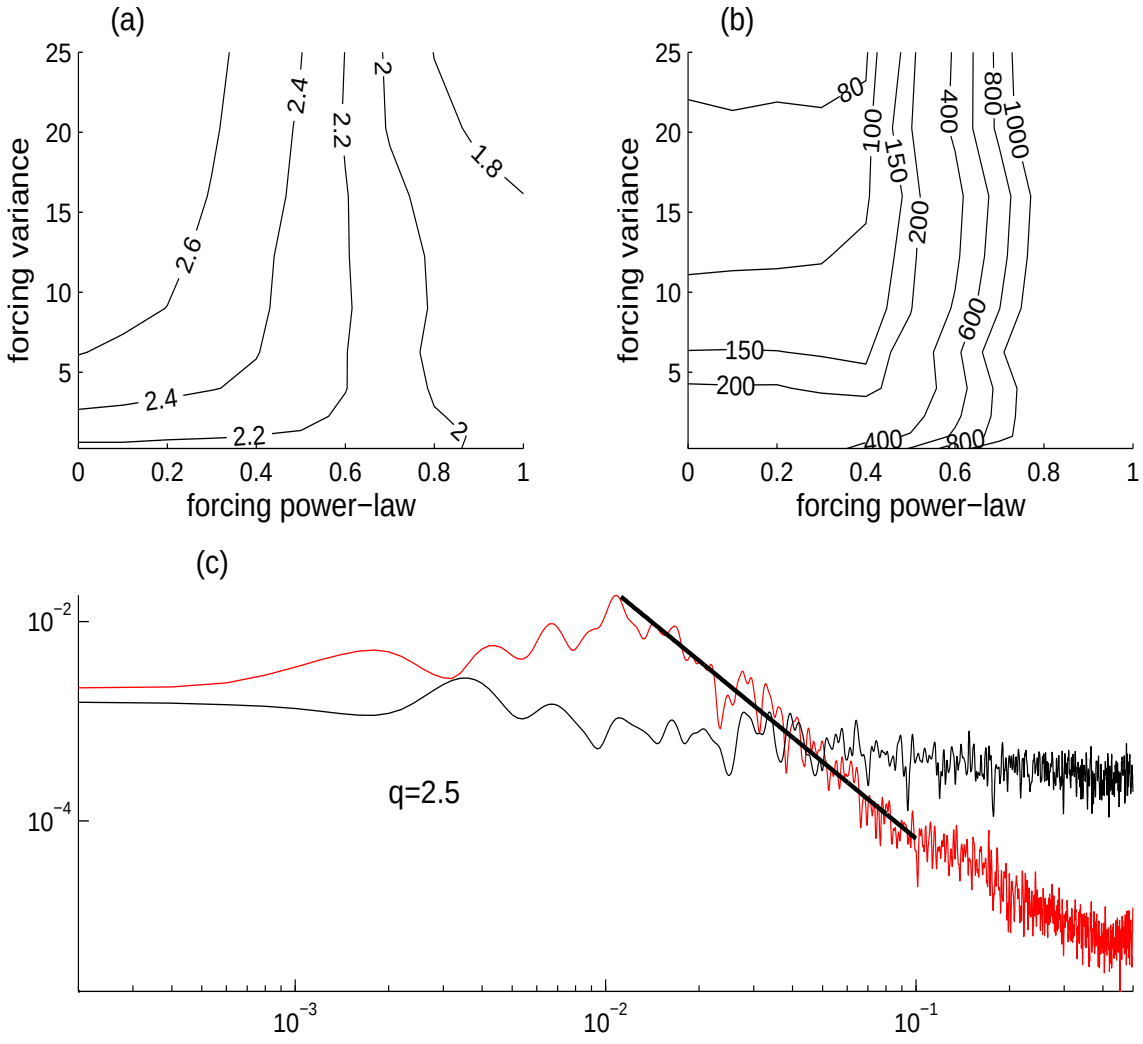

Figure 5-10: Model response to stochastic forcing. **c** Shows an example where the model is forced by noise with a power-law of 0.3 and variance 15. Shown are the spectra of the forcing (black) and model response (red). The solid black line is a fit to the model response between 1/90 and 1/10KY, and has a slope $q = 2.5$. The band associated with maximum variability is near 1/90KY. **a** The power-law of the response spectrum is contoured against forcing power-law and variance. The response spectrum is fit between the point with maximum variance and 1/10KY. **b** Shows the period associated with the band of maximum variability contoured against forcing power-law and variance.

Figure 5-9 characterizes the new model output using a periodogram approach. In this case the $\mathcal{F}_{op}$ parameterizations are used, but the forcing is sinusoidal. The most energetic band in the model's response is contoured against the variance and the period of the forcing. For periods less than 1/20KY the model response is nearly

linear, having a peak in energy at the same period as the forcing. The same linear response holds for forcing periods greater than 1/100KY. More interesting phenomena are observed when the new model is forced by periods between 1/20 and 1/100KY. Depending on the amplitude of the forcing and the exact period, the model generates period-doubling, tripling, and other complicated transitional behaviors. A qualitatively similar model response is also found when the $\mathcal{F}_o$ parameterizations are employed, from which it is inferred that the basic nonlinear response of the model is robust to small changes in parameterizations. Another notable feature of the model is that the variance of the response is primarily controlled by the period of the forcing. Longer period variability gives more time for ice to accumulate before melting and thus gives a greater amplitude response.

It is also useful to evaluate the model response to a purely stochastic forcing. In this case, the forcing is characterized by its variance and power-law behavior. The response is characterized by its power-law and the period with greatest energy. For convenience, the system is assumed to behave discretely. Figure 5-10 shows averaged results for stochastic forcing runs spanning 5000KY. The stochastic forcing results indicate that the band with the greatest variability tends to shift toward lower frequencies as the forcing power-law is increased. For power-laws greater than 0.8, the band with the greatest frequency was indistinguishable from the lowest resolved frequency, 1/5000KY. Although it may at first appear somewhat counter-intuitive, a shift to lower frequency forcing (more red) also causes the power-law of the response to decrease (become more white). That is, the power-law of the forcing and the response are anti-correlated. Note that when the band associated with the most energetic response shifts to lower frequencies, the power-law connecting the high-frequency variability with the most energetic response becomes less steep. Implicit in this explanation is that the energy in the high-frequency continuum is fixed.

When the new model is forced with a power-law below 0.4 and between variances of 10 and 20, the model response exhibits a roughly 100KY variability. In Chapter 1 the surface-air-temperature variability was estimated to have a high-frequency power law relationship of 0.4, suggesting that natural temperature variability could account for the basic period of the glacial variability. One then requires a mechanism for having terminations preferably occur during particular phases of obliquity. Such a model could easily be achieved by, say, the mean of the stochastic forcing being influenced by the Earth's tilt. Indeed, such a shift in the mean is suggested by

the findings of *Wunsch* [2004]. All told, it is difficult to see how glacial variability could be exclusively orbitally or stochastically forced. At this point, however, the juxtaposition of the two forcings is a useful approach in attempting to understand how much of the observed variability might be described solely by stochastic or orbital mechanisms. Eventually one seeks a combined understanding that incorporates the inevitable stochastic variations in insolation and temperature, as well as the orbitally forced insolation.

The cross-correlation between the results of the new model and EOF1 is found to be more sensitive to changes in model forcing and parameterizations than either the Imbrie or Paillard models. The spectral behavior of the new model, however, is found to yield approximately 100KY variability under a wide range of forcing scenarios from periodic to purely stochastic. Further analysis (not shown) indicates that the termination features are also produced so that the basic glacial cycle variability remains intact. Thus is it appears that while the correlation between EOF1 and the results of the new model are sensitive to perturbations, the underlying mechanisms which generate 100KY variability are robust features of the new model.

5.6 Comparing model and observational results

A second rule for assessing model results, as put forward by *Saltzman* [2002], is that a maximum amount of the structure in the observations should be deducible from the model using a minimum number of free parameters. In this part the results of the models are compared with EOF1 using a variety of techniques including cross-correlation and second and higher order spectral estimates. After accounting for the degrees of freedom available to each model, the new model seems to best describe the structure of EOF1.

5.6.1 Correlation and degrees of freedom

Judging the fit between model and observational results requires some objective measure of a model's skill. To make fair comparisons, one needs to account for the varying degrees of freedom (DOF) available to each model. *Roe and Allen*, [1999] compared a number of simple models of the glacial cycles by fitting an auto-regressive model to the residuals between model output and $\delta^{18}O$ observations and making an F-test comparison of the performance of each model accounting for the DOF. The conclu-

sion of *Roe and Allen* [1999] was that no distinction could be drawn between the six simple models they tested, including the Imbrie and Paillard models.

The auto-regressive model fit to the residuals by *Roe and Allen* [1999] makes some restrictive assumptions on the distribution of the data and the class of model error. Here, a simpler approach is adopted for comparing the results of the simple models. First, the parameters of each model are adjusted to maximize the squared-cross-correlation between model results and EOF1. Second, the variance described is divided by the DOF available to each model, and the resulting ratio is used as a score by which to compare the relative skill of the various models. Results are shown in Table 5.1. For both the $\mathcal{F}_{op}$ (with precession) and $\mathcal{F}_{o}$ (obliquity only) parameterizations, the new model has the highest score. The Imbrie model does well by having few adjustable parameters, but its correlation with the observations is low. Conversely, the $\mathcal{F}_{op}$ Paillard model obtains an excellent fit with the observations, but has relatively many DOF.

It is noteworthy that the score associated with each model is similar for both the $\mathcal{F}_{op}$ and $\mathcal{F}_{o}$ parameterizations (the latter of which have two degrees of freedom less), suggesting that the score is an invariant measure of these models' skill relative the DOF permitted each model. In other versions of the new model, additional DOF were added, for instance by requiring precession and obliquity values to exceed separate thresholds. Incorporating such additional rules increased the maximum squared-cross-correlation with EOF1 and the new model to roughly 0.7, but also the model complexity and DOF, so that the score was not much affected.

5.6.2 Periodograms

As noted previously with respect to assessing robustness, the squared-cross-correlation between model results and EOF1 is particularly sensitive to the sequence of events within a record. Omitting or mistiming an event can easily destroy the correlation in a model. For this reason, spectral analysis of model output provides a complementary description of the model behavior. Furthermore, since the spectra were not directly used as a criterion in selecting the model parameterizations, it provides a more independent means by which to compare the model results with observations.

As discussed in Chapter 3, EOF1 shows excesses of energy near frequencies given by the simple relationship $s(n) = 1/41\text{KY} + n/100\text{KY}$, where n equals -1, 0, 1, or 2. This pattern suggest a nonlinear coupling between obliquity variations and the

		r^2	DOF	score
$\mathcal{F}_{op}$	Imbrie	0.24	4	0.06
	Paillard	0.73	11	0.07
	new	0.60	6	0.10
$\mathcal{F}_o$	Imbrie	0.12	2	0.06
	Paillard	0.40	9	0.04
	new	0.43	4	0.11

Table 5.1: Comparing model fit with the observations for the $\mathcal{F}_{op}$ (top, both obliquity and precession forcing) and $\mathcal{F}_o$ (bottom, only obliquity forcing) parameterizations. From left to right are the model name, the squared cross-correlation between model results and EOF1 over the last 650KY, the degrees of freedom available to each model, and the score. The score is measured as the ratio between the squared-cross-correlation and the degrees of freedom. One DOF has been subtracted from the Paillard model because perturbation experiments (Figure 5-4) indicate no sensitivity to the T_G parameter. If the ablation timescale for the $\mathcal{F}_{op}$ Imbrie model is permitted to be arbitrarily small, the squared-cross-correlation can be increased to 0.33, raising its score to 0.08.

100KY variability. Each model produces clear excesses of energy near the 1/100 and 1/41KY ($n = 0$) bands. For the $\mathcal{F}_{op}$, shown in Figure 5-11, the Imbrie model and the new model give peaks in energy at each of the $s(n)$ bands identified in EOF1, while the Paillard model has no identifiable peaks near 1/70 ($n = -1$) and 1/29KY ($n = 1$). For the $\mathcal{F}_o$, both the new model and Paillard model have peaks at the $s(n)$ frequencies, while the Imbrie model generates a red continuum without noticeable concentrations of variability.

It is interesting that when the Paillard model is forced only by obliquity the output has more clearly identifiable spectral peaks. Possibly, when precession forcing terms are included, the Paillard model produces a more energetic background continuum in which some of the peaks resulting from the obliquity forcing are no longer identifiable. This suggests that one mechanism for generating a background continuum is to have a sufficiently nonlinear response to narrow-band forcing that the resulting variability has a continuum of energy extending over all resolved frequencies. Beyond these simple model results and as discussed in Chapter 1, determining the sources of the background variability in the climate spectrum remains an outstanding question.

5.6.3 Power-laws

Introducing a threshold into a system provides a strong nonlinearity. Indeed, if the rapid ablation events are approximated as step functions, one expects energy extending to the highest resolved frequencies [e.g. *Bracewell*, 2001]. Furthermore, the orbital variations are both frequency and amplitude modulated so that the forcing itself contains energy in numerous bands. It is then not surprising that these simple glacial models yield energy at all the frequencies resolved in these discrete realizations. That the models yield distinct power-law relationships is perhaps more surprising. In Chapter 2 the spectra of frequency and amplitude modulated signals was discussed. One result was that, for moderate to weak modulations, energy in bands near the carrier frequency were the strongest. An analogous result may hold here in the response of the models to orbital forcing: the background continuum energy near the orbital and 1/100KY bands is the strongest and diminishes towards higher frequencies (longer model runs indicate that the energy at lower frequencies also diminishes). If one thinks of the overtones and combination tones generated by the model as being more numerous than the resolved bands, the production of a noise-like background continuum which diminishes toward higher frequencies can at least be qualitatively understood.

While the production of the background continuum in the model response is poorly understood, it is none-the-less easy to measure the power-law relationship and this provides another comparison between the model results and EOF1. EOF1 has a power-law with energy falling of at a rate proportional to s^{-q}, where $q = 2.8$. This power-law is probably more steep than those discussed in Chapter 1 because of the smoothing effect of averaging together multiple records [see *Huybers*, 2002]. It is found that the new model has a power-law most similar to that of EOF1 with $q = 2.4$. the Paillard model is too steep at $q = 3.4$, while the Imbrie model is less steep at $q = 2.1$. In view of the less steep $\delta^{18}O$ power-laws discussed in Chapter 1 and found elsewhere [e.g. *Wunsch*, 2003b], the Imbrie model power-law also seems an acceptable result.

5.6.4 Auto-bicoherence

In Chapter 3 it was argued that concentrations of variability at bands centered on the $s(n)$ frequencies, coupled with the strong auto-bicoherence at most of the frequency pairs $\{s(n_1), s(n_2)\}$, demonstrated the presence of a nonlinear climate coupling be-

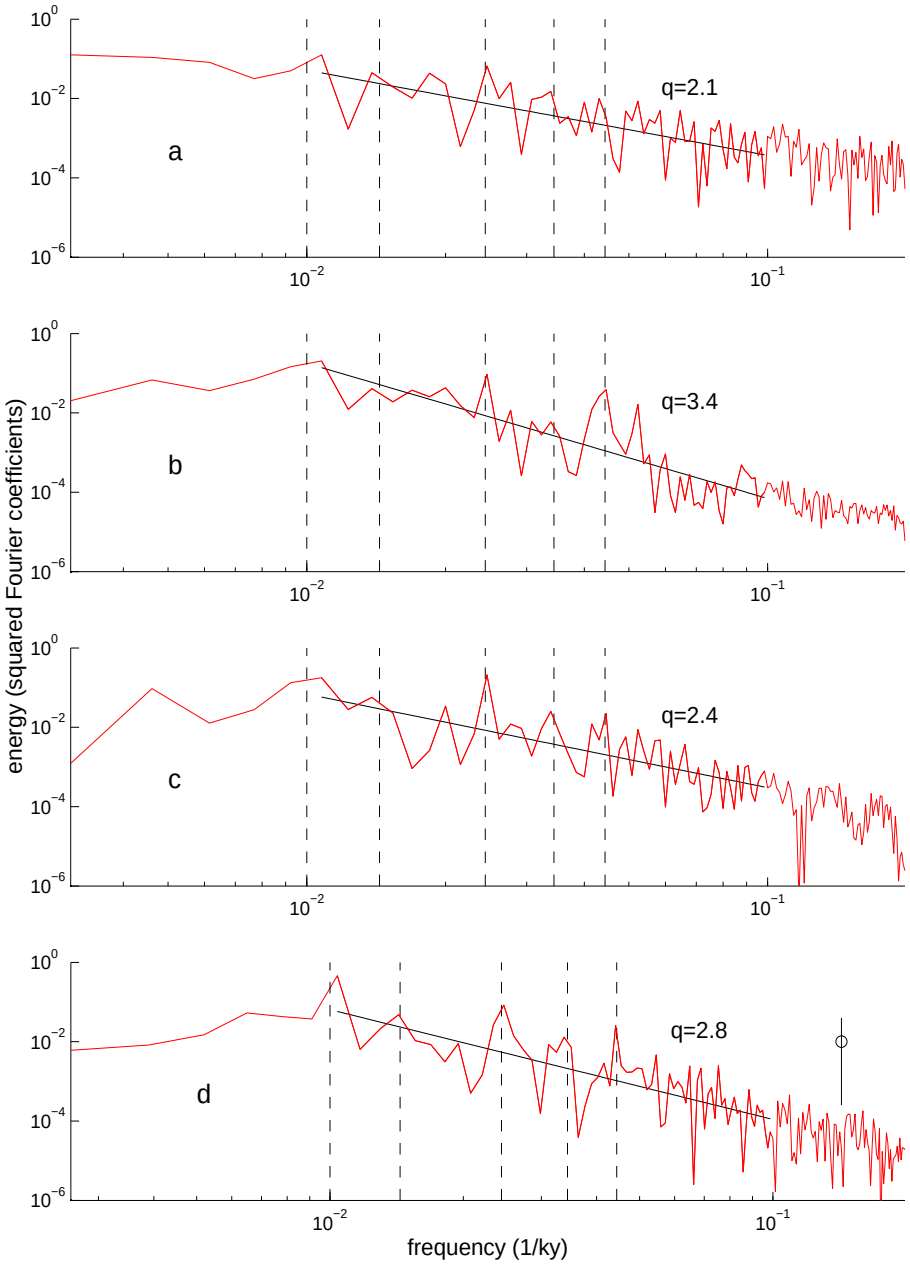

Figure 5-11: Periodograms of model results using the $\mathcal{F}_{op}$ parameterizations: **a** Imbrie model, **b** Paillard model, and **c** new model. **d** is the periodogram of EOF1. Power-laws are indicated by the solid lines fit to the spectra between 1/10 and 1/100KY where the slope is given by q. Vertical dashed lines are centered on the bands in which EOF1 has significant concentrations of energy: 1/100, 1/70, 1/41, 1/29, and 1/23KY. The vertical solid line in **d** indicates the approximate 95% confidence interval. The Imbrie model and the new model have spectral peaks at each of the vertical lines.

tween the 100KY variability and the obliquity band response. The simple model results discussed here indicate that a nonlinear response to obliquity variations can generate 100KY variability similar to that observed in EOF1. Furthermore, the presence of the combinations tones at 1/29 and 1/70KY in the Imbrie model and new model periodograms suggests that the model nonlinearities share some similarity with the nonlinearities present in EOF1. An important further test of whether the nonlinearities in the models reflect those in the climate system is whether the model results have an auto-bicoherence pattern similar to EOF1.

Figure 5-12 shows the auto-bicoherence computed for the $\mathcal{F}_{op}$ model results over the last 780KY BP (the same period discussed in Chapter 3). In general, the model results have weaker auto-bicoherence than those found in EOF1. The new model auto-bicoherence shows local maxima at each frequency pair, $\{s(n_1), s(n_2)\}$, yielding a pattern similar to that of EOF1. Differences are that the auto-bicoherence in EOF1 is stronger and that EOF1 displays no auto-bicoherence at $\{s(2), s(2)\}$. The Imbrie model auto-bicoherence also shows a gridded pattern of auto-bicoherence separated by roughly 1/100KY intervals, but maxima are not centered on the $\{s(n_1), s(n_2)\}$ frequency pairs, suggesting that the Imbrie model only partially describes the nonlinearities found in EOF1. The Paillard model shows moderate auto-bicoherence values, but the pattern is dissimilar to that of EOF1.

5.6.5 Summary of model comparisons

Three measures of how well each model describes the structure of EOF1 were employed: the periodogram, auto-bicoherence, and a score measured as the squared-cross-correlation between the tuned model results and EOF1 divided by the DOF in the model. The score associated with the new model is roughly 50% higher than that of the Imbrie or Paillard models. The periodogram provides a phase-free means of comparing model output with EOF1. The output of each model shows concentrations of energy at the 100KY, obliquity, and precession bands, but the Imbrie model only shows concentrations of energy at the obliquity-100KY combination tones when using the $\mathcal{F}_{op}$ parameterizations and the Paillard model only shows combination tones using the $\mathcal{F}_o$ parameterization. The new model is alone in consistently producing concentrations of energy at each of the significant peaks identified in EOF1. Furthermore, the power-law associated with the new model periodogram is most nearly similar to that associated with EOF1. Finally, the new model results have an auto-bicoherence

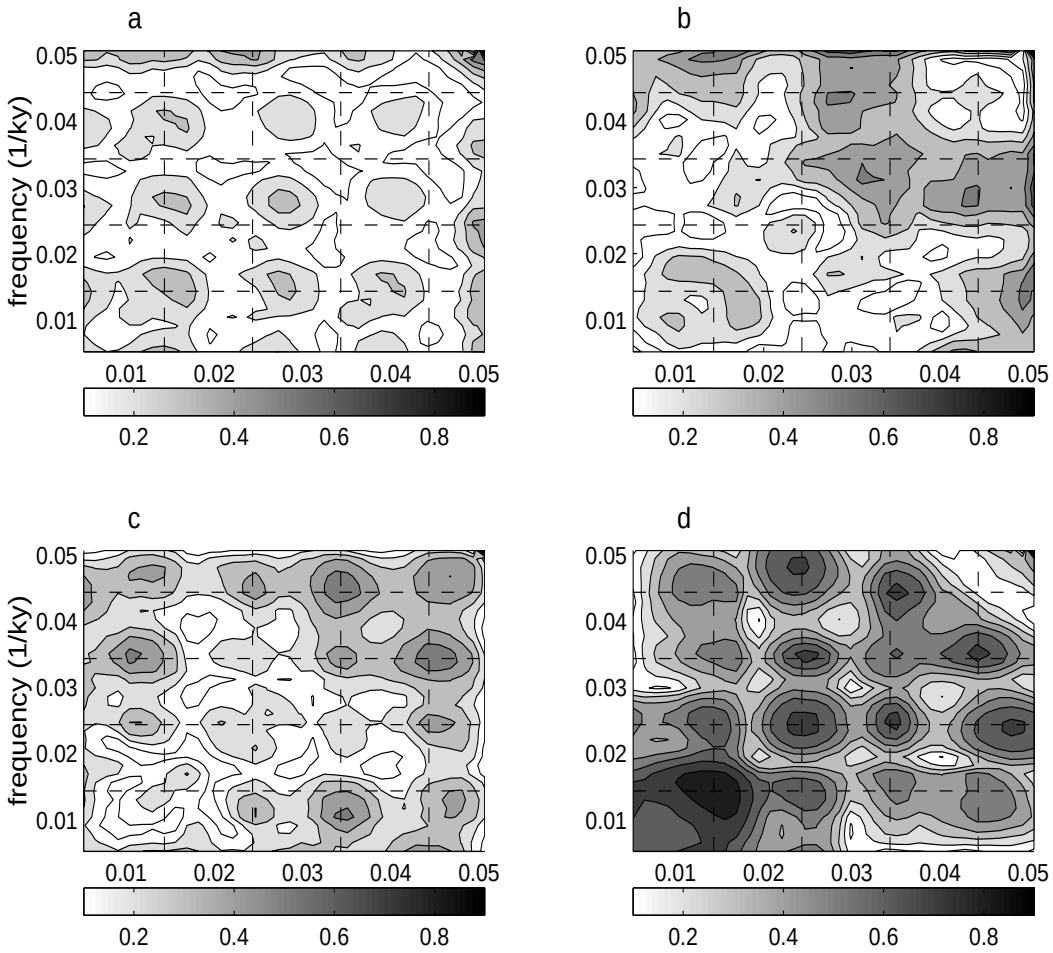

Figure 5-12: Auto-bicoherence estimates for **a** the Imbrie model, **b** the Paillard model, and **c** the new model using the $\mathcal{F}_{op}$ parameterizations. **d** is the auto-bicoherence of EOF1. Horizontal and vertical lines are at frequencies of 1/70, 1/41, 1/29, and 1/23KY. The new model and EOF1 have a similar structure with local maxima in auto-bicoherence tending to occur at intersections of the horizontal and vertical lines.

pattern most similar with that of EOF1. It is thus concluded that of the three models considered, the new model provides the best description of the climate variability recorded in EOF1.

5.7 Dynamical interpretations

In this section the behavior of the new model is interpreted in the context of nonlinear dynamical systems. It is shown that the new model can be classified as an *excitable system*, and that it is capable of chaotic behavior. Features of the model's behavior are

qualitatively similar to those found in a variety of other simple and well-understood systems. By drawing comparisons with these other systems, a context is provided for understanding how the new model works.

5.7.1 Excitable systems

The quasi-periodic variability and state-dependent sensitivity to external forcing are hallmarks features of what are broadly referred to as *excitable* systems [see e.g. *Pikovsky*, 2001]. Excitable dynamics have received much attention as models of neuron behavior [e.g. *FitzHugh*, 1961] and cardiac tissue [e.g. *Glass and Shrier*, 1991], but also in chemical reactions [*Epstein and Pojman*, 1998], electronics [*Postnov et al.*, 1999], and optics [*Barland et al.*, 2003]. A pioneering study by *van der Pol* [1927] of the cardiac pacemaker offers a relevant example in which the heart was modeled as an excitable system paced by quasi-periodic electrical stimuli. Perhaps *Hays et al.* [1976] had such a system in mind when they suggested insolation variability is the pacemaker of the ice-ages.

Another relevant example of an excitable system is the FitzHugh-Nagumo model of the neuron [*FitzHugh*, 1961; *Nagumo et al.*, 1962]. This neuron model has been the subject of much investigation: its solution has been obtained analytically, physical models of the process have been built, and it has thorough observational support. The behavior of the system is characterized by a slow time-constant associated with recharging the neuron potential, and a fast timescale associated with its discharge — collectively referred to as an integrate and fire mechanism. The neuron fires when prompted by an external stimuli, and then enters a refractory state where it is insensitive to further stimulations. Once sufficient potential builds up, and when prompted, the neuron again fires. Subject to fast periodic or (band-limited) white noise forcing, the overall timescale of the neuron is set by the slow integration time. Furthermore, the firing sequence in an excitable system can become nonlinearly phase locked with periodic forcing. A direct analogy can be made between this model of the neuron and with the concept of obliquity pacing of the glacial terminations. In this view, terminations only occur after the climate system has built up a sufficient charge of ice-volume and once triggered by the obliquity forcing.

Chapter 4 began by distinguishing between hypotheses which suppose glacial cycles are internally or externally forced. It is tempting to suppose that an externally forced deterministic system will be wholly predictable, but the further possibility

arises that the climate response could be chaotic so that small perturbations in the forcing or initial conditions would make the climate response unpredictable beyond a certain time horizon. Numerical experiments indicate that excitable systems are capable of chaotic behavior [*Strain and Greenside*, 1997; *Othmer and Xie*, 1999]*Othmer99*, and for certain parameterizations the new model is also found to behave chaotically. The model response is always phase-locked with the insolation forcing, and it is only the amplitude of the glacial cycles which can exhibit chaotic behavior. That is, the secular changes in Earth's orbit pace the glacial cycles but the amplitude of the response is not predictable.

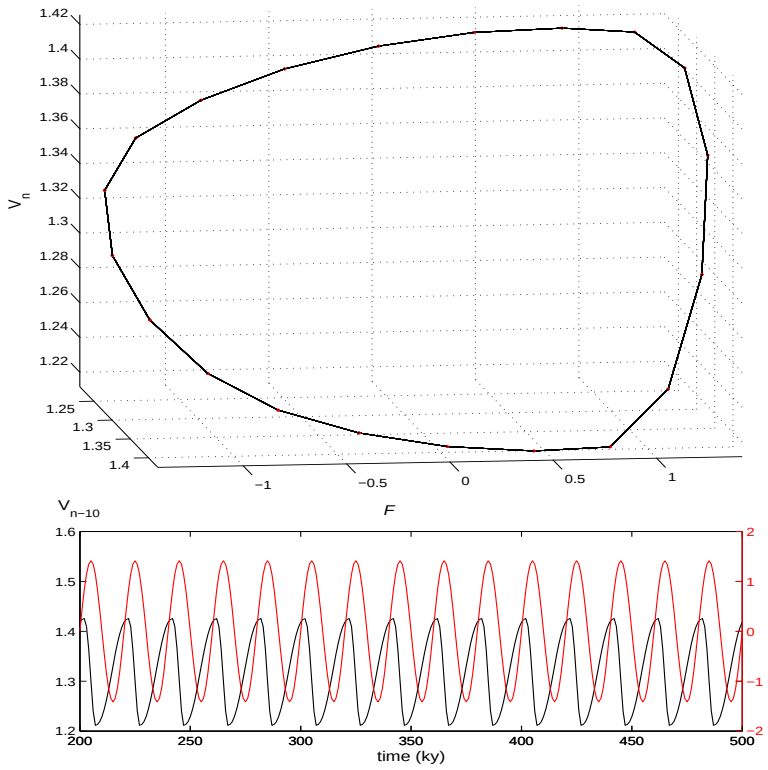

Figure 5-13: Model response to a 20KY unit variance sine wave using the $\mathcal{F}_{op}$ parameterizations. **bottom**, the forcing (red) in normalized units and the model response (black) in hectometers of sea-level plotted for 300KY after the initial transients have become negligible. **top** The state of the model at any time is defined by the forcing (x-axis), ice-volume 10KY prior (y-axis), and the present ice-volume (z-axis). Both the forcing and response are periodic at 20KY. Notable features are the slow trend toward greater ice-volume followed by an abrupt transition to a low ice-volume state.

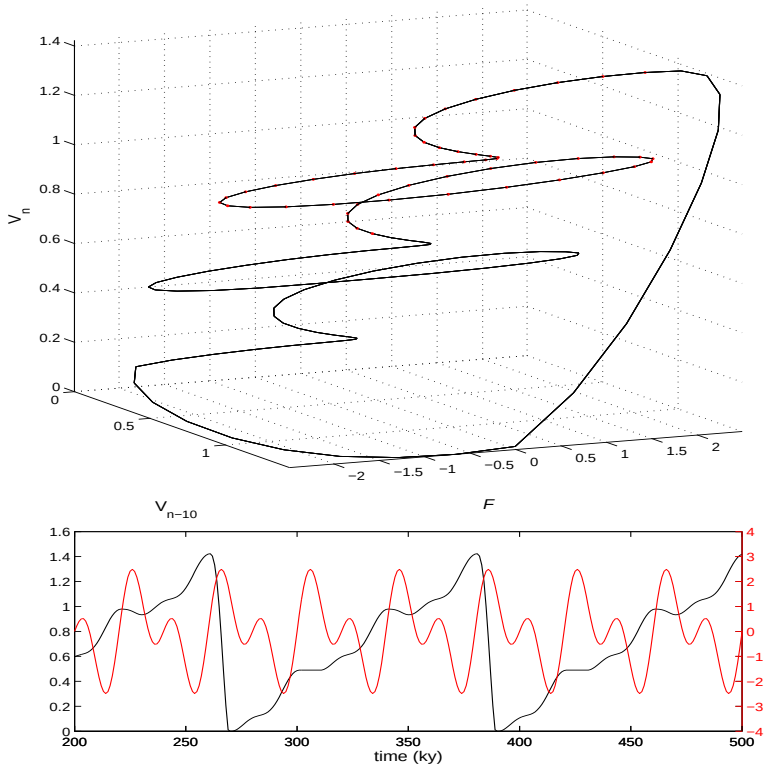

Figure 5-14: Similar to Figure 5-13, but now the model response to a combined 20KY and 40KY periodic forcing. **bottom**, The forcing (red) is periodic at 40 KY while the model response (black) is periodic at 120KY. **top** Model state as determined by ice-volume (z-axis), ice-volume 10KY prior (y-axis), and forcing (x-axis). While more complicated than the response for 20KY forcing alone, the basic pattern is similar: slowly increasing ice-volume followed by a rapid collapse. Observe now that there is a spiraling increase until ice-volume exceeds the level of one hectometer.

5.7.2 Trajectories

To better understand the chaotic and non-chaotic regimes of the new model, it is useful to consider the response of the new model to an idealized forcing function. Figure 5-13 shows model output using the $\mathcal{F}_{op}$ parameterizations, but forced by a unit variance 20KY period sine wave. There are just over two active dimensions in the new model — time, ice-volume, and prior ice-volume — where the last is a mixture of the first two. Plotting the model trajectory in this three-dimensional framework permits viewing the entire state of the model at once. The model response has a one to one relationship with the forcing (i.e. it is periodic at 20KY) and shows asymmetric slow growth in ice-volume alternating with rapid ablation. Because ice-volume is always greater than one hectometer, a termination-like event occurs each

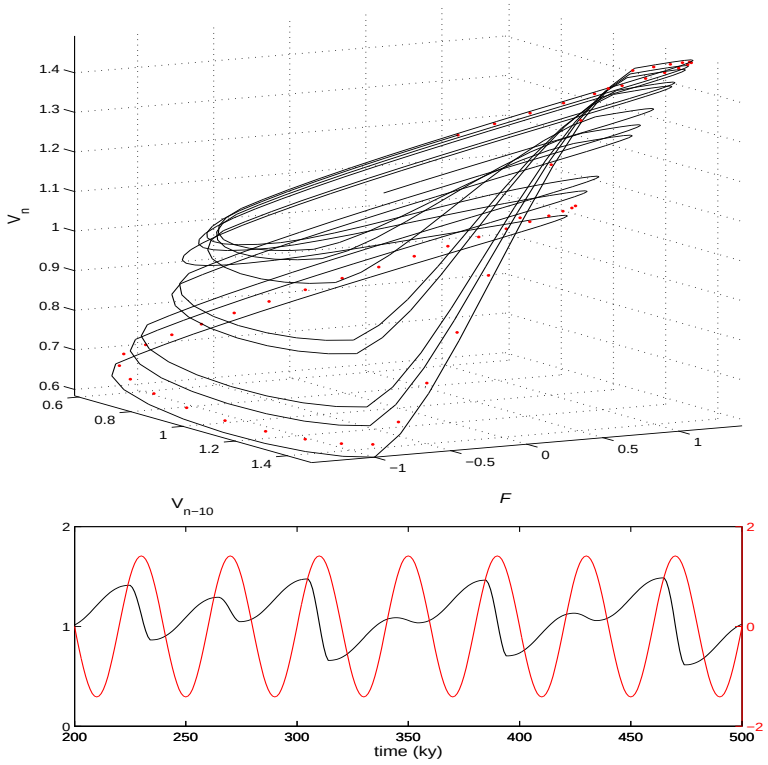

Figure 5-15: Similar to Figures 5-13, but now the new model response to a unit variance 40KY sine wave. The response is much more complicated than for the unit variance 20KY sine wave case. The general behavior is for a small ablation event to be following by a large ablation event. Ablation events occur every time the forcing is greater than the accumulation bias — in this case one. However, from long runs of this model, it appears that the magnitudes of the melting events does not repeat. Thus the model response is phase-locked to the forcing, but the amplitude of the response appears to be chaotic.

time the forcing exceeds the orbital threshold value.

The model exhibits a more complicated periodic response when forced by the sum of two unit variance sine waves with periods of 20 and 40KYs (see Figure 5-14). Now ice slowly spirals upward over three 40KY cycles, or six 20KY cycles, after which a large amplitude termination occurs. Note that the model response and forcing are phase locked: there is still a one to one correspondence between every maximum and minimum in both curves. The difference is in the amplitude of the response which critically depends on the prior ice-volume state.

Figure 5-15 shows model output when forced by a unit variance 40KY sine wave. The response is fundamentally different than that discussed in the previous two ex-

amples. The model accumulates equal amounts every 40KY cycle, but the degree of ablation is variable. Even in long runs, the model is never seen to repeat, suggesting the presence of a chaotic regime. The overall pattern observed in Figures 5-13 through 5-15 is a looping structure comprised of a general trend toward increasing ice-volume followed by a rapid decrease. Note that when the forcing becomes large some melting always occurs, so that the phase of the model response is locked with the forcing —- a chaotic regime referred to as *phase synchronization* by *Rosenblum and Pikovsky* [2003]. To manifest chaotic behavior, trajectories cannot overlap in phase space, thus requiring more than two dimensions. The new model effectively has just over two dimensions: time, ice-volume, and time-lagged ice-volume and so is just capable of chaotic behavior. Also note that the pattern of slow growth and a rapid chaotic decrease is qualitatively similar to the behavior of the very simple chaotic system presented by *Rossler* [1976].

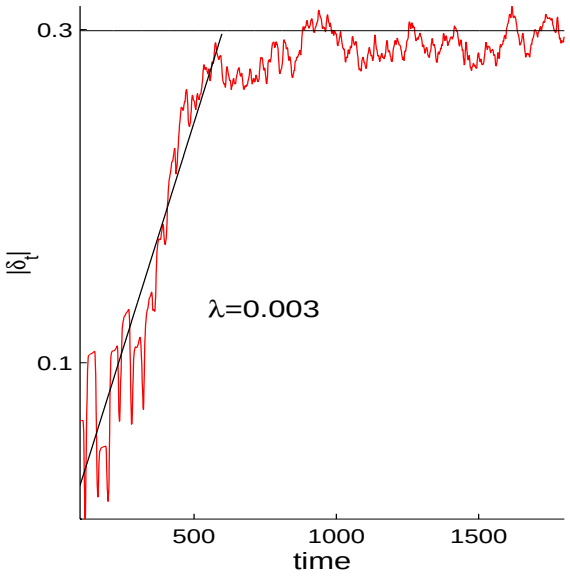

Figure 5-16: Average absolute distance between sets of model runs after applying a small perturbation to the initial conditions for one of the runs. These results indicate the model has a Lyapunov coefficient of 0.003 units/KY, or that perturbations exponentially grow with a timescale of roughly 300KY. Note the y-axis is logarithmic. Eventually the distance between model runs saturates at a value of 0.3. The model was forced using a unit variance sine wave of period 40KY. In general, the value of the Lyapunov coefficient depends on the forcing and parameterizations of the model.

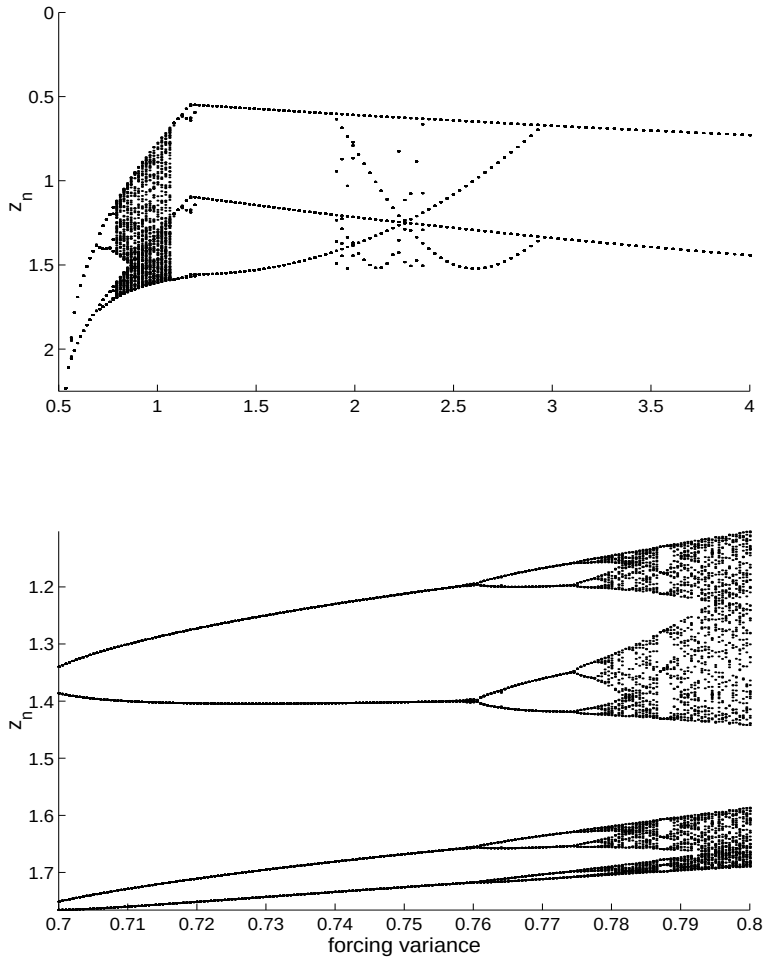

Figure 5-17: An orbit diagram for the model where the variance of each local maximum in ice-volume is plotted against forcing variance. The forcing is a 40KY sine wave, and a local maximum in ice-volume occurs exactly once for each forcing cycle. Thus the number of distinct dots in a vertical row indicates the period of the model response. **top** As the forcing variance increases from 0.5 a period doubling route to chaos is observed, but at values above 1.1, the model response again becomes periodic. For forcings above 3, the response simplifies and is periodic at 80KY. **bottom** Zooming in on the interval between 1.2 and 1.4 shows the period doubling route to chaos more clearly.

5.7.3 Chaos

One hallmark feature of chaos is the exponential divergence of model trajectories subject to a small perturbation. Figure 5-16 shows the average distance between a reference run of the new model and a perturbed model run as a function of time. After allowing the model to run for 2000KY, both ice-volume and prior ice-volume are

rescaled to be within 0.01 hm of the reference model, the time is reset to zero, and the models are run forward again. The divergence is exponential with a rate set by what is termed the Lyapunov exponent [see e.g. *Strogatz*, 2000]. The Lyapunov exponent for this model is estimated from thousands of model runs to be approximately 0.003 KY^{-1}. The small value of the Lyapunov exponent suggests that even when the new model is in a chaotic state, it will be possible to predict its behavior for numerous glacial cycles. The average distance between the reference and perturbed model runs saturates at 0.3. Thus, for small perturbations the model trajectories initially diverge, but because all trajectories are contained within a finite volume, the average separation only grows so far.

Figure 5-17 shows another hallmark feature of chaotic behavior using an orbit diagram. The values of the local maxima in ice-volume are plotted against the forcing variance for a sine wave with a period of 40KY. For forcing variances near 0.5 each successive maximum in ice-volume has the same amplitude and thus the model response has a period which is the same as the forcing. This is analogous to the case presented in Figure 5-13, only that the amplitude is smaller and the frequency of the forcing is lower. As the forcing variance increases, the model undergoes bifurcations until, near 0.78, the model no longer appears to repeat, a phenomenon referred to as a period doubling route to chaos. At unit variance Figure 5-17 shows the same model results plotted in Figure 5-15, but now only plotting the local maximum values. There are also windows of periodic behavior, for instance near a forcing variance of 0.788. At values above 1.2, the model response remains periodic, typically having a period doubling or tripling response. The Rossler system shows a very similar structure in its period doubling route to chaos [*Olsen and Deign*, 1985]. Physical systems have also been shown to manifest similar period doubling phenomena; for instance, *Libchaber et al.* [1982] for convection experiments where the Rayleigh number is slowly increased. Extremely simple chaotic systems such as the logistic map and the sine map also show a simple period doubling route to chaos. See *Strogatz* [2000] for a good introductory review of these phenomena.

The behavior of the new model bears much in common with the simple chaotic El Nino model of *Tziperman et al.* [1994]. Both models are driven by periodic forcing, incorporate a time delay, and exhibit a period doubling route to chaos. The applicability of such simple models to both the glacial cycles and the El Nino variability hints at a physical linkage between the two phenomena. Indeed, it has been speculated that

the dynamical response of the Tropical Pacific to obliquity forcing is responsible for the glacial cycles [*Philander and Fedorov*, 2003]. While this is an interesting notion, establishing such a connection would require much more theoretical and observational study.

The results of the new model suggests that the glacial cycles could be chaotic. It should be pointed, however, that the forcing which gives the best fit between EOF1 and model results is near a chaotic regime, but is not itself chaotic. Furthermore, it is probably not possible to prove whether the climate is or is not chaotic given the finite and noisy observations which are available. To give an example of this difficulty, a new method of detecting chaos in a system was recently presented by *Gottwald and Melbourne* [2004] which requires on the order of 50,000 data points even when the system is very simple and there is no noise. Distinguishing between a chaotic deterministic system and a stochastic system, particularly given noisy data, would likely require many more observations. Note that *Tziperman et al.* [1994] also state that the observational record is insufficient to establish whether El Nino is chaotic.

Feigenbaum [1979] provides a renormalization theory which shows why the orbit diagrams of the iterated maps, the Rossler system, and probably the convective experiments of *Libchaber et al.* [1982] and El Nino model of *Tziperman et al.* [1994] should all appear so similar. A detailed discussion of renormalization theory is beyond the scope of this thesis, but one of its implications is that each of these systems should have trajectories which are only slightly more than two dimensional. That is, only two or three dimensions are active while the others, if they exist, follow along slavishly. The new ice-volume model has barely more than two dimensions: time, ice-volume, and time-lagged ice-volume (a truly slaved third dimension). One manifestation of this low-order chaos is a Lorenz map which is nearly one-dimensional. For continuous systems, this map is made by plotting each local maximum, z_n, against the next one, z_{n+1}, for a long run of the model output [*Lorenz*, 1963].

5.7.4 Multiple climate states

One typical manifestation of low-order chaos is a Lorenz map which is nearly one-dimensional. For continuous systems, this map is made by plotting each local maximum, z_n, against the next one, z_{n+1}, for a long run of the model output [*Lorenz*, 1963]. The Lorenz map for the new ice-volume model is shown in Figure 5-18. In this case, model results are from a 40KY periodic forcing with unit amplitude and,

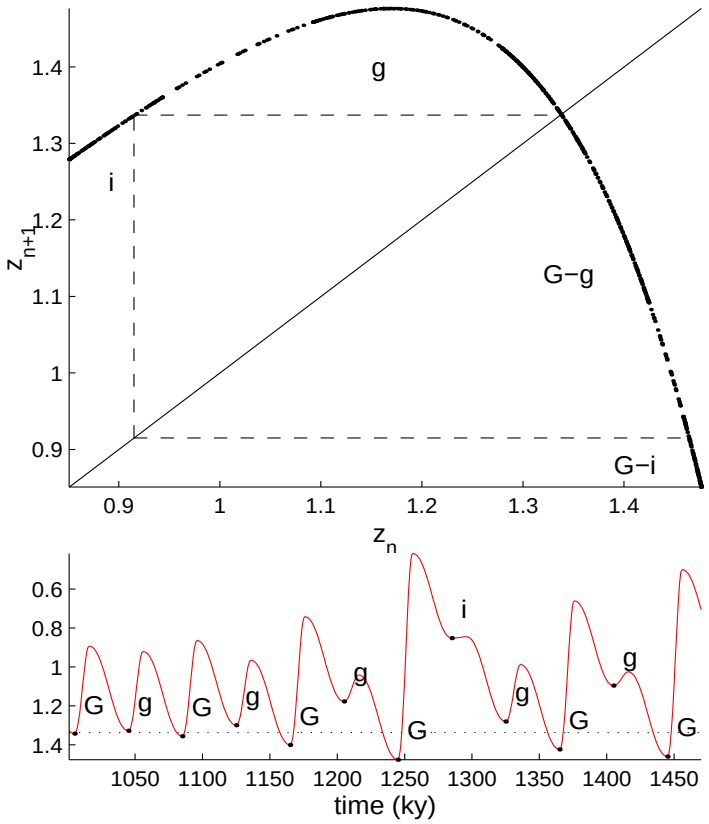

Figure 5-18: Lorenz map of the model's chaotic response to a unit variance, 40KY sine wave. **top** the magnitude of a maximum in ice-volume (z_n) is plotted against the subsequent maximum (z_{n+1}) for a 20,000KY long record, after the initial transients have died down. A simple function-like relationship emerges which is unimodal and concave down. The intersection between this relationship and the solid diagonal indicates an (unstable) fixed point in the system. Reminiscent of the Paillard model, the extent of glaciation can be divided into three categories: i (inter-glacial, $z_n <$ .915), g (mild glacial, .915 $> z_n >$ 1.34), and G (full glacial, $z_n >$ 1.34). When the model is in state i it next transitions to states g and then G. State G is subdivided into G_g (1.34 $< z_n <$ 1.46)and G_i ($z_n >$ 1.46). State G_i leads to state i and the full 3 period cycle begins again. Alternately, state G_g leads to state g, giving rise to a two period cycle. When the trajectory is far from the unstable fixed point, both sequences $\{G-i-g\}$ and $\{G-g\}$ are approximately equally likely, and because the transition time between states is always 40KY, the average re-occurrence time of state G will be 100KY. If the model lands near the fixed point, a train of $G-g$ transitions with nearly equal amplitude ensues. **bottom** A portion of the model output is shown with maxima in ice-volume labeled according to their state. The horizontal line indicates the fixed point. Initially, the trajectory is near the fixed point and the G and g states have nearly equal magnitudes. The model then spontaneously transitions to larger and more unequal ice-volume variations with both 120 and 80KY re-occurrence times.

for variety, the $\mathcal{F}_o$ parameterizations. As long as the model is in a chaotic regime and the selected parameterizations yield a good fit between model results and EOF1, the qualitative structure of the Lorenz map appears insensitive to which forcing is used. The model's Lorenz map has a broad maximum centered at approximately $z_n = 1.15$. This maximum lies above the diagonal so that the subsequent maximum in ice-volume, z_{n+1}, will be larger; that is the ablation between z_n and z_{n+1} is smaller than the accumulation. Toward higher values of z_n the downward slope of the Lorenz map increases, crossing the diagonal with a slope less than minus one. The slope in the vicinity of the diagonal crossing is important because the intersection is a fixed point (i.e. periodic with $z_n = z_{n+1}$), and slopes with an absolute value greater than one indicate that the fixed point is unstable [*Lorenz*, 1963]. The steeper slope toward higher values of z_n also indicates that the model is more sensitive to perturbations during periods of large ice-volume. This is in qualitative agreement with the previous discussion of high-latitude surface air temperature variability during glacial and inter-glacial periods (see Chapter 1, figures 1-2). The Rossler system's Lorenz map [e.g. *Strogatz*, 2000] has a structure nearly identical to that of the new model, suggesting that such behavior is a robust feature of many simple chaotic systems.

It is useful to divide the Lorenz map associated with the new model into three states: inter-glacial (i), mild glacial (g), and full glacial (G). State i is defined as values of z_n for which z_{n+1} is less than the value of the fixed point. State g is defined as values of z_n for which z_{n+1} is greater than the value of the fixed point. Finally, state G comprises all values of z_n greater than the fixed point. Thus, if the model begins in state i it must subsequently enter state g and then state G. The specific ice-volume values which delineate each state are given in the caption to Figure 5-18 for the case of $\mathcal{F}_o$ model parameterizations and a unit variance 40KY sinusoidal forcing. The requirement for the model to cycle through a fixed set of states implies that knowing the current model state permits some predictive skill. A similar rule based approach has been developed for predicting the trajectory of the chaotic Lorenz system [*Evans et al.*, 2003].

So far the model's trajectory has been discussed as if it were a fixed sequence, but consider that state G can lead to either state i or state g. As noted earlier, local maxima in ice-volume are spaced by 40KY intervals in a one to one relationship with the period of the forcing so that the $\{i - g - G\}$ sequence takes 120KY while the $\{g - G\}$ sequence takes only 80KY. For either sequence, the transition out of the G

state is identified with a glacial termination so that the duration of a glacial cycles will be either 80 or 120KY. If the $\{i-g-G\}$ and $\{g-G\}$ sequences are realized an equal number of times, the average glacial cycle will be 100KY, as is observed for late Pleistocene climate variability.

The state transitioning rules for the behavior of the new model are not specified, but rather emerge as intrinsic features of the model's dynamics. In this respect, the new model provides an explanation for the multiple climate states which were explicitly specified in the Paillard model. According to the new model, the multiple climate states are generated by the dependence of the rate of change of ice-volume on the amount of ice present 10KY prior. It is useful to note a difference between the Paillard and new model in that the Paillard model also cycles through the full $i-g_G$ sequence, while the new model switches between short $g-G$ and long $i-g-G$ cycles. In some instances, however, the Paillard model is able to pass quickly from the i to g state, and it appears these more rapid cycles correspond to the $g-G$ cycles in the new model. Thus the state dependent behaviors of both the new model and the Paillard model appear to be very similar. That state dependence emerges from the simple dynamical formulation of the new model supports the notion that the climate exhibits similar state dependent variability.

5.8 Are we still in the 40KY world?

The chaotic behavior exhibited by the new model lends itself to some speculation regarding the long-term evolution of the climate system. In particular, the presence of a fixed point in the Lorenz map of the new model suggests a novel way of explaining the transition the Mid-Pleistocene Transition [e.g.*Schmieder et al.*, 2000]. Figure 5-18 shows a model realization where a series of nearly equally sized and relatively small oscillations in glacial extent transition to larger glacial anomalies with a seemingly longer period. Note that local maxima in glacial extent still occur every 40KY, and it is only that the magnitude of the glaciations vary. This suggests that the period commonly referred to as the 40KY world [e.g. *Raymo and Nisancioglu*, 2003] could have the same dynamics associated with it as the more recent period which is characterized by a dominant 1/100KY band of variability.

The presence of a train of nearly equal amplitude glaciations is a common event for the new model when in a chaotic regime. The reason is that if a local maximum in

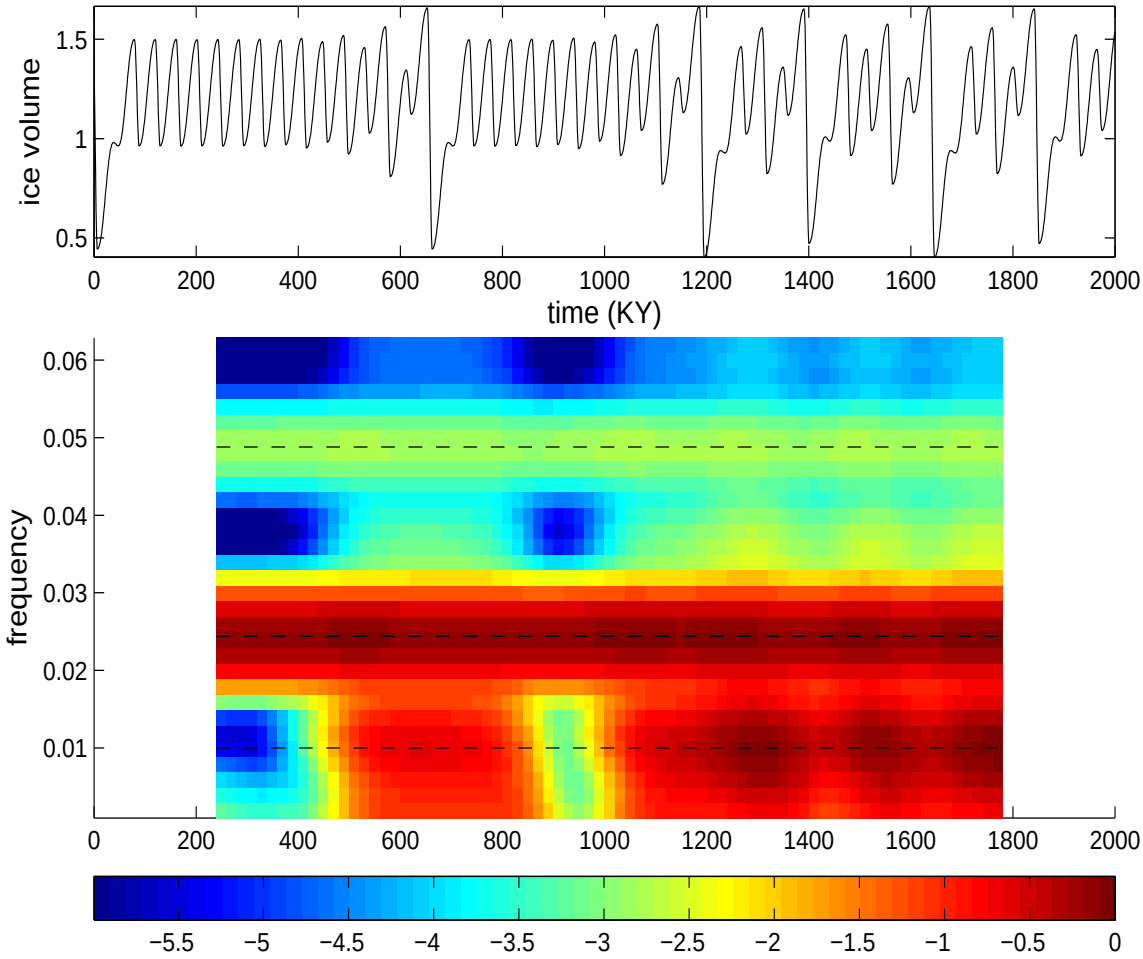

Figure 5-19: Spontaneous switching between 41KY and 100KY regimes. **top** A realization of the new model using the $\mathcal{F}_{op}$ parameterizations but where the forcing is a 41KY periodic signal with an amplitude of 1.3. Ice-volume is plotted in units of hectometers and time is in kiloyears. **bottom** Spectrogram of the model results using a 400KY sliding window. The color scaling is in logarithmic units and the horizontal dashed lines are at frequencies of 1/20, 1/40, and 1/100KY. The x-axis is time in KY and the y-axis is frequency in 1/KY.

glacial ice-volume lands near the fixed point, the next glaciation will also lie near this (weakly unstable) fixed point. For trajectories which land very near the fixed point, it requires a great many cycles to escape. Figure 5-19 shows another model realization where the model spends a significant portion of its time near the unstable fixed point before transitioning to cycles with large differences between successive glaciations. A spectrogram of the model realizations is also shown in Figure 5-19. While the model is near the fixed point, most of the variability is concentrated near the 1/40KY band,

but once it escapes the fixed point variability becomes concentrated in and around the 1/100KY band.

Obliquity had a strong influence on early Pleistocene climate variability. Existing explanations of why 100KY variability appears near 650KY BP have had to postulate a change in the governing dynamics of the system [e.g. *Raymo*, 1997; *Paillard*, 1998]. Here, an alternate explanation is given that the system spontaneously transitioned from obliquity forced glacial cycles in the vicinity of a fixed point to a more variable amplitude response. The best fit for the new model yields a parameterization which is not in a chaotic regime. At first this may seem to argue against a spontaneous onset of 100KY variability. However, the sensitivity of the model solution shown in Figure 5-7 suggests that a small changes in parameterizations or a subtle shift in the forcing, perhaps owing to any of the myriad stochastic influences on climate, could cause a *nearly spontaneous* transition. Whether the climate system is in fact chaotic or simply sensitive, the point is that the transitions to more energetic 100KY variability in the climate system need not be related to large scale shifts in the boundary conditions. The onset of 100KY variability could arise as a mode shift between glacial cycle trajectories involving nearly equal amplitude obliquity responses to a trajectory with terminations occurring only every second or third obliquity cycle.

It is argued that the explanation of the Pleistocene glacial record best in keeping with the observations is as a response to obliquity variations. In this view, precessional and eccentricity variations, to the extent they play a role, act as perturbations to the system. If the climate system is as sensitive during glacial climates as indicated by the new model, then these non-obliquity perturbations as well as a host of stochastic processes could have significant effects on subsequent climate states. Nonetheless, there appears to be good evidence that the basic timescale of the glacial cycles is paced by changes in obliquity. If this view is correct, then we are still in the 40KY world and only the amplitude of the response changed during the Mid-Pleistocene Transition.

5.9 Predictions and closing remarks

On the basis of the model results several predictions can be made regarding glacial variability. Spontaneous switching between 40 and 100KY regimes implies that the most recent shift at 650KY BP does not need to be a singular event. Indeed, there

is some evidence that 100KY variations are present in early Pleistocene records [e.g. *Beaufort*, 1994]. The further possibility exists that distinct 80 and 120KY regimes could occur in parts of the climate record. Identification of multiple transitions between glacial cycles dominated by 40, 80, or 120KY variations would provide support for the new model. An important caveat is that the age-model must be sufficiently accurate and not make assumptions regarding the astronomical origins of the 80 or 120KY variability. Using the depth-derived age-model approach, perhaps coupled with a minimal tuning strategy, it may be possible to test whether the climate system experienced multiple episodes of glacial variability on 80 and 120KY timescales. It may also prove useful to adopt a wavelet based approach to localize 80 or 120KY features in the climate record.

Second, the model suggests that melting events are a highly nonlinear process regardless of the extent of the ice-sheets. Thus, even in the 40KY world, there should be evidence of a nonlinear response to insolation forcing. Observational analysis indicates that such nonlinearities are present [e.g. *Hagelberg et al.*, 1991; *Ashkenazy and Tziperman*, submitted] and suggests that ablation occurs more quickly than accumulation in both the 40KY and 100KY worlds. There are again age-model considerations in that the observed rate of ice-volume change could be distorted by, for example, by squeezing the record during ablation events.

Furthermore, the model results indicate that during the 40KY regime, there should concentrations of variability at 1/20KY owing to the first over-tone of the obliquity forcing. If instead the energy in the 1/20 and 1/100KY bands were attributable to precessional forcing, one might expect that their relative strengths would be positively correlated, but *Pisias and Moore*, [1981] have found that the 100KY and precession energy do not covary. The new model instead suggests that the energy in the 1/20KY precession band is related to the strength of the 40KY variability. Optimally, a depth-derived age-model approach can be used to assess the climate variability during the 40KY world. Otherwise, the energy in any band which has been used for orbital-tuning of the age-model will be suspect and probably biased toward too much energy.

To summarize, this chapter employed simple deterministic models to describe the variability observed in EOF1. The models of *Imbrie and Imbrie* [1980] and *Paillard* [1998] were discussed and compared with a new model of glacial variability. When tuned, the new model produces the correct timing of the glacial cycles and reproduces much of the detailed structure recorded in EOF1. In addition, the periodogram and

auto-bicoherence of the new model results are in close agreement with that of EOF1. When compared to the Imbrie and Paillard models, the new model is considered the better description of EOF1.

Intrinsic to the new model are three distinct states of glaciation, $\{i, g, G\}$. For many parameterizations, the model chaotically cycles through these states and spontaneously switches between 40 and 100KY modes. In the 40KY mode, the model repetitively cycles through $g - G$ states and has nearly equal accumulation and ablation during each obliquity cycle. In the 100KY mode, there is a variable amplitude response involving 80KY $g - G$ or 120KY $i - g - G$ cycles which, on average, give the quasi-100KY glacial variability. Thus, the model offers an explanation of the Mid-Pleistocene transition as a spontaneous mode shift of a chaotic system.

The success of the new model in reproducing the timing of the glacial cycles, spectral and higher order features of EOF1, and shifts between 40 and 100KY modes of glacial variability suggests that its simple dynamics may have some qualitative agreement with the real climate system. Such a relationship, however, remains highly speculative and further research is required to establish the relationship (if any) between this (and other) very simple models and the diffusive, turbulent, and highly complex climate system.

Chapter 6

Summary and Conclusions

The first chapter of this thesis provides an overview of the spectrum of climate variability on timescales ranging from months to millions of years, the second explores modes of insolation forcing over these same timescales. The linchpin required to connect insolation forcing with a climate response is an accurate age-model, and chapter 3 is devoted to developing a chronology for marine sediment cores which is independent of orbital assumptions. Chapter 4 uses this chronology with a composite $\delta^{18}O$ record to test whether the glacial cycles are paced by orbital variations. A significant coupling is found between obliquity and the glacial terminations which is further explored in Chapter 5 through the use of very simple climate models. The conclusions which can be drawn from each of these chapters are summarized below.

Chapter 1 provides an overview of tropical sea surface temperature (SST) and high latitude surface air temperature variability (SAT) by piecing together spectra which resolve bands extending from frequencies of 1/month to 1/800KY (KY = kilo-year). The background continuum of temperature becomes more energetic towards lower frequencies. In the bands between 1/year and 1/800KY, tropical SST energy increases at a rate inversely proportional to frequency; i.e. a power law with $q = 1$. High-latitude SAT energy increases more slowly between bands of 1/2month and 1/100year with $q = 0.4$, and then more rapidly between 1/100year and 1/100KY with $q = 1.8$. The change in slope in the SAT spectrum, which is also weakly present in the SST spectrum, suggests that there is a qualitative change in the mechanisms responsible for climate variability near centennial timescales.

There exist concentrations of energy at the 1/100KY, 1/41KY, and 1/21KY bands in the SST spectrum. A one to one relationship exists between concentrations of SST

and insolation forcing energy at the obliquity (1/41KY), annual, and semi-annual bands. Conspicuously absent are insolation forcing at the 1/100KY and 1/21KY bands, indicating that either a nonlinear response to the insolation forcing or internal variability are required to explain the associated concentrations of SAT energy. In a subsequent chapter, significant concentrations of variability are also identified near 1/70 and 1/29KY, further suggesting the presence of a nonlinearity in the climate system.

There are numerous challenges in accurately estimating the climate spectrum. The net spectral energy at frequencies below 1/15KY is less than a third of the energy in the annual and semi-annual bands. This fact calls attention to the importance of the annual cycle, and the strong potential for non-seasonally resolved records to alias energy into the lower frequencies. When multiple spectra are pieced together to resolve high and low-frequency processes, this aliasing effect tends to bias the composite spectra towards appearing too red; in extreme cases aliasing can make white noise appear to obey a spectral power-law of one. Another complication in interpreting temperature variability is nonstationarity; for example, it is shown that Holocene temperatures in Greenland are much less energetic than during the last glacial.

So far the summary has focused on temporal variability, but there is also a rich spatial structure associated with temperature variability. To highlight the complexity of the temperature variability signal, the one point cross-correlation was computed between temperatures at the GISP2 site with the rest of the world using the NCEP reanalysis SATs after filtering out annual and higher frequencies. There is a strong positive correlation between GISP2 site temperatures and Greenland, weak correlation with the Arctic, and a complex pattern of positive and negative correlations over the rest of the world. A similarly complex pattern emerges if one computes the one point cross-correlation with reanalysis SATs at the Devils Hole site. Contrary to the arguments of *Mitchell* [1976], there does not appear to be a trend towards larger spatial scales with longer timescales, at least between the frequencies of 1/2month and 1/50year resolved by the NCEP reanalysis. The spatial scales of temperature variability at centennial and longer timescales remains an active topic of research. Note that the permanence of many geographical features of climatic relevance (e.g. mountains, oceans, the jet stream, polar night, etc.) ensures that climate will have at least some spatial variability extending out to time-scales approaching the Earth's

age.

Chapter 2 considers Earth's insolation forcing and highlights a few of the subtleties involved in interpreting its effects. Insolation forcing varies on timescales ranging from diurnal to hundreds of thousands of years, making it challenging to account for long-term variations while still resolving the highest frequency variability. A common technique used to simplify the insolation forcing signal into a slowly varying function is to consider only a day of the year or some portion of the year. Various methods include the calendar half-year, solar half-year, and caloric half-year. For most purposes, however, these quantities are an over-simplification of the insolation signal, for instance making it appear as if there is precession period variability directly present in the insolation forcing when, in fact, it is an alias of the seasonal cycle. To facilitate a more physical interpretation of the insolation forcing, a compact representation is put forward which uses a small number of spatial modes (the Legendre polynomials) and time-variable loadings. The time variable loadings are expressed using pairs of singular vectors, one of which represents the seasonal variability and the other the orbital timescale variability. This representation can express over 99% of the variance in the full spatial and temporal variability of insolation using the four leading Legendre polynomials (spatial modes) and four leading sets of singular vectors (temporal modes). It is suggested that insolation forcing should be thought of as a set of time-variable spatial modes whose amplitudes are modulated by changes in the Earth's orbit and orientation. That is, rather than discussing insolation on a given day of the year or at a particular latitude, as is common in the paleoclimate literature, it is more physical to consider modes of insolation forcing.

Only variations in obliquity and, to a much lesser extent, eccentricity cause low-frequency shifts in Earth's insolation forcing. Precession of the equinoxes has no effect on the mean annual insolation, but does modulate the amplitude of the seasonal cycle when eccentricity is non-zero. It is only when a nonlinear mechanism rectifies the seasonal modulation that precession-period variability appears. It is shown that such rectification can arise from physical processes within the climate system, but that the seasonality inherent to many climate proxies will also produce precession-period variability in the records. One should distinguish this *instrumental* effect from true climate responses. Careful examination of regions without seasonal cycles, for example the abyssal non-equatorial ocean, and the use of proxies with different seasonal responses, might permit separation of physical from instrumental effects.

When the age-model of a record is *orbitally-tuned*, there are further complications associated with the interpretation of orbital features in the climate record. In this context, tuning refers to the practice of stretching and squeezing the age-model of a paleo-climate record so as to sharpen and enhance features of its orbital variability. Obviously, tuning can affect the frequency and energy distribution within a record. In the case of pass-band-filtered records, it is shown that orbital-tuning can also build-in eccentricity amplitude modulation of the precession variability, consistent with the results of *Neeman* [1993]. This is because the precession parameter is both amplitude and frequency modulated by changes in precession. To prevent circular reasoning when assessing the relationship between climate and insolation forcing, one should use an age-model which makes no orbital assumptions.

Chapter 3 develops a new chronology of glaciation, spanning the last 780KY, from 21 marine sediment cores using depth as a proxy for time. To avoid biasing this *depth-derived* age estimate, the depth-scale is first corrected for the effects of sediment compaction. To provide age uncertainty estimates, the spatial and temporal variability of marine sediment accumulation rates are estimated and modeled as an autocorrelated stochastic process. Depth-derived ages are estimated to be accurate to within ±9KY and within this uncertainty are consistent with the orbitally-tuned age estimates. Nonetheless, the remaining differences between the depth and orbitally-tuned chronologies produce important differences in the spectral domain. It appears orbital tuning suppresses the presence of nonlinearities in the $\delta^{18}O$ record involving the 100KY and obliquity frequency bands.

Because the depth-derived chronology makes no assumptions concerning the climate response to insolation forcing, it provides an unbiased chronology by which to analyze the relationship between climate variability and insolation forcing. Analysis of the $\delta^{18}O$ record, using the depth-derived age-model, indicates the presence of nonlinear interactions in the climate record. These interactions involve combination tones of the 1/100KY and 1/41KY variability and are significant features of both the periodogram of $\delta^{18}O$ and higher order statistics such as the auto-bicoherence. Using Fourier based methods, however, it is not possible to distinguish between obliquity control of the 100KY variability and a weak nonlinear coupling between obliquity and an independent 100KY variability.

Chapter 4 further investigates the nonlinear coupling between orbital variations and the quasi-100KY glacial cycles. *Rayleigh*'s R is used to quantify phase coupling between the orbital parameters and the Pleistocene glacial terminations. Standard hypothesis testing procedures are used to decide whether the R between glacial terminations and each orbital parameters is significant. Key to determining whether a coupling is significant is the development of an adequate null-hypothesis, and a random-walk glacial model is used to estimate the probability distribution associated with the null-hypothesis of no coupling between orbital variability and the glacial terminations. The null-hypothesis cannot be rejected for precession or eccentricity, but for obliquity the null-hypothesis is rejected at the 95% confidence level.

To investigate the robustness of the obliquity test, the probability distribution of the null-hypothesis was also estimated using other simple models and surrogate data techniques. In all cases, the obliquity null-hypothesis is rejected, indicating that the results are robust. Furthermore, the obliquity nonlinear coherence is consistent with the alternate hypothesis that glacial terminations occur when obliquity is near a fixed phase, and the power of the obliquity test is $P = 0.58$. It is thus concluded that terminations are triggered near maxima in obliquity. Such an obliquity pacing of the glacial cycles implies that terminations occur every second or third obliquity cycle, where the average of the 2×40 and 3×40KY cycles gives the 100KY variability. In agreement with this implication, a histogram of the duration between glacial cycles shows a bimodal distribution with peaks near 80 and 120KY.

Chapter 5 further explores the relationship between orbital variations and glacial variability using simple deterministic climate models. Three simple models of the relationship between climate and orbital forcing are considered. The model of *Imbrie and Imbrie* [1980] is used to argue for the importance of slow ice-volume accumulation in setting the timescale of the glacial cycles, while the model by *Paillard* [1998] highlights the roll of thresholds and state dependence in the climate system. The identified features of the climate variability are incorporated into a new model which has a simple form and a small number of adjustable parameters. When tuned, the new model gives the correct timing for each termination and reproduces the linear and nonlinear spectral features earlier identified in the $\delta^{18}O$ EOF1 record.

Under a broad variety of conditions the model exhibits a chaotic amplitude response to insolation forcing. In this chaotic regime two modes of behavior are distinguished: one where successive ablation events are relatively small and of nearly the

same magnitude, and another where ice accumulates over two or three forcing cycles before rapidly ablating. Thus, when the model is forced by obliquity variations, the former mode is identified with the 40KY world, and the latter with the onset of large quasi-100KY variability roughly 650K ago. Both the 40KY and 100KY modes of glacial variability are intrinsic to the behavior of the chaotic simple model, and suggests that the Mid-Pleistocene Transition may be a spontaneous event independent of any major shifts in the background state of the climate system.

Two predictions can be made on the basis of the simple chaotic model result. First, the major ablation events are expected to be nonlinear and abrupt even during the 40KY world. This form of nonlinearity is expected to generate over-tones so that some part of the energy in the 1/20KY band arises because of obliquity, rather than precession forcing. Second, spontaneous switching between 40 and 100KY modes of variability imply that the Mid-Pleistocene transitions need not be a singular event, and periods of 100KY variability may be discernible prior to the Mid-Pleistocene Transition.

Overall, the origins of the ice-ages can be rationalized from two rather different starting points: the Milankovitch thesis of glacial climate variability as being controlled by deterministic, periodic changes in the distribution and intensity of insolation; or the stochastic antithesis that climate is random, broad-band, and controlled by processes internal to the system. Here it was argued that obliquity paces the glacial cycles, making climate partly deterministic, but also that much of the climate variability is consistent with a stochastic process, identifiable with the broad-band spectral continuum, and which is quantified using spatial and temporal scaling relationships. It is anticipated that future research will turn from debating whether climate is controlled by Milankovitch or stochastic processes towards synthesizing these forcing mechanisms into a more general theory of climate variability.

Bibliography

[1] J. Adkins, K. McIntyre, and D.P. Schrag. The salinity, temperature, *anddelta*^{18}O of the glacial deep ocean. *Science*, 298:1724–1725, 2002.

[2] J. Adkins and D. Schrag. Pore fluid constraints on past deep-ocean temperature and salinity. *Geophysical Research Letters*, 28:771–774, 2001.

[3] J. Adkins and D.P. Schrag. Models of pore fluid chlorinity and the salinity of the southern ocean at the last glacial maximum. *Earth and Planetary Science Letters*, 216:109–123, 2003.

[4] L.F. Athy. Density, porosity and compaction of sedimentary rocks. *AAPG Bull.*, 14:1–24, 1930.

[5] D. Bahr, J. Hutton, E. Syvitski, and L. Pratson. Exponential approximations to compacted sediment porosity profiles. *Computers and Geoscience*, 27:691–700, 2001.

[6] E. Bard, B. Hamelin, and R.G. Fairbanks. U-Th ages obtained by mass spectrometry in corals from Barbados: sea level during the past 130,000 years. *Nature*, 346:241–244, 1990.

[7] S. Barland, O. Piro, M. Giudici, J. Tredicce, and S. Balle. Experimental evdidence of van der Pol-fitzhugh-nagumo dynamics in semiconductor optical amplifiers. *Physical Review E*, 68, 2003.

[8] F.C. Bassinot, E. Beaufort, L. Vincent, F. Labeyrie, P.J. Rostek, Muller, X. Quidelleur, and Y. Lancelot. Coarse fraction fluctuations in pelagic carbonate sediments from the Tropical Indian Ocean: A 1500-kyr record of carbonate dissolution. *Paleoceanography*, 9:579–599, 1994.

[9] L. Beaufort. Climatic importance of the modualtion of the 100 kyr cycle inferred from 16 m.y. long Miocen1e records. *Paleoceanography*, 9:821–834, 1994.

[10] B. Bemis, H. Spero, J. Bijma, and D. Lea. Reevaluation of the oxygen isotopic composition of planktonic foraminifera: Experimental results and revised paleotemperature equations. *Paleoceanography*, 13(2):150–160, 1998.

[11] M. Bender. *Vostok ice core trapped gas concentrations and isotopic compositions*. Boulder, CO: National Snow and Ice Data Center. Digital Media, 2002.

[12] R. Benzi, G. Parisi, A. Sutera, and A. Vulpiani. Stochastic resonance in climatic change. *Tellus*, 34:10–16, 1982.

[13] A. Berger and M. F. Loutre. Astronomical solutions for paleoclimate studies over the last 3 million years. *Earth Planet. Sci. Lett.*, 111:369–382, 1992.

[14] A. Berger, M. F. Loutre, and C. Tricot. Insolation and earths orbital periods. *J. Geophys. Res.-Atmos.*, 98:10341–10362, 1993.

[15] A. Berger, M.F. Loutre, and J.L. Melice. Instability of the astronomical periods from 1.5 MYR BP to .5 MYR AP. *Paleoclimates*, 2(4):239–280, 1998.

[16] A. L. Berger. Astronomical theory of paleoclimates and the last glacial-interglacial cycle. *Quat. Sci. Rev.*, 11:571–581, 1992.

[17] W.H. Berger and E. Jansen. Mid-Pleistocene climate shift - the Nansen connection. In O.M. Johannessen, R.D. Muench, and J.E. Overland, editors, *The Polar Oceans and Their Role in Shaping the Global Environment*, volume 85, pages 295–311, 1996.

[18] R. N. Bhattacharya and E. C. Waymire. *Stochastic Processes with Applications*. John Wiley & Sons, 1990.

[19] T. Bickert, W.B. Curry, and G. Wefer. Late Pliocene to Holocene (2.6-0 MA) Western Equatorial Atlantic deep water circulation: Inferences from benthic stable isotopes. In N.J. Shackleton, W.B. Curry, C. Richter, and T.J. Bralower, editors, *Proceedings of the Ocean Drilling Program Scientific Results*, volume 154, pages 239–253, 1997.

[20] B. Bills. Obliquity-oblateness feedback: Are climately sensitive values of obliquity dynamically unstable? *Geophysical Research Letters*, 21:177–180, 1994.

[21] T. Blunier and E. Brook. Timing of millennial-scale climate change in Antarctica and Greenland during the last glacial period. *Science*, 291:109–112, 2001.

[22] E.W. Bolton and K.A. Maasch. A wavelet analysis of Plio-Pleistocene climate indicators: A new view of periodicity evolution. *Geophysical Research Letters*, 22:2753–2756, 1995.

[23] G. Bond, W. Showers, M. Cheseby, R. Lotti, P. Almasi, P. deMenocal, P. Priore, H. Cullen, I Hadjas, and G. Bonani. A pervasive millennial-scale cycle in North Atlantic Holocene and glacial climates. *Science*, 278:1257–1266, 1997.

[24] R.E. Boyce. Definitions and laboratory techniques of compressional sound velocity parameters and water-wet content, wet-bulk density, and porosity parameters by gravimetric and gamma ray attenuation techniques. In S.O. Schlanger, editor, *Initial Reports of the Deep Sea Drilling Project*, volume 33, pages 931–958, 1976.

[25] R. Bracewell. *The Fourier Transform and its Applications*. McGraw Hill, 2000.

[26] R. S. Bradley. *Paleoclimatology*. Academic Press, San Diego, 1999.

[27] K.R. Briffa, T.J. Osborn, F.H. Schweingruber, I.C. Harris, P.D. Jones, S.G. Shiyatov, and E.A. Vaganov. Low-frequency temperature variatons from a northern tree-ring density network. *Journal of Geophysical Research*, 106:2929–2941, 2001.

[28] W. Broecker, D.L. Thurber, J. Goddard, T.L. Ku, R.K. Matthews, and K.J. Mesolella. Milankovitch hypothesis supported by precise dating of coral reefs and deep-sea sediments. *Science*, 159:297–300, 1968.

[29] W.S. Broecker. Terminations. In Berget et al., editor, *Milankovitch and climate, Part2*, pages 687–698. D. Reidel, 1984.

[30] W. Bruggerman. A minimal cost function method for optimizing the age-depth relationship of deep-sea sediment cores. *Paleoceanography*, 7:467–487, 1992.

[31] N. Caillon, J. Jouzel, and J. Chappeallaz. Reconstruction of the surface temperature change in central Greenland during D/O 12, 45 kyr b.p. *EOS transactions*, 82, 2001.

[32] J.E.T. Channell, D.A. Hodell, and B. Lehman. Relative geomagnetic paleointensity and δ^{18}O at ODP site 983. *Earth and Planetary Science Letters*, 153:103–118, 1997.

[33] J. Chen, J. Farrell, D. Murray, and W Prell. Timescale and paleoceanographic implications of a 3.6 m.y. oxygen isotope record from the Northeast Indian Ocean (ODP site 758). *Paleoceanography*, pages 21–47, 1995.

[34] E.R. Cook, K.R. Briffa, D.M. Meko, D.S. Graybill, and G. Funkhouser. The 'segment length curse' in long tree-ring chronology development for paleoclimatic studies. *The Holocene*, 5(2):229–237, 1995.

[35] T. M. Cronin. *Principles of Paleoclimatology*. Columbia Un. Press, New York, 1999.

[36] J.L. Cullen and W.B. Curry. Variations in planktonic foraminifer faunas and carbonate preservation at site 927: evidence for changing surface water conditions in the Western Tropical Atlantic Ocean during the middle Pleistocene. In N.J. Shackleton, W.B. Curry, C. Richter, and T.J. Bralower, editors, *Proceedings of the Ocean Drilling Program Scientific Results*, volume 154, pages 207–228, 1997.

[37] W. Curry and D. Oppo. Synchronous, high frequency oscillations in tropical sea surface temperatures and north atlantic deep water production during the last glacial cycle. *Paleoceanography*, 12:1–14, 1997.

[38] W.B. Curry and J.L. Cullen. Carbonate production and dissolution in the Western Equatorial Atlantic during the last 1 MY. In N.J. Shackleton, W.B. Curry, C. Richter, and T.J. Bralower, editors, *Proceedings of the Ocean Drilling Program Scientific Results*, volume 154, pages 189–199. Ocean Drilling Program, College Station TX, 1997b.

[39] D. Dahl-Jensen, K. Mosegaard, N. Gundestrup, G. Clow, S. Johnsen, A. Hansen, and N. Balling. Past temperatures directly from the Greenland Ice Sheet. *Science*, 282:268–271, 1998.

[40] J.M.A Danby. *Fundamentals of Celestial Mechanics*. Willmann-Bell, 1992.

[41] P. de Menocal, J. Ortiz, T. Guilderson, and M. Sarnthein. Coherent high- and low-latitude climate variability during the holocene warm period. *Science*, 288:2198–2202, 2000.

[42] J. Devore. *Probability and Statistics for Engineering and the Sciences*. Duxbury, 2000.

[43] B. Efron. Does an observed sequence of numbers follow a simple rule? (Another look at Bode's Law). *Journal of the American Statistical Association*, 66(335):552–559, 1971.

[44] M. Elkibbi and J.A. Rial. An outsider's review of the astronomical theory of the climate: is the eccentricity-driven insolation the main driver of the ice ages? *Earth-Science Reviews*, 56:161–177, 2001.

[45] I. Epstein and J. Pojman. *An introduction to nonlinear chemical dynamics: oscillations, waves, patterns, and chaos*. Oxford Univesity Press, 1998.

[46] R. Fairbanks. A 17,000-year glacio-eustatic sea level record; influence of glacial melting rates on the younger dryas event and deep-ocean circulation. *Nature*, 342:637–642, 1989.

[47] W. Feller. *An introduction to probability theory and its applications*. Wiley mathematical statistics series, 1966.

[48] R. FitzHugh. Impulses and physiological states in theoretical models of nerve membrane. *Biophysical Journal*, 1:445–466, 1961.

[49] B.P. Flower. Planktonic foraminifers from the Subpolar North Atlantic and Nordic Seas: Sites 980-987 and 907. In M.E. Raymo, E. Jansen, P. Blum, and T.D. Herbert, editors, *Proceedings of the Ocean Drilling Program*, pages 19–34, 1999.

[50] C. D. Gallup, H. Cheng, F. W. Taylor, and R. L. Edwards. Direct determination of the timing of sea level change during Termination II. *Science*, 295:310–314, 2002.

[51] M. Ghil. Cryothermodynamics: the chaotic dynamics of paleoclimate. *Physica D*, 77:130–159, 1994.

[52] H. Gildor and E. Tziperman. Sea ice as the glacial cycles' climare switch: Role of seasonal and orbital forcing. *Paleoceanography*, 15:605–615, 2000.

[53] L. Glass and A. Shrier. Low-dimensional dynamics in the heart. In L. Glass, P. Hunter, and A. McCulloch, editors, *Theory of Heart*, pages 289–312. Springer, 1991.

[54] I. Good. A subjective evaluation of Bode's Law and an "objective" test for approximat numerical rationality. *Journal of the American Statistical Association*, 64(325):23–49, 1969.

[55] G. Gottwald and I. Melbourne. A new test for chaos in deterministic systems. *Proceeding of the Royal Society*, 460:603–611, 2004.

[56] P.M. Grootes and M. Stuiver. Oxygen 18/16 variability in Greenland snow and ice with 10^3 to 10^5 year time resolution. *Journal Geophysical Research*, 102:26455–26470, 1997.

[57] T. Hagelberg, N. Pisias, and S. Elgar. Linear and nonlinear couplings between orbital forcing and the marine δ^{18}O record. *Paleoceanography*, 6:729–746, 1991.

[58] T. Hagelberg, N. Pisias, L Mayer, N. Shackleton, and A. Mix. Spatial and temporal variability of Late Neogene equatorial Equatorial Pacific carbonate: Leg 138. In N.G. Pisias, L.A. Mayer, T.R. Janecek, A. Palmer-Julson, and T.H. van Andel, editors, *Proceedings of the Ocean Drilling Program Scientific Results*, volume 138, pages 321–336, 1995.

[59] K. Hasselmann. Stochastic climate models. part I. theory. *Tellus*, 6:473–485, 1976.

[60] K. Hasselmann, W. Munk, and G. MacDonald. Bispectra of ocean waves. In Rosenblatt, editor, *Proc. Symposium on Time Series Analysis*, pages 125–139. J. Wiley, 1963.

[61] W. Hayes and S. Tremaine. Fitting selected random planetary systems to Titius-Bode laws. *Icarus*, 135:549–557, 1998.

[62] J.D. Hays, J. Imbrie, and N.J. Shackleton. Variations in the earth's orbit: Pacemaker of the ice ages. *Science*, 194:1121–1132, 1976.

[63] G. Henderson and N. Slowey. Evidence from U-Th dating against Northern Hemisphere forcing of the penultimate deglaciation. *Nature*, 404:61–66, 2000.

[64] T. Herbert and L. Mayer. Long climatic time series form sediment physical property measurements. *Journal of Sedimentary Petrology*, 61(7):1089–1108, 1991.

[65] T.D. Herbert. Readings orbital signals distorted by sedimentation: models and examples. In P.L. de Boer and D.G. Smith, editors, *Orbital Forcing and Cyclic Sequences*, pages 483–507. Blackwell Scientific Publications, 1994.

[66] T.D. Herbert, J.D. Schuffert, D. Andreasen, L. Heusser, M. Lyle, A. Mix, A.C. Ravelo, L.D. Stott, and J.C. Herguera. Collapse of the California current during glacial maximum linked to climate change on land. *Science*, 293:71–76, 2001.

[67] L. Hinnov. New perspectives on orbitally forced stratigraphy. *Annu. Rev. Earth Planet. Sci.*, 28:419–475, 2000.

[68] P. Huybers. Depth and orbital tuning: a new chronology of glaciation and nonlinear orbital climate change. Master's thesis, MIT, 2002.

[69] P. Huybers and C. Wunsch. Rectification and precession-period signals in the climate system. *Geophysical Research Letters*, 30(19), 2003.

[70] P. Huybers and C. Wunsch. A depth-derived Pleistocene age-model: Uncertainty estimates, sedimentation variability, and nonlinear climate change. *Paleoceanography*, 19, 2004.

[71] J. Imbrie, A. Berger, E. A. Boyle, S. C. Clemens, A. Duffy, W. R. Howard, G. Kukla, J. Kutzbach, D. G. Martinson, A. McIntyre, A. C. Mix, B. Molfino, J. J. Morley, L. C. Peterson, N. G. Pisias, W. L. Prell, M. E. Raymo, N. J. Shackleton, and J. R. Toggweiler. On the structure and origin of major glaciation cycles .2. The 100,000-year cycle. *Paleoceanography*, 8:699–735, 1993.

[72] J. Imbrie, E. A. Boyle, S. C. Clemens, A. Duffy, W. R. Howard, G. Kukla, J. Kutzbach, D. G. Martinson, A. McIntyre, A. C. Mix, B. Molfino, J. J. Morley,

L. C. Peterson, N. G. Pisias, W. L. Prell, M. E. Raymo, N. J. Shackleton, and J. R. Toggweiler. On the structure and origin of major glaciation cycles. 1. Linear responses to Milankovitch forcing. *Paleoceanography*, 6:205–226, 1992.

[73] J. Imbrie, J.D. Hays, D.G. Martinson, A. McIntyre, A.C. Mix, J.J. Morley, N.G. Pisias, W.L. Prell, and N.J. Shackleton. The orbital theory of Pleistocene climate: Support from a revised chronology of the marine delta 18 O record. In A.L. Berger et al., editor, *MIlankovitch and Climate, Part 1*, pages 269–305. D. Reidel Publishing Company, 1984.

[74] J. Imbrie, J.D. Hays, D.G. Martinson, A. McIntyre, A.C. Mix, J.J. Morley, N.G. Pisias, W.L. Prell, and N.J. Shackleton. The orbital theory of Pleistocene climate: Support from a revised chronology of the marine delta 18 O record. In A.L. Berger et al., editor, *MIlankovitch and Climate, Part 1*, pages 269–305. D. Reidel Publishing Company, 1984.

[75] J. Imbrie and J.Z. Imbrie. Modeling the climatic response to orbital variations. *Science*, 207:943–953, 1980.

[76] J.D. Jackson. *Classical Electrodynamics, 3rd Ed.* John Wiley and Sons Inc., 1999.

[77] R.G. Johnson. Brunhes-Matuyama magnetic reversal dated at 790,000yr b.p. by marine-astronomical correlations. *Quaternary Research*, 17:135–47, 1982.

[78] S. Joussaume and P. Braconnot. Sensitivity of paleoclimate simulation results to season definitions. *Journal of Geophysical Research*, 102(D2):1943–1956, 1997.

[79] D. Karner, J. Levine, B.P. Medeiros, and R. Muller. Constructing a stacked benthic δ^{18}O record. *Paleoceanography*, 2002.

[80] D.B. Karner and F. Marra. Correlation of fluviodeltaic aggradational sections with glacial climate history: a revision of the Pleistocene stratigraphy of Rome. *Geological Society of America Bulletin*, 110:748–758, 1998.

[81] M. Kominz and N. Pisias. Pleistocene climate —- determinstic or stochastic? *Science*, 204, 1979.

[82] J Laskar. A numerical experiment on the chaotic behaviour of the solar system. *Nature*, 338:237–238, 1989.

[83] J. Laskar, F. Joutel, and F. Boudin. Orbital, precessional, and insolation quantities for the earth from -20 myrs to +10mrs. *Astronomical Astrophysics*, 270:522–533, 1993.

[84] D. Lea, D. Pak, L. Peterson, and K. Hughen. Synchroneity of tropical and high-latitude atlantic temperatures over the last glacial termination. *Science*, 301(5638):1361–1364, 2003.

[85] D. Lea, D. Pak, and H. Spero. Climate impact of late Quaternary Equatorial Pacific sea surface temperature variations. *Science*, 289:1719–1724, 2000.

[86] B.K Linslye, G. M. Wellington, and D.P. Schrap. Decadal sea surface temperature variability in the sub-tropical south pacific from 1726 to 1997 a.d. *Science*, 290:1145–1148, 2000.

[87] L. Lisiecki and P. Lisiecki. Application of dynamic programming to the correlation of paleoclimate records. *Paleoceanography*, 17:1–1,1–12, 2002.

[88] E. Lorenz. Deterministic nonperiodic flow. *Journal of Atmospheric Science*, 20:130–141, 1963.

[89] M. Lyle. Neogene carbonate burial in the Pacific Ocean. *Paleoceanography*, 18, 2003.

[90] P. Lynch. On the significance of the Titius-Bode law for the distribution of the planets. *Monthly Notices of the Royal Astronomical Society*, 341:1174–1178, 2003.

[91] A.K. MacKillop, K. Moran, K. Jarret, J. Farrell, and D. Murray. Consolidation properties of Equatorial Pacific Ocean sediments and there relationship to stress history and offsets in the leg 138 composite depth sections. In N. Pisias, L. Mayer, T. Janecek, A. Palmer-Julson, and T. van Andel, editors, *Proceedings of the Ocean Drilling Program Scientific Results*, volume 138, pages 357–369, 1995.

[92] G. Manley. Central england temperatures: monthly means 1659 to 1973. *Quarterly Journal of the Royal Meteorological Society*, 100:389–405, 1974.

[93] S. Marshall and P. Clark. Basal temperature evolution of North American ice sheets and impications for the 100-kyr cycle. *Geophysical Resarch Letters*, 29(24), 2002.

[94] D. G. Martinson, W. Menke, and A. Stoffa. An inverse approach to signal correlation. *Journal of Geophysical Research*, 87:4807–4818, 1982.

[95] D. G. Martinson, N. G. Pisias, J. D. Hays, J. Imbrie, T. C. Moore, and N. J. Shackleton. Age dating and the orbital theory of the ice ages - development of a high-resolution-0 to 300,000-year chronostratigraphy. *Quat. Res.*, 27:1–29, 1987.

[96] P.A. Mayewski, L.D. Meeker, M.S. Twickler, S.I. Whitlow, Q. Yang, W.B. Lyons, and M. Prentice. Major features and forcing of high-latitude Northern Hemisphere atmospheric circulation using a 110,000-year-long glaciochemical series. *Journal of Geophysical Research*, 102:26345–26366, 1997.

[97] J.F. McManus, D.W. Oppo, and J.L. Cullen. A 0.5 million year record of millennial-scale climate variability in the North Atlantic. *Science*, 283:971–975, 1999.

[98] J.F. McManus, D.W. Oppo, J.L. Cullen, and S.L. Healey. Marine Isotope Stage 11 (MIS 11): Analog for Holocene and future climate? In A. Droxler, R. Poore, L. Burckle, and L. Osterman, editors, *Earth's Climate and Orbital Eccentricity: The Marine Isotope Stage 11 Question*, volume 137, pages 69–85. AGU, 2003.

[99] J.F. McManus, D.W. Oppo, L.D. Keigwin, J.L. Cullen, and G.C. Bond. Thermohaline circulation and prolonged interglacial warmth in the North Atlantic. *Quaternary Reviews*, 58:17–21, 2002.

[100] D.G. McMillan, C.G. Constable, and R.L. Parker. Limitations on stratigraphic analyses due to incomplete age control and their relevance to sedimentary paleomagnetism. *Earth Planet. Sci. Lett.*, 201:509–523, 2002.

[101] CLIMAP Project Members. The surface of the ice-age earth. *Science*, 191:1131–1137, 1981.

[102] M. Milankovitch. *Kanon der Erdbestrahlung und seine Andwendung auf das Eiszeitenproblem*. Royal Serbian Academy, 1941.

[103] J. Mitchell. An overview of climatic variability and its causal mechanisms. *Quaternary Research*, 6:481–493, 1976.

[104] A.C. Mix, J. Le, and N.J. Shackleton. Benthic foraminifer stable isotope stratigraphy of site 846: 0-1.8 ma. In G. Pisias, N, T.R. Mayer L.A.and Janecek, A. Palmer-Julson, and T.H. van Adel, editors, *Proceedings of the Ocean Drilling Program Scientific Results*, volume 138, pages 839–854, 1995b.

[105] A.C. Mix, N.G. Pisias, W. Rugh, J. Wilson, A. Morey, and T.K. Hagelberg. Benthic foraminifer stable isotope record from site 849 (0-5ma): Local and global climate changes. In G. Pisias, N, T.R. Mayer L.A.and Janecek, A. Palmer-Julson, and T.H. van Adel, editors, *Proceedings of the Ocean Drilling Program Scientific Results*, volume 138, pages 371–412, 1995a.

[106] M. I. Moore and P. J. Thomson. Impact of jittered sampling on conventional spectral estimates. *J. Geophys. Res.-Oceans*, 96:18519–18526, 1991.

[107] K. Moran. Elastic property correction applied to leg 154 sediment, Ceara Rise. In N.J. Shackleton, W.B. Curry, C. Richter, and T.J. Bralower, editors, *Proceedings of the Ocean Drilling Program Scientific Results*, volume 154, pages 151–155, 1997.

[108] R. Muller and G. MacDonald. *Ice Ages and Astronomical Causes*. Springer, 2000.

[109] R. A. Muller and G. J. MacDonald. Glacial cycles and astronomical forcing. *Science*, 227:215–218, 1997.

[110] W. Munk, M Dzieciuch, and S. Jayne. Millennial climate variability: is there a tidal connection? *Journal of Climate*, 15:370–385, 2002.

[111] C. Murray and S. Dermott. *Solar System Dynamics*. Cambridge University Press, 1999.

[112] J. Nagumo, S. Animoto, and S. Yoshizawa. An active pulse transmission line simulating nerve axon. *Proc. Inst. Radio Engineers*, 50, 2061-2070.

[113] B. Neeman. Orbital tuning of paleoclimate records: A reassessment. *Lawrence Berkeley Laboratory Report*, LBNL-39572, 1993.

[114] D.C. Nobes, S.F. Bloomer, J. Mienert, and F. Westall. Milankovitch cycles and nonlinear response in the Quaternary record in the Atlantic sector of the Southern Oceans. *Proceedings of the ODP, Scientific Results*, 114, 1991.

[115] J. Odell. Error estimation in stratigraphic correlation. *Mathematical Geology*, 7:167–182, 1975.

[116] Frank W. Olver. *Tables for Bessel functions of moderate or larger orders*. London, H. M. Stationary Off., 1962.

[117] D. W. Oppo, L.D. Keigwin, J.F. McManus, and J.L. Cullen. Persistent suborbital climate variability in marine isotope stage 5 and Termination II. *Paleoceanography*, 16:280–292, 2001.

[118] D. W. Oppo, J.F. McManus, and J.L. Cullen. Abrupt climate events 500,000 to 340,000 years ago: Evidence from subpolar North Atlantic sediments. *Science*, 279:1335–1338, 1998.

[119] J. Pelletier. The power-spectral density of atmospheric temperature from time scales of 10^{-2} to $10^{6}yr$. *Earth and Planetary Science Letters*, 158:157–164, 1998.

[120] P. Pestiaux and A. Berger. Impacts of deep-sea processes on paleoclimatic spectra. In A.L. Berger et al., editor, *Milankovitch and Climate, Part 1*, pages 493–510. D. Reidel Publishing Company, 1984.

[121] J.R. Petit, J. Jouzel, D. Raynaud, N. Barkov, J. Barnola, I. Basile, M. Bender, J. Chappellaz, M. Davis, G. Delaygue, M. Delmotte, M. Kotlyakov, M. Legrand, V. Lipenkov, C. Lorius, L. Pepin, C. Ritz, E. Saltzman, and M. Stivenard. Climate and atmospheric history of the past 420,000 years from the Vostok ice core, Antarctica. *Nature*, 399:429–436, 1999.

[122] G. Philander and A. Fedorov. Role of tropics in changing the response to Milnakovitch forcing some three million years ago. *Paleoceanography*, 2003.

[123] A. Pikovsky, M. Rosenblum, and J. Kurths. *Synchronization*. Cambridge University Press, 2001.

[124] N. Pisias and A. Mix. Aliasing of the geologic record and the search for long-period milankovitch cycles. *Paleoceanography*, 3:613–619, 1988.

[125] N. Pisias and T. Moore. The evolution of Pleistocene climate: a time series approach. *Earth and Planetary Science Letters*, 52:450–458, 1981.

[126] W. Prell. Oxygen and carbon isotope stratigraphy for the Quaternary of hole 502b: evidence for two modes of isotopic variability. *DSDP Initial Reports*, 68:455–464, 1982.

[127] W.L. Prell, J. Imbrie, D.G. Martinson, J.J. Morley, N.G. Pisias, N.J. Shackleton, and H. Streeter. Graphic correlation of oxygen isotope records: application to the late Quaternary. *Paleoceanography*, 1:137–162, 1986.

[128] W.H. Press, S.A. Teukolsky, W.T. Vetterling, and B.P. Flannery. *Numerical Recipes in C*. Cambridge University Press, 1999.

[129] M.B. Priestly. *Spectral Analysis and Time Series*. Academic Press, 1981.

[130] A.C. Ravelo and N.J. Shackleton. Evolution of surface water circulation in the east equatorial pacific over the past 2.0 ma: Isotopic measurements from ODP site 851. In N.G. Pisias, L.A. Mayer, T.R. Janecek, A. Palmer-Julson, and T.H. van Andel, editors, *Proceedings of the Ocean Drilling Program*, pages 503–514, 1995.

[131] M. E. Raymo. The timing of major climate terminations. *Paleoceanography*, 12:577–585, 1997.

[132] M.E. Raymo and K. Nisancioglu. The 41 kyr world: Milankovitch's other unsolved mystery. *Paleoceanography*, 18(1), 2003.

[133] J.A. Rial. Pacemaking the ice ages by frequency modulation of earth's orbital eccentricity. *Science*, 285:564–568, 1999.

[134] G. Roe and M. Allen. A comparison of competing explanations for the 100,000-yr ice age cycle. *Geophysical Research Letters*, 26:2259–2262, 1999.

[135] M. Rosenblum and A. Pikovsky. Synchronization: from pendulum clocks to chaotic lasers and chemical oscillators. *Contemporary Physics*, 44(5):401–416, 2003.

[136] D.P. Rubincam. Insolation in terms of earth's orbital parameters. *Theoretical Applied Climatology*, 48:195–202, 1994.

[137] W. F. Ruddiman and A. McIntyre. Oceanic mechanisms for amplification of the 23,000-year ice-volume cycle. *Science*, 212:617–727, 1981.

[138] W. F. Ruddiman, M.E. Raymo, D.G. Martinson, B.M Clement, and J. Backman. Pleistocene evolution: Northern Hemisphere ice sheets and the North Atlantic Ocean. *Paleoceanography*, 4:353–412, 1989.

[139] A Salamatin, V Lipenkov, N Barkov, J Jouzel, J Petit, and D. Raynaud. Ice core age dating and paleothermometer calibration based on isotope and temperature profiles from deep boreholes at vostok station (east antarctica). *Jounal of Geophysical Research — Atmospheres*, 103:8963–8977, 1998.

[140] B Saltzman. *Dynamical Paleoclimatology: Generalized Theory of Global Climate Change*. Academic Press, 2002.

[141] F. Schmiedier, T. von Dobeneck, and U. Bleil. The mid-pleistocene climate transition as documented in the deep south atlantic ocean: initiation, interim state and terminal event. *Earth and Planetary Science Letters*, 179 (3-4):539–549, 2000.

[142] D.P. Schrag, G. Hampt, and D.W. Murray. Pore fluid constraints on the temperature and oxygen isotopic composition of the glacial ocean. *Science*, 272:1930–1932, 1996.

[143] N. J. Shackleton, A. Berger, and W. R. Peltier. An alternative astronomical calibration of the lower Pleistocene timescale based on ODP site 677. *Trans. R. Soc. Edinb.-Earth Sci.*, 81:251–261, 1990.

[144] N. J. Shackleton and M. Hall. Oxygen and carbon isotope stratigraphy of Deep-Sea Drilling Project hole 552a: Plio-Pleistocene glacial history. *DSDP Initial Reports*, 81:599–609, 1984.

[145] N. J. Shackleton and J. Imbrie. The δ^{18}O spectrum of oceanic deep water over a five-decade band. *Climatic Change*, 16:217–230, 1990.

[146] N. J. Shackleton and N. D. Opdyke. Oxygen isotope and palaeomagnetic stratigraphy of Equatorial Pacific core V28-238: Oxygen isotope temperature and ice volumes on a 10^5 and 10^6 year scale. *Quaternary Research*, 3:39–55, 1972.

[147] N. J. Shackleton and N. D. Opdyke. Oxygen-isotope and paleomagnetic stratigraphy of Pacific core V28-239: Late Pliocene to latest Pleistocene. *Mem Geol. Soc, Am.*, 145:449–464, 1976.

[148] S. Shackley, J. Risbey, P. Stone, and B. Wynne. Adjusting to policy expectations in climate change modelling; an interdisciplinary study of flux adjustments in coupled atmoshpere-ocean general circulation models. *Climatic Change*, 43:413–454, 1999.

[149] A. Shaw. *Time in Stratigraphy*. McGraw-Hill, 1964.

[150] B. Singer and M Pringle. Age and duration of the Matuyama-Brunhes geomagnetic polarity reversal from $^{40}Ar/^{39}Ar$ incremental analysis of lavas. *Earth and Planetary Science Letters*, 139:47–61, 1996.

[151] H. v. Storch and F. W. Zwiers. *Statistical analysis in climate research*. Cambridge University Press, 1999.

[152] M. Strain and H. Greenside. Size-dependent transition to high-dimensional chaos in a two-dimensional excitable medium. *Physical Review Letters*, 80(11):2306–2309, 1998.

[153] P. Tass, M. Rosenblum, J. Weule, J. Kurths, A. Pikovsky, J. Volkmann, A. Schnitzler, and H. Freund. Detection of $n : m$ phase locking from noisy data: application to magnetoencephalography. *Physical Review Letters*, 81(15):3291–3294, 1998.

[154] H.R. Thierstein, K.R. Geitzenauer, B. Molfino, and N.J. Shackleton. Global synchroneity of late Quaternary coccolith datum levels: validation by oxygen isotopes. *Geology*, 5:400–404, 1977.

[155] D.J. Thomson. Time series analysis of Holocene climate data. *Philosophical Transactions of the Royal Society of London*, A 330:601–616, 1990.

[156] D.J. Thomson. The seasons, global temperature, and precession. *Science*, 268:59–68, 1995.

[157] R. Tiedemann, M. Sarnthein, and N. J. Shackleton. Astronomic timescale for the Pliocene Atlantic $\delta^{18}O$ and dust flux records of ODP site 659. *Paleoceanography*, 9:619–638, 1994.

[158] K Trenberth. Climate diagnostics from global analysis: Conservations of mass in ecmwf analyses. *Journal of Climate*, 4:707–722, 1991.

[159] K Trenberth and A Solomon. Implications of global atmospheric spatial spectra for processing and displaying data. *Journal of Climate*, 6:531–545, 1993.

[160] G. Upton and B. Fingleton. *Spatial Data Analysis by Example*, volume 2. John Wiley and Sons, 1989.

[161] B. Van Der Pol. Forced ocscillations in a circuit with nonlinear resistance (receptance with reactive triode). *London, Edinburgh, and Dublin Philisophical Magazine*, 3:65–80, 1927.

[162] K.A. Venz, D.A. Hodell, C. Stanton, and D.A. Warnke. A 1.0 Myr record of glacial North Atlantic intermediate water variability from ODP site 982 in the Northeast Atlantic. *Paleoceanography*, 14:42–52, 1999.

[163] A. D. Vernekar. *Long-period variations of incoming solar radiation.* American Meteorological Society, Boston, 1972.

[164] M. Wara, C. Ravelo, and J. Revenaugh. The pacemaker always rings twice. *Paleoceanography*, 15:616–624, 2000.

[165] D. Williams, R. Thunell, E. Tappa, D. Rio, and I. Raffi. Chronology of the Pleistocene oxygen isotope record: 0-1.88 m.y. b.p. *Palaeogeography, Palaeoclimatology, Palaeoecology*, 64:221–240, 1988.

[166] I. Winograd, T. Coplen, J. Landwehr, A. Riggs, K. Ludwig, B. Szabo, P. Kolesar, and K. Revesz. Continuous 500,000-year climate record from vein calcite in Devils Hole, Nevada. *Science*, 258:255–260, 1992.

[167] I. Winograd, J. Landwehr, K. Ludwig, T. Coplen, and A. Riggs. Duration and structure of the past four interglacials. *Quaternary Research*, 48:141–154, 1997.

[168] C. Wunsch. The spectrum from two years to two minutes of temperature fluctuations in the main thermocline at bermuda. *Deep-Sea Research*, 19:577–593, 1972.

[169] C. Wunsch. Global-scale sea surface variability from combined altimetric and tide-gauge records. *Journal of Geophysical Research*, 505:15,053–15,082, 1991.

[170] C. Wunsch. *The Ocean Circulation Inverse Problem*. Cambridge University Press, 1996.

[171] C. Wunsch. On sharp spectral lines in the climate record and the millennial peak. *Paleoceanography*, 15:417–424, 2000.

[172] C. Wunsch. The spectral description of climate change including the 100ky energy. *Climate Dynamics*, 20:353–363, 2003a.

[173] C. Wunsch. Determining the paleoceanographic circulations, with emphasis on the Last Glacial Maximum. *Quaternary Science Reviews*, 22:371–385, 2003b.

[174] C. Wunsch. Greenland-Antarctic phase relations and millennial time-scale climate fluctuations in the Greenland cores. *Quaternary Science Reviews*, 22:1631–1646, 2003c.

[175] C. Wunsch. Quantitative etimate of the milankovitch-forced contribution to observed climate change. *submitted*, 2004.

[176] C. Wunsch and D. Gunn. A densley sampled core and climate variable aliasing. *Geo-marine Letters*, pages DOI 10.1007/s00367–003–0125–220033, 2003.

[177] P. Yiou, C. Genthom, M. Ghil, J. Jouzel, J.M. Barnola, C. Lorius, and Y.N. Korotkevitch. High-frequency paleovariability in climate and CO_2 levels from Vostok ice core records. *Journal of Geophysical Research*, 96:20,365–20,378, 1991.